EFFECT OF MICROSTRUCTURE ON ARCHITECTED MATERIALS FABRICATED BY ADDITIVE MANUFACTURING

by

SHRUTI BANAIT

A dissertation submitted in partial fulfilment of the requirements for the degree of Doctor of Philosophy in

Materials Science & Engineering

Universidad Carlos III de Madrid

Advisors

María Teresa Pérez-Prado

Mónica Campos-Gómez

June 2023

To,

Mom, Dad

ACKNOWLEDGEMENTS

This Ph. D. thesis has come to fruition with many helping hands. First and foremost, I am deeply indebted to my advisors Dr María Teresa Pérez-Prado and Prof. Mónica Campos-Gómez for their valuable insights, guidance and support during the course of the thesis. Their unwavering trust and patience have made this venture possible. This journey saw a lot, from a world-halting pandemic to me walking down the aisle! But more importantly, the journey witnessed me grow, both personally and professionally. My advisors have been a source of constant inspiration throughout this roller coaster of a ride!

It is a pleasure to express my gratitude to Prof. Minh-Son Pham and Dr Chen Liu from Imperial College London for their fruitful collaboration in this dissertation. The research stay at Imperial College was indeed a value-addition experience and I am grateful to have been hosted by them.

I would like to offer my heartfelt thanks to numerous people from Imdea. I appreciate Rosa Bazán, Mariana Huerta and Ainhoa Zapatero for their administrative assistance. I would also like to expresses my warmest regards to Amalia San Román and Vanesa Martínez for their assistance in additive manufacturing and mechanical testing, even well past their working time! I would like to thank Paco, Cris and Jema for the warmest greetings and the lovely chitchat every day! And finally my dearest friends, Nacho Escobar, Nacho Rodríguez, Saumya Sadanand, Marcos Rodríguez, Shegufta Upama, Guille Domínguez, Venkatesh Sivagana, Dr Xueze Jin, Dr Dongfeng Shi, Dr Moumita Rana, Dr Venkata Sai and Dr Chandrashekhar Pilgar for their valuable help and support over the course of this PhD.

I am eternally thankful to my parents who dared to send their beloved daughter away to pursue her dreams. My sister has been a rock in all the hardships and I am extremely grateful to have her support. And last but not the least, my significant other, Saurabh. His exceptional support in everything made this journey so much easier and enjoyable.

PUBLISHED AND SUBMITTED CONTENT

- **S. Banait**, C. Liu, M. Campos, M.S. Pham, M.T. Pérez-Prado, "Coupled effect of microstructure and topology on the mechanical behavior of Inconel718 additively manufactured lattices", Materials & Design, (2022), 111294.
  https://doi.org/10.1016/j.matdes.2022.111294

  The content from the article is wholly included in Chapter 4. The material from this source included in this thesis is not singled out with typographic means and references.

- **S. Banait**, X. Jin, M. Campos, M. T. Pérez-Prado, "Precipitation-induced transition in the mechanical behavior of 3D printed Inconel 718 bcc lattices", Scripta Materialia, 203 (2021) 114075.
  https://doi.org/10.1016/j.scriptamat.2021.114075

  The content from the article is wholly included in Chapter 5. The material from this source included in this thesis is not singled out with typographic means and references.

- **S. Banait**, X. Jin, M. Campos, M.T. Pérez-Prado, "Optimization of SLM Lattice Structures of Inconel 718 For Improving the Mechanical Behaviour", Proc. EuroPM 2021. Edited by The European Powder Metallurgy Association, ISBN: 978-1-899072-54-5; Oct. 2021.

  The content from the article is wholly included in Annex B. The material from this source included in this thesis is not singled out with typographic means and references.

- **S. Banait**, C. Liu, M. Campos, M.S. Pham, M.T. Pérez-Prado, "Effect of microstructure on the effectiveness of hybridization in architected metallic materials", Materials & Design, submitted.

  The content from the article is wholly included in Chapter 6. The material from this source included in this thesis is not singled out with typographic means and references.

- **S. Banait**, M. Campos, M. T. Pérez Prado, "Dynamic strain aging in Inconel 718 additively manufactured lattice structures" Scripta Materialia, submitted.

  The content from the article is wholly included in Chapter 7. The material from this source included in this thesis is not singled out with typographic means and references.

OTHER RESEARCH MERITS

- **Shruti Banait**, Dr Chen Liu, Prof. Mónica Campos-Gómez, Prof. Minh-Son Pham, Prof. María Teresa Pérez-Prado, "*Effect of meta precipitate distribution on the mechanical behaviour of additively manufactured Inconel 718 lattices*" Alloys for Additive Manufacturing Symposium 2022, Munich, Germany, 12-14th Sept 2022.

- **Shruti Banait**, Dr Chen Liu, Prof. Mónica Campos-Gómez, Prof. Minh-Son Pham, Prof. María Teresa Pérez-Prado, "*Coupling micro and mesostructure in additively manufactured Inconel 718 lattice structures*" 18th European Mechanics of Materials Conference, Oxford, United Kingdom, 4-6th April 2022.

- **Shruti Banait**, Prof. Mónica Campos-Gómez, Prof. María Teresa Pérez-Prado, "*Optimization of SLM lattice structures of Inconel 718 for improving the mechanical behaviour*", Euro PM2021 Virtual Congress & Exhibition, Online, 18-22nd Oct 2021.

- **Shruti Banait**, Prof. Mónica Campos-Gómez, Prof. María Teresa Pérez-Prado, "*Manufacturability of Inconel 718 lattices by selective laser melting*" ESAFORM 2020, 23rd International Conference on Material Forming, Online, 4-6th May 2020.

- **Shruti Banait**, Prof. Mónica Campos-Gómez, Prof. María Teresa Pérez-Prado, "*Additive manufacturing of architectured materials*", Women in 3D printing Madrid Chapter, IMDEA Materials Institute, 9th Dec 2019.

Abstract

Additive manufacturing has found its niche in the manufacturing industry. It has become a widespread technology encompassing a vast range of feedstock materials. The ability to manufacture near net-shape end components combined with unprecedented design freedom brands additive manufacturing as a convenient technique to fabricate sophisticated components in high-end industries such as aerospace, automotive and biomedicine. An example of such sophisticated components is a lattice structure, which possess a high strength to weight ratio and is exceptionally useful for light-weighting and energy absorption.

Strut-based lattice structures are characterized by a three-dimensional periodic topological arrangement of beams. The mechanical behaviour of the lattice structures is categorized as either bending-dominated, which features a very compliant and homogeneous response, or stretch-dominated, which is characterized by periodic oscillations in the plastic stress occurring due to strut collapse along specific planes. Until recent times, the topology of the lattice was considered the primary factor determining the mode of collapse of the lattice structures, as captured by the classical Maxwell's criterion and the Gibson-Ashby model.

This research aims at investigating the effect of the microstructure of the base material, coupled with the topology, on the mechanical behaviour of additively manufactured lattice structures. In the first part, the effect of two different microstructure states, i.e., precipitated versus solid solution, on the mechanical behaviour of body centred cubic (BCC), face centred cubic (FCC) and hexagonal close

packed (HCP) single crystalline Inconel 718 lattice structures fabricated via laser powder bed fusion, is analyzed. Secondly, the influence of the base material microstructure on the efficacy of hybridization by the introduction of meta-precipitates, is reported. The phenomenon of dynamic strain aging in the lattice structures is investigated as well at the end.

This thesis effectively pinpoints the crucial role of the base material microstructure on the mechanical behaviour of the lattice structures. In particular, precipitation is observed to induce a transition in the mechanical behaviour mode from bending-dominated to stretch-dominated, which is rationalized based on the alteration of the strut deformation mechanism. The study also reports an optimal meta-precipitate distribution to enhance the mechanical performance of hybrid lattice structures, highlighting hybridization as an effective mean to improve the strength of the lattice structures with a controlled deformation response. Lastly, the research puts forth the novel observation of the topology of the lattice dictating the occurrence of dynamic strain aging in the lattice structures.

The research globally attests that the synergistic effect of microstructural features and unit cell topology widens the avenue of design of lattice structures with exceptional properties.

Contents

List of Figures

List of Tables

CHAPTER 1

Introduction, motivation and research objectives

1.1. Preamble

The advent of additive manufacturing (AM) has revolutionized the manufacturing industry. By virtue of its operating principle of layer-wise construction, AM offers the realization of complex designs, otherwise near-impossible for the traditional subtractive manufacturing [1]. This innate ability of AM to produce complex parts with high geometrical complexity and high reproducibility has inevitably accelerated the use of AM in high-end industries such as aerospace, biomedical and automotive [2]. The absence of tooling or specific jigs and fixtures to build the parts makes AM to possess higher flexibility.

Lattice structures are an emerging class of materials of great interest to industries such as aerospace, automotive and biomedical since they enable the replacement of solid parts with lighter components of higher specific strength [3]. A strut-based lattice structure (Figure 1.1) is characterized by a specific spatial arrangement of beams in a uniform or random pattern. The mechanical behaviour of strut-based lattice structures is generally categorized either as bending-dominated or stretch-dominated [3,4]. In bending-dominated structures yielding is followed by a plateau stress and, finally, by a sharp increase in the stress when the geometrical separation between the struts is diminished during the deformation, triggering densification. In stretch-dominated structures yielding leads to stress drops due to the periodic collapse by buckling or brittle fracture of struts along specific planes, subsequently reaching the densification stage. Bending-dominated structures are more compliant, while stretch-dominated structures have higher stiffness and higher strength for a given relative density, but are more susceptible to sudden failures and thus are not as effective at absorbing energy [5,4].

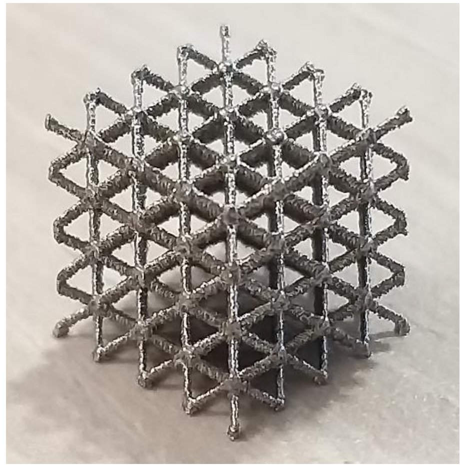

Figure 1.1. A strut-based lattice with body centred cubic topology

It is well known that the mechanical behaviour of lattice structures is highly influenced by their topology and several models have been put forward in an attempt to describe this dependency. The Maxwell's criterion relates the deformation mode (bending or stretch-dominated) to the number of struts and nodes in the lattice [4]. The Gibson-Ashby model [6] predicts that the ratios of the mechanical properties (elastic modulus, yield strength) of a given lattice with respect to those of the constituent base material are proportional to the lattice relative density. However, in a recent systematic attempt carried out by Maconachie et. al. [3] to validate these models by fitting the mechanical properties data, the correlation between experimental observations and model predictions was very small for most topologies investigated. This fact suggests that, besides topology, the properties of the base metallic material, which in metallic alloys are highly dictated by its microstructure, might have a critical influence on the mechanical behaviour of lattices.

This doctoral thesis was designed based on the hypothesis that the material microstructure could have a strong effect on the mechanical behaviour and on the damage and fracture mechanisms of additively manufactured architected materials. This hypothesis will be tested in Inconel 718 strut-based lattices with different unit cells and orientations, as well as on hybrid lattices containing meta-precipitates.

1.2. Research objectives

In order to methodically bridge the aforesaid gap in the literature, following objectives were set for this doctoral thesis:

- Analysis of the effect of precipitates versus solid solution microstructure on the mechanical behaviour of Inconel 718 single crystalline lattice structures with BCC, FCC and HCP topologies.
- Study on the effect of microstructure on the efficacy of hybridization of and FCC lattice structure by the addition of octet-truss meta-precipitates.
- Investigation of the phenomenon of dynamic strain aging in additively manufactured lattice structures.

1.3. Outlook

The research conducted to accomplish the stated objectives is systematically structured as follows:

Chapter 2 recounts the theoretical background of additive manufacturing and lattice structures. Reviewed literature on the development of lattice structures is also summarized.

Chapter 3 describes the methods and equipment utilized in the experimental section of the work.

Chapter 4 reports the critical influence of precipitation on the transition in the mechanical behaviour of BCC lattice structures.

Chapter 5 extends the analysis of the effect of microstructure on the mechanical behaviour to FCC and HCP lattice structures with different orientations. The chapter also unfolds the mechanics of strut deformation to reason the transition in the mechanical behaviour.

Chapter 6 highlights the influence of microstructure on the efficacy of hybridization to improve the mechanical performance of the lattice structures.

Chapter 7 unveils the dependence of dynamic strain aging on the topology of the lattice structures.

Chapter 8 outlines the major conclusions drawn from the research work.

Chapter 9 sets forth the future research lines that can be pursued as an extension of the presented work.

Finally, the bibliography cited in the dissertation work is presented at the end of each chapter. Additional details regarding structural and parametrical optimization of lattice structures and laser powder bed fusion are mentioned in the Annex A and B respectively. The investigation on oxidation of heat-treated lattice structures is narrated in Annex C. Supplementary data for Chapters 5, 6 and 7 are correspondingly incorporated in Annexes D, E and F at the end.

Bibliography

[1] I. Gibson, D. W. Rosen, B. Stucker, Additive Manufacturing, New York: Springer, 2010.

[2] T. DebRoy, H. L. Wei, J.S. Zuback, T. Mukherjee, J.W. Elmer, J.O. Milewski, A.M. Beese, A. Wilson-Heid, A. De, W. Zhang, Additive manufacturing of metallic components – Process, structure and properties, Prog. Mater. Sci. 92 (2018) 112–224.

[3] T. Maconachie, M. Leary, B. Lozanovski, X. Zhang, M. Qian, O. Faruque, M. Brandt, SLM lattice structures: Properties, performance, applications and challenges, Mater. Des. 183 (2019) 108137.

[4] V.S. Deshpande, M.F. Ashby, N.A. Fleck, Foam topology: bending versus stretching dominated architectures, Acta Mater. 49 (2001) 1035.

[5] M. Benedetti, A. du Plessis, R.O. Ritchie, M. Dallago, S.M.J. Razavi, F.Berto, Architected cellular materials: A review on their mechanical properties towards fatigue-tolerant design and fabrication, Mater. Sci. Eng. R 144 (2021) 100606.

[6] M. F. Ashby, A. G. Evans, N. A. Fleck, L. J. Gibson, J. W. Hutchinson, H. N. G. Wadley, Metal Foams: A Design Guide, Butterworth-Heinemann, 2000.

CHAPTER 2

State of the art

2.1. Additive manufacturing

Evolving from rapid prototyping (RP), the technology of additive manufacturing (AM) has witnessed a historic change in the manufacturing space. As opposed to the traditional subtractive manufacturing methods, additive manufacturing is a process of joining materials to make objects from 3D model data, usually layer upon layer, as defined by ASTM F2792-12a [1]. The product can be manufactured directly from computer aided design (CAD) data without any necessity of process planning [1]. The basic workflow of AM starts with part design. The part is then converted to a standard tessellation language (STL) file format for further processing. This step of build processing includes support generation if necessary, by the virtue of the geometry of the part and/or defining the process parameters. Upon required pre-processing, the file is then transferred to the AM machine to build. Once the building is complete, the finished part is subjected to post processing, depending upon the technique of AM that is utilized [2].

2.1.1. Historical perspective

The history of manufacturing a 3D object layer by layer dates back to 1902. After around a half century, during 1960-80, many patents were filed for the manufacturing of prototypes, using this layer by layer approach. Later, in 1987, with the term 'rapid prototyping', 3D Systems produced the world's very first commercialized 3D printing system, 'SLA-1' (Stereolithography Apparatus). Many other systems like 'Solid Object Ultraviolet Plotter' (SOUP) from Japan's NTT Data CMET and 'Solid

Creation System' (SCS) from Sony/D-MEC followed. All these systems were based on the principle of photopolymerization. Meanwhile, Electro Optical System (EOS) and Quadrax introduced the stereolithography system in the Europe.

Rapid prototyping machines kept evolving over time and it was the year 1991 in which the current landscape of AM took shape. Stratasys introduced Fused Deposition Model (FDM), Cubital introduced 'Solid Ground Curing' (SGC) and Helisys introduced 'Laminated Object Manufacturing' (LOM) in the year 1991. Shortly after this, DTM launched 'Selective Laser Sintering' (SLS) and Soligen launched 'Direct Shell Production Casting' (DSPC).

Since then, AM has accelerated its growth over the course of the past three decades, transitioning from the fabrication of prototypes to the manufacturing of fully functional end-user parts. The existing systems kept evolving and many new technologies including 'Laser Engineered Net Shaping' (LENS), 'Polyjet materials printing', 'Ultrasonic Additive Manufacturing' (UAM), 'Selective Laser Melting' (SLM), 'Continuous Interface Production' and 'Fused Filament Fabrication' (FFF) technologies emerged. During the same period of time, AM expanded to cover as well a wide variety of feedstock materials including polymers, metals, ceramics, composites, bio-materials and food for numerous applications [3,4]. The key events that marked the milestones in the advancement of AM are illustrated in Figure 2.1.

In the current scenario, the tool of machine learning (ML) is being utilized to complement human intellect for detecting the anomalies in the manufacturing and ultimately enhancing the part quality in AM [5]. The inherent digital nature of AM coupled with data collection from designs, products, machines, inventory, suppliers, logistics etc., makes AM one of the pillars of the fourth industrial revolution that is Industry 4.0 [6-8].

AM is a broad manufacturing concept that incorporates the numerous technologies mentioned beforehand. These technologies are clustered and categorized together in several different ways such as feedstock material used (metal, polymer, ceramic), type of bonding (direct and indirect), state of feedstock material (liquid, powder, wire, sheet), etc [9,10]. In particular, ASTM F2792-12a [1] classifies the technologies in seven categories on the basis of the machine architecture employed and of the transformation physics of the feedstock materials. Figure 2.2 illustrates the schematics of the seven

AM categories accompanied with a brief description. The corresponding major AM associated commercial technologies are mentioned as well at the bottom.

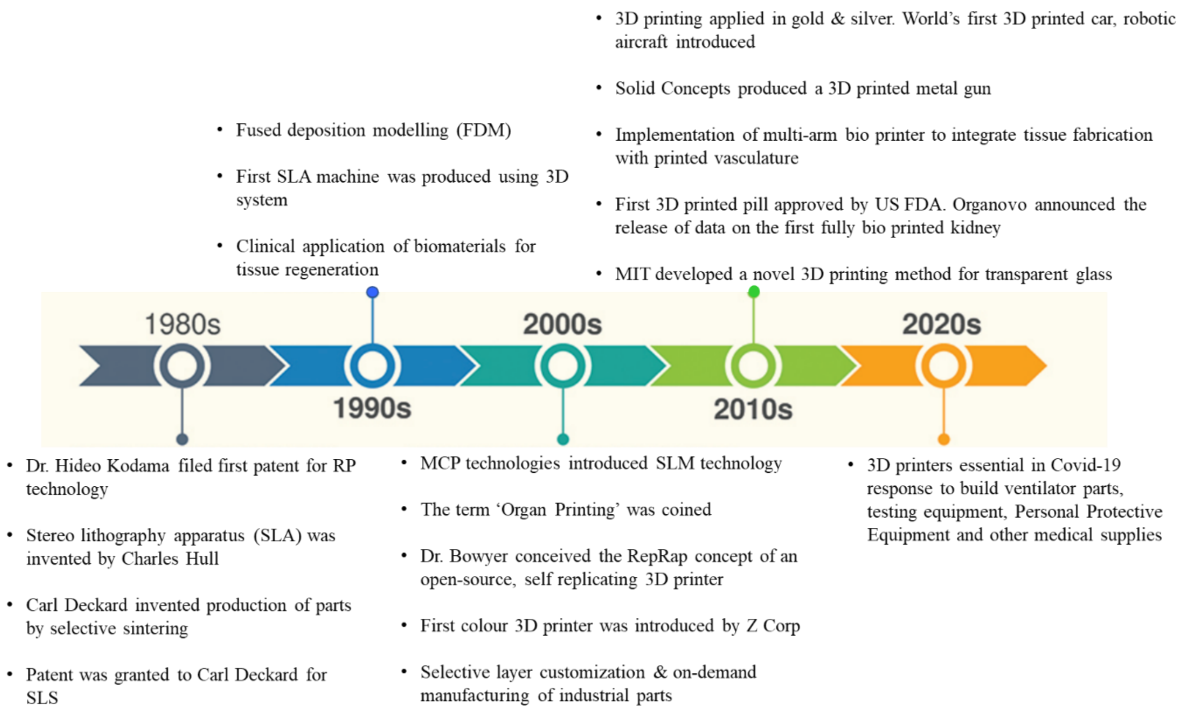

Figure 2.1. Evolution of additive manufacturing [11]

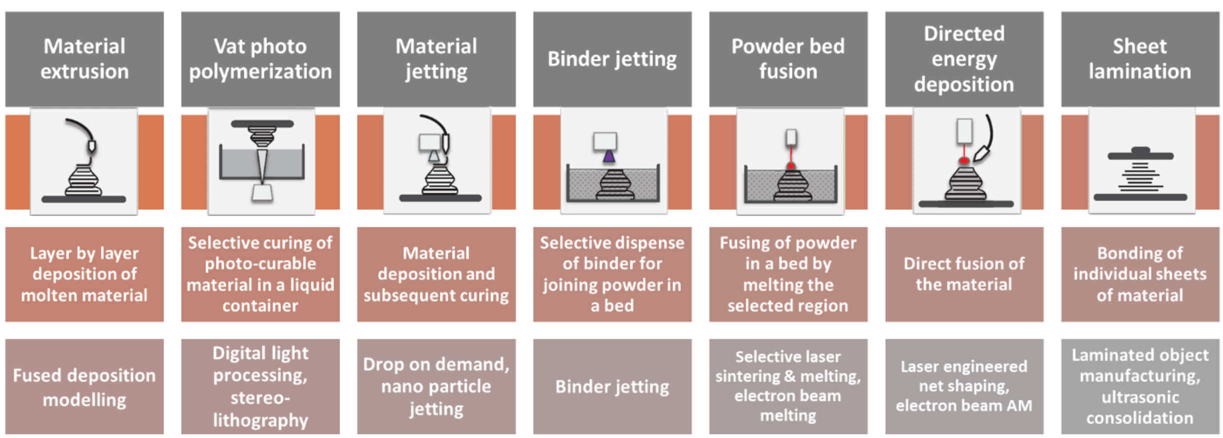

Figure 2.2. Different additive manufacturing processes with schematics, brief description and commercial associated processes [8]

The absence of tooling or specific jigs and fixtures to build the parts makes AM to possess higher flexibility. By virtue of its operating principle of layer-wise construction, AM offers the realization of complex designs, otherwise near-impossible for the traditional subtractive manufacturing [12].

However, the industrial adoption of AM for mass production is limited due to several nontrivial limitations. The multi-scale and highly nonlinear multi-physics phenomena that occur due to the layered nature of AM are still not understood completely. Product quality is greatly affected by various uncertainties such as fluctuations in thermal conditions during the build, natural fluctuation in powder absorptivity and properties of powder particles, high production costs [13,14].

2.1.2. Metal additive manufacturing

AM transitioned from its conceptional 'rapid prototyping' phase, primarily used for design purposes, into a state-of-the-art manufacturing process. The greatest impact of this transition has perhaps been on the use of feedstock materials, initially from polymers to now metals and alloys. This evolution in the use of the feedstock materials, combined with the innate ability of AM to produce complex parts with high geometrical complexity and high reproducibility, has inevitably accelerated the use of AM in high-end industries such as aerospace, biomedical and automotive [15].

The main AM technologies that employ metals and alloys as the feedstock materials are binder jetting (BJ), directed energy deposition (DED), and powder bed fusion (PBF). High melting temperatures of the feedstock materials prompt the use of intense energy sources such as lasers and electron beam for consolidation. The technology of BJ works closely with the principle of powder metallurgy. A binder is deposited on a metal powder bed in the desired shape. Curing of this binder ensures the clustering the metal powder together, followed by sintering to consolidate the powder. DED employs a focused energy source such as laser or electron beam to melt the feedstock metal powder or wire. The feedstock material and the energy source flow concurrently through a nozzle and the molten material is deposited on a substrate endowed with axial motions.

PBF employs laser (LPBF) or electron beam (EB-PBF) to selectively sinter or melt metal powder layer deposited on a substrate from a powder bed [16]. The advantage of PBF lies in its capability to produce complex features with high resolution up to the micrometre scale. The parts produced are highly dense and are in a near-net or net shape. PBF is further categorized into selective laser melting (SLM) and selective laser sintering (SLS), based upon whether the melting is complete or partial, respectively. Since SLM melts the feedstock powder completely, it is favoured over SLS to use metals and alloys in AM [17].

The use of a laser or of an electron beam in PBF processing can be justified on the basis of energy transfer to the matter and setup requirements. A laser source, being a concentrated beam of photons, transfers its energy via electron-photon interaction, consequently transferring heat energy to the matter. In turn, during electron beam processing the kinetic energy of high-speed electrons is converted into heat energy via electron-nuclei interaction. Given that the thermal energy imparted by the laser melts the metal powders, LPBF processing is carried out in an inert environment to keep the level of oxidation in both the part and the metal powders at minimum. On the contrary, a high vacuum is maintained in EB-PBF processing to avoid electrons colliding with gas molecules in the build chamber. EB-PBF can only be used with conductive powders since non-conductive powders tend to accumulate with negative charge. The spot size achieved in the case of electron beam is usually larger than that of laser beam spot size. The smaller spot size in LPBF yields a better surface quality and higher resolution [18]. Metal AM is dominated by lasers since the laser power can be varied over a wide range with a precise spatial and temporal control, leading to the possibility to better tailor the heat affected zone.

Typical laser systems that are used in metal AM are CO_2, Nd:YAG, and fibre, with power ranging from 1 W to 6 kW [19]. There are several laser parameters to be considered while determining the type of laser for the AM system. Since phase transformations in metal AM occur by absorbed radiation, shorter laser wavelengths (e.g. Yb-fibre laser with 1064 nm wavelength as opposed to CO_2 laser with 10.6 μm wavelength) result in better material absorptivity. The intensity of the laser beam, i.e., the laser power per unit area, is another factor governing the process throughput in metal AM. Consequently, higher laser intensities result in higher build rates although at the expense of achievable feature definition. Since the incidental area is essentially proportional to the spot size, the resultant feature quality can be improved using a smaller spot diameter. Laser spot size is ultimately determined by laser wavelength as the intensity of the beam is inversely proportional to the square of the wavelength. Yb-fibre lasers possess higher intensities compared to CO_2 lasers due to their shorter wavelength, despite possessing the same average power [20].

The emission mode employed by the laser system is perhaps the most crucial factor, since continuous wave (CW) or pulsed wave (PW) emission determine the average and peak laser power which directly affect the part quality. True to the name, CW emission mode yields a constant power level over the time while PW emission mode emits pulsed power at constant intervals of time. Figure 2.3 highlights the distinction in the output power profiles of CW and PW emission. Q-switching, mode locking and pulsed pumping mechanisms are used to generate pulses of variable duration. Q-switching is commonly used for Nd:YAG lasers, which produces nanosecond pulses, whereas mode locking produces ultra-short pulses in the range of picoseconds to femtoseconds [21]. Fibre lasers allow fast power modulation through pulsed pumping mechanism where the output is in a square wave. Thus, the peak power obtained in pulsed mode is same as the average power that can be obtained with continuous emission.

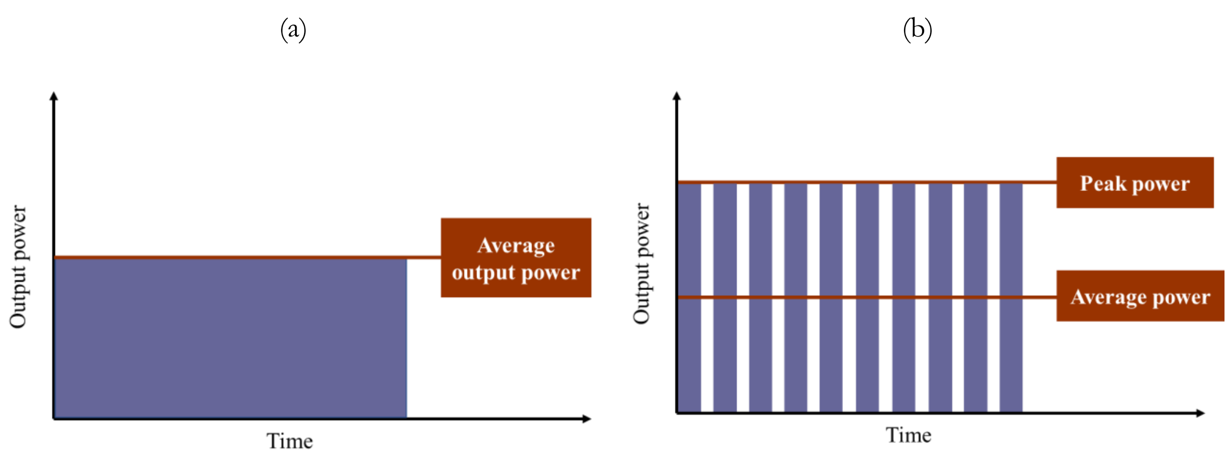

Figure 2.3. Output power profile for (a) continuous wave laser and (b) pulsed wave laser vs time [21]

Higher part densities can be achieved with CW emission since a constant incident laser beam ensures a continuous melt pool but with increased width, which hampers the geometrical accuracy of the part. Contrary to CW emission, PW mode can instantaneously increase the temperature of the powder, owing to the high peak powers. This results in reduced heat dissipation to the surrounding powder. Because of the control over heat input, PW emission is highly useful for small and intricate geometries such as lattice structures. PW mode improves the geometrical accuracy of the part since the pulse can be accurately positioned over the desired scan area [22,23].

The quality of the laser beam is quantified using the term 'beam parameter product (BPP)'. It is the product of the half angle of the beam divergence (mrad) and the beam radius (mm) at the beam waist. The lower the value of BPP, the higher is the energy confinement and ultimately the beam quality. A Gaussian beam profile possesses the lowest BPP, but it is difficult to achieve a perfect Gaussian shape since the refractive indices vary in the laser system, optical surfaces have imperfections, etc. [20].

A comparative account on typical lasers used in metal AM is shown in Table 2.1. Fibre lasers significantly outperform their counterparts owing to their high quantum yield (~94%) (% of incident photons contributing to the emission). Fibre lasers also offer relatively high electrical to optical conversion efficiency and robust but compact system. They exhibit an almost perfect Gaussian profile with a high beam brilliance and a smaller spot. This is possible because of the beam propagation through the optical fibre, which ensures the omission of higher order spatial modes, resulting in limited spatial modes to propagate [20].

Table 2.1. Typical lasers used in metal AM and their characteristics [20]

Laser	**CO_2**	**Nd:YAG**	**Yb-fibre**
Application	SLM, SLS	SLM, SLS	SLM, SLS
Operation wavelength	9.4 & 10.6 μm	1.06 μm	1.07 μm
Efficiency	5-20 %	10-20 %	10-30 %
Output power	Up to 20 kW	Up to 16 kW	Up to 10 kW
Operational mode	CW & PW	CW & PW	CW & PW
Pulse duration	Hundreds of ns-tens of μs	Few ns-tens of ms	Tens of ns-tens of ms
Beam parameter product (BPP)	3-5	0.4-20	0.3-4
Fibre delivery	Not possible	Possible	Possible
Maintenance period	2000 hrs	10,000 hrs	Maintenance free (25,000 hrs)

A laser beam is partly reflected, absorbed, and transmitted when impinged upon the powder according to its optical properties. The fraction of the energy that is absorbed is converted into heat energy that is further used to melt the material. As mentioned earlier, the laser power, its spatial and temporal distribution, the spot size and the beam divergence affect the heat energy transferred to the material. Powder properties such as the particle size distribution (PSD) and the particle shape also influence the absorption of the incident radiation. Once absorbed, the heat flow within the material is determined by the thermal conductivity and diffusivity of the material, as well as by other properties such as the density, and the specific and latent heat. The molten material often possesses a temperature gradient throughout the melt pool. This temperature gradient is the function of beam profile and beam intensity. The surface tension gradient induced by the temperature gradient governs the mass flow within the melt pool through Marangoni convection currents. Melt pool dynamics and the last stage of solidification are affected by the alloy composition, by the diffusion coefficients of the constituent metals and by the liquid-solid range [24]. A summary of the parameters influencing the laser-matter interaction is illustrated in Table 2.2.

Table 2.2. Process parameters in metal AM influencing laser-matter interaction [18]

	Parameters
Optical properties	Absorption, optical penetration
Powder properties	Particle size distribution, particle shape, particle roughness
Thermal properties	Thermal conductivity, diffusivity, specific heat, latent heat, melting temperature, coefficient of thermal expansion
Chemical properties	Reaction enthalpy, chemical solvency
Metallurgical properties	Alloy composition, diffusion coefficients, liquid-solid range
Rheological properties	Surface tension, viscosity

2.1.3. Laser powder bed fusion

LPBF has been increasingly utilized to manufacture high end products from Ni based superalloys, Ti, Al, and Fe alloys, etc [24]. The process of LPBF starts by preparing the CAD data of the component to be built. The CAD data is then converted into STL format using an appropriate software package. According to the geometrical requirements of the component, a support structure is generated prior to the conversion into STL format. The building process then starts with the laser scanning the powder layer by layer to match the sliced data from the STL file. The recoater blade applies consecutive powder layers with pre-defined thickness over the scanned surface as the powder supply piston goes up and the build platform goes down. The excess powder is poured into the overflow container by the recoater blade. This process of layer-wise scanning is repeated until the component is fully built. The schematic of an LPBF process is illustrated in Figure 2.4.

As mentioned earlier, the process is carried out in an inert environment to prevent oxidation. The presence of inert gas in the build chamber is also accompanied by a controlled oxygen content, usually below 1000 ppm. The flow of the inert gas inside the chamber serves the secondary purpose of carrying out vaporized powder plumes away from the powder bed, as they can interfere with the laser beam, affecting its quality [27].

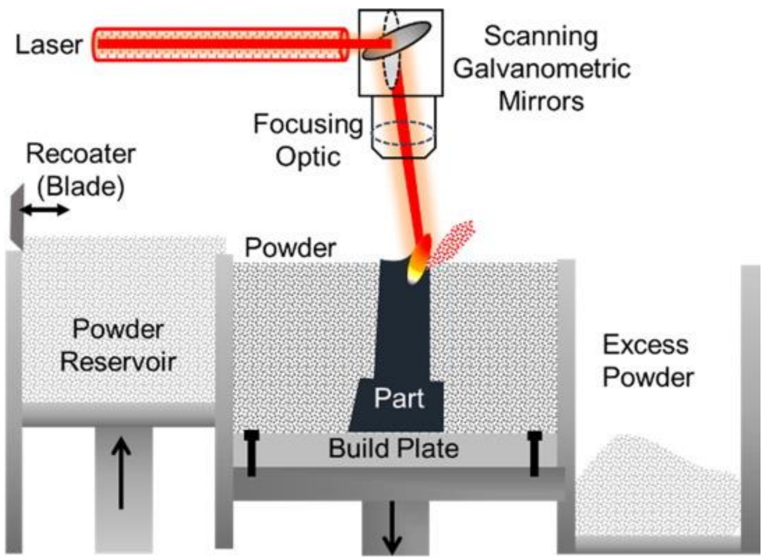

Figure 2.4. Schematic illustration of the LPBF process [25]

Based on the process described above it is apparent that a seamless interplay between process parameters is of utmost importance to ensure a high-quality end product. These parameters are numerous and can be roughly categorized into three groups. Laser power, laser wavelength, spot size, pulse duration and pulse frequency are dependent on the laser system. On the other hand, laser scan speed, hatch distance and scan strategy together make up the parameters that are scan-related. Associated to the feedstock powder, particle shape, particle size and distribution, layer thickness and powder bed density determine the part quality [27]. On the manufacturing level, laser wavelength, pulse duration and pulse frequency are usually pre-set since they depend on the type of laser. For a given feedstock powder, properties such as shape, size and distribution are fixed as well. Consequently, the key parameters that are optimized at the user end to get a fully dense and defect-free part are the laser power (P), the scan speed (v), the hatch distance (h), the spot size (s), the layer thickness (t), and the scan strategy. However, the process optimization is still complex when considering the individual effect of the parameters. Therefore, the parameters are combined into an index called the volumetric energy density (Ev), which is formulated as:

$$Ev = \frac{P}{v \cdot h \cdot t} \quad (1)$$

Although it is apparent that different combinations of parameters can yield the same values of Ev, considering this index is still useful in the early stages of process parameter optimization [28]. Establishing a relationship between Ev and the part density, measured by optical microscopy, may allow for a first determination of the processability window. The definition of the parameters contributing to the Ev is shown in Figure 2.5.

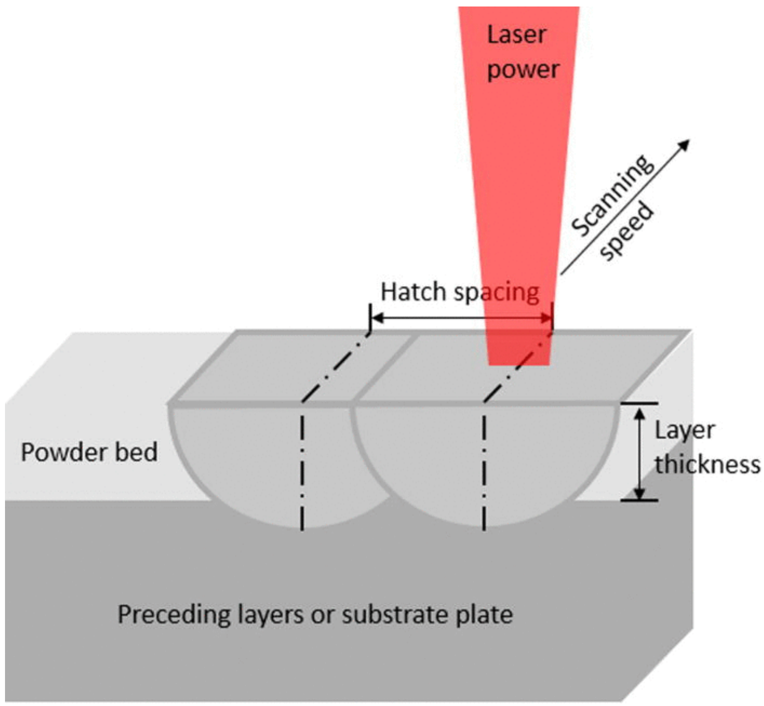

Figure 2.5. Schematic representation of parameters contributing to volumetric energy density [29]

Figure 2.6 represents a processability window with Ev as the determining factor. LPBF processing parameters for the material Ti6Al4V are classified into four zones, I (fully dense), II (over-melting), III (incomplete-melting) and IV (over-heating) in a study by Gong et.al. [30]. It was observed that zones II and III obviously result in internal porosity, attributing to keyhole pores and lack of fusion defects respectively. In the fourth zone (IV), the energy is so intense that material irradiation occurs. Parameter combinations in zone I yield a fully dense sample.

The beam diameter (*d*) and the spot size (*s*) are represented schematically in Figure 7.6 (a). The spot size of the beam with respect to the surface of the powder bed is controlled by the focal length (*f*), as evidenced in Figure 7.6 (b). Positive focal length focuses the beam below the powder bed and negative focal length focuses the beam above the powder bed. The laser beam is usually focused at the surface of the powder bed ($f = 0$) in order to ensure the smallest possible spot size [23].

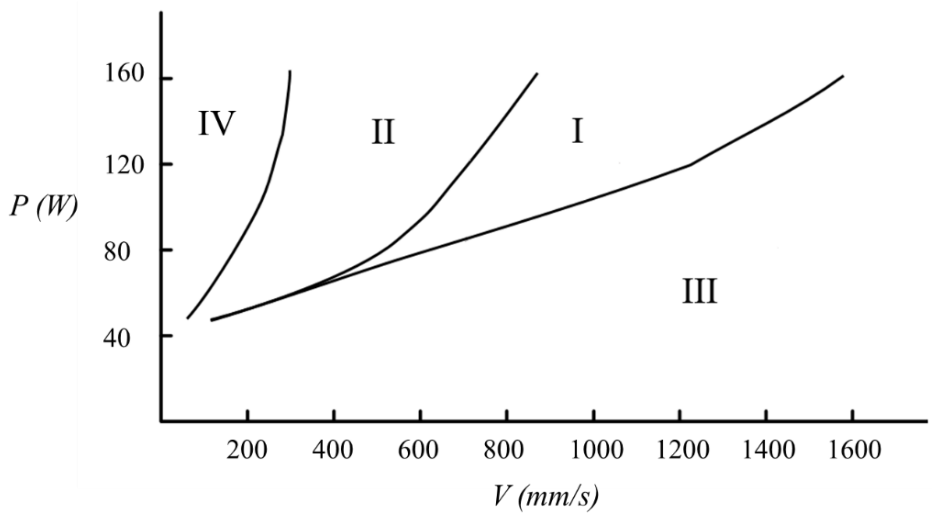

Figure 2.6. Processability window for Ti6Al4V fabricated via LPBF [30]

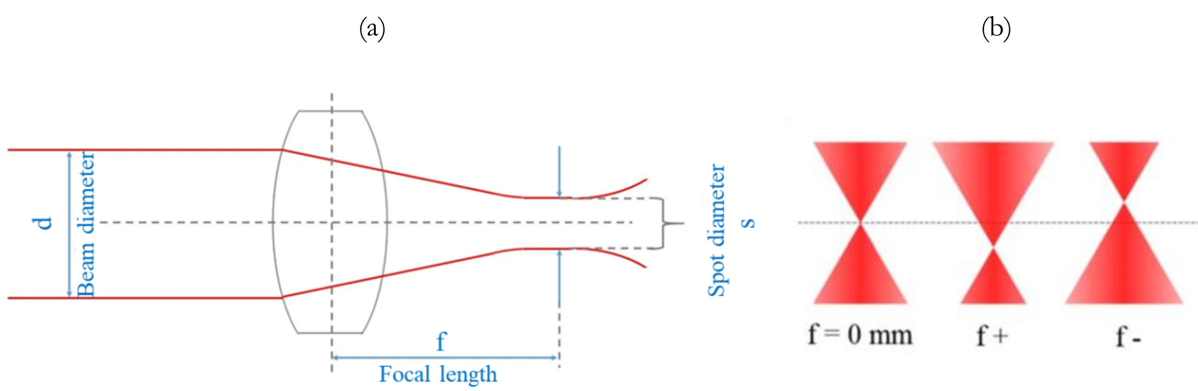

Figure 2.7. (a) Main beam parameters [31] (b) variation of the spot size with respect to the focal length [23]

The scan strategy is the spatial path that is followed by the laser beam when scanning the powder bed. The scan strategy has an obvious effect on part quality since it controls the thermal gradients and the texture of the material. Residual stresses arising from high thermal gradients can cause the build to deform and subsequently develop cracks. Thus, selection of an optimal scan strategy is deemed important. There are many variations of the scan strategies, a few of which are illustrated in figure 2.8.

Unidirectional and bidirectional scan strategies are the most common strategies which are characterized by long scanning vectors. Opposed to that, the island scan strategy consists of short scan vectors divided in small squares on the scan area. The island scan strategy is particularly useful for large parts as the absence of long scan vectors will reduce the residual stress [32].

A bidirectional scan strategy is preferred over a unidirectional scan strategy since unidirectional scan vectors usually impart a severe texture, coarser grains, and ultimately anisotropic elastic properties compared with bidirectional vectors [33]. The bidirectional scan strategy is being increasingly employed in LPBF with a rotation of 67° in each layer. The specific use of 67° rotation is justified on the basis that the scan vector direction is not repeated for the maximum number of layers. This results in minimal warping, surface roughness, anisotropy, and defects in the finished part [34].

(a) Unidirectional (b) Bidirectional (c) Island (d) Helix

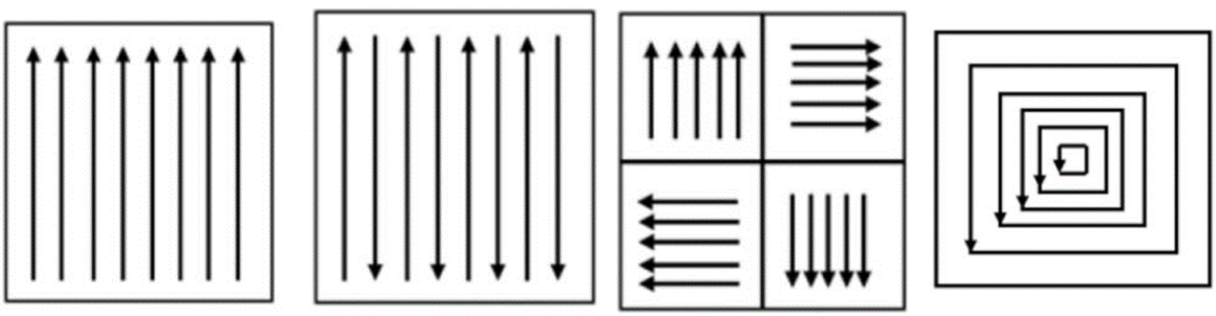

Figure 2.8. Schematic representation of some scan strategies [32]

2.1.3.1. Properties of feedstock

The morphological properties of the feedstock powder greatly influence the layer thickness in LBPF and in turn the part quality. Consistent powder properties are beneficial to ensure the repeatability of the prints. There are several indices to characterize the powder to deem it suitable for LPBF such as particle morphology, particle size distribution (PSD), powder flowability, powder densities, etc. In the case of particle morphology, a spherical shape is preferred since it enhances the flowability of the powder due to the presence of a small contact area. Irregular particle shapes restrict the powder flow by interlocking mechanically and ultimately entangling with each other. The strength, density and surface finish of the end part is hugely dependent on the powder packing density. A higher packing density is achieved when the PSD is wider as the smaller particles fill the interstices between larger particles. However, a wide particle size range is prone to uneven melting in the case of LPBF, therefore forming a trade-off between PSD and laser melting. The upper and lower bounds of the PSD are important while deciding the layer thickness in the LPBF process. All the particles, irrespective of their size, get deposited in a single layer when the layer thickness is larger than the size of the biggest particles. On the other hand, if the layer thickness is smaller than the biggest particle size, finer particles are preferentially deposited. A high fraction of large particles increases the surface roughness of the part whereas finer particles tend to agglomerate, impeding the powder flow. Thus, an optimal particle distribution is essential to ensure a uniform and dense powder layer [35-38].

The method of powder manufacturing has an enormous impact on the morphological, microstructural and rheological properties of the powder particles. There are several techniques that are used to atomize a solid feedstock such as an ingot into powder. The technique of water atomization uses a high-pressure water jet to atomize the molten metal. Water atomized particles are usually irregular in shape because of the impingement of a high energy water jet on the molten metal plus the rapid quenching induced by the water. Water atomization is employed for certain metals and alloys such as steels since the setup is simple and low-cost. To eliminate the irregular shape of powder particles and compromised purity because of oxygen, an inert gas is used to atomize the molten metal. This process of gas atomization typically produces round particles with a diameter ranging from 10 to 300 μm. The method of atomization by plasma uses an inert gas plasma to spheroidize the feedstock material inside a nozzle. This atomization method offers distinct advantages over atomization by gas and water. Firstly, since the atomizing gas is hot, it prevents rapid solidification of the particles. Secondly, smaller volumes of the feedstock materials can be used, for example, a wire instead of a bar or an ingot. In fact, plasma atomization can be a viable method to upcycle reused and poor-quality powders, although the atomization setup can be expensive [16,40,41].

2.1.3.2. Characteristic microstructure

The solidification microstructure in LPBF which essentially involves a melt-pool structure can be effectively described by a set of variables similar to welding. These variables consist of the temperature gradient (G) at the solid-liquid interface, the growth rate or the travel speed of the solid-liquid interface (R), the temperature difference across the interface ($\Delta T = T_{liquidus} - T_{solidus}$), and the diffusion coefficient (D_L) of solute atoms in the liquid. Additionally, the morphology of the melt pool plays a key role as it affects the local solidification rate and the subsequent formation of grains in the fusion zone. Unless a severe degree of supercooling is involved, the solid-liquid interface usually possesses a planar nature. The planar nature changes to cellular, columnar dendritic, and equiaxed dendritic, respectively, as the degree of supercooling rises. Supercooling ensues when the temperature at the solid-liquid interface falls below the liquidus temperature of the alloy system. The insurgence of supercooling results in the co-existence of liquid and solid below the liquidus temperature which manifests as solid cells or dendrites coexisting with intercellular or interdendritic liquid. The planar nature is maintained when the solid-liquid interface is stable with following criterion:

$$\frac{G}{R} \geq \frac{\Delta T}{D_L} \tag{2}$$

Since the process of LPBF involves very high growth rates with moderate temperature gradients due to the remelting of previous layers, columnar dendritic and equiaxed dendritic microstructures are commonly observed [42]. However, the desired microstructure can be obtained to a large degree by adjusting the process parameters. A solidification microstructure map constructed using GR and G/R is widely referred to as a reference to map the possible microstructures that can be attained (Figure 2.9).

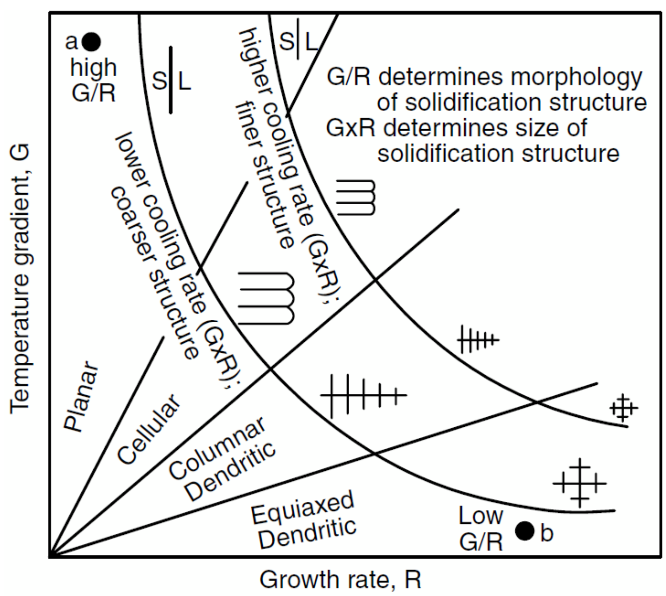

Figure 2.9. Solidification map depicting effect of temperature gradient and growth rate on the solidification microstructure [43]

The layer by layer fabrication in LPBF eliminates the need of nucleation for grain growth since the layer deposited has the same composition as the previous layer. The grains grow epitaxially from the substrate only when using identical or similar metals. In the case of dissimilar metals, the nucleation of phases at the melt pool border is required. The grain size, shape and overall texture of the build are of critical importance since the mechanical properties are acutely affected by the solidification structure [15,16,42,43].

2.1.3.3. Melt pool & associated defects

Defects formed during LBPF processing such as porosity, lack of fusion, evaporation of molten metal, residual stresses, surface roughness, cracking and delamination, etc, greatly depend on the melt pool dynamics.

Melt pool is formed by two different modes, namely conduction and keyhole, each of which prevails depending on the laser power and the scan speed, as shown in Figure 2.10. The melt pool shape is shallow and wide in the conduction mode whereas it is deep and narrow in the keyhole mode. For sufficiently high intensity of the laser beam, a part of the metal gets evaporated in the keyhole mode, resulting in the formation of almost spherical holes in the melt pool. On the other hand, irregularly shaped voids may form in the melt pool as a result of inadequately low energy density. Under such conditions, the laser beam is unable to penetrate into the previously deposited layer or the substrate, creating a lack of fusion [44,45]. An additional source of porosity can be the entrapment of gas in the feedstock powder itself, that may occur during atomization [15].

The surface roughness of built components is a concerning factor when considering the mechanical performance of the part, especially the fatigue properties. For high end applications, additively fabricated parts require an average surface roughness value smaller than 1 μm. There are two major sources of surface roughness. The first kind of surface roughness ensues due to the 'stair-stepping' effect, which arises due to the approximation of layers forming curved or inclined geometries. The stair stepping effect increases with increasing layer thickness, thus becoming a trade-off between intricacy and improved build time. The second and most commonly observed type of surface roughness arises due to the improper fusion of powder particles and due to the balling phenomenon. Lower energy densities cause partially melted powder particles to stick to the surface of the build, forming a rough surface.

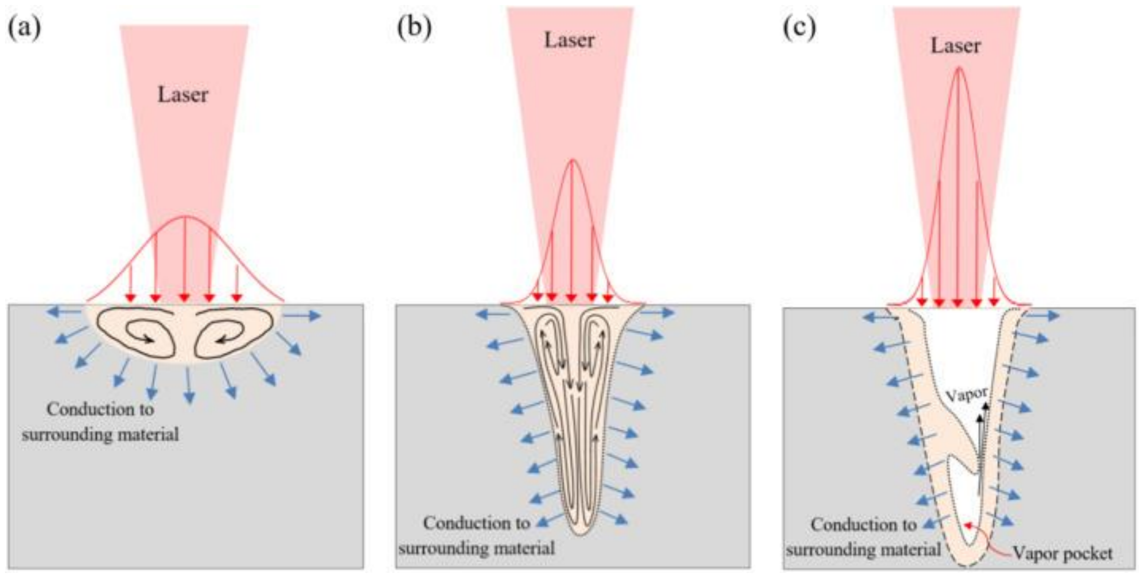

Figure 2.10. Mechanisms of melt pool formation. (a) Conduction mode, (b) keyhole mode and (c) collapse of keyhole mode and formation of porosity [47]

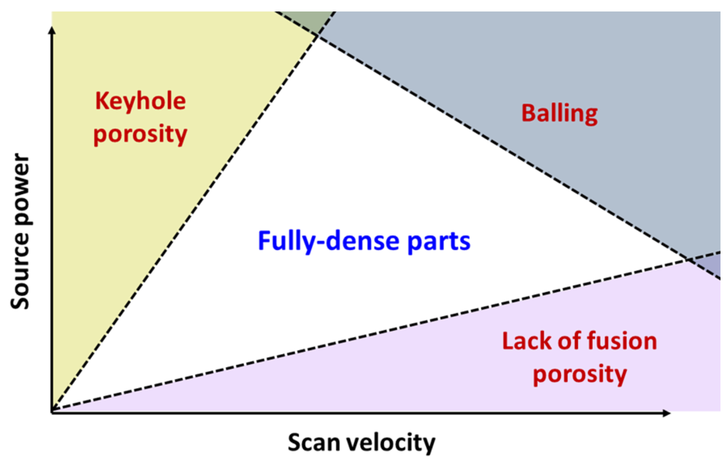

Figure 2.11. Effect of power source and scan velocity on the formation of defects [42]

The magnitude of the average surface roughness that is caused by insufficient melting is of the order of the diameter of the powder particles. The balling phenomenon occurs when the elongated melt pool collapses and breaks into small islands. The surface tension gradient drives these small islands towards the edge of the melt pool, where they solidify creating a rough surface profile. High energy input combined with lower scan velocities ensure a complete melting of powder particles and a reduced balling phenomenon [15,42,45]. The effect of the power source (laser/electron beam) and of the scanning velocity on the formation of porosities and on the balling defect is depicted in Figure 2.11.

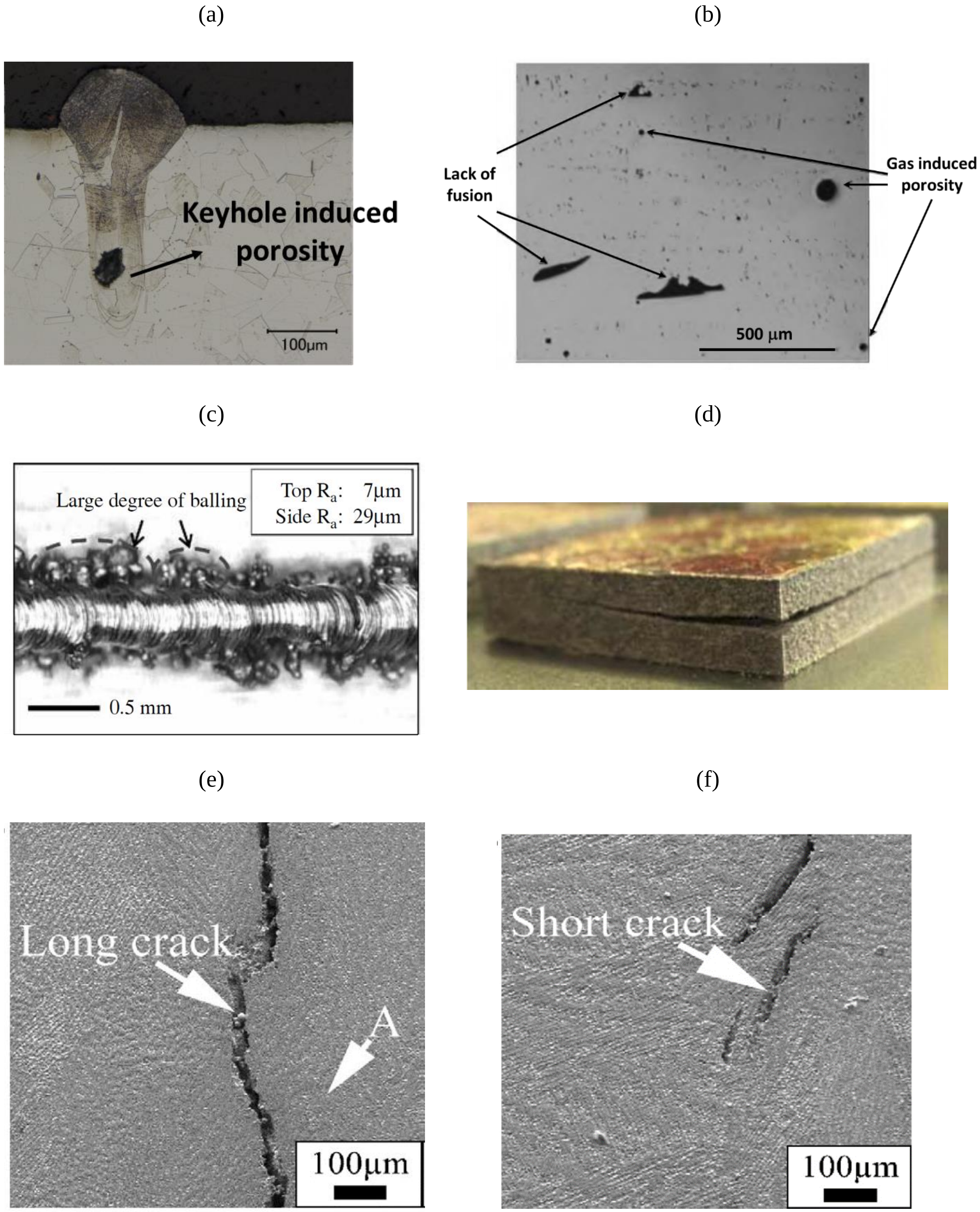

Figure 2.12. Various defects in LPBF. (a) Keyhole induced porosity [47], (b) lack of fusion and gas induced porosity [48], (c) balling [49], (d) delamination [50], (e), (f) cracking [51]

Residual stresses are inherent to the deposition of molten metal on a comparatively cooler substrate or formerly deposited layer. Residual stresses are particularly detrimental to the part quality since they can cause delamination of layers, part distortion, and compromised fracture resistance of the part. Effective mitigation of residual stresses is important since the distortion can be large enough to disturb the raking of powder in successive layers [15,16]

Finally, cracking is also one of the defects that occur in LPBF processed parts. Solidification cracks arise due to the thermal contraction of the deposited layer with respect to the preceding layer or the substrate. The contraction of the solidifying layer generates a tensile stress, which upon surpassing the strength of the material, generates a crack. On the other hand, liquation cracking is seen in the mushy zone. When the alloy is rapidly heated below the liquidus temperature, certain phases such as carbides with low melting points melt first. During the course of solidification, the mushy zone suffers a tensile stress because of solidification shrinkage. Under this stress field, the liquid surrounding the carbide phases may act as crack initiation site. Susceptibility to cracking increases when the alloys possess a wide mushy zone, larger magnitude of solidification shrinkage, and high thermal contraction [43]. Figure 2.12. depicts some of the defects explained above.

The presence of defects such as residual stresses, porosity, surface roughness and undesired microstructures compromises the build quality, rendering the build prone to failure. Several post-processing techniques are employed to alleviate these defects considerably and to thus enhance the part performance. The technique of hot isostatic processing (HIP) is commonly used to diminish the porosity in the build. This technique uses high temperature and pressure to plastically deform the material in an inert environment causing densification. This leads to (at least partial) pore collapse, forcing the entrapped gases to dissolve in the material.

Heat treatment of the material is arguably the most important post processing technique as the desired metallurgical microstructure is nearly unachievable otherwise. There are varying types of heat treatments employed depending on the alloy and on the corresponding as-built microstructures. Heat treatments also serve the additional purpose of alleviating the residual stresses formed during fabrication. Polishing and machining processes are usually used to improve the surface finish of the build. Lower surface roughness greatly augments the fatigue performance, dimensional accuracy and aesthetics of the part [16].

2.1.4. Typical alloys by LPBF

AM of pure metals is largely unexplored since they exhibit poor mechanical properties and reduced oxidation resistance [52]. On the other hand, countless alloys have been assessed to test their feasibility for AM fabrication. However, the majority of the alloy systems consist of limited base metals. Typical alloy systems popular with LBPF include Fe-based, Ti-based, Al-based, and Ni-based. Fe-based alloy systems usually consist of the most commonly utilized engineering material that is steel. Various steel grades such as austenitic, maraging, duplex, precipitation hardened and martensitic have been explored extensively in the LBPF literature. AM offers the advantage of generating unique microstructures in the case of Fe-based alloys due to the high thermal gradients involved and the allotropic properties of ferrous alloys. At the same time, a careful control of process parameters is necessary in order to avoid the formation of unwanted phases such as retained austenite and martensite [15,16,29,40,53].

Ti-based alloy systems remain one of the most vastly explored materials due to their excellent light-weighting properties while maintaining high strength, resistance to fatigue and corrosion. Ti-alloys such as Ti-6Al-4V are extremely attractive for aerospace and biomedical applications due, additionally, to their biocompatible properties. Studies have shown that LPBF processed Ti-6Al-4V alloy possess superior strength compared to their cast counterpart, due to the formation of acicular martensitic α' phase. The martensitic α' phase increases the strength of the alloy at the expense of ductility. Heat treatments are then employed to enhance the ductility by transforming α' phase into α and β phases. In the case of Al-based alloys, the number of alloys available for AM is rather limited as some Al alloys are barely weldable. High strength Al alloys, such as Al7075, undergo severe hot cracking during LPBF processing and thus mitigation strategies including alloy design, nanoparticle addition, and others, have been put in place to allow for a limited defect density [54,55]. However, on a more favourable side, the high thermal conductivity of Al allows for high processing speeds and reduced thermal stresses. Typical Al-alloys that have been processed by AM include AlSi10Mg, 6061, 1000 and 2000 series [15,16,29,40,53].

Ni-based alloys are the most researched metallic materials after steels and Ti-alloys. They are widely used in aerospace industry due to their notable property of strength retention at elevated service temperatures. Furthermore, they offer outstanding creep, corrosion, oxidation and stress rupture resistance at temperatures around 850 °C, rightfully gaining the tag as superalloys [57]. The Ni in these superalloys makes up for at least 50% by weight of the total alloy composition. In the majority of the alloy compositions, the number of alloying elements usually exceeds ten. Table 2.3. enlists the major alloying elements in Ni-based superalloys with their functions. There are numerous Ni-based alloys that are paired with LBPF fabrication: Hastelloy-X, Rene 95, Inconel 625, Inconel 718, Inconel 939, Nimonic 75, Astroloy being some examples [57,58].

Table 2.3. Major alloying elements in Ni-based alloys and their respective roles [56]

Alloying element	Function
Chromium	Solid solution strengthening; corrosion resistance
Molybdenum	Solid solution strengthening; creep resistance
Tungsten	Solid solution strengthening; creep resistance
Cobalt	Solid solution strengthening
Niobium	Precipitation hardening; creep resistance
Aluminium	Precipitation hardening; creep resistance
Carbon	Carbide hardening; creep resistance

Inconel 718 is the most important alloy for the aerospace sector because it is primarily used in jet engines. It retains high strength, corrosion and oxidation resistance up to around 750 °C. The high room and elevated temperature strength of Inconel 718 comes from a fine dispersion of hard intermetallic precipitates [56]. The precipitation strengthened alloy contains two primary precipitates, γ′ and γ″ dispersed in γ matrix. The high temperature strength is mainly derived by γ″ (Ni_3Nb) precipitates with body centred tetragonal (BCT) structure, its fraction is 3x larger than that of γ′. The γ′ phase has cubic structure with a composition as Ni_3(Al, Nb, Ti) with a $L1_2$ structure. Both the precipitate phases are found coherent with the FCC γ matrix. The strengthening from γ″ arises due to the larger lattice misfit between γ″ and γ, since there is a considerable difference between the lattice parameters of both the phases [59]. γ″ precipitates appear as disc-shaped particles in the microstructure of Inconel 718, whereas γ′ pose spheroidal/cuboidal morphology [60], as seen from Figure 2.13. It illustrates a dark field electron micrograph of a Ni-based superalloy after aging heat treatment.

Other than γ′ and γ″, carbides ($M_{23}C_6$ and M_6C) and borides are also present in Ni-superalloys which reside on γ grain boundaries. Topologically close-packed (TCP) phases are also seen which include μ, σ, Laves etc. Alloying elements such as Cr, Mo, W when present in excessive quantities, promote the formation of TCPs. Precipitation of TCPs is detrimental to the mechanical performance of Ni-superalloys due to a number of reasons. They are arranged in a non-metallic and highly directional bonding, they form complex crystal structures tessellated in layers of hexagonal, pentagonal and triangular shapes, forming a Kasper coordination polyhedral. This topological arrangement causes naming the phases as topologically close-packed [62].

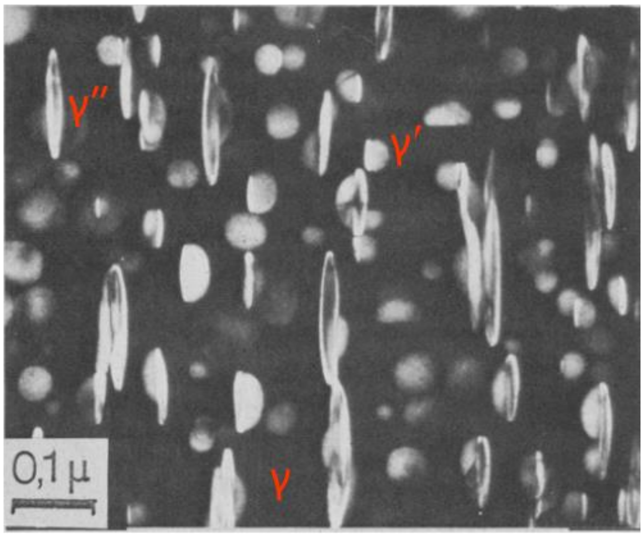

Figure 2.13. Morphology of γ′ and γ″ in a Ni-superalloy aged at 750 °C for 128 h [61]

The microstructure of LPBF processed Inconel 718 consists of smaller grains by a factor of 10 when compared with as-cast Inconel 718 [16]. Usually a columnar dendritic network of grains stretched parallel to the building direction is observed in the as-built state, resulting in anisotropic mechanical properties [63,64]. The major strengthening phase is γ″ owing to the high Nb content in Inconel 718, Additionally, carbide phases such as MC, $M_{23}C_6$ and M_6C (M can be Ti, Cr or Mo) also strengthen the γ-Ni matrix. Undesirable phases such as δ (Ni_3Nb, orthorhombic) and Laves also appear in LBPF processed Inconel 718. The δ phase segregates in the Nb-rich interdendritic regions. It is an acicular phase which reduces the fracture toughness, fatigue properties, high-temperature strength and resistance to corrosion in LPBF fabricated Inconel 718. On the other side, the Laves phase acts as a preferential site for crack nucleation [65].

Appropriate heat treatments are used to strengthen Ni-superalloys depending upon the type of strengthening mechanism intended for specific alloy. Severe anisotropy, segregation and residual stresses present in the microstructure of LPBF processed Inconel 718 necessitate homogenization treatments or high-temperature solutionizing [65]. Inconel 718 has been extensively used for turbine blades, discs and shafts in the jet engines [66]. Lower amounts of Al and Ti in the composition of Inconel 718 alloy improves its weldability, and therefore, plentiful literature is available on LBPF processed bulk Inconel 718 [66,67,68,69,70, 71]. However, despite being widely researched and having excellent printability, Inconel 718 is scarcely explored to manufacture intricate geometries such as lattice structures.

2.2. Lattice structures

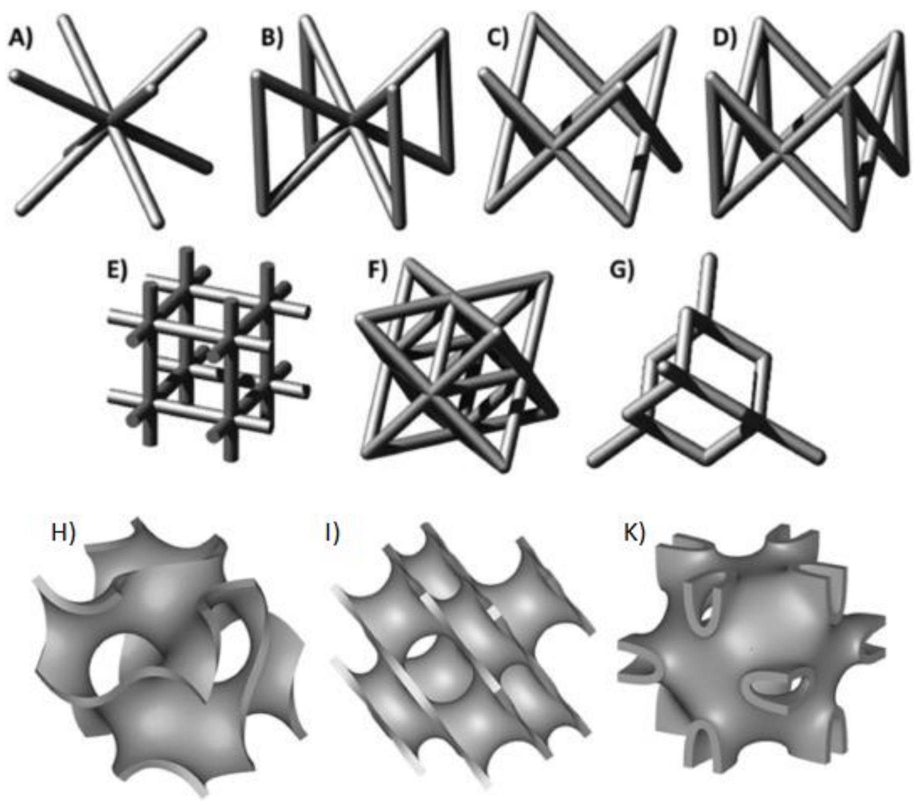

Figure 2.14. Various strut-based and TPMS lattice structures. (a) BCC, (b) BCCZ, (c) FCC, (d) FCCZ, (e) cubic, (f) octet-truss, (g) diamond, (h) Schoen gyroid, (i) Schwarz diamond and (k) Neovius [72]

A lattice structure is characterized by a specific spatial arrangement of beams or walls in a uniform or random pattern, resembling to cellular structural configuration. Lattice structures are of great interest to industries such as aerospace, automotive and biomedical since they enable the replacement of solid parts, maintaining similar absolute strength but much higher specific strength [72]. A lattice structure is formed by a 3D arrangement of unit cells.

Lattice structures are classified as follows. Firstly, they can be open-celled or closed-celled. Lattice structures are categorized based on the structural element as well. The element can be beam (strut) or wall (sheet). There are numerous configurations in strut-based lattices inspired from crystalline lattice structures which include body centred cubic (BCC), face centred cubic (FCC), octet truss, hexagonal close packed (HCP), diamond, truncated octahedron, etc. In the case of walled structures, triply periodic minimal surfaces (TPMS) are very popular since their architecture can be manipulated by trigonometric equations. Gyroid, primitive, Neovius are some of the examples of TPMS lattices [41,72]. Figure 2.14 summarizes commonly used strut-based and TPMS lattice structures. Strut-based lattices are suitable for structural applications whereas walled lattices are apt for thermal applications such as heat exchangers by virtue of their large surface area.

Lattice structures can also either be ordered or disordered. Non-uniformity in the configuration is induced by functional grading, random cell size (foams) etc. [41]. The collapse response of uniform lattice structures is more reliable, and this feature makes them suitable for energy absorption applications [73].

The Maxwell number criterion has been utilized to characterize the behaviour of the strut-based lattice structures. If the structure has 's' struts with 'n' nodes, the Maxwell number 'M' is given as [74],

$$M = s - 3n + 6 \tag{3}$$

When $M < 0$, bending stresses prevail in the structure upon loading, due to the presence of fewer struts to equilibrate the external acting forces without the bending moments induced at the nodes. Thus, the structure is said to be bending-dominated. On the other hand, when $M \geq 0$, the external acting forces are equilibrated by the forces of tension and compression induced in the struts and no bending occurs at the nodes, resulting in a stretch-dominated structure [75]. Figure 2.15 summarizes the mechanical behaviour of strut-based lattice structures and associated mechanical properties, while Figure 2.16. enlists the Maxwell numbers pertaining to few lattice topologies.

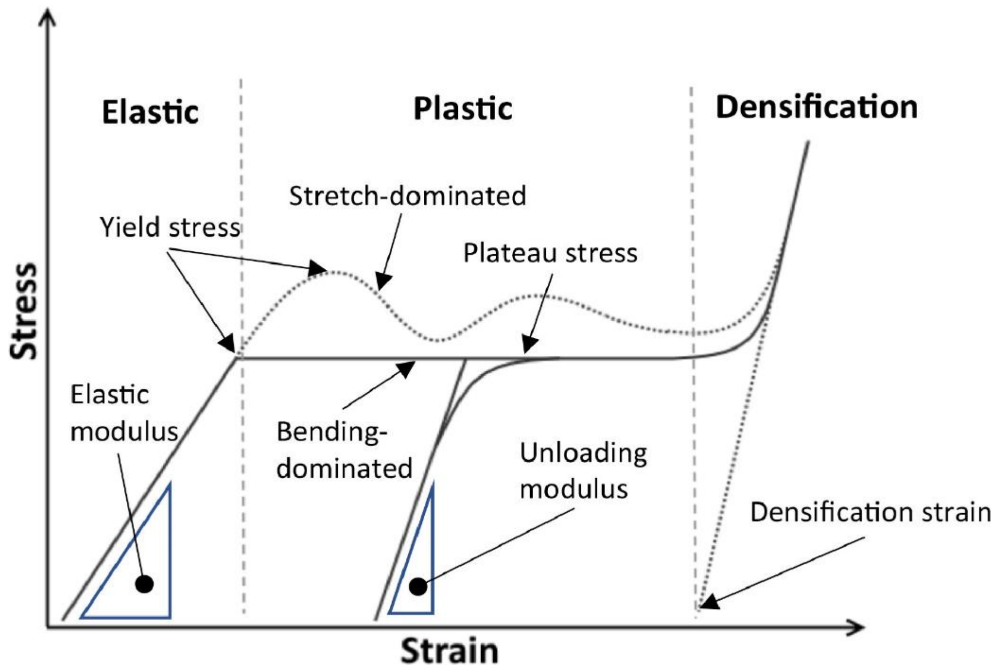

Figure 2.15. Stress-strain curves for bending-dominated and stretch-dominated lattice structures and associated mechanical properties [72]

	(a) BCC	(b) FCC	(c) CP
Unit Cell Type			
Maxwell Nr.	-13	-12	-6
	(d) BCC+CP	(e) FCC+CP	(f) BCC+FCC
Unit Cell Type	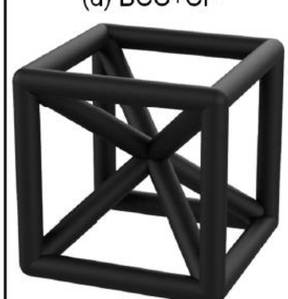		
Maxwell Nr.	-1	0	-7

Figure 2.16. Maxwell number for few lattice topologies [77]

While Maxwell's number predicts the mechanical behaviour of the lattice structures, the Gibson-Ashby model approximates the mechanical properties of cellular structures with respect to their bulk equivalents. According to the model, the ratio of the elastic modulus of the lattice structure to the elastic modulus of the bulk material (E'/E) and the strength of lattice structure to the yield strength of the bulk material (σ'/σ_{ys}) are proportional to the relative density of the lattice structure (ρ'/ρ). In particular,

$$E'/E = C_E\,(\rho'/\rho)^{nE} \tag{4}$$

and $$\sigma'/\sigma_{ys} = C_\sigma\,(\rho'/\rho)^{n\sigma} \tag{5}$$

where C and n are constants dependent upon the topology of the lattice and are derived experimentally [76].

Recent research on lattice structures relates the variation of the mechanical behaviour with respect to different topologies using an array of base materials [78-85]. In a particularly distinctive study by Pham et. al. [86] translated the metallurgical hardening mechanisms to the metamaterial scale in order to enhance the damage tolerance of strut-based lattices. For example, grain boundary hardening was achieved by printing an architected lattice containing two meta-grains (meta-grains are the grains at the mesoscale), separated by a meta-twin boundary, as shown in Figure 2.17 (a) below. They observed that, when loaded in the direction parallel to the twin boundary, shear bands formed in the direction parallel to the plane of maximum shear stress, as shown by Figure 2.17 (b). Grain boundary strengthening was also pursued by increasing the number of meta-grains, essentially reducing their size. Figure 2.17 (c) displays architected lattices with 8, 16, 18 and 27 meta-grains respectively. They observed that, under same loading conditions, the propagation of shear bands is effectively hindered when the size of the meta-grain decreases due to more frequent changes in the orientation of the meta-grains along the shear band propagation path. The yield strength of the architected lattice thus increased with the increase in the number of meta-grains, as evident from Figure 2.17 (d). Both phenomena altogether confirmed the applicability of grain boundary strengthening into the architected lattices.

The phenomenon of meta-precipitation hardening was also achieved by Pham et.al. [86] incorporating face centred tetragonal (FCT) meta-precipitates in an FCC matrix, as illustrated in Figures 2.18 (a) and

(b) below. The meta-precipitates were designed in such a way that they possessed different lattice parameters from that of the FCC matrix, as shown in Figure 2.18 (c) and (d).

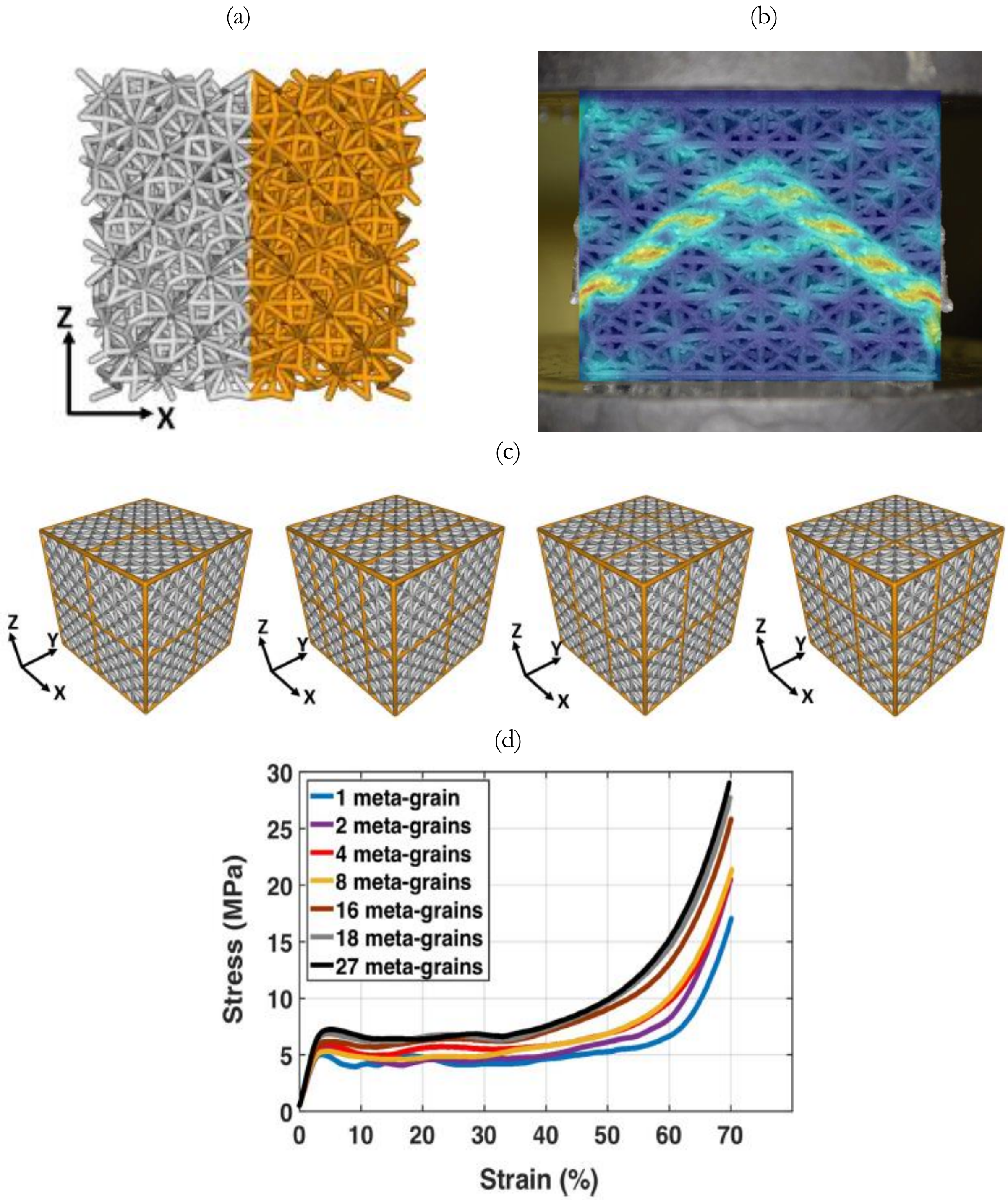

Figure 2.17. a) A twinned architected FCC lattice, (b) formation of shear bands in twinned meta-crystal on maximum shear plane, (c) number of meta-grains in the architected FCC lattices and (d) stress-strain curve of lattices containing different meta-grains [86]

The same researchers observed that shear band propagation was prevented and that shear bands bowed at the interface between the matrix and the meta-precipitates [87], as seen in Figure 2.19 (a). This proved that mechanical response of the architected lattice can be manipulated by controlling the distribution & volume fraction of the meta-precipitates. This effect can be seen from the stress-strain curve shown in Figure 2.19 (b). It can be observed that the strength of architected lattice with meta-precipitates is comparably higher than the strength of the architected lattice without meta-precipitates.

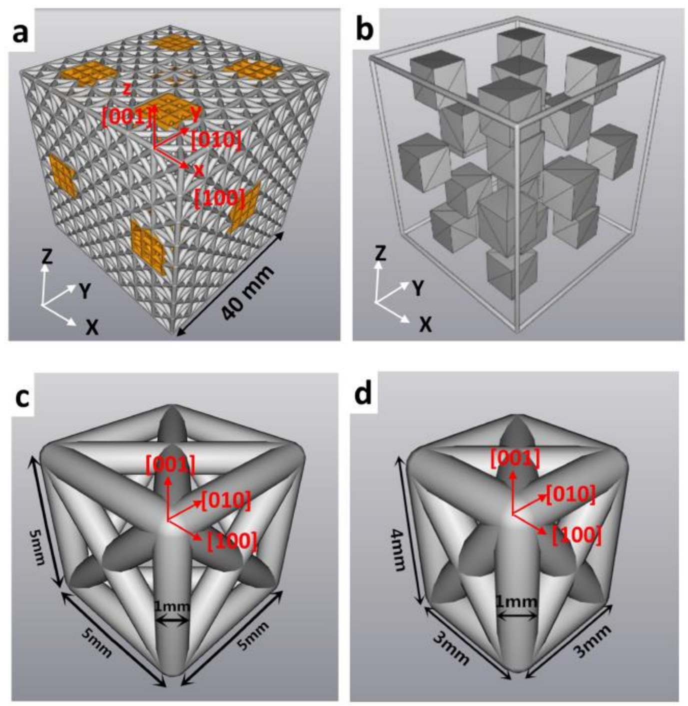

Figure 2.18. (a), (b) Distribution of meta-precipitates inside architected FCC lattice, (c) unit cell configuration of matrix and (d) unit cell configuration of precipitate [86]

Finally, in order to achieve the effect of multi-phase hardening, an architected lattice comprising two different phases (FCC and BCC), was designed, as shown in Figure 2.20 (a) [86]. It can be seen that the top and the bottom layers of the architected lattice are made of an FCC meta-phase, whereas, the middle layer is comprised of a BCC meta-phase. Because of the higher connectivity and higher density, the strength of the lattice largely depends upon the FCC phase. On the other hand, the softer BCC phase accommodates the plastic deformation and confines the shear bands. This phenomenon is clearly seen in Figure 2.20 (b). It can also be observed that the strength of multi-phase architected lattice (solid black line) is higher than that of individual FCC (solid grey line) and BCC (dotted grey line) meta-phases.

(a) (b)

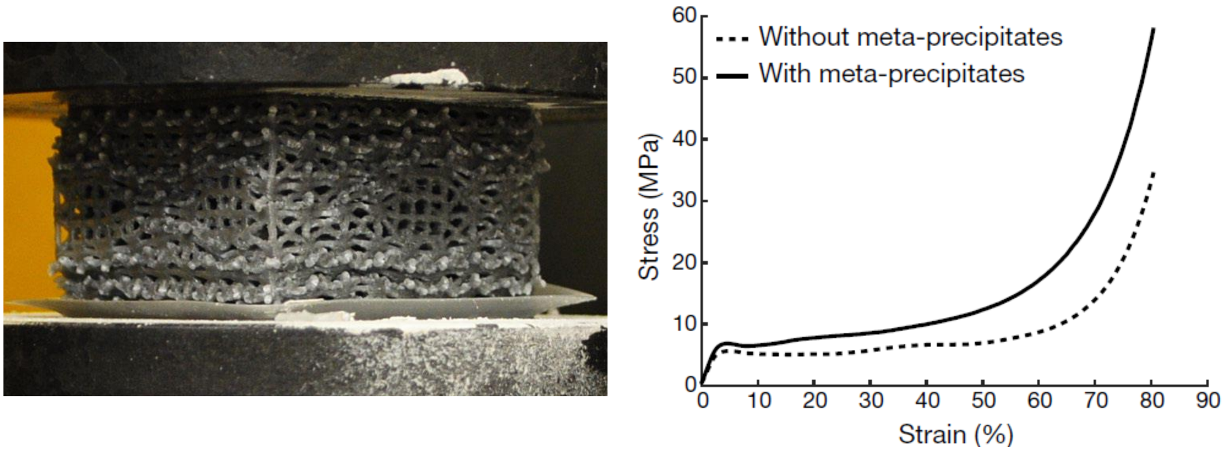

Figure 2.19. (a) Formation and restriction of shear bands in FCC architected lattice containing FCT meta-precipitates and (b) stress-strain curve of architected lattices with and without meta-precipitates [86]

(a)

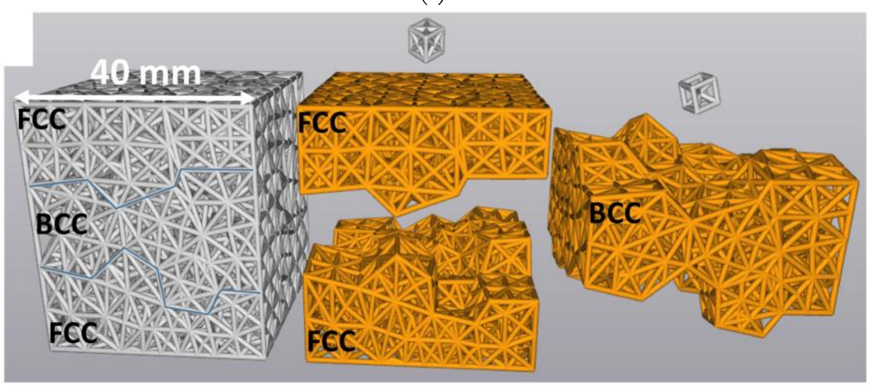

(b)

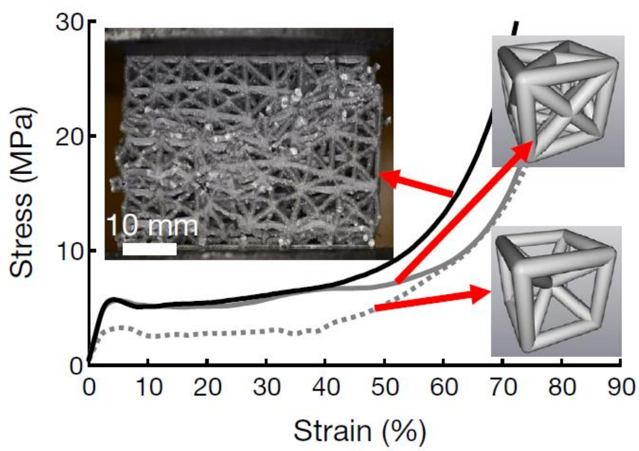

Figure 2.20. (a) Architected lattice containing two different phases and (b) stress-strain curve indicating compressive response of multi-phase architected lattice and single-phase architected lattices [86]

2.3. Additive manufacturing of lattice structures

Manufacturing methods such as powder metallurgy, vapour deposition, direct forming, etc. have been traditionally utilized to fabricate lattice structures with limited geometrical-freedom. AM processes, on the other and, exactly deliver the design freedom needed for outstanding control of the size and of the architecture of such structures [18,41]. AM processes are convenient to fabricate open-celled structures alone, as removal of entrapped powder inside the closed-celled structures is not feasible.

Many earlier studies have investigated the relationship between the lattice topology and the mechanical behaviour of additively manufactured lattices [78-85,88,89]. In general, it has been seen that there is a wide dispersion of data, and that the predictions based on the Maxwell number and on the Gibson-Ashby model are not always accurate to describe the mechanical behaviour of architected materials manufactured by laser powder bed fusion [72].

There are comparatively fewer works investigating the influence of the material microstructure. Wauthle et.al. [90] investigated diamond lattice topology with Ti6Al4V alloy as the base material. The researchers observed that stress relieved lattice structures were stiffer with higher yield strength than as-built and HIPed lattice structures in compression testing. They attributed the change in the mechanical properties to transformation of martensitic α' in the as-built lattice into transformed α-platelets after stress relief treatment. In the case of HIPed lattice structures, the maximum strength was lower than that of stress-relieved lattices but the ductility was increased due to the transformation of α' (as-built) into $\alpha+\beta$ phases.

Maskery et.al. [73] compared the compressive behaviour of AlSi10Mg double gyroid lattice structures in as-built and heat-treated conditions. They noted that the mechanical behaviour of the lattice structure changed from stretch-dominated (as-built) to bending-dominated after the solution treatment followed by aging. Finally Hazeli et.al. [91] fabricated Inconel 718 lattice structures with octet-truss, rhombic dodecahedron, dode-medium and diamond topologies. After employing stress-relief, HIP and solution aging treatments on the lattice structures, they detected the change in the deformation behaviour, on comparing with the as-built lattice structures especially for rhombic dodecahedron and diamond topologies. In all cases, post processing treatments caused an increase in the yield strength of the material. They ascribed the change in the mechanical behaviour of the lattice structures to the change in the grain sizes induced by the respective heat-treatments.

Bibliography

[1] ASTM F2792-12a, Standard Terminology for Additive Manufacturing Technologies, (Withdrawn 2015), ASTM International, West Conshohocken, 2012.

[2] E. M. Sefene, State-of-the-art of selective laser melting process: A comprehensive review, J. Manuf. Syst. 63 (2022) 250–274.

[3] L. Yang, K. Hsu, B. Baughman, D. Godfrey, F. Medina, M. Menon, S. Wiener, Additive Manufacturing of Metals: The Technology, Materials, Design and Production, Springer, Switzerland, 2017.

[4] T. Wohlers, T. Gornet, Wohlers Report, 2016.

[5] Z. Jin, Z. Zhang, K. Demir, G. X. Gu, Machine Learning for Advanced Additive Manufacturing, Matter 3 (2020) 1541–1556.

[6] M. Collan, K. E. Michelsen, Technical, Economic and Societal Effects of Manufacturing 4.0, Springer Nature, Switzerland, 2020.

[7] B. Motyl, S. Filippi, Trends in engineering education for additive manufacturing in the industry 4.0 era: a systematic literature review, IJIDeM 15 (2021) 103–106.

[8] U. M Dilberoglu, B. Gharehpapagh, U. Yaman, M. Dolen, The role of additive manufacturing in the era of Industry 4.0, Procedia Manuf. 11 (2017) 545 – 554.

[9] M. Yakout, M. A. Elbestawi, S. C. Veldhuis, A Review of Metal Additive Manufacturing Technologies, Solid State Phenom. 278 (2018) 1-14.

[10] N. Guo, M. C. Leu, Additive manufacturing: technology, applications and research needs, Front. Mech. Eng. 8(3) (2013) 215–243.

[11] National strategy for additive manufacturing booklet, https://www.meity.gov.in/content/national-strategy-additive-manufacturing

[12] I. Gibson, D. W. Rosen, B. Stucker, Additive Manufacturing, New York: Springer, 2010.

[13] Y. Xiong, Y. Tang, Q. Zhou, Y. Ma, D. W. Rosen, Intelligent additive manufacturing and design: state of the art and future perspectives, Addit. Manuf. 59 (2022) 103139.

[14] Z. Wang, C. Jiang, P. Liu, W. Yang, Y. Zhao, M. F. Horstemeyer, L. Q. Chen, Z. Hu, L. Chen, Uncertainty quantification and reduction in metal additive manufacturing, NPJ Computational Materials 6.1 (2020) 175.

[15] T. DebRoy, H. L. Wei, J.S. Zuback, T. Mukherjee, J.W. Elmer, J.O. Milewski, A.M. Beese, A. Wilson-Heid, A. De, W. Zhang, Additive manufacturing of metallic components – Process, structure and properties, Prog. Mater. Sci. 92 (2018) 112–224.

[16] S. Cooke, K. Ahmadi, S. Willerth, R. Herring, Metal additive manufacturing: Technology, metallurgy and modelling, J. Manuf. Process. 57 (2020) 978–1003.

[17] A. Vafadar, F. Guzzomi, A. Rassau, K. Hayward, Advances in Metal Additive Manufacturing: A Review of Common Processes, Industrial Applications, and Current Challenges, Appl. Sci. 11 (2021) 1213.

[18] E. Toyserkani, D. Sarker, O. O. Ibhadode, F. Liravi, P. Russo, K. Taherkhani, Metal Additive Manufacturing, John Wiley & Sons, Hoboken, USA, 2022.

[19] A. J. Pinkerton, Lasers in additive manufacturing, Opt. Laser Technol. 78 (2016) 25–32.

[20] H. Lee, C. Huat, J. Lim, M. J. Low, N. Tham, V. M. Murukeshan, Y. J. Kim, Lasers in Additive Manufacturing: A Review, Int. J. Precis. Eng. Manuf. Green Technology, 4 (2017) 307-322.

[21] S. P. Kumar, S. Elangovan, R. Mohanraj, V. S. Narayanan, Significance of continuous wave and pulsed wave laser in direct metal deposition, Mater. Today: Proceedings 46 (2021) 8086–8096.

[22] C.A. Biffi, J. Fiocchi, P. Bassani, A. Tuissi, Continuous wave vs pulsed wave laser emission in selective laser melting of AlSi10Mg parts with industrial optimized process parameters: Microstructure and mechanical behaviour, Addit. Manuf. 24 (2018) 639–646.

[23] A. G. Demir, P. Colombo, B. Previtali, From pulsed to continuous wave emission in SLM with contemporary fibre laser sources: effect of temporal and spatial pulse overlap in part quality, Int. J. Adv. Manuf. Technol. 91 (2017) 2701–2714.

[24] M. Brandt, Laser additive manufacturing, Woodhead Publishing, UK, 2017.

[25] R. Yavari, A. Riensche, E. Tekerek, L. Jacquemetton, H. Halliday, M. Vandever, A. Tenequer, V. Perumal, A. Kontsos, Z. Smoqi, K. Cole, P. Rao, Digitally twinned additive manufacturing: Detecting flaws in laser powder bed fusion by combining thermal simulations with in-situ melt pool sensor data, Mater. Des. 211 (2021) 110167.

[26] B. Ferrar, L. Mullen, E. Jones, R. Stamp, C.J. Sutcliffe, Gas flow effects on selective laser melting (SLM) manufacturing performance, J. Mater. Process. Technol. 212 (2012) 355– 364.

[27] N. T. Aboulkhair, N. M. Everitt, I. Ashcroft, C. Tuck, Reducing porosity in AlSi10Mg parts processed by selective laser melting, Addit. Manuf. 1–4 (2014) 77–86.

[28] R. Zhao, C. Chen, W. Wang, T. Cao, S. Shuai, S. Xu, T. Hu, H. Liao, Ji. Wang, Z. Ren, On the role of volumetric energy density in the microstructure and mechanical properties of laser powder bed fusion Ti-6Al-4V alloy, Addit. Manuf. 51 (2022) 102605.

[29] C. Y. Yap, C. K. Chua, Z. L. Dong, Z. H. Liu, D. Q. Zhang, L. E. Loh, S. L. Sing, Review of selective laser melting: Materials and applications, Appl. Phys. Rev. 2 (2015) 041101.

[30] H. Gong, K. Rafi, T. Starr, B. Stucker, The Effects of Processing Parameters on Defect Regularity in Ti-6Al-4V Parts Fabricated By Selective Laser Melting and Electron Beam Melting, 24th International SFF Symposium, 2013.

[31] https://wavelength-oe.com/optical-calculators/focus-spot-size/

[32] H. Jia, H. Sun, H. Wang, Y. Wu, H. Wang, Scanning strategy in selective laser melting (SLM): a review, Int. J. Adv. Manuf. Technol. 113 (2021) 2413–2435.

[33] O. Zinovieva, V. Romanova, R. Balokhonov, Effects of scanning pattern on the grain structure and elastic properties of additively manufactured 316L austenitic stainless steel, Mater. Sci. Eng. A, 832 (2022) 142447.

[34] J. H. Robinson, I. R. T. Ashton, E. Jones, P. Fox, C. Sutcliffe, The effect of hatch angle rotation on parts manufactured using selective laser melting, Rapid Prototyp. J. 25/2 (2019) 289–298.

[35] A. Strondl, O. Lyckfeldt, H. Brodin, U. Ackelid, Characterization and Control of Powder Properties for Additive Manufacturing, JOM, 67 (2015).

[36] A. T. Sutton, C. S. Kriewall, M. C. Leu, J. W. Newkirk, Powder characterisation techniques and effects of powder characteristics on part properties in powder-bed fusion processes, Virtual Phys. Prototyp. 12:1 (2016) 3-29.

[37] M. Qian, Metal Powder for Additive Manufacturing, JOM, 67 (2015).

[38] S. Vock, B. Klöden, A. Kirchner, T. Weißgärber, B. Kieback, Powders for powder bed fusion: a review, Prog. Addit. Manuf. (2019) 4:383–397.

[40] D. Herzog, V. Seyda, E. Wycisk, C. Emmelmann, Additive manufacturing of metals, Acta Mater. 117 (2016) 371-392.

[41] I. Yadroitsev, I. Yadroitsava, A. D. Plessis, E. MacDonald, Fundamentals of Laser Powder Bed Fusion of Metals, Elsevier, 2021.

[42] J. P. Oliveira, A. D. LaLonde, Processing parameters in laser powder bed fusion metal additive manufacturing, J. Ma, Mater. Des. 193 (2020) 108762.

[43] S. Kou, Welding metallurgy, John Wiley & Sons, Hoboken, USA, 2003.

[44] A. R. A. Dezfoli, W. S. Hwang, W. C. Huang, T. W. Tsai, Determination and controlling of grain structure of metals after laser incidence: Theoretical approach, Sci. Rep. 7 (2017) 41527.

[45] M. C. Brennan, J. S. Keist, T. A. Palmer, Defects in Metal Additive Manufacturing Processes, JMEPEG 30 (2021) 4808–4818.

[46] M. Balbaa, S. Mekhiel, M. Elbestawi, J. McIsaac, On selective laser melting of Inconel 718: Densification, surface roughness, and residual stresses, Mater. Des. 193 (2020) 108818.

[47] W. E. King, H. D. Barth, V. M. Castillo, G. F. Gallegos, J. W. Gibbs, D. E. Hahn, C. Kamath, A. M. Rubenchik, Observation of keyhole-mode laser melting in laser powder-bed fusion additive manufacturing, J. Mater. Process. Technol. 241/12 (2014) 2915-2925.

[48] W. J. Sames, F. Medina, W.H. Peter, S. S. Babu, R. R. Dehoff, Effect of Process Control and Powder Quality on Inconel 718 Produced Using Electron Beam Melting, 8th International Symposium on Superalloy 718 and Derivatives, TMS, 2014.

[49] K. Mumtaz, N. Hopkinson, Top surface and side roughness of Inconel 625 parts processed using selective laser melting, Rapid Prototyp. J. 15/2 (2009) 96–103.

[50] K. Kempen, L. Thijs, B. Vrancken, S. Buls, J. Van Humbeeck, J. P. Kruth, Producing crack-free, high density M2 HSS parts by Selective Laser Melting: Pre-heating the baseplate, International Solid Freeform Fabrication Symposium, 2013.

[51] X. Zhao, X. Lin, J. Chen, L. Xue, W. Huang, The effect of hot isostatic pressing on crack healing, microstructure, mechanical properties of Rene88DT superalloy prepared by laser solid forming, Mater. Sci. Eng. A, 504 (2009) 129–134.

[52] A. Basak, S. Das, Epitaxy and Microstructure Evolution in Metal Additive Manufacturing, Annu. Rev. Mater. Res. 2016 46:1, 125-149

[53] A. Bandyopadhyay, Y. Zhang, S. Bose, Recent developments in metal additive manufacturing, Curr. Opin. Chem. Eng. 28 (2020) 96–104.

[54] M.T. Pérez-Prado, A. Martin, D.F. Shi, S. Milenkovic, C.M. Cepeda-Jiménez, An Al-5Fe-6Cr alloy with outstanding high temperature mechanical behavior by laser powder bed fusion, Addit. Manuf. 55 (2022) 102828.

[55] J. H Martin, B. D. Yahata, J. M. Hundley, J. A. Mayer, T. A. Schaedler, T. M. Pollock, 3D printing of high-strength aluminium alloys, Nature 549/7672 (2017) 365-369.

[56] A. P. Mouritz, Introduction to aerospace materials, Woodhead Publishing, Cambridge, UK, 2012.

[57] A. Mostafaei, R. Ghiaasiaan, I. T. Ho, S. Strayer, K. C. Chang, N. Shamsaei, S. Shao, S. Paul, A. C. Yeh, S. Tin, A. C. To, Additive Manufacturing of Nickel-based superalloys: a state-of-the-art review on process-structure-defect-property relationship, Prog. Mater. Sci. 136 (2023) 101108.

[58] S. Sanchez, P. Smith, Z. Xu, G. Gaspard, C. J. Hyde, W. W. Wits, I. A. Ashcroft, H. Chen, A. T. Clare, Powder Bed Fusion of nickel-based superalloys: A review, Int. J. Mach. Tools Manuf. 165 (2021) 103729.

[59] R. Y. Zhang, H. L. Quin, Z. N. Bi, J. Li, S. Paul, T. L. Lee, S. Y. Zhang, J. Zhang, H. B. Dong Evolution of Lattice Spacing of Gamma Double Prime Precipitates During Aging of Polycrystalline Ni-Base Superalloys: An In-Situ Investigation, Metall. Mater. Trans. A. 51 (2020) 574–585.

[60] M. Sundararaman, P. Mukhopadhyay, S. Banerjee, Some Aspects of the Precipitation of Metastable Intermetallic Phases in INCONEL 718, Metall. Mater. Trans. A. 23 (1992) 2015–2028.

[61] R. Cozar, A. Pineau, Morphology of γ' and γ'' Precipitates and Thermal Stability of Inconel 718 Type Alloys, Metall. Mater. Trans. B 4, 47–59 (1973).

[62] R. Reed, The Superalloys: Fundamentals and Applications, Cambridge University Press, Cambridge, UK, 2006.

[63] J. Strößner, M. Terock, U. Glatzel, Mechanical and Microstructural Investigation of Nickel-Based Superalloy IN718 Manufactured by Selective Laser Melting (SLM), Adv. Eng. Mater. 17/8 (2015) 1099-1105.

[64] Y. L. Kuo, S. Horikawa, K. Kakehi, The effect of interdendritic δ phase on the mechanical properties of Alloy 718 built up by additive manufacturing, Mater. Des. 116 (2017) 411-418.

[65] G. M. Volpato, U. Tetzlaff, M. C. Fredel, A comprehensive literature review on laser powder bed fusion of Inconel superalloys, Addit. Manuf. 55 (2022) 102871.

[66] T. Trosch, J. Strößner, R. Völkl, U. Glatzel, Microstructure and mechanical properties of selective laser melted Inconel 718compared to forging and casting, Mater. Lett. 164 (2016) 428–431.

[67] K. N. Amato, S. M. Gaytan, L. E. Murr, E. Martinez, P.W. Shindo, J. Hernandez, S. Collins, F. Medina, Microstructures and mechanical behavior of Inconel 718 fabricated by selective laser melting, Acta Mater. 60 (2012) 2229–2239.

[68] A. Hilaire, E. Andrieu, X. Wu, High-temperature mechanical properties of alloy 718 produced by laser powder bed fusion with different processing parameters, Addit. Manuf. 26 (2019) 147-160.

[69] O. Gokcekaya, T. Ishimoto, S. Hibino, J. Yasutomi, T. Narushima, T. Nakano, Unique crystallographic texture formation in Inconel 718 by laser powder bed fusion and its effect on mechanical anisotropy, Acta Mater. 212 (2021) 116876.

[70] S. Sanchez, G. Gaspard, C. J. Hyde, I.A. Ashcroft, G.A. Ravi, A.T. Clare, The creep behaviour of nickel alloy 718 manufactured by laser powder bed fusion, Mater. Des. 204 (2021) 109647.

[71] T. Huynh, A. Mehta, K, Graydon, J. Woo1, S. Park1, H. Hyer1, L. Zhou, D. D. Imholte, N. E. Woolstenhulme, D. M. Wachs, Y. Sohn, Microstructural Development in Inconel 718 Nickel-Based Superalloy Additively Manufactured by Laser Powder Bed Fusion, Metallogr. Microstruct. Anal. 11 (2022) 88–107.

[72] T. Maconachie, M. Leary, B. Lozanovski, X. Zhang, M. Qian, O. Faruque, M. Brandt, SLM lattice structures: Properties, performance, applications and challenges, Mater. Des. 183 (2019) 108137.

[73] I. Maskery, N. T. Aboulkhair, A. O. Aremu, C.J. Tuck, I.A. Ashcroft, Compressive failure modes and energy absorption in additively manufactured double gyroid lattices, Addit. Manuf. 16 (2017) 24-29.

[74] V. S. Deshpande, M. F. Ashby and N. A. Fleck, Foam topology: bending versus stretching dominated architectures, Acta Mater. 49, (2001) 1035–1040.

[75] A. Zargarian, M. Esfahanian, J. Kadkhodapour, S. Ziaei-Rada, D. Zamani, On the fatigue behavior of additive manufactured lattice structures, Theor. Appl. Fract. Mech. 100 (2019) 225-232.

[76] L. J. Gibson, M. F. Ashby, Cellular solids, Cambridge University Press, Cambridge, UK, 1997.

[77] J. Austermann, A. J. Redmann, V. Dahmen, A. L. Quintanilla, S. J. Mecham, T. A. Osswald, Fiber-Reinforced Composite Sandwich Structures by Co-Curing with Additive Manufactured Epoxy Lattices, J. Compos. Sci. 3 (2019) 53-66.

[78] M. Leary, M. Mazur, H. Williams, E. Yang, A. Alghamdi, B. Lozanovski, X. Zhang, D. Shidid, L. Farahbod-Sternahl, G. Witt, I. Kelbassa, P. Choong, M. Qian, M. Brandt, Inconel 625 lattice structures manufactured by selective laser melting (SLM): Mechanical properties, deformation and failure modes, Mater. Des. 157 (2018) 179-199.

[79] R. Gümrük, R. A.W. Mines, S. Karadeniz, Compressive behaviour of stainless steel micro-lattice structures, Mater. Sci. Eng. A, 586 (2013) 392-406.

[80] P. Köhnen, C. Haase, J. Bültmann, S. Ziegler, J. H. Schleifenbaum, W. Bleck, Mechanical properties and deformation behavior of additively manufactured lattice structures of stainless steel, Mater. Des. 145 (2018) 205-217.

[81] M. Mazur, M. Leary, S. Sun, M. Vcelka, D. Shidid, M. Brandt, Deformation and failure behaviour of Ti-6Al-4V lattice structures manufactured by selective laser melting (SLM), Int. J. Adv. Manuf. Technol. 84 (2015) 1393-1411.

[82] R. Mahshid, H. N. Hansen, K. L. Højbjerre, Strength analysis and modeling of cellular lattice structures manufactured using selective laser melting for tooling applications, Mater. Des. 104 (2016) 276-283.

[83] C. Li, H. Lei, Y. Liu, X. Zhang, J. Xiong, H. Zhou, D. Fang, Crushing behavior of multi-layer metal lattice panel fabricated by selective laser melting, Int. J. Mech. Sci. 145 (2018) 389-399.

[84] J. Song, W. Zhou, Y. Wang, R. Fan, Y. Wang, J. Chen, Y. Lu, L. Li, Octet-truss cellular materials for improved mechanical properties and specific energy absorption, Mater. Des. 173 (2019) 107773.

[85] S. Y. Choy, C. N. Sun, K. F. Leong, J. Wei, Compressive properties of Ti-6Al-4V lattice structures fabricated by selective laser melting: Design, orientation and density, Addit. Manuf. 16 (2017) 213-223.

[86] M. S. Pham, C. Liu, I. Todd, J. Lertthanasarn, Damage-tolerant architected materials inspired by crystal microstructure, Nature 565 (2019) 305-325.

[87] C. Liu, J. Lertthanasarn, M. S. Pham, The origin of the boundary strengthening in polycrystal-inspired architected materials, Nat. Commun. 12 (2021) 4600.

[88] D. S.J. Al-Saedi, S.H. Masood, M. Faizan-Ur-Rab, A. Alomarah, P. Ponnusamy, Mechanical Performance of Functionally Graded Lattice Structures Made with Selective Laser Melting 3D Printing, Mater. Des. 144 (2018) 32-44.

[89] X. Lijun, S. Weidong, Additively-manufactured functionally graded Ti-6Al-4V lattice structures with high strength under static and dynamic loading: Experiments, Int. J. Imp. Eng. 111 (2018) 255-272.

[90] R. Wauthle, B. Vranckenc, B. Beynaerts, K. Jorissen, J. Schrooten, J.-P. Kruth, J. Van Humbeeck, Effects of build orientation and heat treatment on the microstructure and mechanical properties of selective laser melted Ti6Al4V lattice structures, Add. Manuf. 5 (2015) 77-84.

[91] K. Hazeli, B. B. Babamiri, J. Indeck, A. Minor, H. Askari, Microstructure-topology relationship effects on the quasi-static and dynamic behavior of additively manufactured lattice structures Mater. Des. 176 (2019) 107826.

CHAPTER 3

Experimental methods

Several experimental techniques were employed to fabricate, evaluate and correlate lattice structures and their microstructural and mechanical properties. The first section explains the feedstock powder characterization. Different properties such as apparent and tapped densities, flow rate, morphology and particle size distribution were investigated for the studied Inconel 718 powder. The second section focuses on the additive manufacturing setup for the fabrication of lattice structures. The third part deals with the techniques employed for microstructural characterization and the fourth chapter describes the characterization of mechanical properties of the lattice structures.

3.1. Feedstock material characterization

The feedstock material used in the course of this Thesis is the Ni-based superalloy Inconel 718, supplied by Oerlikon. Since the technique of LPBF uses feedstock in a powder form, powder properties such as apparent, tapped and true densities, powder flow rate and particle size distribution were analysed using various characterization setups. The importance of proper powder characterisation has been demonstrated by several works [1,2]. The following subsections describe the tools and methods utilized to examine powder properties.

3.1.1. Apparent, tapped and true densities

The apparent density is a measure of the mass of loosely packed powder per unit volume. The apparent density was measured by following the procedure detailed in the ASTM B212-21 [3] standard, as a reference. A container of 25 cm^3 volume was assembled along with the Hall flowmeter. The powder was made to fill the container completely by pouring it down through the funnel. A non-magnetic spatula was utilized to remove extra powder and to level the powder with the top edge of the container. The apparent density was then calculated by taking the ratio of weight of the powder inside the container and the volume of the container. The procedure was repeated three times for the sake of repeatability.

The tapped density was measured with a tapping apparatus (Quantachrome Autotap AT-6) and the procedure was carried out according to the ASTM B527-15 [4] standard. A measured weight of 10 g of powder was taken in a graduated container. The container was fixed to the apparatus with the help of clamps. It was tapped 2500 times with 260 taps per minute as the frequency of tapping. The magnitude of the initial volume before tapping and of the final volume after tapping were noted down, and the difference was taken as the tapped volume.

An automated Helium gas pycnometer (AccuPyc 1330, Micrometrics) was employed for the measurement of the true density of the feedstock powder. The ASTM B923-22 [5] standard served as the reference for the procedure. The procedure was performed on a measured mass of powder of approximately 7.2 g.

3.1.2. Flowability

Flowability is the ease with which a powder flows [6]. The ASTM B213-20 [7] standard was taken as reference for measuring the Hall flow rate of the powder. A measured mass of 50 g of powder was transferred to the Hall flowmeter funnel, keeping its orifice blocked. The latter was then unblocked gently to let the powder flow freely. A timer was operated instantaneously to record the duration of the powder flow. The procedure was repeated three times for the sake of repeatability.

3.1.3. Particle size distribution

Particle size distribution is a mean of indicating a percentage of specific powder diameters [8]. The technique of laser diffraction is commonly used to indicate the particle size. The working principle involves scattering of laser beam by the powder particles, since smaller particles scatter the incident beam at larger scattering angles. The output signal from scattering is plotted as cumulative percentage versus particle size.

A Malvern Mastersizer 2000 laser interferometer was used to obtain the particle size distribution for Inconel 718. The flow of the powder particles in a jet of compressed air was controlled by a vibrating tray. A laser then analyzed the particle size of the dispersed powder particles in the air stream.

3.2. Laser powder bed fusion

The LPBF system used to fabricate lattice structures was AM 400, a Renishaw product. The system is equipped with a reduced build volume (RBV) with dimensions 78 mm x 78 mm x 55 mm. The RBV enables the fabrication of small components, reducing the powder usage and the overall fabrication time. The total allowed build volume offered is 250 mm x 250 mm x 300 mm, suitable to fabricate large components. The system utilizes a pulsating Yb fibre laser to melt the metal powders. It comprises a 400 W optical system, which gives out a focused beam of diameter 70 µm. The LPBF system utilized in this work is depicted in Figure 3.1 below.

Figure 3.1. Renishaw AM 400 LPBF system

Prior to LPBF fabrication, a CAD file serves as a precursor for a digital input file that the AM system uses. A software called nTopology was used to create the lattice structures. A lattice structure of desired dimensions and topology can be created using various modules that the software offers. Not only strut-based, but surface-based lattice structures can also be created using the mentioned software, equipped with various design modules, similar to a typical CAD software. Once the stl file is created, the support structure and various process parameters are manipulated with the help of QuantAM software, which is a proprietary of Renishaw. Different types of support structures are inbuilt in QuantAM and the user can choose depending upon the geometrical requirements of the structure to be printed.

3.3. Microstructural characterization

The feedstock powder and the fabricated lattice structures were subjected to several microstructure analysis techniques in order to gain information about morphology, porosity, grain size and shape, texture, precipitate distribution, etc. The following subsections detail the techniques used for microstructural assessment at different length scales.

A systematic sample preparation campaign was carried out to achieve the necessary surface quality wherever mandated. Fabricated lattice sample was hot mounted (Buehler Simplimet 2) in Bakelite resin. The sample was then manually ground using SiC papers with grit sizes of 320, 600, 1200, 2500 and 4000, respectively. The scratches from the grinding process were removed by surface polishing in a Metaserv 250 polishing machine with diamond pastes of 9 μm, 6 μm, 3 μm and 1 μm abrasive size, respectively. A colloidal silica solution was used at the end to achieve the finest polished surface.

3.3.1. Optical microscopy

True to its name, an optical microscope uses light to illuminate the specimen and a number of lenses including objective and eyepiece to create a magnified image of the specimen when focused properly. The ability to magnify a specimen depends on lenses used, while the clarity with which two points can be differentiated is the resolution of the microscope [9]. Optical microscopy is a surface imaging procedure.

Optical microscopy was used in this work to characterize the fraction of porosity formed in the lattice structures, in conjunction with ImageJ free software. The software processes the optical micrographs as 8-bit black and white images. The fraction of porosity is calculated using simple subtraction of total solid area (white) and pore area (black) from the micrograph. In the present research an Olympus BX-51 polarizing microscope with magnification levels of 2.5x, 5x, 10x, 20x, 50x and 100x was used. The sample preparation employed for the specimens to be examined with the mentioned microscope consisted of steps till diamond polishing, as explained in section 3.3.

3.3.2. Scanning electron microscopy

Scanning electron microscopy uses electrons instead of light to produce far-magnified images as opposed to optical microscopy. The electrons are produced by an electron gun at the top of the microscope. The path of electrons from the point of origin until the sample is held in vacuum. Instead of optical lenses, the electron beam is focused with the help of electromagnetic fields [10]. When the incident electrons hit the surface of the sample, the interaction results in many types of emergent electrons, as depicted in Figure 3.2. These signals are collected by suitable detectors and then sent to a screen for viewing.

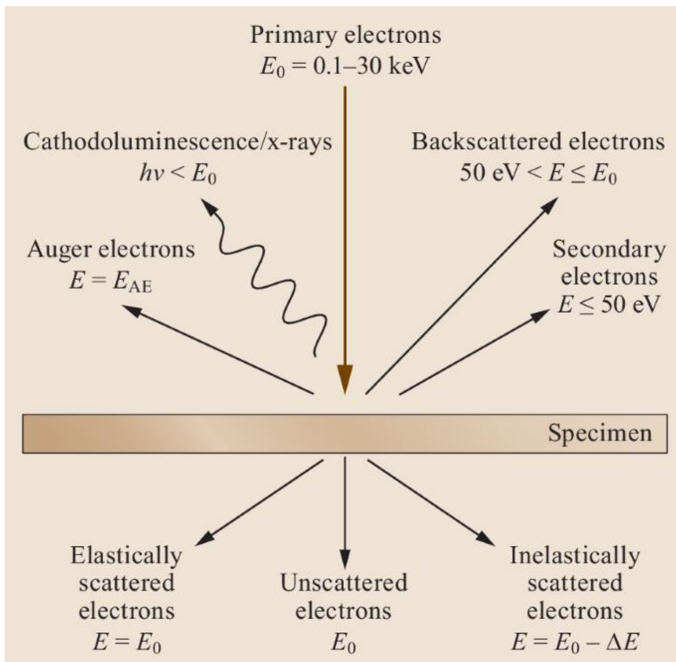

Figure 3.2. Various signals created by impinging electrons in a thin sample [10]

To evaluate the surface features of the lattice structures, secondary electrons were used. In the case of powder particles, various features including particle shape and size, surface roughness and texture and satellites were examined using secondary electrons. Backscattered electrons were used to investigate the microstructural features of the lattice structures such as grain shape, size and texture, with the help of the electron backscatter diffraction (EBSD) technique. The backscattered signal was also used to observe the degree of oxidation in the heat-treated samples. The scanning electron microscope used in this work was a FEI Helios Nano-Lab 600i. The sample preparation employed for the specimens to be examined with the mentioned microscope consisted of all the steps, as explained in section 3.3.

3.3.3. Focused ion beam

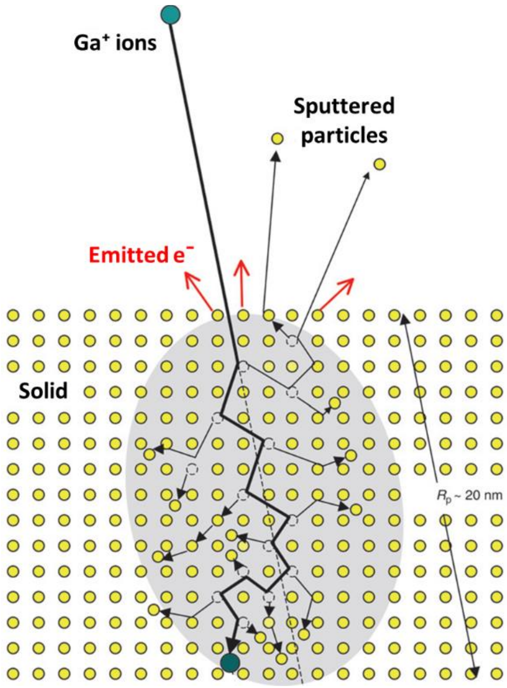

Figure 3.3. Various signals created by incident Ga^+ ions in a sample [11]

A focused ion beam (FIB) setup is used to image the specimens using Ga^+ ions. The ion beam is also used for local sputtering or sample milling. Upon hitting the sample surface, a small amount of the material is sputtered away in the form of secondary ions or neutral atoms. At the same time, secondary electrons are also generated, as seen from Figure 3.3. The necessary signal (secondary electrons/sputtered ions) is captured to gain information about the specimen in the form of an image. Imaging with Ga^+ ions is usually done at low beam currents, as a smaller fraction of material is sputtered away. The resolution achieved at lower beam currents corresponds to around 5 nm [11].

Since higher beam currents can sputter the material in larger quantities, Ga^+ ions are very commonly utilized to precisely mill the material down to micrometre or even nanometre scale. In the presented work, a FIB accessory equipped in FEI Helios NanoLab600i FIB FEG-SEM was used to mill electron transparent lamellae from strut interiors of as-built and heat-treated lattice structures to observe microstructural features by transmission electron microscopy.

3.3.4. Transmission electron microscopy

A transmission electron microscope (TEM) is a very powerful analytical tool used in biological, chemical and physical sciences since it offers a very high resolution. High-quality imaging is achieved by forward electron diffraction across thin lamellae. The incident electron beam is partly transmitted and partly diffracted through the specimen. Depending upon the type of signal collected for image formation, there are two modes of imaging, bright field and dark field, as seen from Figure 3.4 (a) and (b).

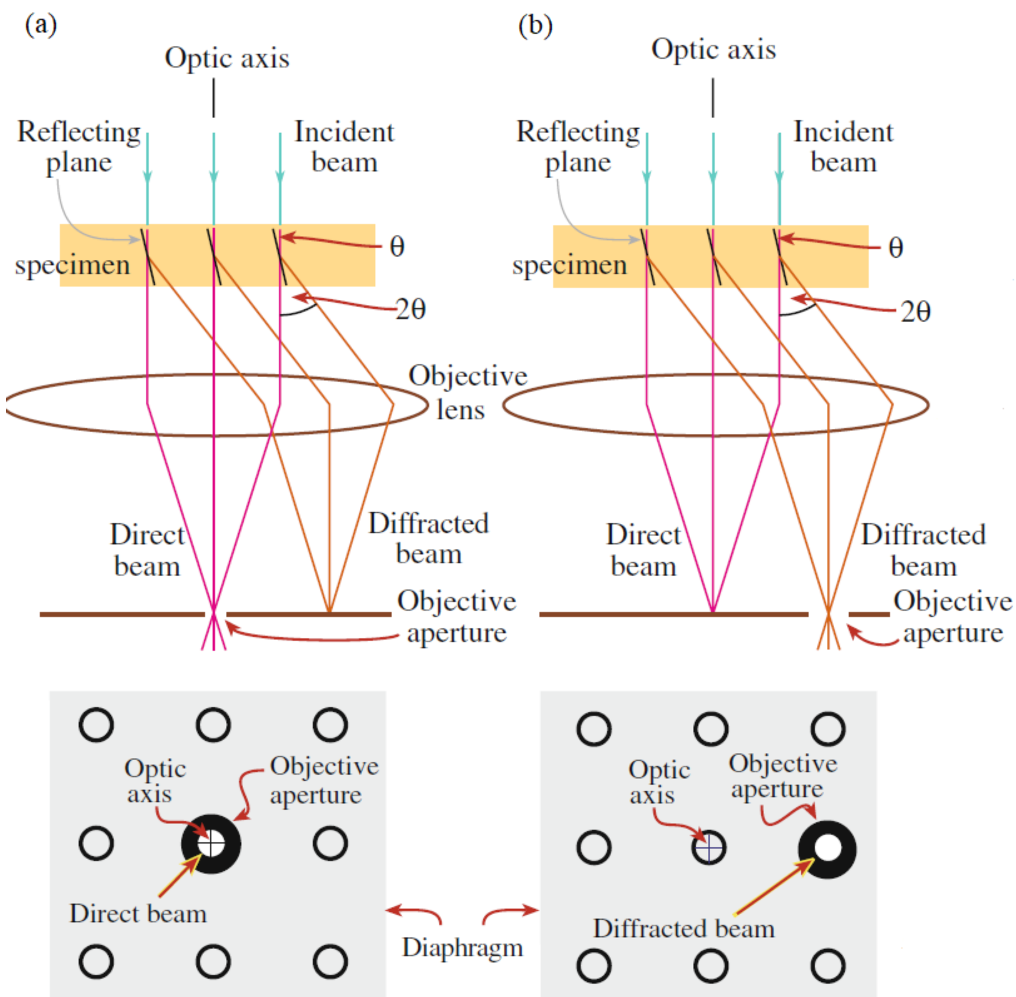

Figure 3.4. A schematic illustrating the working of (a) bright field mode and (b) schematic of dark field mode [13]

In the bright field mode, only unscattered (transmitted) electrons are imposed at the Ewald sphere. The resultant bright field image forms due to pure elastic scattering. Highly crystalline or high mass areas appear dark in the bright field mode. On the contrary, the dark field mode is activated when using a scattered (diffracted) signal alone. Therefore, areas where the electrons scatter now appear bright. The dark field mode is especially useful to examine dislocations, crystal structure, stacking faults, defects, etc [12].

3.3.5. X-ray computed tomography

X-ray computed tomography (XCT) employs X-rays to visualize the interior of specimens. It is a non-destructive technique which constructs a 3D volume with the help of complex mathematical algorithms. A narrow X-ray beam scans a rotating specimen sequentially in several hundred images called slices. A slice image is composed of voxels (volume pixels). These slices are then stacked together to gain useful information such as the porosity distribution inside the sample, inclusions, etc. The contrast obtained depends on the X-ray absorption degree [14]. Figure 3.5 illustrates the working flow of an XCT process.

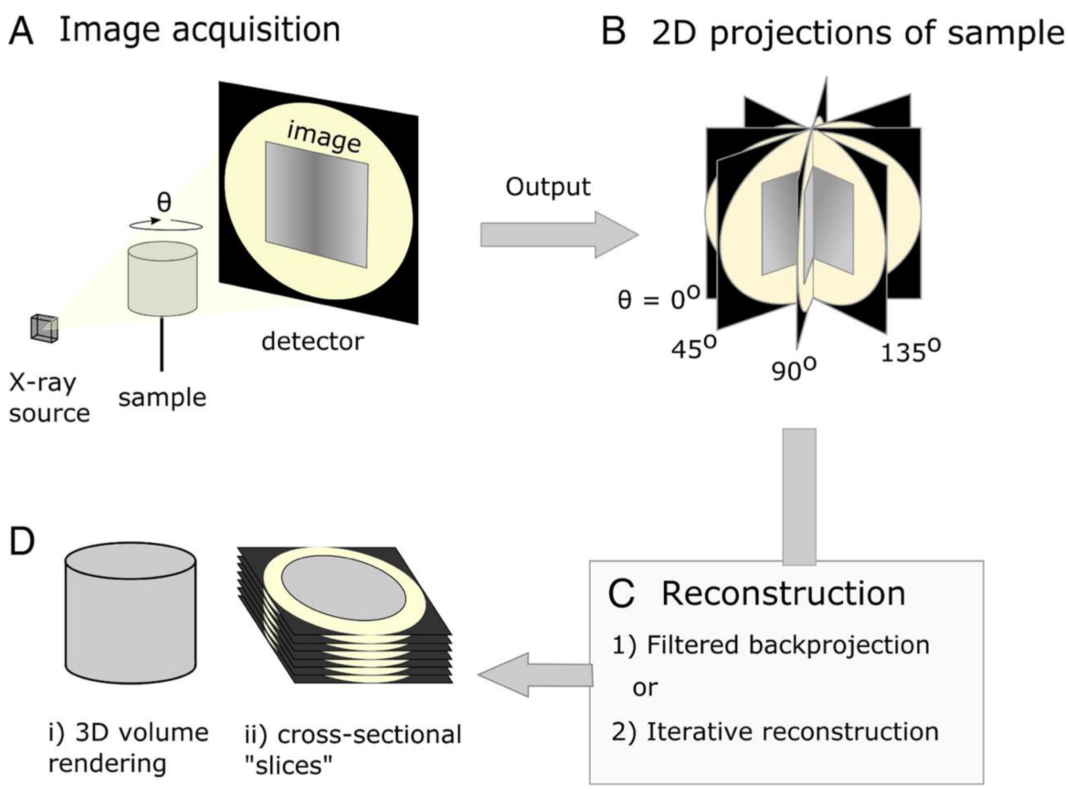

Figure 3.5. Workflow of the X-ray computed tomography technique [15]

XCT was used in this research to evaluate the percentage of internal porosity formed during LPBF of the manufactured strut-based lattice structures. A tensile sample possessing a cylindrical dog-bone shape was utilized to quantitatively investigate the internal porosity in the gauge length using a Phoenix Nanotom 160NF system. The dimensions of the sample are specified in more details in Chapter 5.

3.4. Mechanical property evaluation

The lattice structures fabricated with LPBF were evaluated to gain information about the mode of collapse, yield strength, microhardness, ductility, absorbed energy and many more. Following subsections feature the techniques used for mechanical property evaluation.

3.4.1. Microhardness

The hardness of a material is an indicator of the resistance against plastic deformation. Hardness is usually measured by indentation, in which a constant compressive load is applied on the material for a definite period of time. The measured penetration is then related to the hardness via an equation [16]. The Vickers microhardness test was devised by the engineers at Vickers Ltd. in the 1920s. It uses a diamond indenter with a square-based pyramid shape to indent the material, as displayed in Figure 3.6.

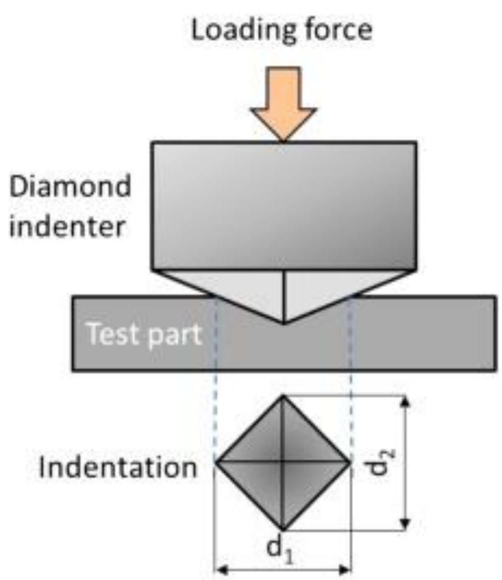

Figure 3.6. Working principle of Vickers microhardness testing [18]

The testing usually employs loads ranging from 9.8×10^{-3} to 9.8 N (1 to 1000 gf), applied for a duration of 10 to 15 seconds. The hardness is calculated by a simple formula as mentioned in ASTM E384-05a [17]:

$$HV = 1.854\ (F/d^2) \tag{4}$$

where, F is the applied force in kgf and d^2 (d is the mean of two diagonals, d_1 and d_2) is the area of indentation in mm^2.

In the presented work, a Shimadzu T2 E microhardness indenter was used to evaluate the hardness of the lattice structures in the as-built and heat-treated conditions. The final microhardness was an average of eight indentations along a specific area in the nodes of the lattice structures.

3.4.2. Compression and tensile testing

A series of uniaxial compression tests were carried out at various strain rates in order to evaluate the mode of collapse, the yield strength, and the absorbed energy of the LPBF manufactured lattice structures. The choice of load cell depends upon the maximum strength reached by the lattice during compression. An Instron 3384 universal electromechanical testing machine was employed to carry out the testing campaign at room and high temperature. To facilitate high temperature testing, an Ibertest IB TR331100 climatic chamber was installed on the universal testing machine. Several photographs and videos were captured over the course of testing with the help of a high-resolution camera from Correlation Solutions (Stingray Allied F504B ASG) to observe the formation of shear bands and homogeneous compression in the lattice structures in-situ during deformation. Further details regarding the testing conditions are included in subsequent chapters.

The uniaxial compression tests were complemented with digital image correlation (DIC) in order to compute the evolution of the local distribution of maximum shear strain during deformation. In the technique of DIC, the strain field is obtained by a comparison of a set of points in the first reference image in the absence of loading with the corresponding set in the successive deformation images. Numerically, the set of points is represented by a matrix and the individual points are represented by pixels. The displacement field corresponding to these pixels is determined using a correlation coefficient, resulting in a mapping function that relates the deformation images. A Nikon D7100 camera equipped with a 200 mm Nikkor macro lens was used to capture images during deformation which were analyzed with DaVis 8 software.

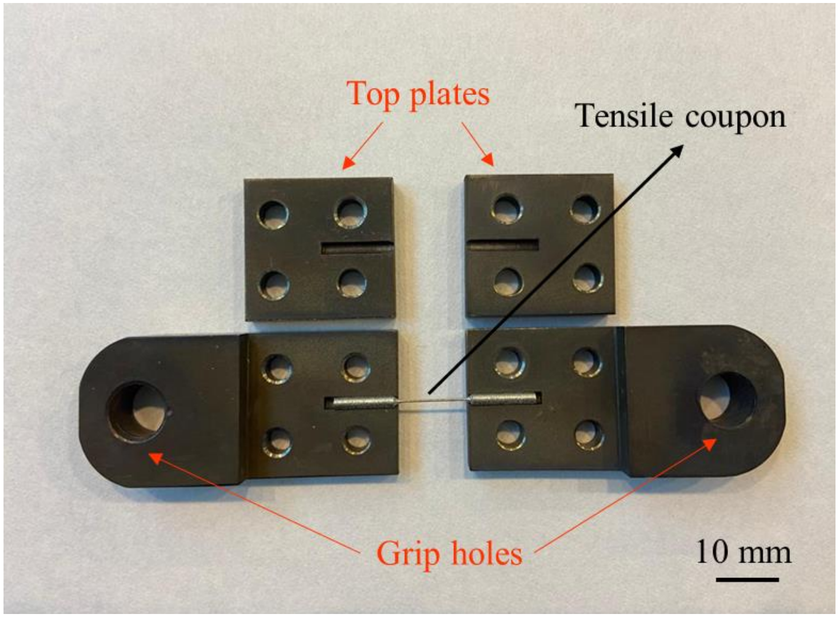

Figure 3.6. Customized tensile grips for tensile testing of cylindrical dog-bone shaped coupons

In order to observe the mechanical properties such as ductility and yield strength in the base material, the tensile coupons were examined in uniaxial tension with the help of specialized grips made of Inconel 718 in the same setup of Instron 3384 universal testing machine. The grips were customized to accommodate a cylindrical dog-bone shaped tensile sample of 1 mm grip diameter and 0.4 mm gauge diameter, as seen from Figure 3.7. The customized grips were used to test the coupons at room and high temperatures using aforementioned climactic chamber in uniaxial tension, as detailed in Chapter 5.

Bibliography

[1] S. F. Islam, S. M. Hawkins, J. L.L. Meyer, A. R.C. Sharman, Evaluation of different particle size distribution and morphology characterization techniques, Addit. Manuf. Let. 3 (2022) 100077.

[2] M. Mehrabi, J. Gardy, F. A. Talebi, A. Farshchi, A. Hassanpour, A. E. Bayly, An investigation of the effect of powder flowability on the powder spreading in additive manufacturing, Powder Technol. 413 (2023) 117997.

[3] ASTM B212-21, Standard Test Method for Apparent Density of Free-Flowing Metal Powders Using the Hall Flowmeter Funnel, ASTM International, West Conshohocken, 2021.

[4] ASTM B527-15, Standard Test Method for Tap Density of Metal Powders and Compounds, ASTM International, West Conshohocken, 2015.

[5] ASTM B923-22, Standard Test Method for Metal Powder Skeletal Density by Helium or Nitrogen Pycnometry, ASTM International, West Conshohocken, 2022.

[6] Q. B. Nguyen, M. L. S. Nai, Z, Zhu, C. N. Sun, J. Wei, W. Zhou, Characteristics of Inconel Powders for Powder-Bed Additive Manufacturing, Eng. 3 (2017) 695–700.

[7] ASTM B213-20, Standard Test Methods for Flow Rate of Metal Powders Using the Hall Flowmeter Funnel, ASTM International, West Conshohocken, 2020.

[8] A. T. Sutton, C. S. Kriewall, M. C. Leu, J. W. Newkirk, Powder characterization techniques and effects of powder characteristics on part properties in powder-bed fusion processes Virtual Phys. Prototyp. 12:1 (2016) 3-29.

[9] J Mertz, Introduction to optical microscopy, Cambridge University Press, Cambridge, UK, 2019.

[10] P. W. Hawkes, J. C. H. Spence, Springer handbook of microscopy, Springer Nature, Switzerland, 2019.

[11] C. A. Volkert, A. M. Minor, MRS Bulletin, Cambridge University Press, 32 (2007).

[12] M. Winey, J. B. Meehl, E. T. O'Toole, T. H. Giddings Jr., Conventional transmission electron microscopy, Mol. Biol. Cell. 3 (2014) 319-23.

[13] D. B. Williams, C. B. Carter, Transmission electron microscopy, Springer, New York, 2009.

[14] A. Thompson, I. Maskery, R. K. Leach, X-ray computed tomography for additive manufacturing: a review, Meas. Sci. Technol. 27 (2016) 072001.

[15] J. D. B. O'Sullivan, J. Behnsen, T. Starborg, A. S. MacDonald, A. T. Phythian-Adams, K. J. Else, S. M. Cruickshank, P. J. Withers, X-ray micro-computed tomography (μCT): an emerging opportunity in parasite imaging Parasitology 145 (2017) 848–854.

[16] A. E. Giannakopoulos, P. L. Larsson, R. Vestergaard, Analysis of Vickers Indentation, Int. J. Solid Structures, 31 (1994) 2679-2708.

[17] ASTM B384-05, Standard Test Method for Microindentation Hardness of Materials, ASTM International, West Conshohocken, 2020.

[18] D. Adamovic, F. Zivic, Encyclopedia of Materials: Composites, Elsevier, 2021.

CHAPTER 4

Precipitation induced transition in the mechanical behaviour of additively manufactured Inconel 718 BCC lattice structures

4.1. Background and design of the study

The mechanical behaviour of lattice structures is generally categorized either as bending-dominated or stretch-dominated [1,5]. In bending-dominated structures yielding is followed by a plateau stress and, finally, by a steep increase in the stress once cell components deform enough that they enter into contact with other components, triggering densification. In stretch-dominated structures yielding leads to an oscillating stress due to the periodic collapse by buckling or brittle crush of struts along selected layers before, ultimately, reaching the densification stage. While bending-dominated structures are more compliant, stretch-dominated structures have usually higher stiffness and higher strength for a given relative density, but are more prone to sudden failures and thus are not as effective at dissipating energy [2,5].

Earlier studies have predominantly focused on tuning the mechanical behaviour of AM lattices by altering their topology [6-16]. A few pioneer works have also explored the effect of the number and size of metagrains [15] and of continuous multilattice embedding [16]. Preliminary research has been carried out on the effect of post-processing heat treatments on the structural properties of LPBF-manufactured lattices [17-20] with a few selected topologies. However, the influence of microstructural parameters such as grain size, texture, grain boundaries, and precipitate distributions on the mechanical behaviour of LPBF fabricated lattices remains widely unknown. Gaining this understanding is critical to optimize lattice design for structural performance. The present study aims to investigate the effect of precipitation on the room temperature compression behaviour of body centred cubic (BCC) Inconel 718 lattices manufactured by LPBF.

The composition of the material under study is summarized in Table 4.1. Gas atomized powders of this superalloy were purchased from Renishaw Ibérica. Figure 4.1 illustrates the relatively spherical powder morphology (Figure 4.1 (a)) and the negligible porosity level in the particle interiors (Figure 4.1 (b)). The particle size distribution was unimodal, with d_{10} = 15 µm, d_{50} = 30 µm and d_{90} = 45 µm. The flowability, apparent density and tapped density of the powder were, respectively, 18 s, 4.2 g/cm^3, and 4.8 g/cm^3.

Table 4.1. Chemical composition of Inconel 718 alloy

	Ni	**Cr**	**Co**	**Al**	**Nb**	**Ti**	**Fe**	**Zr**
Amount (wt.%)	50	19	0.07	0.4	4.8	0.5	13.8	<0.005
	Ta	**Mn**	**Si**	**Cu**	**Mo**	**P**	**V**	
Amount (wt.%)	<0.010	0.057	0.39	0.25	1.65	<0.010	<0.005	

BCC lattice structures with external dimensions of 20x20x40 mm^3, with 2.5x2.5x2.5 mm^3 unit cells, and with a strut diameter of 0.4 mm, were manufactured by SLM in a Renishaw AM 400 system furnished with a reduced build volume platform. Printing was performed using a bidirectional scanning strategy with 67° rotation per layer and a layer thickness of 30 µm. The process parameter set utilized was laser power = 200 W, scan speed = 1166.7 mm/s, exposure time = 50 s and point distance = 70 µm, and hatch distance = 90 µm. Under these conditions, lattices with high geometric accuracy were produced.

Figure 4.1 (c) illustrates one of the as-built lattice structures after support removal. The relative density of this lattice (ρ/ρ_s), where ρ_s is the density of the base material, which amounts to 8.2 g/cm^3, is 0.14. Following printing, few lattice structures were heat treated using a standard three-step treatment widely utilized for this alloy class [21-23], including homogenization at 926 °C for 1 h followed by water quenching, aging at 718 °C for 8 h, cooling down to 621 °C in the furnace, aging at this temperature for 10 h, and finally cooling down to room temperature in air.

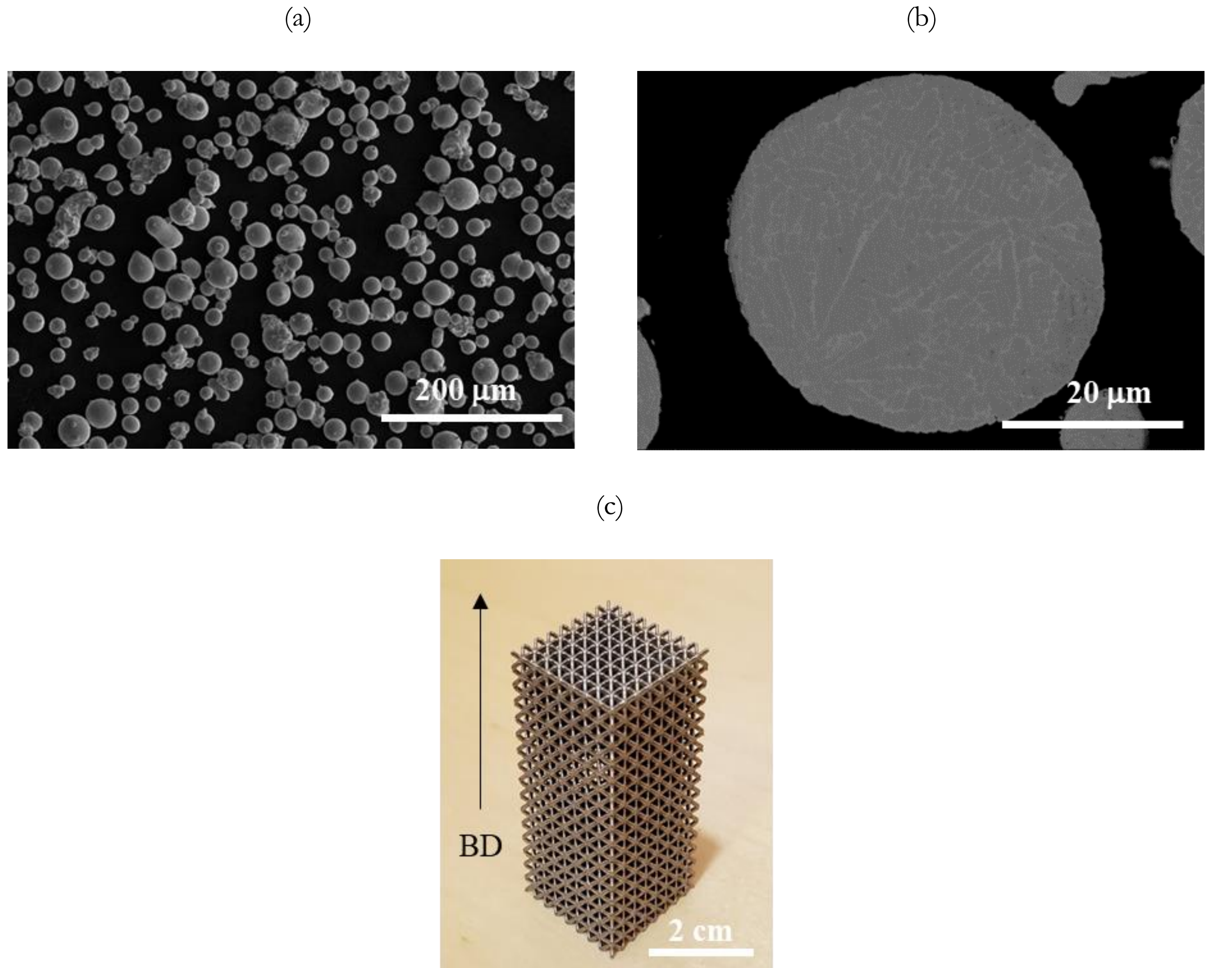

Figure 4.1. (a) SEM secondary electron image illustrating the morphology of the Inconel 718 powders utilized for the present study; (b) cross-section of a powder particle; (c) LPBF fabricated BCC lattice structure. The building direction (BD) is indicated.

The microstructure and the micro-texture of the as-built and heat-treated lattices were characterized by electron backscattered diffraction (EBSD) using a focused ion beam field emission gun scanning electron microscope (FIB-FEGSEM, FEI Helios NanoLab DualBeam 600i), utilizing a step size of 1.1 µm, an accelerating voltage of 30 kV, and a beam current of 2.7 nA. The intercept size distribution was measured from the EBSD inverse pole figure maps, counting only high angle grain boundaries, i.e., those with misorientation angles (θ) higher than 15°. The average grain size was calculated by multiplying the average intercept size by 1.74. The as-built and heat-treated microstructures were also examined by transmission electron microscopy (TEM) using a FEI Talos F200x microscope operating at 200 KV. TEM lamellae were extracted from selected regions of the strut interiors using a trenching-and- lift-out method, described exhaustively in [24]. The Vickers microhardness was measured in the as-built and heat- treated conditions using a Shimadzu microhardness tester, with loads of 0.5 and 1 kg, respectively, and a dwelling time of 15 s. The as-built and heat-treated lattices were compressed at room temperature along the building direction (BD) on an Instron 3384 universal testing machine using a cross-head speed of 0.5 mm/min.

4.2. Results

The Inconel 718 microstructures and micro-textures in the as-built and heat-treated lattice structures were examined along a plane perpendicular to the BD and they are compared in Figure 4.2. It can be seen that heat treatment does not appear to induce any significant changes at this scale. In both conditions the superalloy microstructures are polycrystals formed by randomly oriented grains of irregular morphology. In the areas close to the surface (border regions) grains tend to be elongated along the maximum heat flow direction, i.e. from the surface to the centre.

The average grain size values in the as-built and heat-treated conditions are, respectively, 20±29 μm and 22±35 μm. The misorientation angle distributions (MAD) (Figure 4.2 (c)) and the line intercept distributions (Figure 4.2 (d)) are also very similar in the as-built and heat-treated lattices. The MADs are endowed with a Mackenzie-type shape [25], with a maximum at 45°, as is typical of weak cubic textures.

An excess of low angle boundaries can also be seen, which reflects the presence of cell boundaries in the interior of some grains. The area fraction of porosity in the as-built condition amounts to 1.5 % (pores are depicted as white areas in Figure 4.2) and does not decrease after the heat treatment.

The Inconel 718 lattice microstructures were also examined before and after heat treatment using TEM and the results are illustrated in Figure 4.3. In the as-built condition (Figure 4.3 (a)), the microstructure is mostly a supersaturated solid solution. The grey contrast in the micrograph of Figure 4.3 (a) denotes the presence of solute clusters and a minor fraction of nanoparticles which do not give rise to any additional reflections in the corresponding selected area diffraction pattern (SAED), that is included as an inset. However, the heat treatment results in the formation of precipitates with an average length of 546±31 nm and an average width of 96±7 nm in width (Figure 4.3 (b)). The corresponding SAED, taken from along a <001> zone axis, reveals that these particles are metastable γ″ phases ($Ni_3(Nb, Ti)$) lying parallel to (001) planes [26].

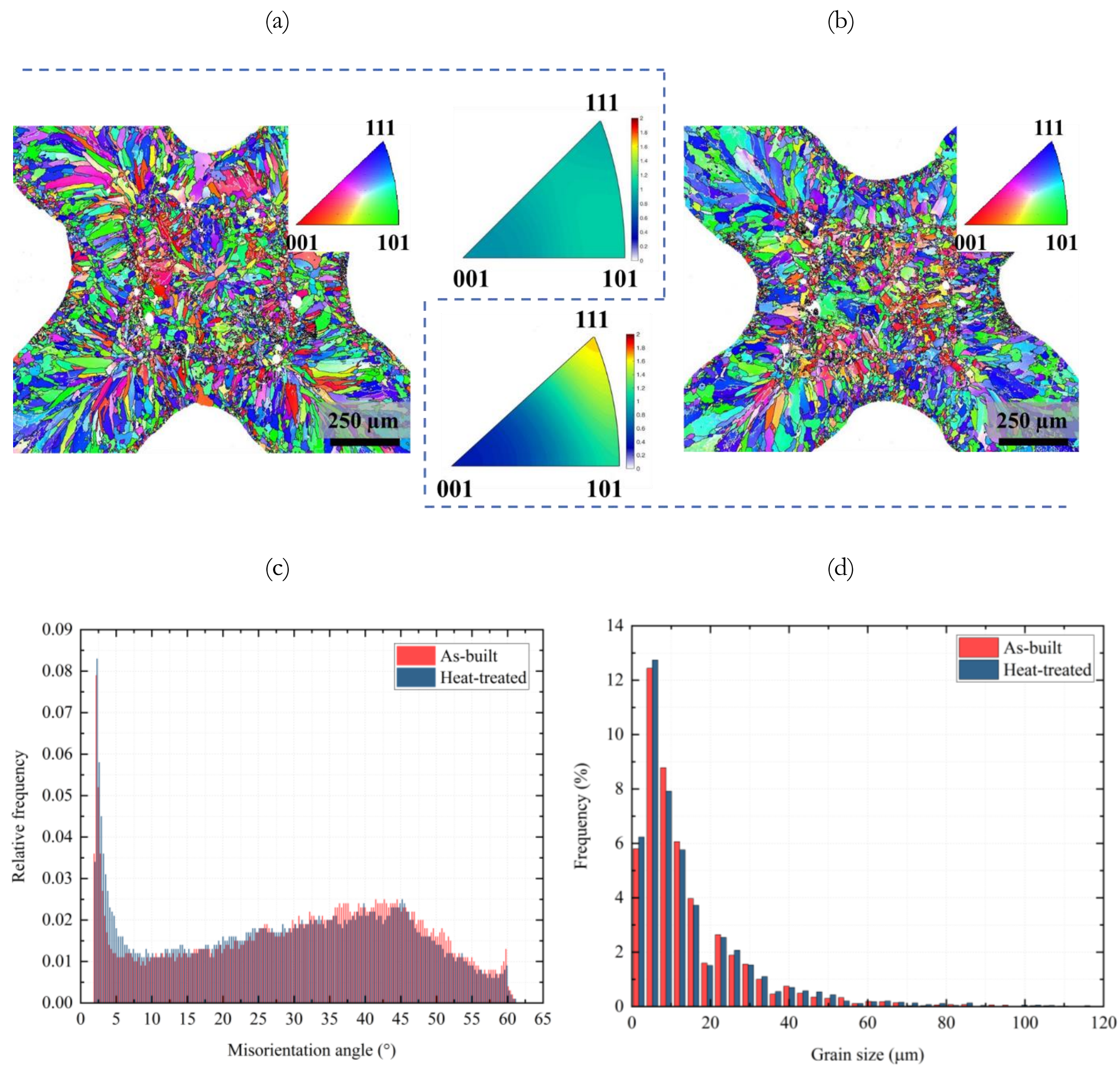

Figure 4.2. EBSD IPF maps and inverse pole figures illustrating the microstructure and the orientation of the BD along cross-sections of the printed lattices perpendicular to BD in the (a) as-built and (b) heat treated conditions. Comparison of the (c) misorientation angle distribution and (d) intercept size distribution of as-built and heat-treated lattice structures.

In summary, heat treatment leads to solute depletion and precipitation but does not alter the grain size, grain orientation, and grain boundary misorientation distribution. It must be noted that the microstructure of the Inconel 718 as-built lattice structures described above is different to that characteristic of LPBF manufactured bulk specimens [27-29], even when processed using the same processing parameters and LPBF system [30]. The latter are typically formed by large columnar grains, often exceeding several hundred microns in length, elongated along BD, and predominantly oriented with a <001> direction parallel to BD. Additionally, grain interiors in bulk specimens usually present a connected network of cell boundaries which are populated by (Nb, Ti)-rich precipitates [30,3].

Finally, application to bulk specimens of the standard solution plus aging treatment carried out in the present work often leads to the retention of the cell structure and to the formation of a fine dispersion of the strengthening γ'' disk-shaped particles, of about 20-30 nm in diameter [30]. However, in as-built lattice structures, grain growth and precipitation are limited owing to the high cooling rates associated to the fine nature of the struts. Additionally, the same heat treatment leads to an overaged microstructure, with γ'' particles with dimensions two orders of magnitude larger than in bulk specimens. These observations confirm that the evolution of the microstructure of superalloys during heat treatments is a function of the solidification rate [31,32]. Understanding these microstructure development paths is critical to optimize lattice design by additive manufacturing.

(a) (b)

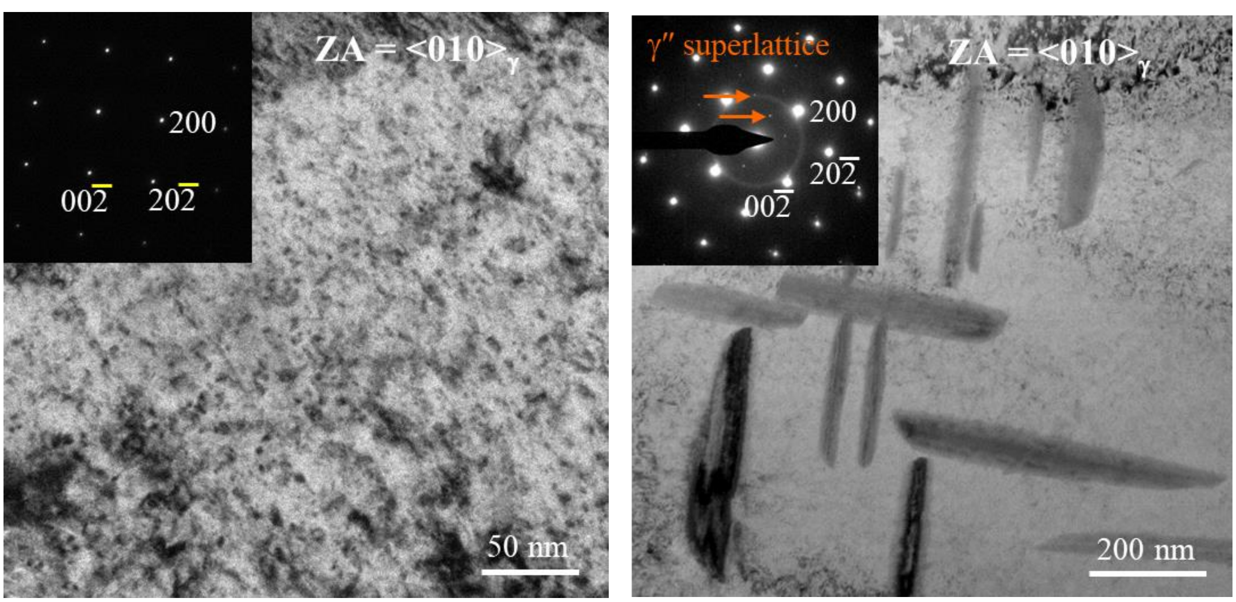

Figure 4.3. TEM bright field images illustrating the superalloy microstructure in the (a) as-built and (b) heat-treated lattice structures. The zone axis is <010>. The corresponding selected area electron diffraction (SAED) patterns are added as insets.

Figure 4.4 illustrates the room temperature compression stress-strain curves corresponding to as-built (red curve) and heat- treated (blue curve) lattice structures, as well as snapshots of the structures before deformation and at selected strains. A clear transition from a bending-dominated behaviour to a stretch dominated behaviour takes place as a consequence of precipitation during the heat treatment. In the as-built lattice structure, yielding at 20 MPa is followed by a plateau regime before starting densification at a strain of approximately 0.4. The as-built lattice structure, with highly compliant struts, deforms homogeneously, and a minor degree of barrelling can be noticed.

In the heat-treated lattice structure, yielding at 40 MPa is followed by stress oscillations corresponding to the successive formation of diagonal shear bands by the collapse of struts due to crushing along selected planes. Densification starts at a strain of approximately 0.4. Figure 2.4 reveals, additionally, that precipitation leads to higher energy absorption capacity. The absorbed energy increases, in particular, from 14511 kJ/m^3 in the as-built condition to 20372 kJ/m^3 in the heat-treated condition. The reported changes in the room temperature compression behaviour of the LPBF fabricated lattice structures can be attributed to the alteration of the mechanical properties of the Inconel 718 superalloy as a consequence of precipitation.

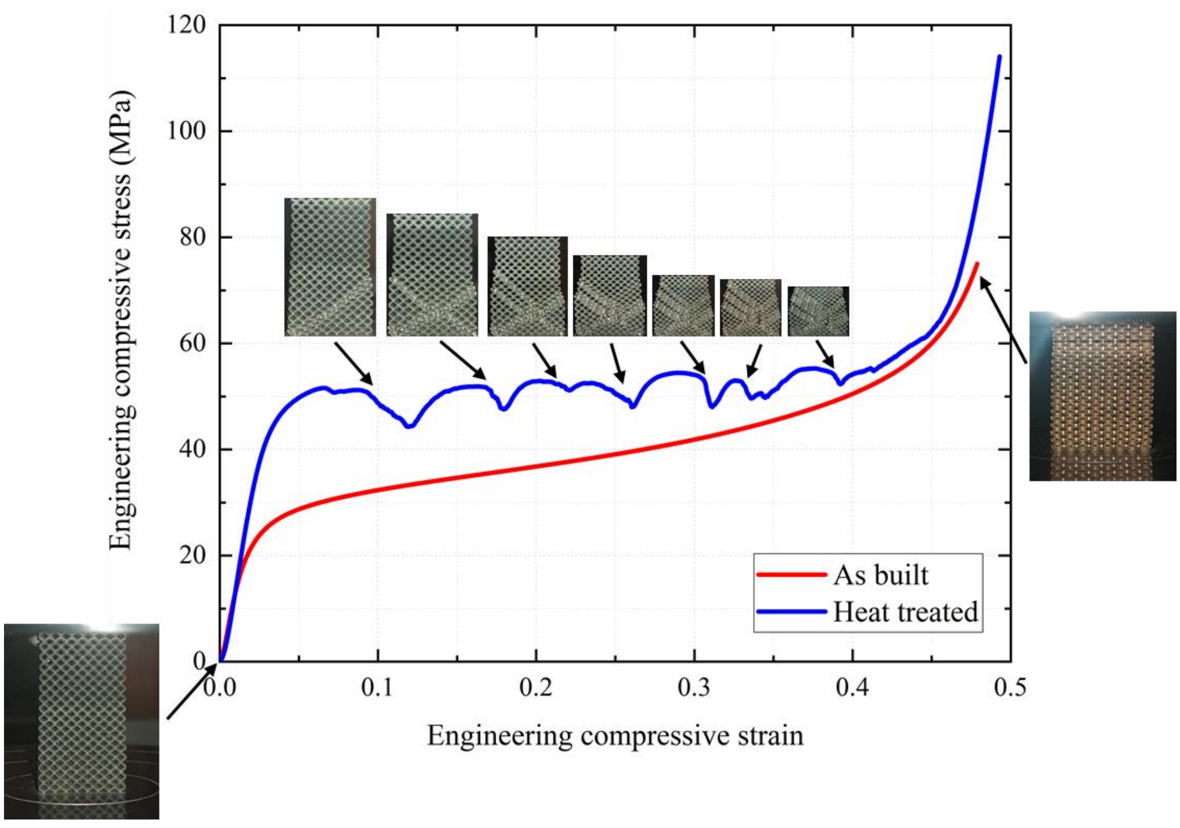

Figure 4.4. Room temperature compression engineering stress-strain curves corresponding to the as-built (red curve) and heat-treated (blue curve) LPBF fabricated Inconel 718 lattice structures.

4.3. Discussion

The Vickers microhardness increases from 305±17 HV in the as-built condition to 405±10 HV after the heat treatment. Altogether, the loss of compliance and increase in strength following precipitation are consistent with the observed transition from bending-dominated to stretch-dominated mechanical behaviour of the LPBF fabricated BCC lattice structures (Figure 4.4).

Strut-based topologies may be classified according to the Maxwell number (M), $M = s-3n+6$, where s is the number of struts, and n is the number of nodes. According to the Maxwell criterion, if $M<0$, the lattice would exhibit a bending-dominated behaviour, whereas if $M > 0$ the lattice would present a stretch-dominated behaviour [1]. In BCC lattices, such as that of the present study, s=8 and n=6, and therefore M = -13. BCC lattices would, therefore, behave as bending-dominated. Our results show that that is in- deed the case in the as-built condition, but that precipitation leads to a transition to a stretch-dominated behaviour, thus contradicting Maxwell criterion, in which microstructure does not play a role. The observed transition to a stretch-dominated behaviour is attributed to the high increase in the elastic modulus and the yield strength conferred by the heat treatment.

The Gibson-Ashby model is the most commonly accepted to predict the mechanical properties of cellular materials, including lattice structures [1]. This model states that the ratio of the elastic modulus of the lattice with respect to that of the bulk material (E^*/E_s) as well as the ratio of the lattice strength with respect to the yield strength of the bulk material ($\sigma^*/\sigma_{y,s}$) are a function of the lattice relative density (ϱ/ϱ_s). In particular, $(E^*/E_s) = C_E\, (\varrho/\varrho_s)^{nE}$ and $(\sigma^*/\sigma_{y,s}) = C_\sigma\, (\varrho/\varrho_s)^{n\sigma}$. A wide dispersion of coefficients (C_E, C_σ) and exponents (n_E, n_σ) have been reported for different materials and lattice structures.

In an effort to reconcile all the existing evidence, Maconachie et al. [1] carried out a regression analysis of all the available experimental data and obtained 'unified' parameters for each lattice topology (the analysis included 11 different topology types). For the data analysis, a single value of E s was utilized for each alloy type. In particular, for BCC structures, this regression analysis yielded the following results: $C_E = 0.07$, $n_E = 1.71$, $C_\sigma = 0.14$ and $n_\sigma = 1.14$. These parameters were utilized to calculate the yield strength of the BCC lattices investigated here, with the approximation that $\sigma_{y,s} = HV/3$ [39,40] , and the obtained results are $\sigma^*_{\text{as-built}} = 14$ MPa and $\sigma^*_{\text{heat-treated}} = 18.5$ MPa. The difference between the prediction and the experimental measurement is considerable for the as-built lattice (-6 MPa ~ -

30%), and even larger for the heat-treated lattice (22 MPa ~ -55%). Maconachie et al. [1] also found a relatively low correlation factor (R^2) of 66% for the regression analysis of the BCC data. It is our contention that the dispersion in the experimental data regarding the mechanical behaviour of BCC lattice structures might be attributed, at least partially, to the wide variety of microstructures that might be generated as a consequence of the different cooling rates and thermal history associated to LPBF manufacturing of structures with different strut diameters, cell sizes and overall lattice dimensions, as well as with sub- sequent post-processing treatments.

4.4. Remarks

In summary, this research shows that the high cooling rates associated with LPBF manufacturing of BCC Inconel 718 lattice structures with fine struts allow to generate supersaturated solid solutions with high compliance and bending-dominated behaviour that might be converted into stiffer, stronger structures exhibiting a stretch dominated behaviour by precipitation during post-processing solution plus aging treatments. This work proves that careful microstructural design provides a useful tool to tailor the mechanical behaviour of strut-based lattice structures. It is expected that the coupling between microstructure and lattice topology might give rise to unprecedented mechanical behaviour in LPBF fabricated strut-based lattice structures.

Bibliography

[1] T. Maconachie, M. Leary, B. Lozanovski, X. Zhang, M. Qian, O. Faruque, M. Brandt, SLM lattice structures: Properties, performance, applications and challenges, Mater. Des. 183 (2019) 108137.

[2] M. Benedetti, A. du Plessis, R.O. Ritchie, M. Dallago, S.M.J. Razavi, F. Berto, Architected cellular materials: A review on their mechanical properties towards fatigue-tolerant design and fabrication, Mater. Sci. Eng. R 144 (2021) 100606.

[3] T. DebRoy, H.L. Wei, J.S. Zuback, T. Mukherjee, J.W. Elmer, J.O. Milewski, A.M. Beese, A. Wilson-Heid, A. De, W. Zhang, Additive manufacturing of metallic components – Process, structure and properties, Prog. Mater. Sci. 92 (2018) 112–224.

[4] D. Herzog, V. Seyda, E. Wycisk, C. Emmelmann, Additive manufacturing of metals, Acta Mater. 117 (2016) 371-392.

[5] V.S. Deshpande, M.F. Ashby, N.A. Fleck, Foam topology: bending versus stretching dominated architectures, Acta Mater. 49 (2001) 1035.

[6] C. Pan, Y. Jan, J. Lu, Design and Optimization of Lattice Structures: A Review, Appl. Sci. 10 (2020) 6374.

[7] A.A. Zadpoor, Mechanical performance of additively manufactured meta-biomaterials, Acta Biomat. 85 (2019) 41.

[8] M. Leary, M. Mazur, H. Williams, E. Yang, A. Alghamdi, B. Lozanovski, X. Zhang, D. Shidid, L. Farahbod-Sternahl, G. Witt, I. Kelbassa, P. Choong, M. Qian, M. Brandt, Inconel 625 lattice structures manufactured by selective laser melting (SLM): Mechanical properties, deformation and failure modes, Mater. Des. 157 (2018) 179.

[9] T. Yu, H. Hyer, Y. Sohn, Y. Bai, D. Wu, Structure-property relationship in high strength and lightweight AlSi10Mg microlattices fabricated by selective laser melting Mater. Des. 182 (2019) 108062.

[10] A. Takezawa, K. Yonekura, Y. Koizumi, X. Zhang, M. Kitamura, Isotropic Ti–6Al–4V lattice via topology optimization and electron-beam melting, Addit. Manuf. 22 (2018) 634.

[11] A. Moussa, D. Melancon, A. El Elmi, D. Pasini, Topology optimization of imperfect lattice materials built with process-induced defects via Powder Bed Fusion, Addit. Manuf. (2020) 101608.

[12] L. Bai, J. Zhang, Y. Xiong, X. Chen, Y. Sun, C. Gong, H. Pu, X. Wu, J. Luo, Influence of unit cell pose on the mechanical properties of Ti6Al4V lattice structures manufactured by selective laser melting, Addit. Manuf. 34 (2020) 101222.

[13] L. Zhang, B. Song, J.J. Fu, S.S. Wei, L. Yang, C.Z. Yan, H. Li, L. Gao, Y.S. Shi, Topology-optimized lattice structures with simultaneously high stiffness and light weight fabricated by selective laser melting: Design, manufacturing and characterization, J. Manuf. Process. 56 (2020) 1166.

[14] Y. Liu, J. Zhang, X. Gu, Y. Zhou, Y. Yin, Q. Tan, M. Li, M.X. Zhang, Mechanical performance of a node reinforced body-centred cubic lattice structure manufactured via selective laser melting, Scr. Mater. 189 (2020) 95.

[15] M.S. Pham, C. Liu, I. Todd, J. Lertthanasarn, Damage-tolerant architected materials inspired by crystal microstructure, Nature 565 (2019) 305.

[16] E.D. Sanders, A. Pereira, G.H. Paulino, Optimal and continuous multilattice embedding, Sci. Adv. 7 (2021) 4838.

[17] R. Wauthle, B. Vranckenc, B. Beynaerts, K. Jorissen, J. Schrooten, J. P. Kruth, J. Van Humbeeck, Effects of build orientation and heat treatment on the microstructure and mechanical properties of selective laser melted Ti6Al4V lattice structures, Add. Manuf. 5 (2015) 77-84.

[18] I. Maskery, N.T. Aboulkhair, A.O. Aremu, C.J. Tuck, I.A. Ashcroft, Compressive failure modes and energy absorption in additively manufactured double gyroid lattices Addit. Manuf. 16 (2017) 24-29.

[19] P. Köhnen, C. Haase, J. Bültmanna, S. Ziegler, J. H. Schleifenbaum, W. Bleck, Mechanical properties and deformation behavior of additively manufactured lattice structures of stainless steel, Mater. Des. 145 (2018) 205-217.

[20] K. Hazeli, B. B. Babamiri, J. Indeck, A. Minor, H. Askari, Microstructure-topology relationship effects on the quasi-static and dynamic behavior of additively manufactured lattice structures, Mater. Des. 176 (2019) 107826.

[21] D. Zhang, W. Niu, X. Cao, Z. Liu, Effect of standard heat treatment on the microstructure and mechanical properties of selective laser melting manufactured Inconel 718 superalloy, Mater. Sci. Eng. A 644 (2015) 32.

[22] M. Pröbstle, S. Neumeier, J. Hopfenmüller, L.P. Freund, T. Niendorf, D. Schwarze, M. Göken, Superior creep strength of a nickel-based superalloy produced by selective laser melting, Mater. Sci. Eng. A 674 (2016) 299.

[23] Inconel 718 data sheet, Publication Number SMC-045, Spec. Met. Coorparation (2007).

[24] C.M. Cepeda-Jiménez, M. Castillo-Rodríguez, M.T. Pérez-Prado, Origin of the low precipitation hardening in magnesium alloys, Acta Mater. 165 (2019) 164.

[25] J. K. Mason, C.A. Shuh, The generalized Mackenzie distribution: Disorientation angle distributions for arbitrary textures, Acta Mater. 57 (2009) 4186-4197.

[26] R. Lawitzki, S. Hassan, L. Karge, J. Wagner, D. Wang, J. von Kobylinski, C. Krempaszky, M. Hofmann, R. Gilles, G. Schmitz, Differentiation of γ' and γ'' precipitates in Inconel 718 by a complementary study with small-angle neutron scattering and analytical microscopy, Acta Mater. 163 (2019) 28–39.

[27] J.P. Choi, G.H. Shin, S. Yang, D.Y. Yang, J.S. Lee, M. Brochu, J.H. Yu, Densification and microstructural investigation of Inconel 718 parts fabricated by selective laser melting, Powder Technol. 310 (2017) 60–66.

[28] Y. Kuo, S. Horikawa, K. Kakehi, The effect of interdendritic δ phase on the mechanical properties of Alloy 718 built up by additive manufacturing, Mater. Des. 116 (2017) 411–418.

[29] M. Ni, C. Chen, X. Wang, P. Wang, R. Li, X. Zhang, Anisotropic tensile behavior of in situ precipitation strengthened Inconel 718 fabricated by additive manufacturing, Mater. Sci. Eng. 701 (2017) 344–351.

[30] C. Galera, E. Nieto-Valerias, M. Gardon, M.T. Pérez-Prado, J. Llorca, Effect of ZrH_2 particles on the microstructure and mechanical properties of IN718 manufactured by selective laser melting, Mater. Sci. Eng. A, 813 (2021) 141123.

[31] Y. Zhao, K. Li, M. Gargani, W. Xion, A comparative analysis of Inconel 718 made by additive manufacturing and suction casting: Microstructure evolution in homogenization, Addit. Manuf. 36 (2020) 101404.

[32] H. Peng, Y. Shi, S. Gong, H. Guo, B. Chen, Microstructure, mechanical properties and cracking behaviour in a nickel-base superalloy fabricated by electron beam melting, Mater. Des. 159 (2019) 155-169.

CHAPTER 5

Coupled effect of microstructure and topology on the mechanical behaviour of Inconel 718 additively manufactured lattice structures

5.1. Background and design of the study

It has been well established that lattice topology has a governing influence on the mechanical behaviour of lattices [1-11] and several models have been put forward to relate architecture and mechanical performance with the aim of improving the predictability and of optimizing the lattice design. For example, the Maxwell criterion, based on the Maxwell number ($M = s - 3n + 6$; where s is the number of struts, and n is the number of nodes) [12,13,14], states that topologies with $M < 0$ are bending-dominated, whereas those with $M \geq 0$ are stretch-dominated. This model predicts that typical strut-based lattices, including BCC, BCCZ, FCC, FCCZ, and diamond architectures, among others, are bending-dominated [15,3]. Experimental data, however, do not always comply with these predictions. For example, Leary et al. [3] reported a stretch-dominated response in Inconel 625 BCCZ and FCCZ lattices. Similarly, Yu et al. [4] observed a stretch-dominated response in AlSi10Mg microlattices with a diamond structure ($M = -14$). On the other hand, the Gibson-Ashby model [16] predicts that the ratios of the mechanical properties (elastic modulus, yield strength) of a given lattice with respect to those of the constituent base material are proportional to the lattice relative density. However, systematic attempts to rationalize all the existing evidence within the frame of this model, such as that carried out by Maconachie et. al. [12], also yielded a relatively small correlation between experimental observations and model predictions for several lattice architectures. All this evidence suggests that, besides topology, the properties of the base metallic material, which in metallic alloys are highly dictated by its microstructure, might have a critical influence on the mechanical behaviour of lattices. A handful of studies have analyzed the influence of annealing following LPBF processing on the mechanical behaviour of lattices [17-21]. However, in these works the isolated effect of individual microstructural parameters were not thoroughly explored. Moreover, the coupled effect of architecture and individual microstructural features in LPBF processed strut-based lattices is still widely unexplored.

The aim of this work is to analyze the isolated influence of precipitation in Inconel 718 additively manufactured lattices with multiple architectures at room and high temperatures. With that purpose, several cubic and hexagonal strut-based lattices were printed and tested at room temperature and at 600 °C at quasi-static rates. Post-LPBF aging heat treatments were carefully optimized to induce controlled precipitation without altering other microstructural parameters. The mechanical behaviour of the peak-aged lattices thus developed was also measured under similar testing conditions and compared to that of the as-built lattices. The feedstock material utilized for this work was gas atomized Inconel 718 powder purchased from Oerlikon. The composition of the powder is summarized in Table 5.1. Figure 5.1. (a) illustrates the monomodal particle size distribution and the corresponding d_{10}, d_{50}, and d_{90} values, which amounted, respectively, to 25, 40, and 63 μm. The apparent density, tapped density and flowability values of the powder, which were measured using a standard Hall apparatus, are, respectively, 4.5 g/cm^3, 4.9 g/cm^3, and 15 s. Figure 5.1. (b) confirms that the morphology of the powders ranges from spherical to ellipsoidal and that most particles contain satellites. Six strut-based lattices with external dimensions of approximately 20x20x40 mm^3, and with FCC and HCP topologies, were printed by LPBF in a Renishaw AM400 system furnished with a reduced build volume (RBV) platform. In all cases, the build direction (BD) was parallel to the long axis of the lattice.

Table 5.1. Chemical composition of Inconel 718 powder (wt.%)

Ni	**Cr**	**Co**	**Al**	**Nb**	**Ti**	**Fe**
49.5-50	18.7-19	0.066-0.070	0.38-0.4	4.6-4.8	0.45-0.5	13.5-13.8
Mo	**Mn**	**Si**	**Cu**	**Ta**	**P**	**Zr**
1.6-1.65	0.054-0.057	0.35-0.39	0.23-0.25	<0.01	<0.01	<0.005

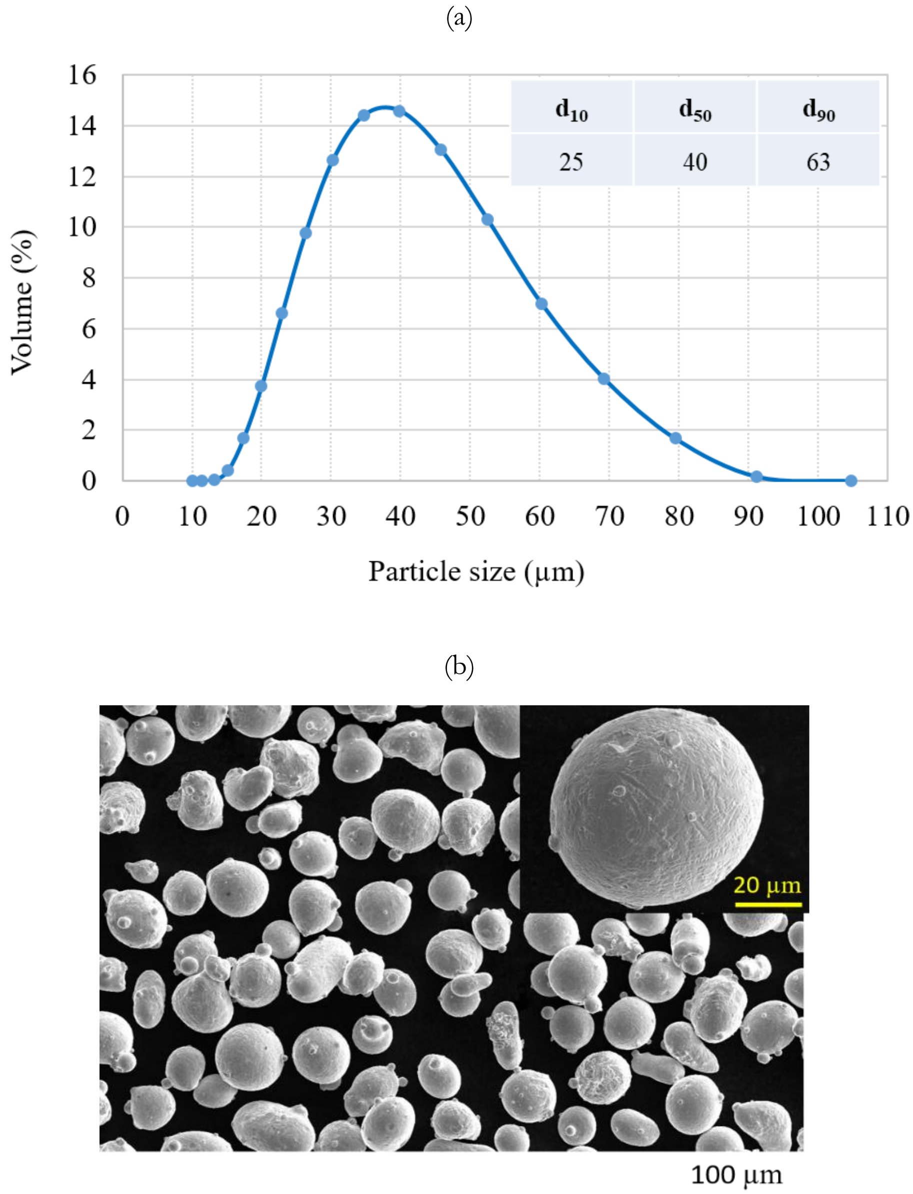

Figure 5.1. (a) Particle size distribution of the feedstock Inconel 718 powders, including d_{10}, d_{50} and d_{90} values (in μm); (b) SEM micrograph illustrating particle morphology.

Figure 5.2 illustrates the as-built LPBF lattices after support removal: FCC (Figure 5.2. (a)), FCCXYZ, i.e., FCC with additional struts parallel to the X, Y and Z directions (Figure 5.2. (b)), HCP with the c-axis parallel to BD (HCP0, Figure 5.2. (c)), HCP with the c-axis perpendicular to BD (HCP90, Figure 5.2. (d)), HCP with the c-axis at 45° with respect to BD and with open ends (HCP45, Figure 5.2. (e)), and HCP with the c-axis at 45° with respect to BD and with an outer frame boundary (HCP45B, Figure 5.2. (f)).

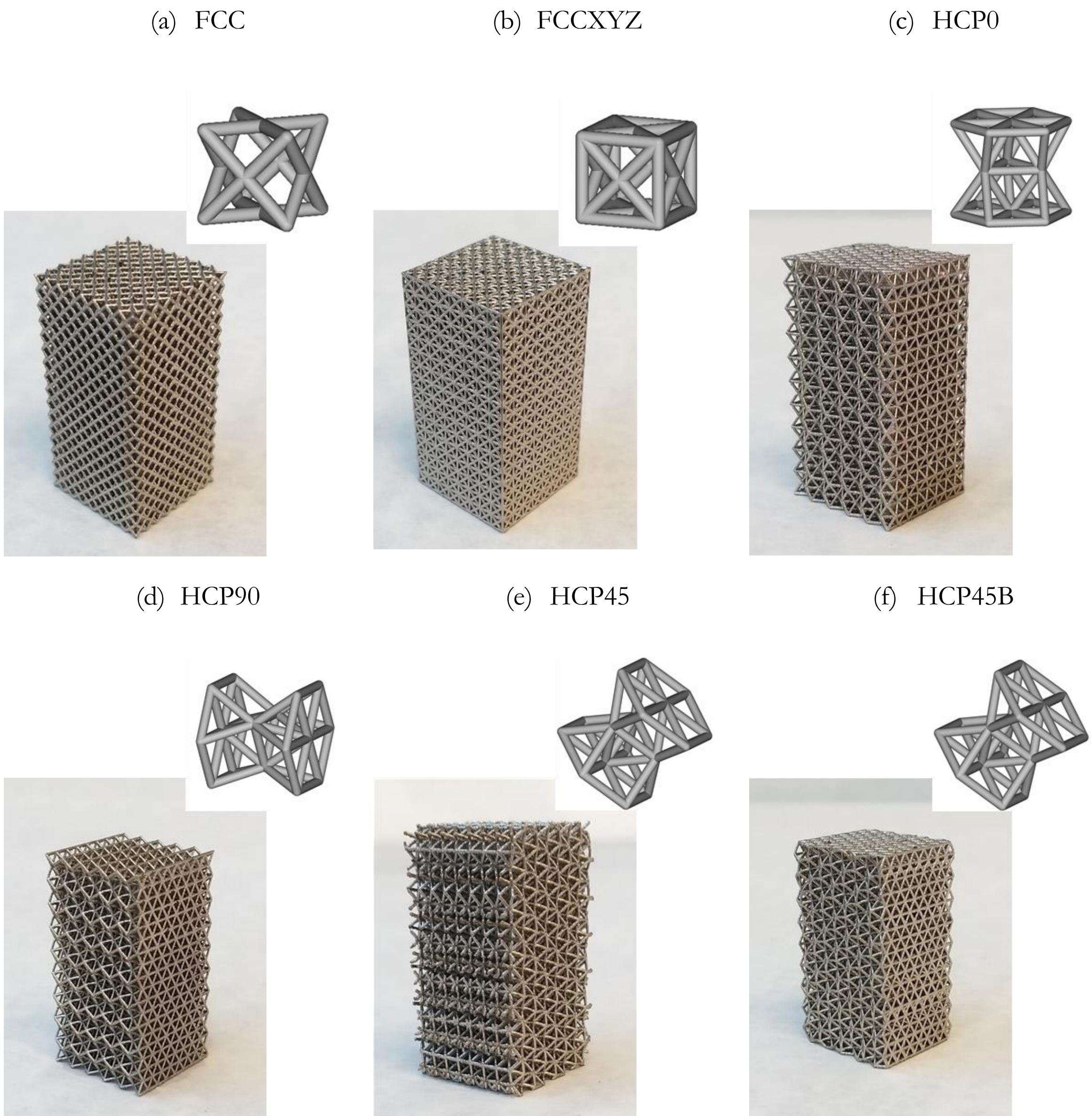

Figure 5.2. LPBF fabricated lattice structures, with six different topologies. (a) FCC; (b) FCCXYZ; (c) HCP with the c-axis parallel to the vertical direction (HCP0); (d) HCP with the c-axis parallel to the horizontal direction (HCP90); (e) HCP with the c-axis at 45° with respect to the vertical direction and with open ends (HCP45); (f) HCP with the c-axis at 45° with respect to the vertical direction and with an outer boundary (HCP45B).

Lattice structures were designed using nTopology. In all cases, the strut diameter was 0.4 mm. The cubic lattices were manufactured with 2.5x2.5x2.5 mm^3 unit cells. In the HCP lattices, a=2.5 mm and the c/a ratio was chosen to be equivalent to that of a typical HCP alloy such as pure magnesium (1.624), where the most compact plane is the basal plane. The relative densities of the six lattices investigated ((ρ/ρ_s, where (ρ_s is the density of bulk Inconel 718, amounting to 8.2 g/cm^3) are the following: FCC (0.15), FCCXYZ (0.2), HCP0 (0.14), HCP90 (0.14), HCP45 (0.13), and HCP45B (0.15).

LPBF manufacturing was carried out using a bidirectional scanning strategy with a layer thickness of 30 μm and with 67° rotation between two consecutive layers. The processing parameters, which were optimized to obtain high consolidation using a Design of Experiments (DoE) strategy, were P (laser power) =100 W, v (scan speed) = 875 mm/s (exposure time = 50 μs and point distance=70 μm), and h (hatch distance) = 90 μm. Under these conditions, a robust manufacturing campaign could be put in place to print lattices with high geometric accuracy and high reproducibility. The average area fraction of porosity, measured from optical micrographs of cross sections perpendicular to BD using the ImageJ image analysis software, was 0.44%.

(a) (b)

Figure 5.3. LPBF fabricated tensile specimens, designed to measure the mechanical behaviour of single-struts at room and high temperature. (a) Specimens attached to the build plate, prior to support removal; (b) 3D tomographic reconstruction of the gauge length, where internal pores have been coloured in blue.

In order to better understand the mechanical behaviour of the LPBF-processed lattices, tensile coupons with the cylindrical gauge's diameter and length identical to those of individual lattice struts

(0.4 mm in diameter and 10 mm in length) were manufactured by LPBF using the same set of processing parameters that were utilized to manufacture the lattices. Figure 5.3. (a) illustrates the additively manufactured tensile coupons attached to the RBV platform, prior to support removal. The porosity volume fraction in these specimens, measured by tomography using a Phoenix X-ray (General Electric) Nanotom 160NF system, was 0.21 ± 0.1%. The experimental conditions used to carry out the tomography measurements were 130 kV, 60 μA and a W target with a Cu filter of 0.2 mm. The resolution achieved was of 6 μm/pixel. Figure 5.3. (b) is a 3D image reconstruction of the gauge length of one tensile specimen, illustrating the internal porosity distribution.

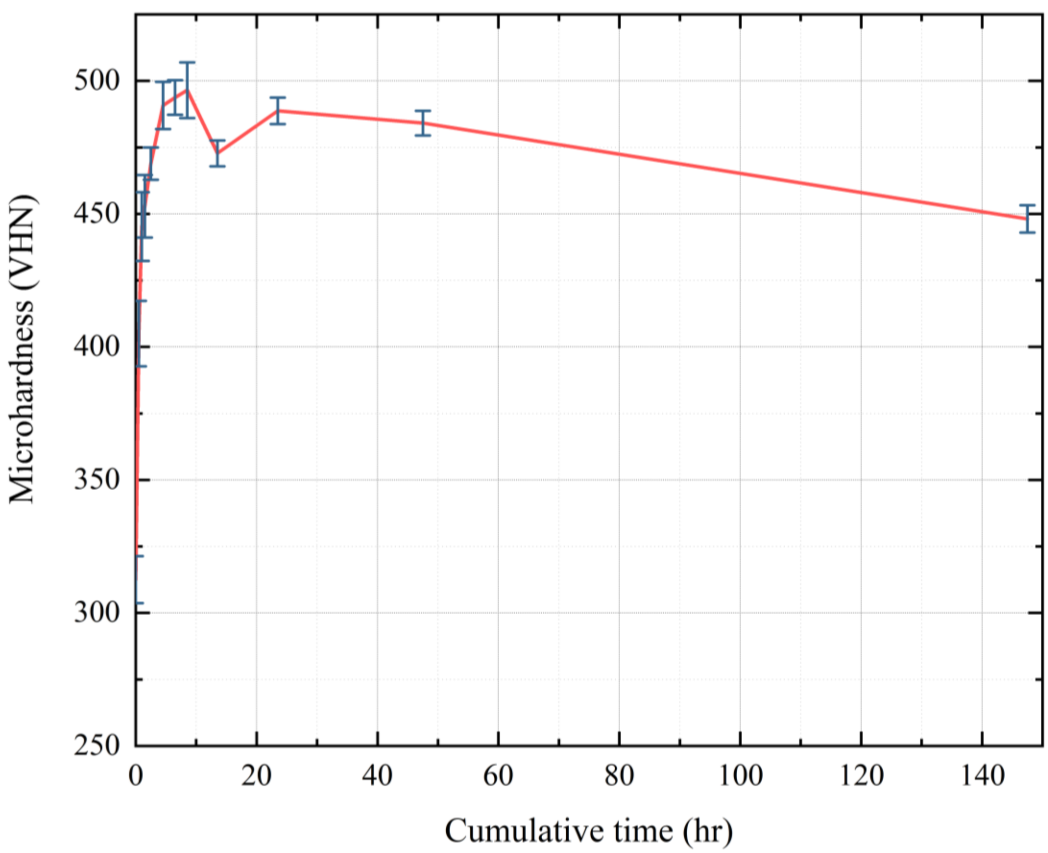

Figure 5.4. Aging curve illustrating the evolution of the Vickers microhardness following heat treatments at 718°C up to a cumulative time of 150 h.

Following LPBF manufacturing selected lattices were subjected to an aging heat treatment study at 718 °C by introducing them in a muffle furnace for increasing periods of time followed by air cooling to room temperature. The mentioned aging temperature was chosen because it is commonly used in standard Inconel 718 aging treatments [22-24]. Figure 5.4 illustrates the evolution of the Vickers hardness with aging time. The hardness was measured in polished cross sections of the as-built and aged lattices perpendicular to the BD using a Shimadzu microhardness indenter, with forces of 4.9 and 9.8 N, respectively, and a dwelling time of 15 s. Ten hardness measurements were performed for each condition. The hardness of the as-built lattices (317 ± 8 HV) increased during aging up to a maximum of 502 ± 9 HV after 6 h.

It must be noted that the measured hardness levels achieved following the direct aging treatment, and in the absence of any solutionizing step, are similar or higher than those reported for peak aged Inconel 718 following the standard two-stage heat treatment [25,26], and somewhat lower than those achieved by direct double aging (535 HV) [27,28]. Treatments longer than about 8-10 h resulted in softening of the lattice material. On the light of these findings, several lattices with the six topologies investigated, as well as some single-strut tensile specimens, were heat treated under peak-aging conditions (718 °C, 6h) in order to understand the effect of aging on the mechanical behaviour.

The microstructures of the as-built and peak-aged lattices were examined at different magnifications using several complementary techniques. First, electron backscattered diffraction (EBSD) was used to characterize the grain size, measured by the linear intercept method, the microtexture, and the grain boundary distribution. EBSD was performed in a focused ion beam field emission gun scanning electron microscope (FIB-FEGSEM, FEI Helios NanoLab DualBeam) equipped with an HKL system, a CCD camera, and both the Aztec and the Channel 5.0 data acquisition and analysis software packages. EBSD measuring conditions included a current of 2.7 nA, a step size of 1.1 μm, and an accelerating voltage of 30 kV. The as-built and peak-aged microstructures were also examined by transmission electron microscopy (TEM) with a FEI Talos F200x microscope operating at 200 KV. Energy dispersive spectrometry (EDS) was utilized to analyze the composition of segregated species and second phase particles. Sample preparation for TEM consisted on the extraction of electron-transparent thin lamellae from selected regions of the strut interiors by FIB milling, as described in detail in [29].

As-built and peak-aged lattices with each of the six topologies investigated were compressed at room temperature and at 600 °C using an initial crosshead speed of 0.3 mm•min-1 in an Instron 3384 universal testing machine. The compression axis was parallel to BD. Tests were observed to be highly reproducible (see Supplementary Figure S1 in Annex D), which attests to the robustness of the printing process. At least two tests were carried out per testing condition. High temperature tests were performed using an Ibertest IB TR331100 climatic chamber. A high-resolution camera (Correlation Solutions Stingray Allied F504B ASG) was used to capture live videos of the compression of the lattices at both room and high temperatures in order to facilitate the investigation of the deformation and fracture mechanisms. Additionally, the tensile behaviour of the LPBF processed single-strut tensile coupons was also measured in the as-built and peak-aged conditions, at room temperature and 600 °C, and at an initial crosshead speed of 0.3 mm•min^{-1} in order to study the effect of microstructure on the material properties.

FEA modelling was carried out using Abaqus/Explicit to simulate the deformation and strain localization during compression of some of the studied lattice structures. Lattice models for FEA were meshed using Timoshenko B31 beam elements with an approximate element length of 1.5 mm. The orientations of beams were assigned parallel to the directions of struts. The material properties for simulations (shown in Table 5.2) were obtained from the tensile true stress-strain curves of as-built and peak-aged samples.

To produce a good fit with the experimental data of lattice structures, the input values of strength were recalibrated by rescaling the values using a factor of 1.1 for as-built and 1.3 for peak-aged conditions. The values of the apparent elastic modulus for the as-built and peak-aged Inconel 718 were adjusted to 72 GPa and 92 GPa, respectively. Although the elastic modulus of the alloy should be significantly higher than the used values, this recalibration was necessary to reflect the effect of porosity and surface roughness that degraded the stiffness of the lattice fine struts.

Table 5.2. Mechanical properties of the base material for FEA

	Density (g/cm^3)	**Young's Modulus (GPa)**	**Poisson's Ratio**	**Yield strength (MPa)**	**Ultimate tensile strength (MPa)**
As-built	8.2	72	0.284	539	920
Peak-aged	8.2	92	0.284	1357	1615

To simulate the compression, two rigid plates meshed by R3D4 elements with a size of 2 mm were created as compression plates. The bottom plate was fixed with tie constraints applied to the bottom nodes and struts of lattice. The top plate was moving in the direction perpendicular to the plate towards the bottom plate to compress the lattice. A general hard contact and a friction coefficient of 0.2 were used for all lattice simulations. To simultaneously ensure the quasi-static simulation and reduce the computing time, the mass of lattice was scaled by a factor of 256 with kinetic energy of lattice controlled less than 1% of total energy during the compression.

5.2. Results

5.2.1. Microstructure of Inconel 718

The as-built material microstructure was found to be similar for all lattices, irrespective of their architectures. This is consistent with the fact that a common set of processing parameters was used to print all the lattices and that they all have the same strut dimensions. For the sake of brevity, we will show here only the microstructure of the FCC lattice. Figure 5.5 compares the polycrystalline microstructure and the microtexture of the Inconel 718 FCC as-built and peak-aged lattices along cross sections parallel to BD (Figures 5.5. (a) and 5.5. (b), respectively) and perpendicular to BD (Figures 5.5. (c) and 5.5. (d), respectively). Several EBSD inverse pole figure maps showing the crystallographic orientations with respect to the BD are included. Figure 5.5 reveals that the aging treatment did not lead to any significant changes in the grain size, shape, and orientation. Grains were slightly elongated along BD both in the as-built and peak-aged conditions.

The corresponding line intercept size distribution histograms, measured along cross sections parallel and perpendicular to BD, are presented in Figures 5.6. (a) and (b), respectively. The average grain length and width are, respectively, 16 ±2 8 μm and 10 ± 14 μm in the as-built lattice, and 13 ± 26 μm and 9 ± 10 μm in the peak-aged lattice. The crystallographic texture is basically random in both conditions, with only a slight tendency for the <001> directions to align with the BD, as indicated in the corresponding inverse stereographic triangles. Figure 5.7 compares the misorientation distribution histograms of the FCC as-built and peak-aged lattices on cross sections parallel to BD (Figure 5.7. (a)) and perpendicular to BD (Figure 5.7. (b)). It can be seen that the aging treatment did not lead to any major changes in the misorientation of the grain boundary network. In both cases, as is typical of LPBF processed superalloys [25-27], a high fraction of low angle boundaries, with misorientations smaller than 5°, was present.

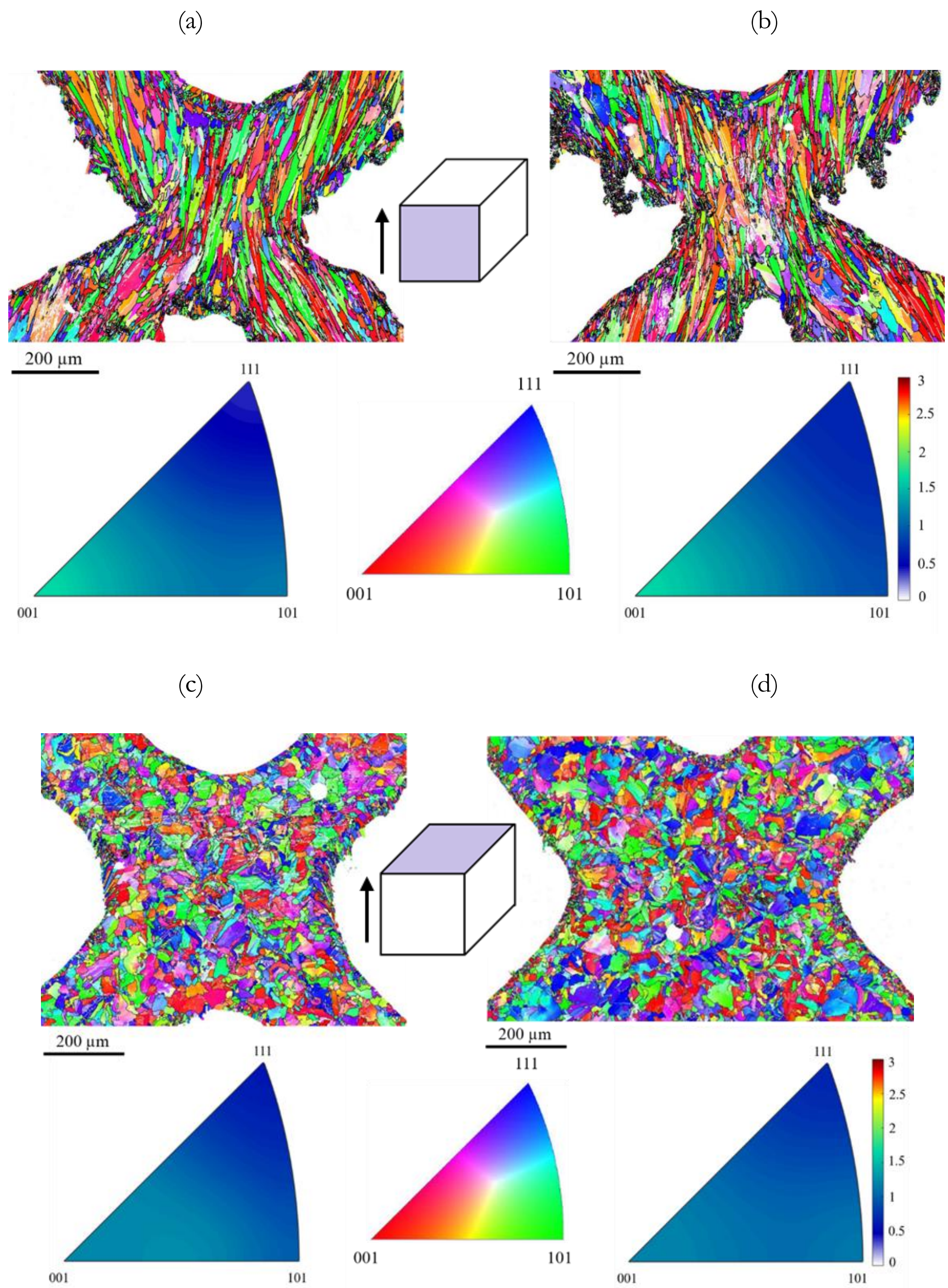

Figure 5.5. EBSD inverse pole figure maps (IPF) in the BD (indicated by black arrow) illustrating the microstructure and the microtexture of the FCC as-built (a, c) and peak-aged (b, d) lattices. (a, b) Cross-section parallel to BD; (c, d) cross section perpendicular to BD. An inverse stereographic triangle illustrating the orientation of the BD has been placed next to each condition, along with the orientation colour coding.

(a)

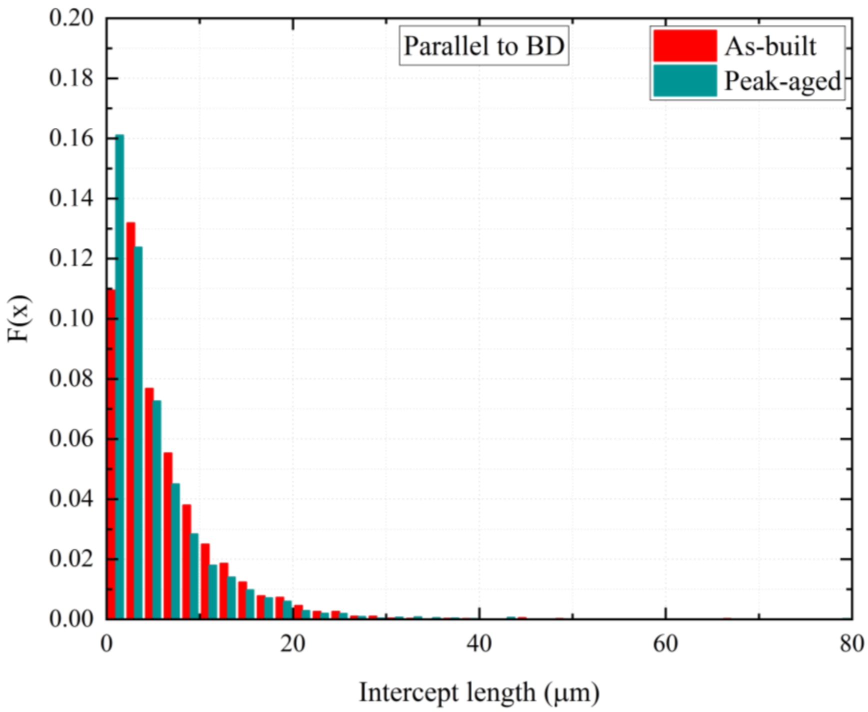

(b)

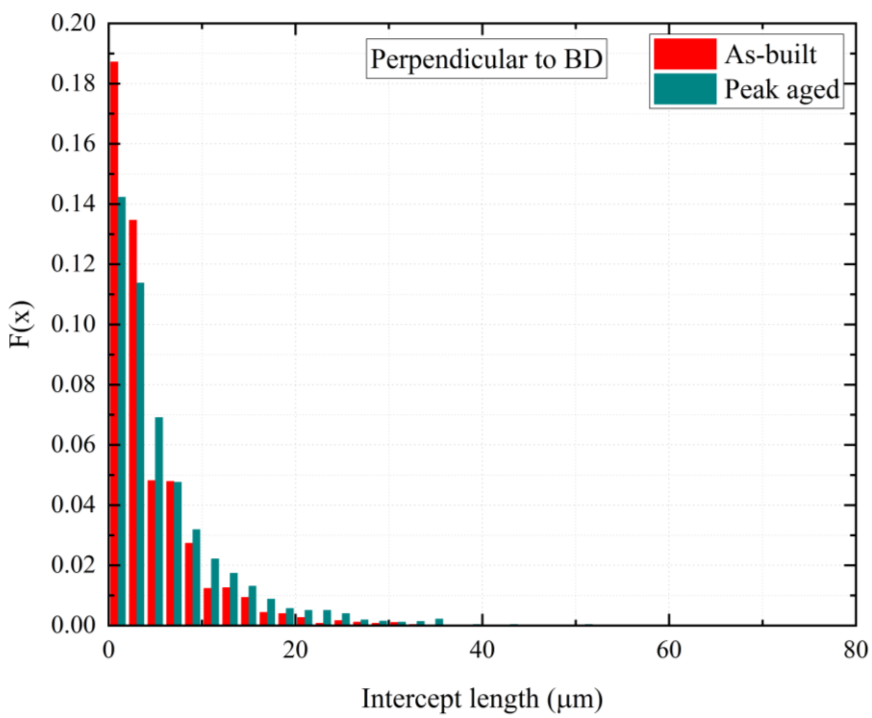

Figure 5.6. Comparison of the line intercept size distributions of the as-built and peak-aged FCC lattices. (a) Cross-section parallel to BD; (b) cross-section perpendicular to BD.

(a)

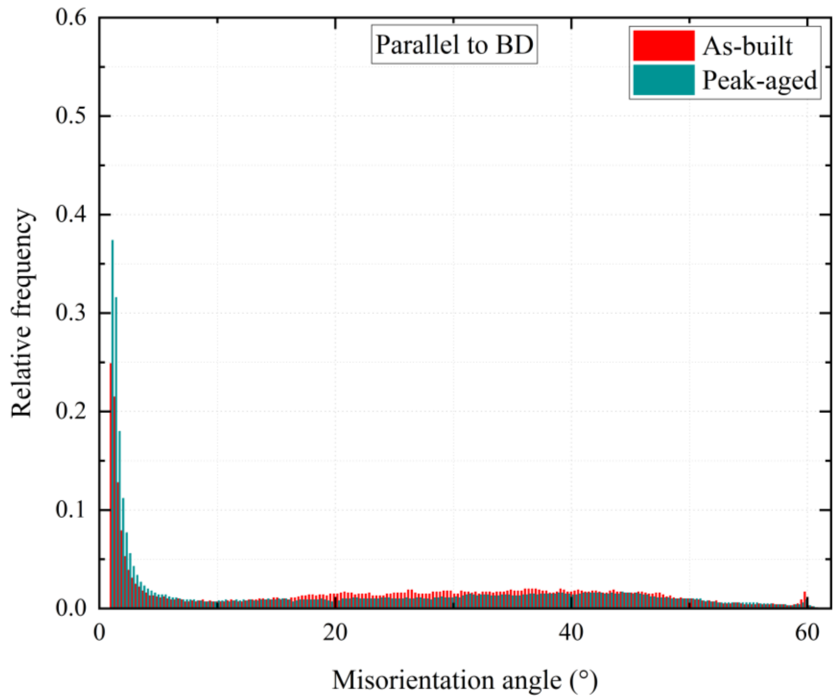

(b)

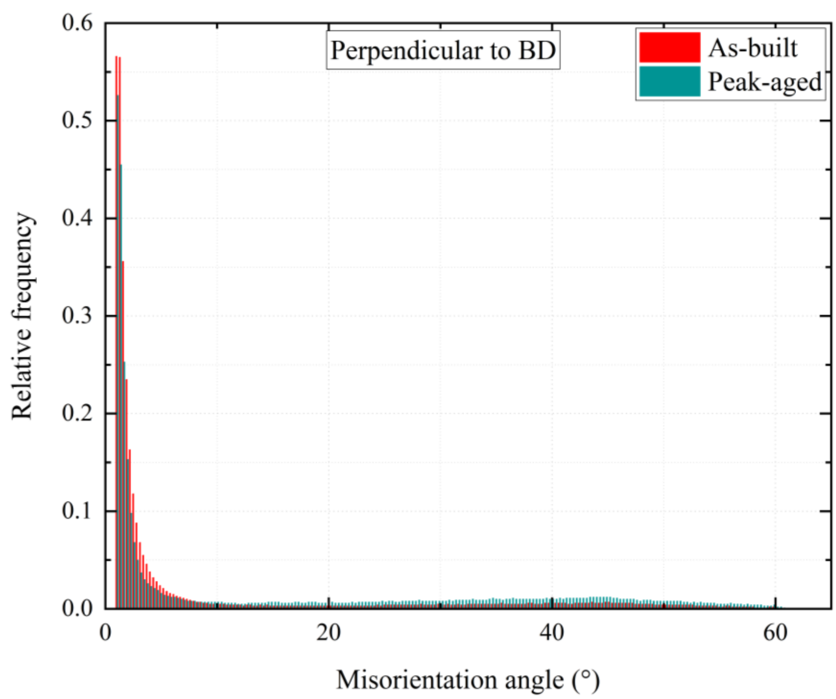

Figure 5.7. Comparison of the misorientation distribution histograms corresponding to the FCC as-built and peak-aged lattices. (a) Cross-section parallel to BD; (b) cross section perpendicular to BD.

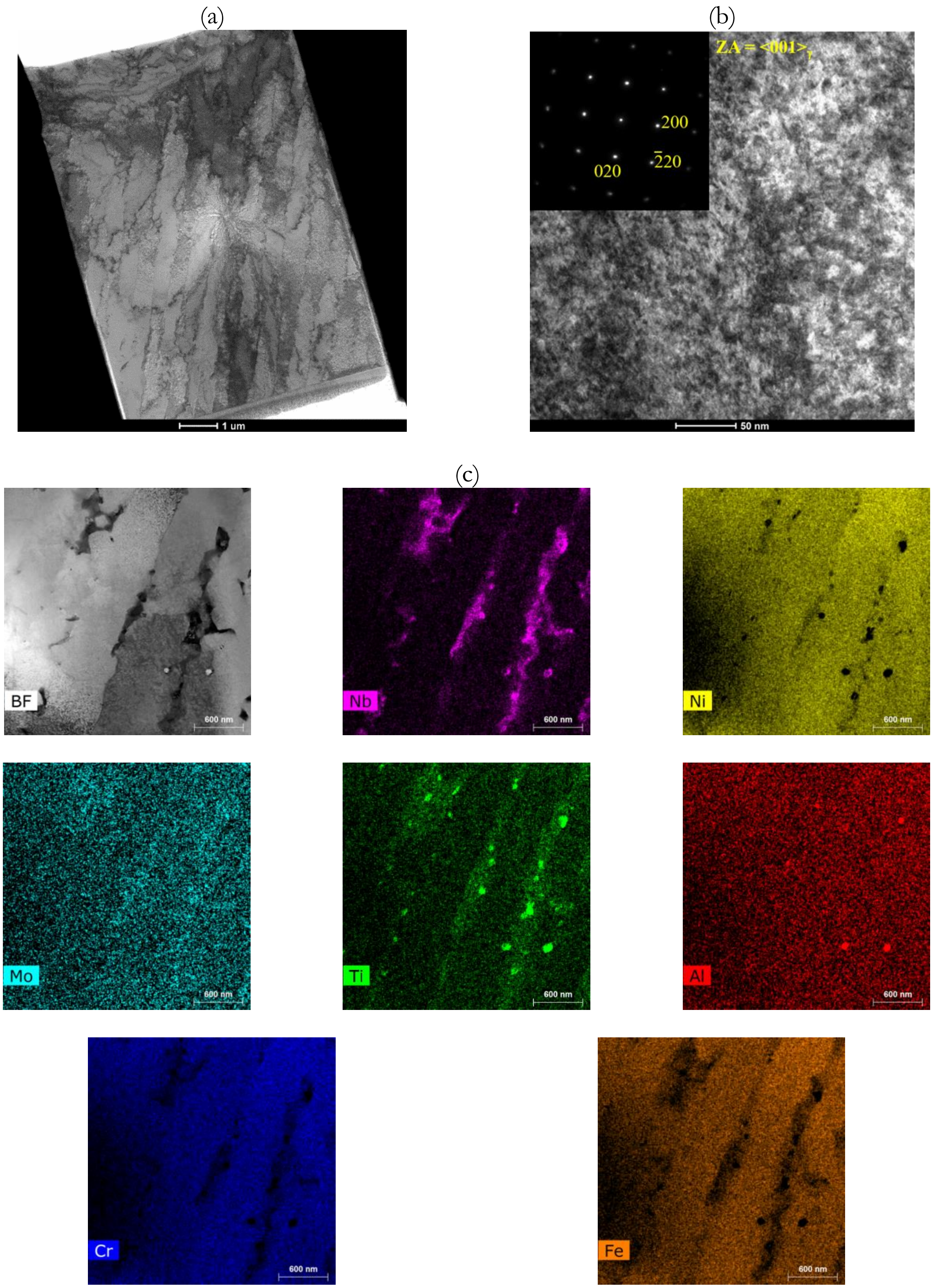

Figure 5.8. TEM examination of the as-built FCC lattice along a <001>$_\gamma$ zone axis. (a) Bright field micrograph illustrating the cellular structure; (b) Bright field micrograph and the corresponding selected area diffraction pattern illustrating the interior of a cell; (c) EDS maps depicting the distribution of different elements in a selected area.

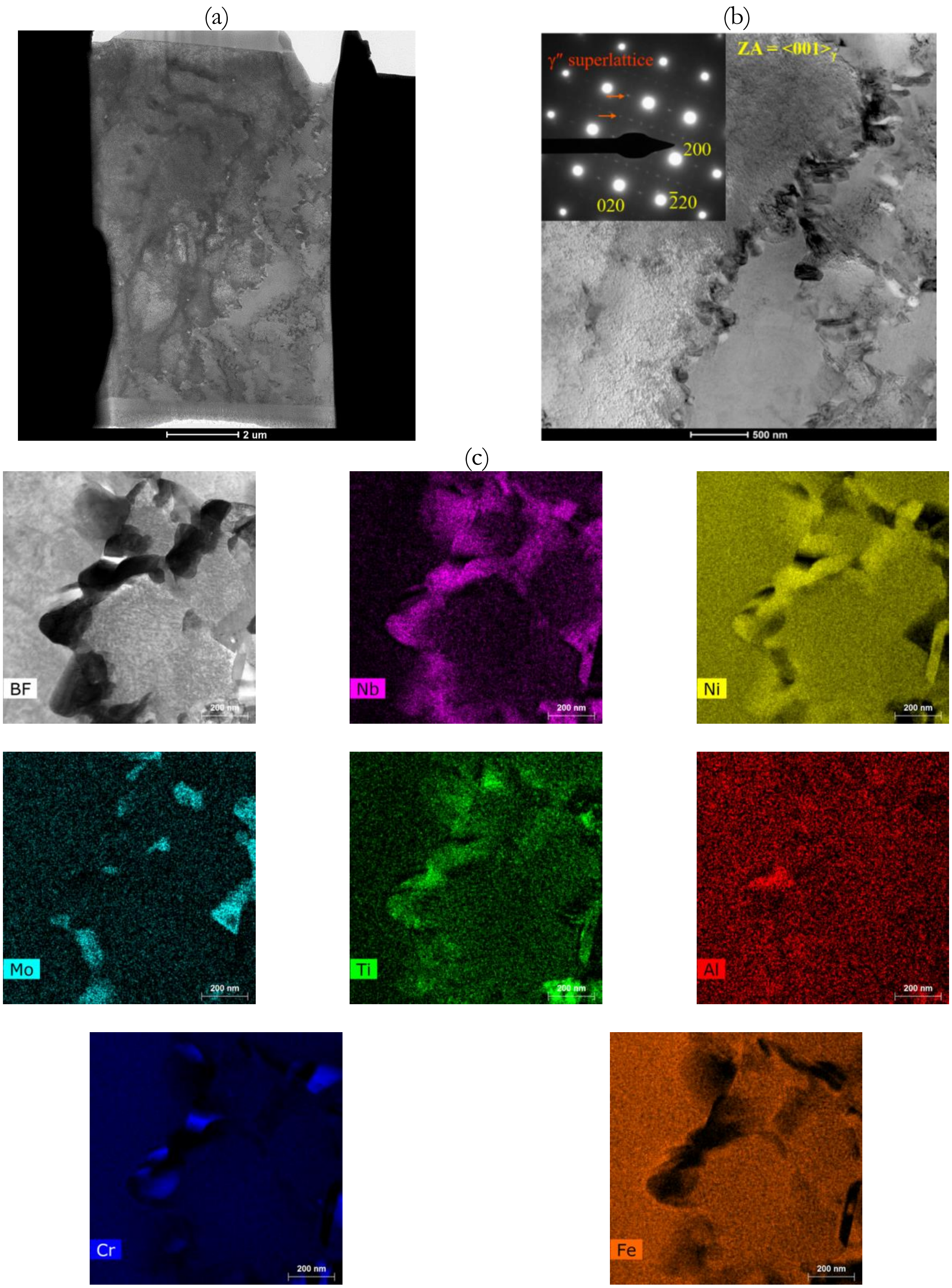

Figure 5.9. TEM examination of the heat-treated FCC lattice along a <001>$_{\gamma}$ zone axis. (a) Bright field micrograph illustrating the cellular structure; (b) Bright field micrograph at higher magnification and the corresponding selected area diffraction pattern. The orange arrows highlight the superlattice spots; (c) EDS maps depicting the distribution of different elements in a selected area.

Figure 5.8 shows the microstructure of the as-built FCC lattice in more detail. Figure 5.8. (a) is a bright field TEM micrograph illustrating the cell structure. The interior of an individual cell, and the corresponding selected area diffraction (SAD) pattern are included in Figure 5.8 (b). It can be seen that cell interiors are supersaturated solid solutions and therefore only one set of diffraction spots, corresponding to the Ni superalloy matrix (γ), is visible in the SAD pattern. Such spots have been labelled using yellow indexes. The grey contrast in Figure 8b denotes the presence of some solute clusters and some dispersed nanoparticles, which do not give rise to any additional reflections in the corresponding SAD pattern. Figure 5.8 (c) is a collection of EDS maps in which it can be seen that segregation, mostly of Nb, takes place at cell boundaries

Following aging (Figure 5.9) the cell size remained similar (Figure 5.9. (a)), but precipitation of γ″ particles clearly took place. The presence of such precipitates is evidenced by the appearance of additional reflections in the corresponding SAD pattern (Figure 5.9. (b)), which are highlighted using orange arrows. The EDS maps of Figure 5.9. (c) reveal Nb, Mo, and Ti segregation at cell boundaries. In summary, the key difference between the as-built and peak-aged lattices is, thus, the presence of γ″ precipitates in the treated samples, while other microstructural features such as the cell size, the grain size, morphology and orientation, as well as the nature of the grain boundaries, are similar in both conditions.

5.2.2. Influence of precipitation on the mechanical behaviour of cubic lattice structures

Figure 5.10 illustrates the specific (i.e., normalized by the relative density) compressive stress-strain curves corresponding to the as-built and peak-aged lattices with FCC (Figure 5.10. (a)) and FCCXYZ (Figure 5.10. (b)) topologies. The corresponding room temperature and high temperature (600°C) mechanical behaviour are compared in the same figure and the yield strength values are summarized in Table 5.3.

Several trends can be inferred from Figure 5.10. First, the FCC lattice is weaker than the FCCXYZ lattice due to the presence of added <001> struts in the latter. Second, in the as-built condition, both cubic lattices exhibit predominantly a bending dominated behaviour, in which a stress plateau is clearly apparent following yielding and prior to the densification stage.

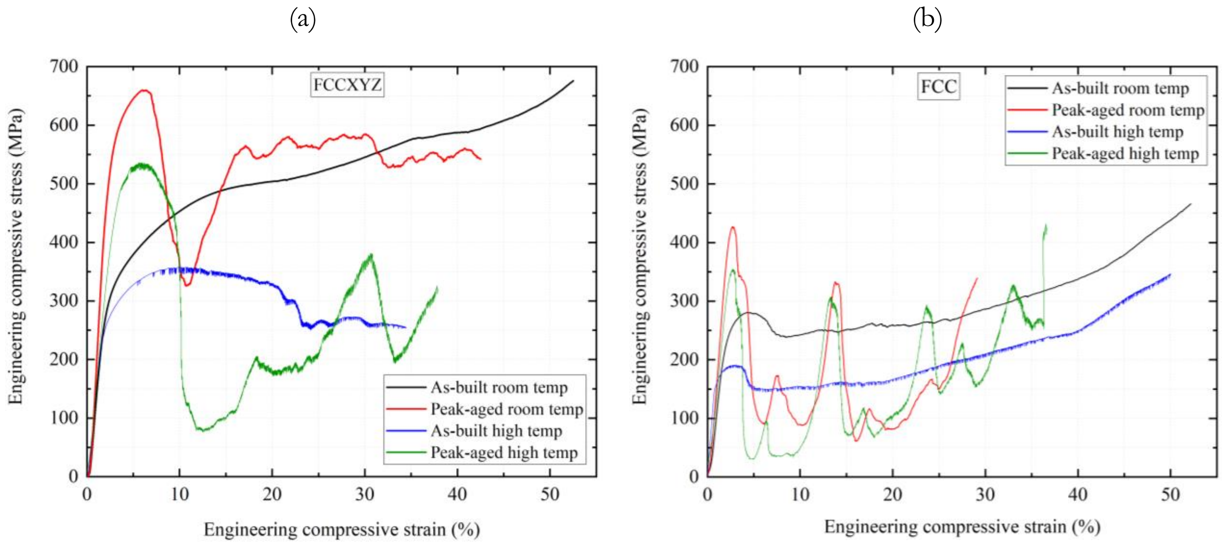

Figure 5.10. Specific engineering compressive stress-strain curves corresponding to the (a) FCC and (b) FCCXYZ Inconel 718 3D printed lattices tested at room and high (600°C) temperatures. Data corresponding to the two microstructures investigated (as-built and peak-aged) are shown. Tests were carried out using an initial cross-head speed of 0.3 mm·min^{-1}

In the FCC lattice, however, a stress peak, similar to a yield point phenomenon often seen in metals [30], is observed prior to the stress plateau. At the two temperatures investigated, precipitation due to the age treatment leads to strengthening and to a transition to a stretch-dominated behaviour. For a given microstructure, increasing the test temperature to 600 °C does not give rise to any change in the deformation mode (bending or stretch-dominated) but it leads to a reduction in the average width of the stress serrations (i.e., the average strain amplitude of the serrations) of the peak-aged lattices (Figure 5.10. (a)).

Figure 5.11. (a) shows the surfaces of the as-built and peak-aged FCC lattices at different nominal strain levels, both at room and high temperatures. In the as-built condition, at the two temperatures investigated, strain concentrated during the first deformation stages along a band that makes an angle of about 45° with respect to the compression axis.

Within the mentioned band, which became wider with increasing strain, struts deformed plastically to a large extent without fracture (i.e. plastic hinges). The stages of band formation and band propagation were associated, respectively, to the stress maximum and to the stress plateau observed following yielding in the curves corresponding to the as-built FCC lattices in Figure 5.10. (a). On the other hand, the peak-aged FCC lattices failed by the break-up of the struts along a plane making an angle of about

45° with respect to the compression axis at the two temperatures investigated, leading to the dramatic stress decrease observed in Figure 5.10. (a) at strains close to 0.05.

Table 5.3. Lattice yield strength values corresponding to Inconel 718

Lattice yield strength (MPa)	As-built	Peak-aged
FCC, RT	132	332
FCCXZ, RT	213	365
HCP0, RT	122	450
HCP90, RT	100	250
HCP45, RT	90	220
HCP45B, RT	85	212
FCC, 600°C	142	265
FCCXZ, 600°C	116	335
HCP0, 600°C	100	300
HCP90, 600°C	55	160
HCP45, 600°C	84	185
HCP45B, 600°C	93	180

Figure 5.12 provides a magnified view of strut plastic deformation (Figure 5.12. (a)) and strut failure (Figure 5.12. (a)) in as-built and peak-aged lattices, respectively. All observations suggest that little or no plastic deformation occurred before fracture of peak-aged struts. Figure 5.11. (b) illustrates the surfaces of the as-built and peak-aged FCCXYZ lattices at different strain levels, both at room and high temperature. In the as-built condition, irrespective of temperature, homogeneous lattice deformation can be observed at a strain of 10%. In the peak-aged lattices, at that same strain, premature strut breaking along a band formed by steps that were both perpendicular and at approximately 45° with respect to the compression axis takes place, leading to the dramatic stress decrease observed in Figure 5.10. (b). Due to the presence of the additional struts in FCCXYZ lattice,

the path of the shear band consisted of steps perpendicular to the compression axis and at 45° with respect to the compression axis.

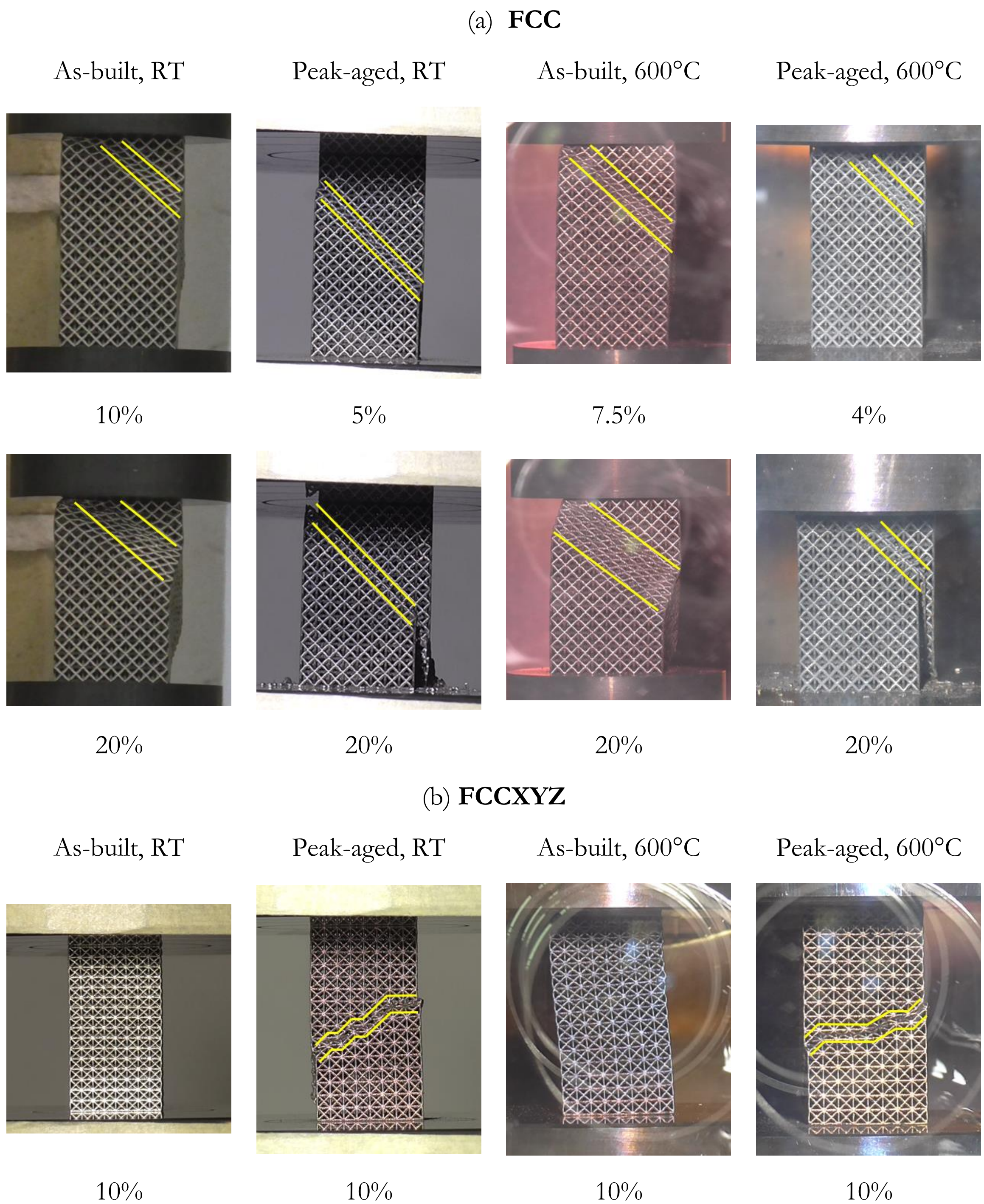

Figure 5.11. Surfaces of the as-built and peak-aged (a) FCC and (b) FCCXYZ lattices at different nominal strain levels. The corresponding engineering strains are indicated below each image.

(a) As-built, RT (b) Peak-aged, high T

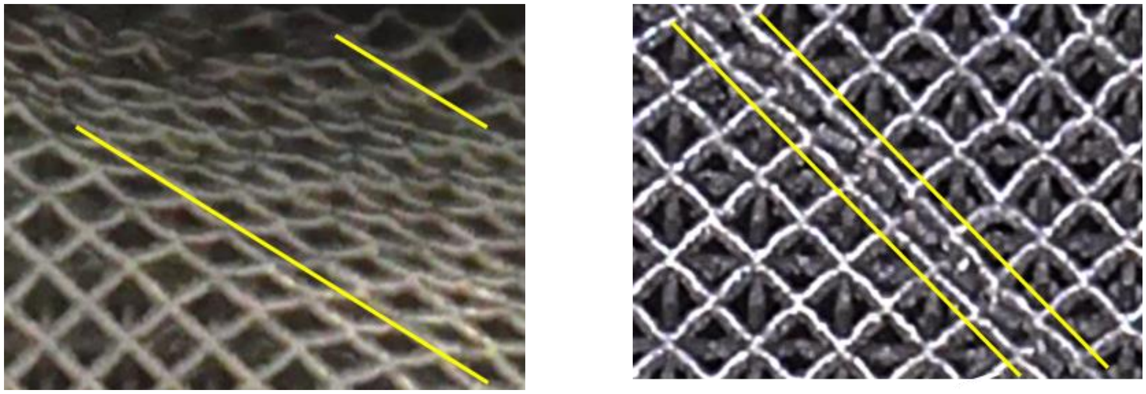

Figure 5.12. Magnified view of strut deformation and failure as a function of the material microstructure in FCC lattices. (a) Strut plastic deformation during compression an as-built lattice (e=17%); (b) strut breakage along localized shear bands during compression of a peak-aged lattice (e=5%).

5.2.3. Influence of precipitation on the mechanical behaviour of hexagonal lattice structures

Figure 5.13 illustrates the specific compressive room and high temperature stress-strain curves corresponding to the as-built and peak-aged lattices with HCP0 (Figure 5.13. (a)), HCP90 (Figure 5.13. (b)), HCP45 (Figures 5.13. (c, d)), and HCP45B (Figures 5.13. (e, f)) topologies. The yield strength values are summarized in Table 5.3.

Several trends can be inferred from Figure 5.13. First, a distinctive characteristic of the deformation of the HCP90 lattice is the presence of a serration at strains comprised between 0.02 and 0.03 (Figure 5.13. (b)), irrespective of microstructure and temperature. Second, for a given temperature, precipitation in both peak-aged HCP0 and HCP90 lattices leads to strengthening and to a transition from a bending-dominated response to a stretch-dominated response. Finally, for a given microstructure, increasing the test temperature results in softening and in a decrease in the width of the stress serrations of the peak-aged lattices, but it does not lead to any change in the deformation mode.

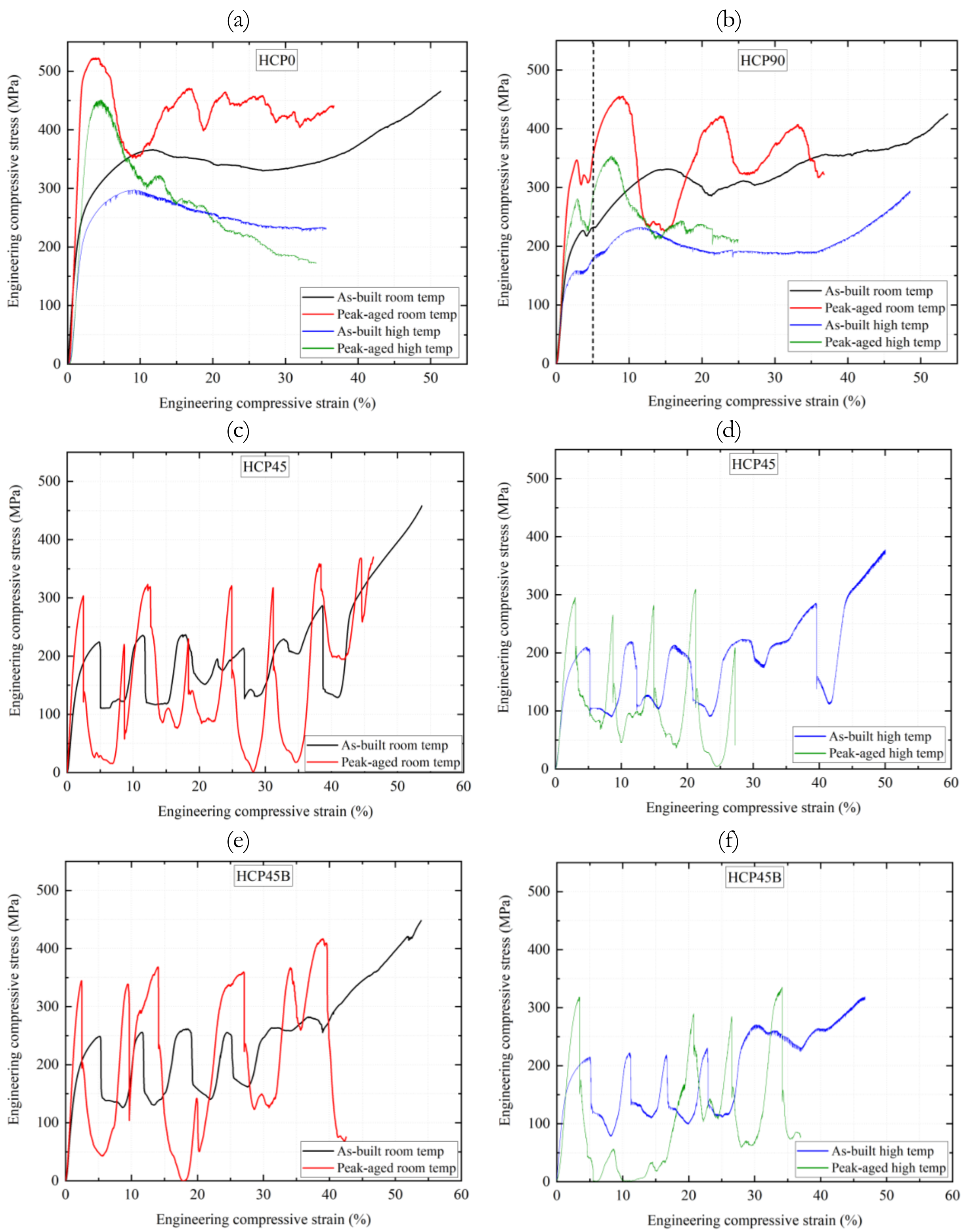

Figure 5.13. Specific engineering compressive stress-strain curves corresponding to the as-built and peak-aged hexagonal Inconel 718 3D printed lattices tested at room and high (600°C) temperatures: (a) HCP0, (b) HCP90, (c) HCP45, and (d) HCP45B.

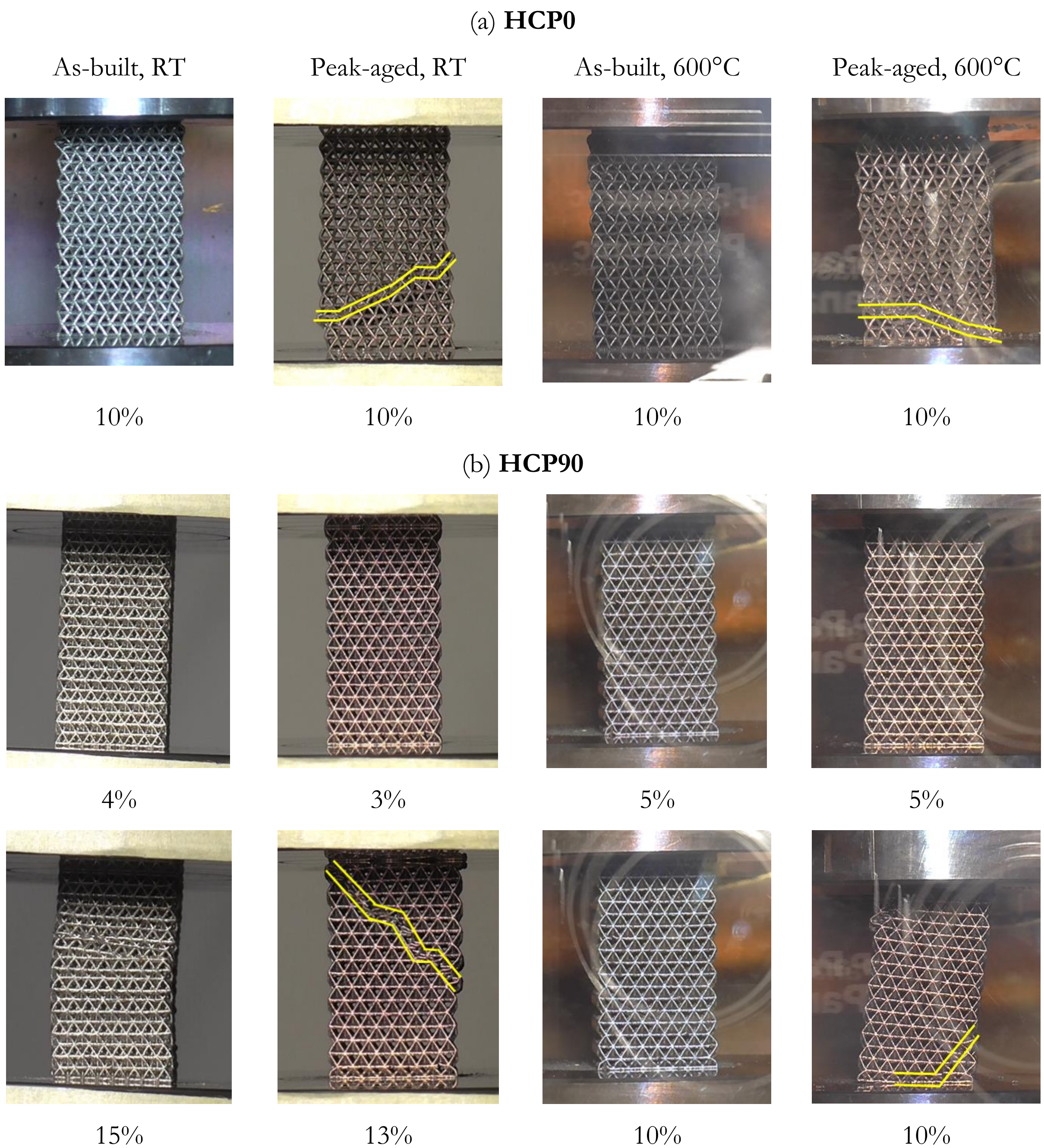

Figure 5.14. Surfaces of the as-built and peak-aged (a) HCP0 and (b) HCP90 at different strain levels. The corresponding engineering strains are indicated below each image. The bands along which strut breakage was observed are highlighted in yellow.

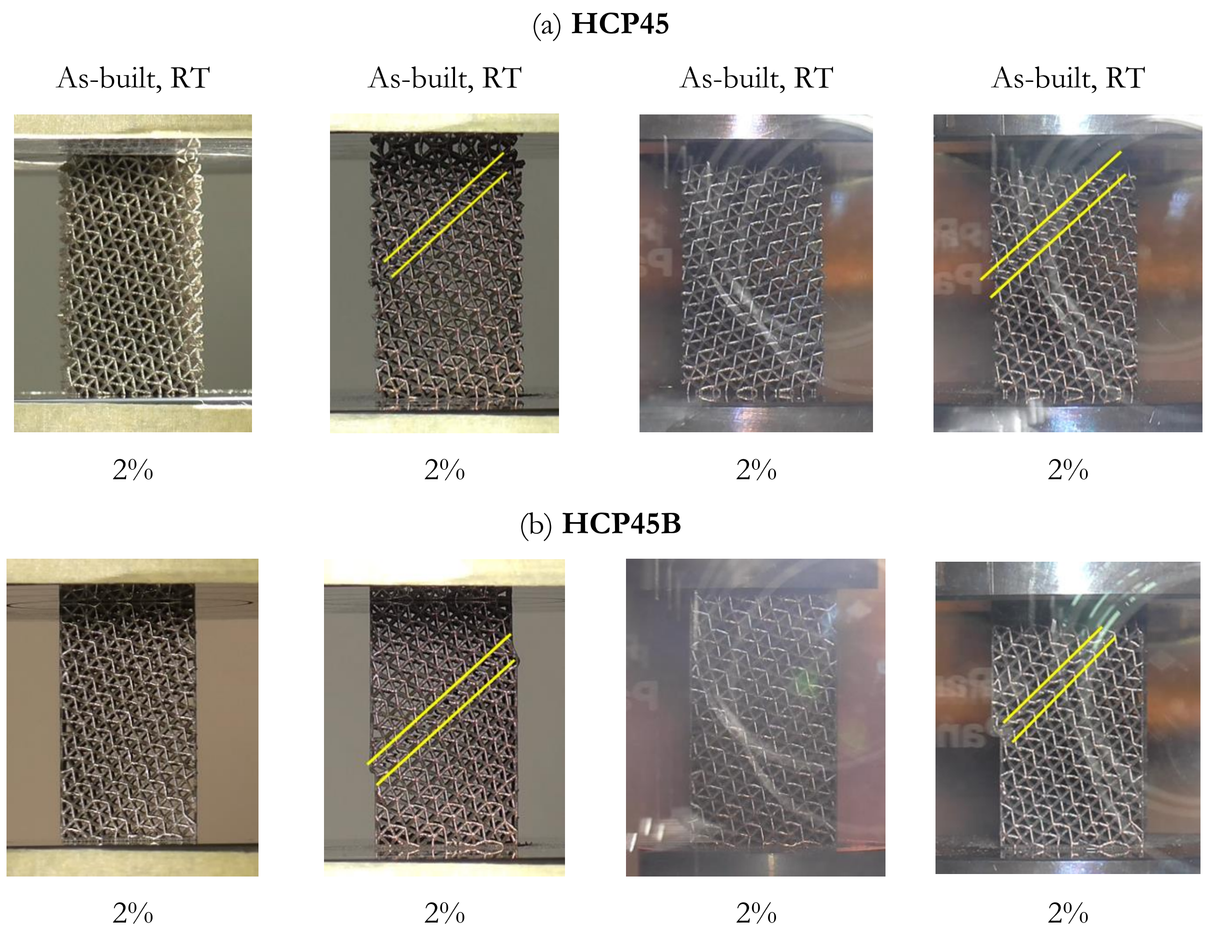

Figure 5.15. Surfaces of the as-built and peak-aged (a) HCP45 and (b) HCP45B at different strain levels. The corresponding engineering strains are indicated below each image. The bands along which strut breakage was observed are highlighted in yellow.

In the HCP45 and HCP45B lattices (Figures 5.13. (c, d) and (e, f) respectively) the mechanical behaviour was stretch-dominated irrespective of microstructure, and consecutive stress serrations are observed from the early stages of deformation. The HCP45B lattice was stronger due to the presence of the outer boundary segments. On average, for a given temperature, precipitation leads to strengthening and to an increase in the stress drop associated to the observed stress serrations. For a given microstructure, increasing the test temperature did not alter the deformation mode but it resulted in moderate softening and in a reduction of the average width of the stress serrations.

Figure 5.14 illustrates the surfaces of the as-built and peak-aged HCP0 (Figure 5.14. (a)), and HCP90 (Figure 5.14. (b)) lattices at different strain levels, both at room and high temperature. In the as-built condition, irrespective of architecture, lattice deformation was seen to proceed by the homogeneous bending of struts, while in the aged lattices precipitation led to strut break-up along stepped bands, which were highlighted in yellow. Additionally, Figure 14b confirms that a stress serration appearing in the HCP90 lattices following yielding (see black dotted line in Figure 5.13. (b)) was not associated to the formation of a shear band, as no such band was visible in the lattices deformed up to strains close to 5%, which was larger than that at which the serration was observed. The origin of this small stress serration is elucidated with the aid of FEM modelling in the 'Discussion' section.

Figure 5.15 illustrates the surfaces of the as-built and peak-aged HCP45 (Figure 5.15. (a)), and HCP45B (Figure 5.15. (b)) lattices, compressed at room and high temperature up to a nominal strain of 2%. In both cases, it can be seen that the structures deformed and failed along bands that make an angle of 45° with respect to the compression axis. Inside these bands, struts in the as-built lattices were plastically deformed, while they were already fractured in the peak-aged lattices.

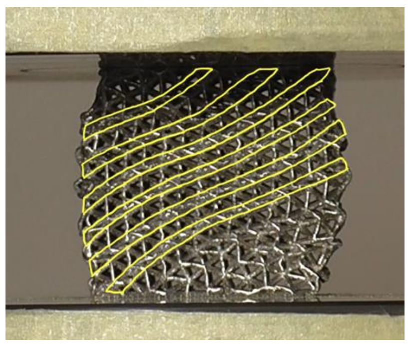

Figure 5.16. Surface of an as-built HCP45B lattice deformed at room temperature to a strain of 30%. The bands formed with increasing deformation levels are highlighted in yellow.

With increasing strain, parallel shear bands encompassing the entire lattice volume develop in both the as-built and peak-aged lattices, irrespective of temperature. Fig. 16 shows, as an example, a HCP45B as-built lattice deformed up to a strain of 30%.

5.3. Discussion

5.3.1. Effect of precipitation and test temperature on the properties of the base material

In order to rationalize the mechanical behaviour of the investigated lattices, it is necessary to examine first the influence of microstructure on the mechanical response of the as-built and peak-aged Inconel 718 superalloy (base material). Figure 5.17 illustrates the room and high temperature engineering stress-strain curves corresponding to the single strut tensile specimens that were additively manufactured using the optimized set of LPBF processing parameters (Figure 5.3). It can be seen that, for a given temperature, aging leads to a significant increase in the yield strength and in the ultimate tensile strength thanks to the precipitation hardening induced mainly by γ'' (Figure 5.9. (b)), and to a decrease in ductility. Conversely, for a given microstructure, increasing the testing temperature results in softening and, in the peak-aged condition, in a significant reduction in ductility.

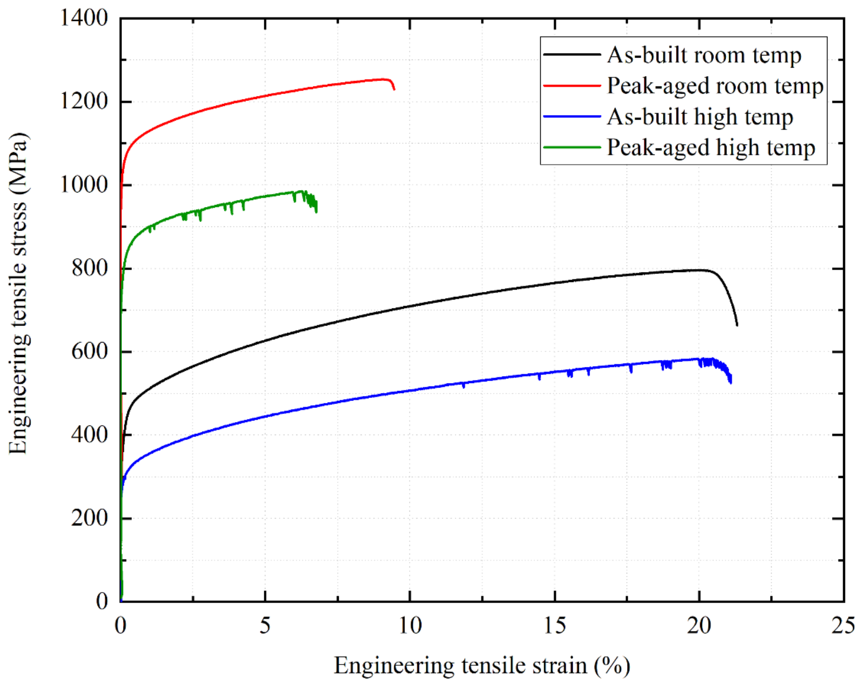

Figure 5.17. Room and high (600°C) temperature tensile stress-strain curves corresponding to the 3D printed Inconel 718 single-strut specimens in the as-built and peak aged conditions.

Table 5.4. Ductility, yield strength, and ultimate tensile strength values corresponding to the as-built and peak-aged single strut tensile samples, tested at room and high temperature.

Microstructure, Temperature	**Ductility (%)**	**Yield strength (MPa)**	**Ultimate tensile strength (MPa)**
As-built, RT	22.5±1.5	490±15	836±17
Peak-aged, RT	12±2	1044±21	1243±17
As-built, 600°C	22.7±1	321±11	572±8
Peak-aged, 600°C	7±2	873±25	1028±17

Table 5.4 summarizes the average yield strength, the ultimate tensile strength, and the tensile ductility corresponding to all the tests. The measured values lie within the relatively wide property ranges published for LPBF-processed Inconel 718, which are often better than those reported for the as-cast condition [25,26,31-35].

5.3.2. Coupled effect of microstructure and architecture on the mechanical behaviour of additively manufactured Inconel 718 lattice structures

Our results show that microstructure, and in particular precipitates, influences the mechanical response of Inconel 718 LPBF-processed lattice structures at the two studied temperatures in several ways. Firstly, for all the architectures investigated, precipitation leads to significant increase in the yield strength of the lattice structures at room and high temperatures (Figures 5.10, 5.13) and increasing the test temperature leads to a decrease in the lattice yield strength in both the as-built and peak-aged conditions. These variations of the strength of the lattice structures with precipitation and with the test temperature can be directly correlated to the variation of the strength of the base material described in section 5.4.1.

Secondly, in the HCP45 and HCP45B lattices, which already exhibit a stretch-dominated response in the as-built condition, precipitation leads to a reduction of the width of the stress serrations and to more severe stress drops after the plastic yielding (Figure 5.13). These two observations can be attributed to the decrease in the material ductility with precipitation (Figure 5.17). Thirdly, in the peak-aged lattices, which exhibit a behaviour similar to the stretch-dominated behaviour irrespective of topology, the increase in the test temperature results in a reduction of the width of the stress serrations. This phenomenon can be ascribed to the reduction in strength and ductility with increasing temperature (Figure 5.17), increasing the frequency of collapse and fracture of the peak-aged struts.

On the other hand, in the FCC, FCCXYZ, HCP0, and HCP90 lattices precipitation leads to a transition from bending-dominated to stretch-dominated behaviour (Figures 5.10, 5.11, 5.13, 5.14) and thus to a larger degree of strain localization (Figures 5.11, 5.12, 5.14). It is believed that such transition may be attributed to a change in the strut deformation mode (from plastic hinging to elastic buckling) with aging. For example, in the case of FCCXYZ lattices, the yield strength is mainly governed by the deformation behaviour of [100] struts, whose slenderness ratio is larger than that of [110] struts. The elastic room temperature buckling stress (σ_{cr}) values may be calculated according to the Johnson´s formula (Equation1) (assuming the compressive stress was uniaxial and parallel to the [100] strut's axis):

$$\sigma_{cr,Johnson} = \sigma_y - \frac{1}{E}\left(\frac{\sigma_y}{2\pi}\right)^2 R^2 \tag{1}$$

where σ_y refers to the yield strength of the base material, R is the slenderness ratio (R=L/r, where L is the effective strut length and r is the radius of gyration) and E is the elastic modulus of the base material. It is worth noting that process defects (such pores or surface roughness) can significantly lower the apparent elastic modulus, in particular for the small features fabricated by LPBF. To reflect this effect on fine struts, apparent values (instead of the true value) of the elastic modulus (72 GPa and 92 GPa) were used for the as-built and peak-aged conditions, respectively, as in the FEA simulations. Considering that both ends of the struts are fixed, L is equal to half of the strut length (1.25 mm). Additionally, since r = 0.1, R = 12.5 and $\sigma_{cr\ Johnson}$ is equal to 476 MPa and to 997 MPa for the as-built and peak-aged conditions, respectively. The use of the Johnson´s formula over the Euler formulation is justified based on the fact that R is smaller than the critical slenderness ratio (R_c), calculated using Equation 2 below, which amounts, respectively, to 54 and 41 for the struts in the as-built and peak-aged conditions.

$$R_c = \sqrt{\frac{2\pi^2 E}{\sigma_y}} \tag{2}$$

The calculated elastic buckling stress is relatively close to the yield stress of the as-built Inconel 718 (490 ± 15 MPa, Table 5.4) and significantly smaller than the yield stress of the peak-aged Inconel 718 (1044 ± 21 MPa, Table 5.4). The above is consistent with the observed predominance of plastic hinges in the as-built lattices and of elastic buckling in the peak-aged lattices. Additionally, the relatively large room temperature elongation measured in the as-built material (22.5%) would explain the onset of homogenous lattice deformation and thus the bending dominated behaviour. Given the elongation of the peak-aged Inconel 718 (12%) was much smaller than that of as-built part (Table 5.4 and Figure 5.17), the peak-aged struts fractured at relatively small strains, resulting in a stretching-dominated behaviour.

5.3.3. Origin of the low stress peak in HCP90 lattice structures

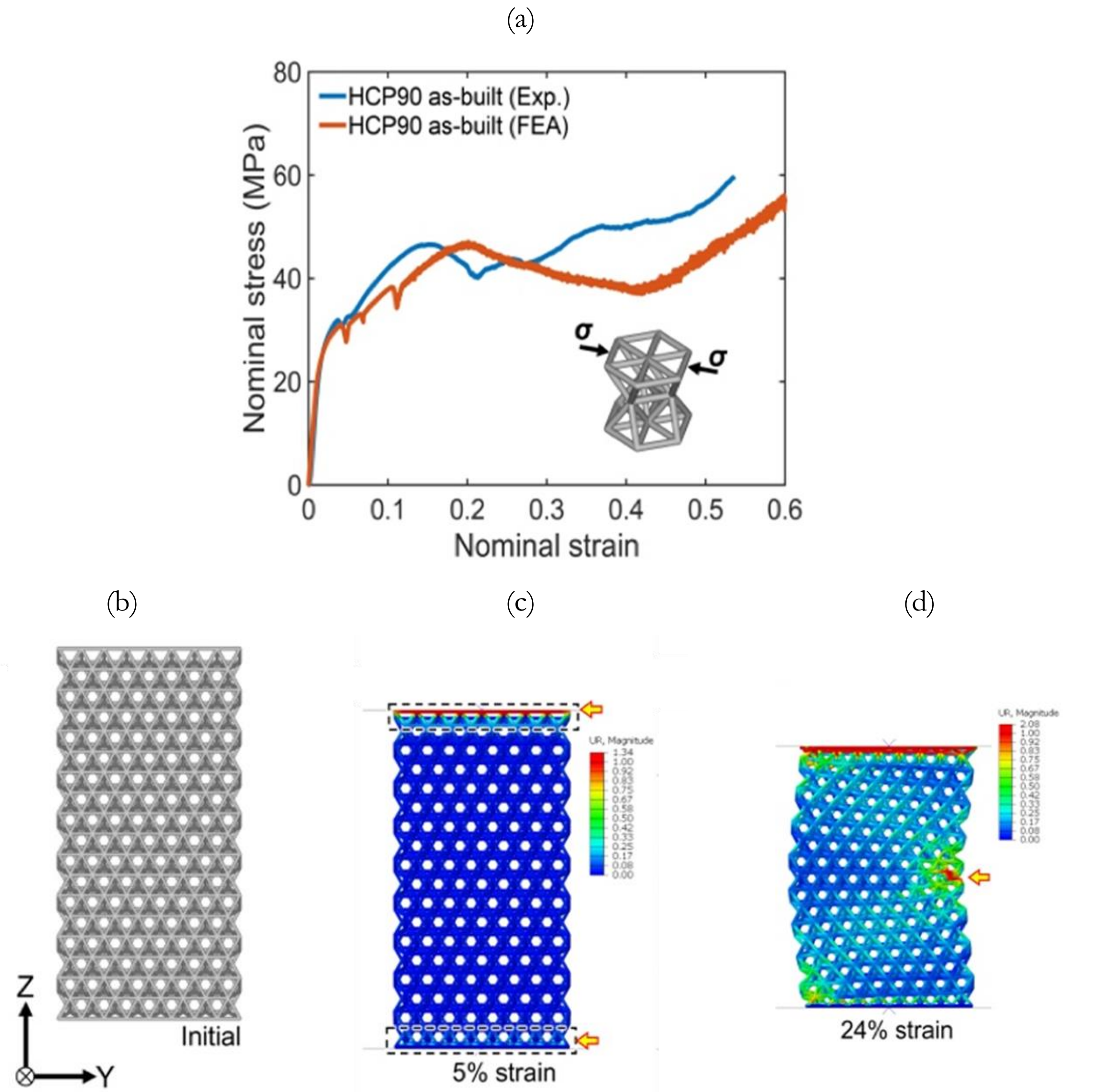

Figure 5.18. (a) Comparison of the stress-strain behaviour between experiment and FE simulation of the HCP90 lattice in the as-built condition. (b-d) Deformation behaviour simulated by FEA: (b) un-deformed condition, (c) 5% nominal strain and (d) 24% nominal strain. Note: The colour represents the rotational displacement of nodes.

As illustrated in Figure 5.13, irrespective of microstructure and temperature, the HCP90 lattices exhibit a small stress serration at strains between 0.02 and 0.03. Figure 5.14 proves that the origin of this serration cannot be attributed to the formation of a shear band as, at these low strains, homogeneous deformation still prevails. In order to elucidate the origin of the mentioned stress serration, FE modelling was carried out to determine the local stress and strain levels in the HCP90 lattice with increasing compressive strain. Figure 5.18. (a) compares the HCP90 compression stress-strain curves obtained from experiments and simulation, showing that the simulation was able to reasonably capture the measured stress-strain behaviour. In particular, the first stress serration observed experimentally at a nominal strain smaller than 5% was also predicted by the FE analysis.

The simulation (Figure 5.18. (c)) shows that this serration is originated by the collapse of the struts at the very top and very bottom layers, which were much less supported compared to the struts inside the lattice. Once the struts were in contact with the compression plates, they were plastically deformed and collapsed right away. Subsequently, local densification led to the regain of stress levels. A few more similar serrations are observed at larger strains (Figure 5.13. (b)) until the initiation of the first shear band at about 15 % to 20 % (Figure 5.18. (d)) that caused a large reduction in stress.

5.4. Remarks

The aim of this work is to investigate the coupled effect of microstructure and topology on the mechanical behaviour of Inconel 718 lattices fabricated by LPBF. With that purpose, lattices with FCC, FCCXYZ, HCP0 (c-axis parallel to BD), HCP90 (c-axis at 90° to BD), HCP45 (c-axis at 45° to BD) and HCP45B (c-axis at 90° to BD and with borders) topologies were manufactured by LPBF and their mechanical behaviour in the as-built and peak-aged conditions was tested in compression at room and high temperature. The following conclusions can be drawn from the present study:

- The microstructure of as-built lattices is a polycrystal formed by randomly oriented grains, slightly elongated along BD. The average grain length and width were, respectively, 16 ± 28 μm and 10 ± 14 μm. The grain boundary misorientation distribution resembled that of a random distribution of grains (Mackenzie), with an additional strong peak at misorientation angles lower than 5°, that is characteristic of LPBF-processed alloys. Grain interiors are populated by cells, and cell interiors are mostly a solid solution. Nb segregates to cell boundaries. Peak-aging of the lattices following LPBF processing gives rise to a precipitation, while the remaining microstructural features, including grain size, shape, and orientation, and grain boundary network, remained almost unchanged. Segregation of Mo and Ti to cell boundaries is observed following the heat treatment.
- For all the topologies investigated, precipitation leads to significant strengthening of the lattice structures at room and high temperature; in turn, increasing the test temperature resulted in

lattice softening in both the as-built and peak-aged conditions. These variations of the lattice strength with precipitation and with the test temperature can be directly correlated to the variation of the strength of the base material in similar microstructure and testing conditions, which is measured using dedicated printed specimens with gauge length with dimensions identical to those of single struts.

- In the peak-aged lattices, which exhibit a stretch-dominated response irrespective of topology, increasing the test temperature results in a reduction in the width of the stress serrations. This can be ascribed to the decrease in strength and ductility of the peak-aged Inconel718 superalloy with increasing temperature.
- In the FCC, FCCXYZ, HCP0, and HCP90 lattices, precipitation induced a transition from bending-dominated to stretch-dominated mechanical response. This may be attributed, in turn, to a transition in the dominant strut deformation mechanism, which is governed by plastic hinges in the as-built condition and by elastic buckling in the peak-aged condition.

This study proves the influential role of microstructure in the behaviour of additively manufactured metallic lattices and, as such, it highlights an exciting avenue of research focused on combining structure design and microstructure engineering.

Bibliography

[1] C. Pan, Y. Jan, J. Lu, Design and optimization of lattice structures: a review, Appl. Sci. 10 (2020) 6374.

[2] A.A. Zadpoor, Mechanical performance of additively manufactured meta- biomaterials, Acta Biomat. 85 (2019) 41.

[3] M. Leary, M. Mazur, H. Williams, E. Yang, A. Alghamdi, B. Lozanovski, X. Zhang, D. Shidid, L. Farahbod-Sternahl, G. Witt, I. Kelbassa, P. Choong, M. Qian, M. Brandt, Inconel 625 lattice structures manufactured by selective laser melting (SLM): Mechanical properties, deformation and failure modes, Mater. Des. 157 (2018) 179.

[4] T. Yu, H. Hyer, Y. Sohn, Y. Bai, D. Wu, Structure-property relationship in high strength and lightweight AlSi10Mg microlattices fabricated by selective laser melting, Mater. Des. 182 (2019) 108062.

[5] A. Takezawa, K. Yonekura, Y. Koizumi, X. Zhang, M. Kitamura, Isotropic Ti–6Al–4V lattice via topology optimization and electron-beam melting, Addit. Manuf. 22 (2018) 634.

[6] A. Moussa, D. Melancon, A. El Elmi, D. Pasini, Topology optimization of imperfect lattice materials built with process-induced defects via Powder Bed Fusion Addit. Manuf. (2020) 101608.

[7] L. Bai, J. Zhang, Y. Xiong, X. Chen, Y. Sun, C. Gong, H. Pu, X. Wu, J. Luo, Influence of unit cell pose on the mechanical properties of Ti6Al4V lattice structures manufactured by selective laser melting, Addit. Manuf. 34 (2020) 101222.

[8] L. Zhang, B. Song, J.J. Fu, S.S. Wei, L. Yang, C.Z. Yan, H. Li, L. Gao, Y.S. Shi, Topology-optimized lattice structures with simultaneously high stiffness and light weight fabricated by selective laser melting: Design, manufacturing and characterization, J. Manuf. Process. 56 (2020) 1166.

[9] Y. Liu, J. Zhang, X. Gu, Y. Zhou, Y. Yin, Q. Tan, M. Li, M.X. Zhang, Mechanical performance of a node reinforced body-centred cubic lattice structure manufactured via selective laser melting, Scr. Mater. 189 (2020) 95.

[10] M.S. Pham, C. Liu, I. Todd, J. Lertthanasarn, Damage-tolerant architected materials inspired by crystal microstructure, Nature 565 (2019) 305.

[11] E.D. Sanders, A. Pereira, G.H. Paulino, Optimal and continuous multilattice embedding, Sci. Adv. 7 (2021) 4838.

[12] T. Maconachie, M. Leary, B. Lozanovski, X. Zhang, M. Qian, O. Faruque, M. Brandt, SLM lattice structures: Properties, performance, applications and challenges, Mater. Des. 183 (2019) 108137.

[13] V.S. Deshpande, M.F. Ashby, N.A. Fleck, Foam topology: bending versus stretching dominated architectures, Acta Mater. 49 (2001) 1035.

[14] J. C. Maxwell, On the calculation of the equilibrium and stiffness of frames, Lond. Edinburgh Dublin Philos. Mag. J. Sci. 27 (1864) 294.

[15] L.Y. Chen, S.X. Liang, Y. Liu, L.C. Zhang, Additive manufacturing of metallic lattice structures: Unconstrained design, accurate fabrication, fascinated performances, and challenges, Mater. Sci. Eng. R 146 (2021) 100648.

[16] M. F. Ashby, A. G. Evans, N. A. Fleck, L. J. Gibson, J. W. Hutchinson, H. N. G. Wadley, Metal Foams: A Design Guide, Butterworth-Heinemann, 2000.

[17] R. Wauthle, B. Vranckenc, B. Beynaerts, K. Jorissen, J. Schrooten, J.-P. Kruth, J. Van Humbeeck, Effects of build orientation and heat treatment on the microstructure and mechanical properties of selective laser melted Ti6Al4V lattice structures, Addit. Manuf. 5 (2015) 77-84.

[18] I. Maskery, N.T. Aboulkhair, A.O. Aremu, C.J. Tuck, I.A. Ashcroft, Compressive failure modes and energy absorption in additively manufactured double gyroid lattices, Addit. Manuf. 16 (2017) 24-29.

[19] P. Köhnen, C. Haase, J. Bültmanna, S. Ziegler, J. H. Schleifenbaum, W. Bleck, Mechanical properties and deformation behavior of additively manufactured lattice structures of stainless steel, Mater. Des. 145 (2018) 205-217.

[20] K. Hazeli, B. B. Babamiri, J. Indeck, A. Minor, H. Askari, Microstructure-topology relationship effects on the quasi-static and dynamic behavior of additively manufactured lattice structures, Mater. Des. 176 (2019) 107826.

[21] S. Banait, X. Jin, M. Campos, M.T. Pérez-Prado, Precipitation-induced transition in the mechanical behavior of 3D printed Inconel 718 bcc lattices, Scr. Mater. 203 (2021) 114075.

[22] D. Zhang, W. Niu, X. Cao, Z. Liu, Effect of standard heat treatment on the microstructure and mechanical properties of selective laser melting manufactured Inconel 718 superalloy, Mater. Sci. Eng. A 644 (2015) 32.

[23] M. Pröbstle, S. Neumeier, J. Hopfenmüller, L.P. Freund, T. Niendorf, D. Schwarze, M. Göken, Superior creep strength of a nickel-based superalloy produced by selective laser melting, Mater. Sci. Eng. A 674 (2016) 299.

[24] Inconel718 data sheet, Publication Number SMC-045, Spec. Met. Corporation (2007).

[25] C. Galera-Rueda, E. Nieto-Valeiras, M. Gardon, M.T. Pérez-Prado, J. LLorca, Effect of ZrH2 particles on the microstructure and mechanical properties of IN718 manufactured by selective laser melting, Mater. Sci. Eng. A 813 (2021) 141123.

[26] E. Hosseini, V.A. Popovich, A review of mechanical properties of additively manufactured Inconel 718, Addit. Manuf. 30 (2019) 100877.

[27] V. Vieira Reilli, A. Piglione, M.S. Pham, S. Primig, On the detailed morphological and chemical evolution of phases during laser powder bed fusion and common post-processing heat treatments of IN718, Addit. Manuf. 50 (2022) 102540.

[28] R. Reed, The Superalloys: Fundamentals and Applications, Cambridge University Press, Cambridge, UK, 2006.

[29] C.M. Cepeda-Jiménez, M. Castillo-Rodríguez, M.T. Pérez-Prado, Origin of the low precipitation hardening in magnesium alloys, Acta Mater. 165 (2019) 164.

[30] R. Schwab, V. Ruff, On the nature of the yield point phenomenon, Acta Mater. 61 (2013) 1798-1808.

[31] Z. Wang, K. Guan, M. Gao, X. Li, X. Chen, X. Zeng, The microstructure and mechanical properties of deposited-IN718 by selective laser melting, J. Alloys Compd. 513 (2012) 518–523.

[32] A.T. Clare, R.S. Mishra, M. Merklein, H. Tan, I. Todd, L. Chechik, J. Li, M. Bambach, Alloy design and adaptation for additive manufacture, J. Mater. Proc. Tech. 199 (2022) 117358.

[33] M.J. Donachie, S.J. Donachie, Superalloys: A Technical Guide. ASM International, Materials Park, OH, USA, 2002.

[34] K.N. Amato, S.M. Gaytan, L.E. Murr, E. Martinez, P.W. Shindo, J. Hernandez, S. Collins, F. Medina, Microstructures and mechanical behavior of Inconel 718 fabricated by selective laser melting, Acta Mater. 60 (2012) 2229-2239.

[35] A. Piglione, B. Attard, V. Vieira Rielli, C.T. Santos Maldonado, M. M. Attallah, S. Primig, M. S. Pham, On the constitutive relationship between solidification cells and the fatigue behaviour of IN718 fabricated by laser powder bed fusion, Addit. Manuf. 47 (2021) 102347.

CHAPTER 6

Effect of microstructure on the effectiveness of hybridization in architected metallic materials

6.1. Background and design of the study

The smart design of architected materials has become a widely recognized tool to fabricate components with properties that are clearly superior to those of bulk materials. The metamaterials thus produced are finding a wide range of applications in the light-weighting and strengthening of structural components [1-3], as well as in the optical [4] and electromagnetic [5] fields. More recently, they are also widely sought in the biomedical sector as advanced tissue engineering scaffolds [6]. Strut-based lattice structures, consisting of the periodic repetition of a structural unit called "unit cell", which is composed, in turn, of a particular spatial arrangement of struts, are currently the most common type of architected materials [7]. Optimizing lattice design for the achievement of unprecedented properties is complex, as it involves the coupling of a large number of design variables at the material, unit cell and structure levels [8-10].

Additive manufacturing (AM) [11-13], or the layer-by-layer fabrication of parts guided by a previously defined three-dimensional computer-aided-design, is a very suitable method for the production of strut-based metallic lattices as it is endowed with enormous design flexibility. In particular, laser powder bed fusion (LPBF), which involves the successive selective melting of powder layers deposited on a build platform, is usually the technique of choice due to its comparatively high dimensional accuracy and fine resolution [14-16].

It is now well established that the architecture has a strong influence on the mechanical behaviour of lattices [8, 17-27]. Altering the lattice structure allows, for example, to induce a transition in the mechanical response from bending-dominated to stretch-dominated [15,28]. A bending-dominated behaviour involves homogeneous deformation at a plateau stress following yielding, and is associated to large absorbed energy; a stretch-dominated behaviour is usually linked to higher yield stress values but involves a large degree of instability due to the onset of strain localization, leading often to failure by the formation of shear bands. While stretch-dominated lattice structures have clearly beneficial effects in terms of an increase in the lattice yield strength, the inherent instability of the stretch-dominated response limits the mechanical stability and increases the probability of sudden failures. It is, thus, desirable to eliminate the instability while benefiting from the high strength offered by the stretch-dominated lattice structure.

In contrast to the considerable understanding of the architecture effects, the influence of the material microstructure on the mechanical behaviour of additively manufactured lattices is less well understood [29-36]. Indeed, there are very few studies on the effect of isolated microstructural parameters, such as the grain size, the texture, the precipitate distribution, or the nature of grain boundaries, on the mechanical behaviour of strut-based lattices. It is generally accepted that any variation in microstructure leading to higher strength in the base material, such as, for example, a reduction of grain size [37-39], an increase of the latent dislocation density [40,41], or the precipitation of second phase particles [42], will, in turn, translate into a higher lattice strength [29-34], and vice versa.

Altering the strength of the base material might also lead to a transition in the mechanical behaviour of the corresponding lattice. For example, Maskery et al. [30] reported a transition from stretch-dominated to bending dominated behaviour, with the concomitant decrease in yield strength, in an LPBFed AlSi10Mg alloy following a post-processing heat treatment which reduced the strength of the base material by about 25%. Also, the present authors and others [33,34,36] have recently reported a bending-dominated to stretch-dominated transition in the mechanical response of Inconel 718 LPBFed lattices thanks to changes in metallurgy only, e.g. by post-processing precipitation hardening of the base superalloy. Further work on the coupled effect of microstructure and architecture [34,43,44] is required in order to fully exploit microstructural design as a tool for the development of lattices with enhanced properties.

In recent years lattice structure hybridization has been put forward as an effective approach to improve the lattice strength, the damage tolerance, and the energy absorbed (EA) [45-49]. Hybrid lattices may be formed, for example, by an array of neighbouring domains with different types of unit cells (allocation) [50-57], by two or more assembled, but disconnected, lattices that occupy the same volume (interpenetration) [58], by arranging two unit cells (e.g. FCC, BCC) into a more complex one (nesting) [59-61], or by a combination of several of these approaches. Many hybrid designs have been bioinspired by nature´s functionally optimized materials [62].

Although most studies have been performed using polymers, the beneficial effects of hybridization in additively manufactured metallic architected materials have also been recently demonstrated both experimentally and virtually [50-61]. However, the design space for hybrid metallic lattices is vast and remains hugely unexplored. Moreover, to our knowledge, only stainless steel [52,55,56,57,59] and AlSi10Mg [54,61] lattices have been investigated to date. The influence of microstructure on the mechanical behaviour of hybrid metallic lattices has, to date, not been explored.

The aim of this work is to investigate the coupled influence of the material microstructure and of structure hybridization on the mechanical behaviour of Inconel718 strut-based lattices. The superalloy Inconel 718 was selected owing to its considerable improvement in strength via aging. Dual-phase structures consisting of octet-truss (OT) domains of different sizes dispersed in a face-centred cubic (FCC) matrix will be analyzed. The effect of FCC-OT hybridization on the mechanical behaviour of the additively manufactured lattices will be explored for two material microstructures, namely the as-built solid solution state, and a peak-aged condition. The effectiveness of hybridization as a strategy to reduce the mechanical instability of aged LPBFed Inconel 718 lattices with stretch-dominated behaviour will be explored.

Gas atomized Inconel 718 alloy powder, supplied by Oerlikon, and with the elemental composition indicated in Table 6.1, was used as the feedstock material for lattice fabrication. The relatively spherical morphology of the powder particles, which nevertheless contain a non-negligible fraction of satellites, was confirmed by scanning electron microscopy (SEM) and is presented in Figure 6.1. This figure also illustrates the cumulative particle size distribution, as well as the corresponding d_{10}, d_{50} and d_{90} values, which amount to 25, 40, and 63 μm, respectively.

Table 6.1. Composition of the feedstock Inconel 718 powder (wt.%).

Ni	Cr	Fe	Nb	Mo	Ti	Al
Balance	18.7-19	13.5-13.8	4.6-4.8	1.6-1.65	0.45-0.5	0.38-0.4
Si	**Cu**	**Co**	**Mn**	**P**	**Ta**	**Zr**
0.35-0.39	0.23-0.25	0.066-0.07	0.054-0.057	<0.01	<0.01	<0.005

(a)

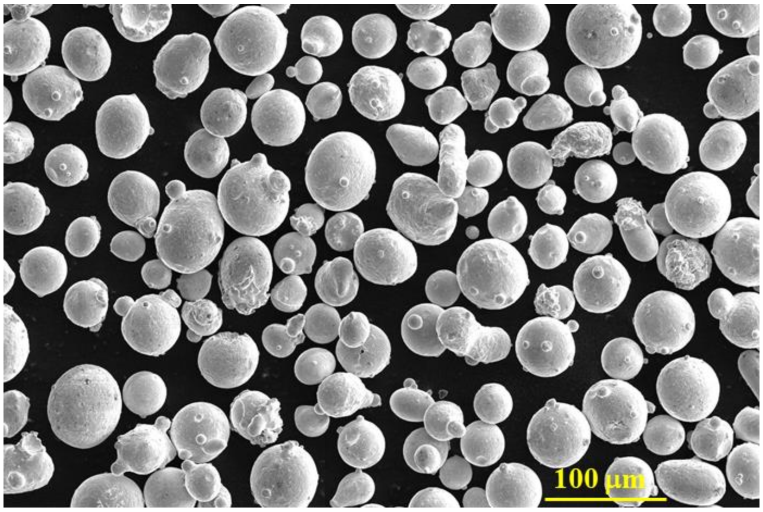

(b)

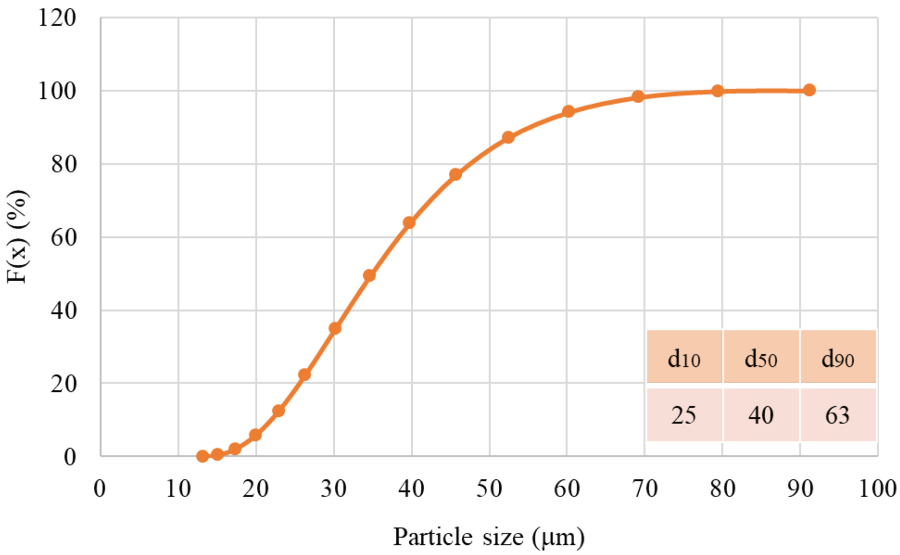

Figure 6.1. Gas atomized Inconel 718 feedstock powder. (a) Bright field SEM micrograph illustrating the spherical particle morphology; (b) Cumulative particle size distribution, with d_{10}, d_{50} and d_{90} values in µm.

Additional powder properties, including the apparent density, the tapped density and the flowability (measured using a Hall flowmeter) are summarized in Table 6.2.

Table 6.2. Properties of the Inconel 718 powder feedstock.

Apparent density	4.5 g/cm^3
Tapped density	4.9 g/cm^3
Flowability	15 s/50 g

The computer-aided-designs of the hybrid lattices investigated here are shown in Figure 6.2. An FCC structure was selected for the matrix, and comparatively stronger OT domains, mimicking the precipitates found in metallic alloys (meta-precipitates), were selected as reinforcements. In order to isolate the mechanical behaviour of the individual phases (FCC and OT), single-oriented lattices with FCC (Figure 6.2. (a)) and OT (Figure 6.2. (b)) structures were first built. Three different reinforcement distributions were designed for the current study (named D1, D2, D4, Figure 6.2. (c-e)). In all cases, the volume fraction of reinforcement was kept constant at 50%. Specifically, distribution D1 (Figure 6.2. (c)) consists of alternating FCC and OT domains where each domain contains one unit cell; distribution D2 (Figure 6.2. (d)) consists of alternating FCC and OT cubic domains, each containing 8 unit cells; distribution D4 (Figure 6.2. (e)) consists of alternating FCC and OT cubic domains, each containing 64 unit cells.

The five strut-based lattice structures described above (FCC, OT, D1, D2 and D4) were manufactured by LPBF with external dimensions of 20x20x30 mm^3 using a Renishaw AM 400 machine. The unit cell dimensions were 2.5x2.5x2.5 mm^3 and the strut diameter was fixed at 0.4 mm (refer Annex A). The processing parameters used for fabricating the lattice structures (listed in Table 6.3) were optimized to achieve an average material density of 99.56% [33,34]. The scanning strategy utilized for LPBF manufacturing was bidirectional, with a rotation of 67° between two successive layers. The lattices were placed in the reduced build volume platform with their long axes parallel to the building direction (BD). Six samples were fabricated for each of the five investigated architectures (FCC, OT, D1, D2 and D4). Figure 6.3 illustrates the Inconel 718 lattices that were manufactured for this study via LPBF. Figure 6.3. (a) and 6.3. (b) depict the FCC (Figure 6.3. (a)) and OT (Figure 6.3. (b)) structures, while Figure 6.3. (c-e) show, respectively, the lattices with D1, D2, and D4 distributions.

(a) (b)

(c) (d) (e)

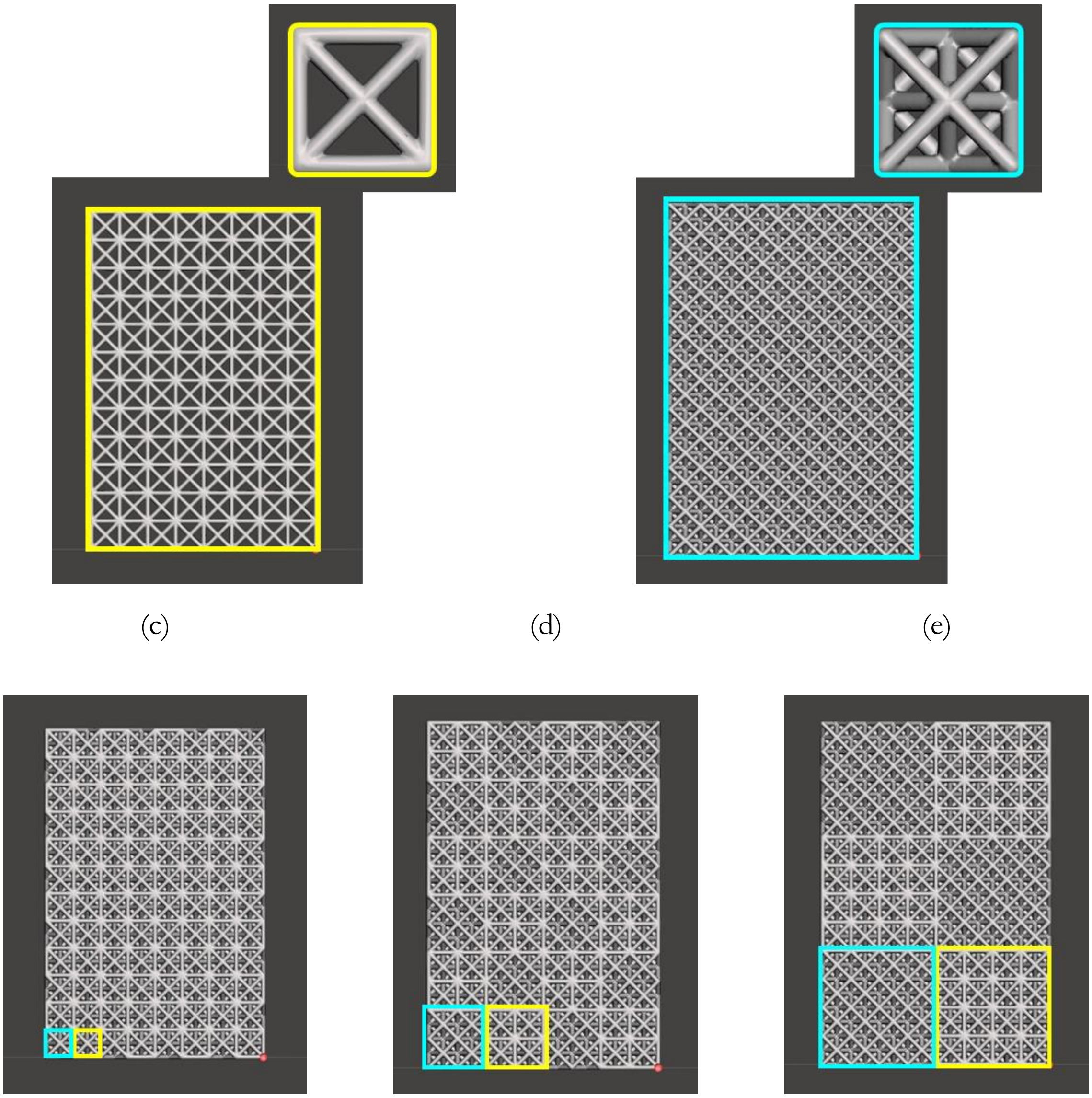

Figure 6.2. Computer-aided-designed lattice structures. (a) 'Single-crystalline' FCC, (b) 'single-crystalline' octet truss, (c) D1, (d) D2, and (e) D4. The unit cells of FCC and octet truss are indicated as insets in (a) and (b) respectively, and they are highlighted in yellow and blue, respectively, in the D1, D2, and D4 structures.

Table 6.3. Optimized laser powder bed fusion process parameter set utilized for lattice structure fabrication.

Laser power	Scan speed	Layer thickness	Hatch distance	Scan strategy
100 W	875 mm/s	30 μm	90 μm	Bidirectional

As shown earlier [33,34], the microstructure of the as-built Inconel 718 lattices is a polycrystalline solid solution consisting of randomly oriented grains, with an average size of approximately 20 μm, and with a hardness of 317±8 HV. It was also found earlier [34] that peak-aging of the as-built lattices at 718 °C for 6 hours followed by water quenching led to γ″ precipitation and to a maximum hardness of 502±9 HV. In the present study, the above-mentioned heat treatment [34] was applied to selected manufactured structures in order to evaluate the coupled influence of material microstructure and lattice topology on the mechanical behaviour of the hybrid lattices. The two 'material microstructure conditions' under investigation will be termed hereafter 'as-built' and 'peak-aged'.

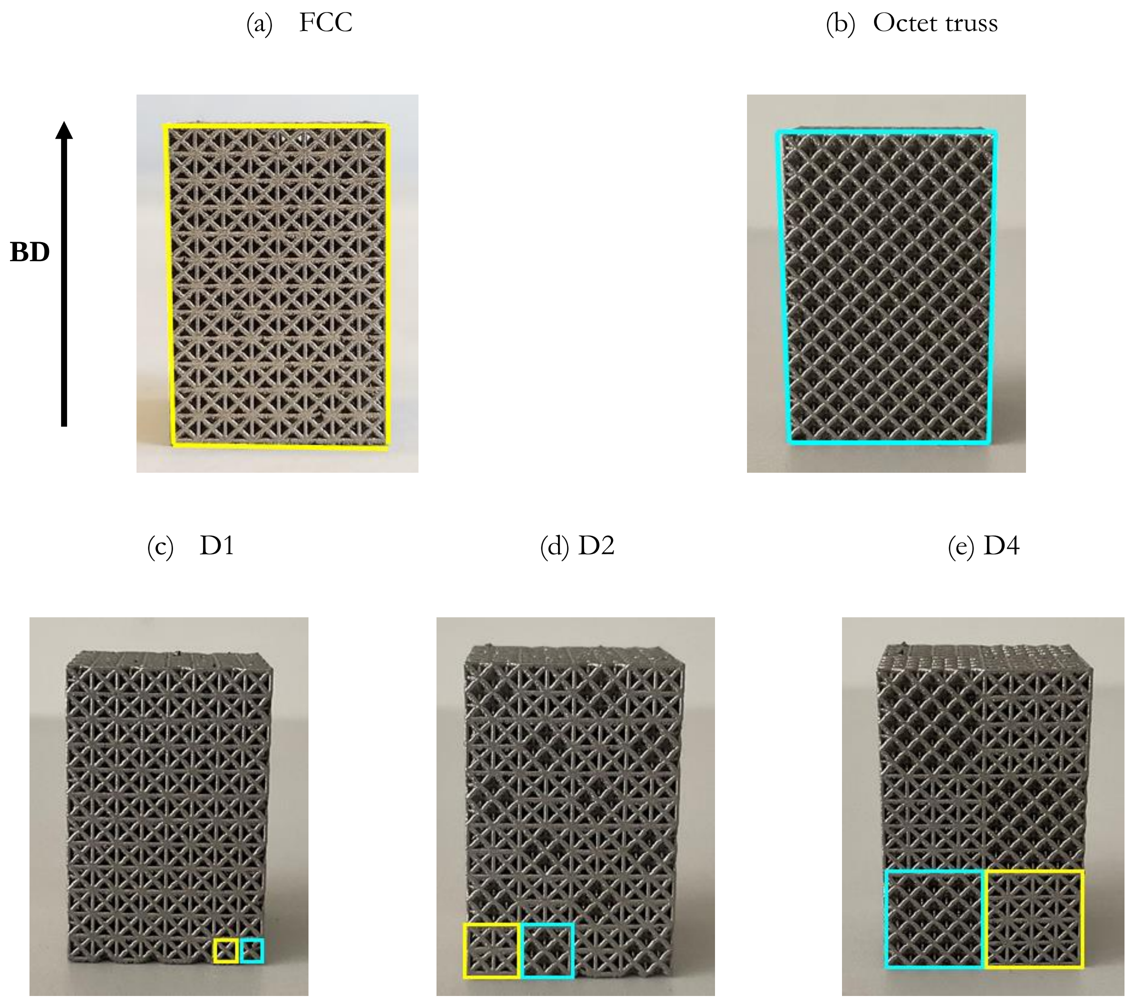

Figure 6.3. Inconel 718 lattice structures manufactured by laser powder bed fusion using optimized processing parameters. (a) FCC, (b) OT, (c) D1, (d) D2 and (e) D4. The BD is parallel to the long axis of the lattice structures.

In order to verify that the microstructure of the LPBF Inconel 718 lattices was equivalent to that published in earlier works [33,34], electron backscattered diffraction (EBSD) was carried out in as-built and heat-treated specimens using a FEI Helios NanoLab focused ion beam field emission gun SEM (FIB FEGSEM) equipped with a CCD camera and with the softwares Aztec and Channel 5.0 for data acquisition and analysis, respectively. The microstructure in as-built and peak-aged conditions was further examined by transmission electron microscopy (TEM) using a FEI Talos F200x microscope operating at 200 kV. The preparation of thin specimens for TEM involved milling an electron transparent lamella by FIB, as described in detail in [63].

The mechanical behaviour of the FCC, the OT and the hybrid lattice structures was investigated in the as-built and peak-aged conditions under uniaxial compression at room temperature. Testing was carried out along the BD (i.e., along the long axis of the lattices) in a Zwick-Roell testing machine furnished with a 100 kN load cell. A constant crosshead speed of 3×10^{-2} mm.s^{-1}, which is equivalent to an initial quasi-static strain rate of 10^{-3} s^{-1}, was utilized. Three tests were performed for each microstructure and architecture condition to ensure reproducibility.

It must be noted here that in the samples exhibiting a bending-dominated behaviour the yield strength (σ_y) was calculated as the stress at which the mechanical behaviour deviates from linearity, while in the samples exhibiting a stretch-dominated behaviour, σ_y was calculated as the stress corresponding to the first stress peak. The energy absorption (EA) was calculated as the area under the stress-strain curve up to different selected nominal strains.

Digital image correlation (DIC) analysis was performed in order to evaluate the time-dependent local shear strain distributions during room temperature lattice compression using the commercial software DaVis 8. With that purpose, images of the front face of lattice structures (see Figure 6.2) were captured at 1 second intervals during compression using a Nikon D7100 camera equipped with a 200 mm Nikkor macro lens. The DIC used a subset size of 101 x 101 pixels with a step size of 25 pixels in relation to 6000 x 4000 pixels of the captured images. The strain field corresponding to each nominal strain was presented with their deformation referenced to the undeformed image. Spray-painting was not applied as the surface feature of lattice struts provided sufficient surface contrast to correlate successive images.

To facilitate understanding of the stress distribution within lattice structures, finite element analysis (FEA) was also carried out using Abaqus/Explicit. Two rigid plates, top and bottom, were created to act as compression plates. The nodes of the bottom surface of the lattices (normal to loading direction) were tied with the fixed bottom plates and the top plate was placed at the top surface of the lattices and moved towards the bottom using an Abaqus built-in smooth ramping step. Such loading method was checked to ensure a quasi-static condition with dynamic energy smaller than 5% of the total energy. The lattice structures were meshed using Timoshenko beam elements with approximately size of 1 mm.

To achieve a relatively good agreement between FEA and experiments, the material properties obtained from tensile tests of as-built and peak-aged single-strut samples [34] were adjusted due to the effects of the processing defects (e.g. porosity) and geometrical differences between the lattice structures and cylindrical dog-bone specimens (for uniaxial tension). The material properties thus identified for FEA of lattice structures (Table 6.4) provided a good match in the early stage of stress-strain responses between the FEA versus experiment data of D1 as-built and peak-aged conditions (Supplementary Figure S1 in Annex E).

Table 6.4. Mechanical properties of the base material used for FEA.

	Density (g/cm^3)	**Poisson's ratio**	**Young's modulus (MPa)**	**Yield stress (MPa)**	**Ultimate tensile stress (MPa)**
As-built	8.19	0.284	50151	672	1750
Peak-aged	8.19	0.284	91898	1417	2073

6.2. Results

6.2.1. Microstructure of as-built and peak-aged lattice structures

Figure 6.4 illustrates the microstructure of the as-built (Figure 6.4. (a)) and peak-aged (Figure 6.4. (b)) FCC and OT Inconel 718 FCC lattices along a cross-section perpendicular to the BD. In agreement with earlier works [33,34], the microstructure in both conditions is a polycrystal formed by randomly oriented grains, with an average size of approximately 10 μm. The EBSD inverse pole figure maps in the BD included in Figure 6.4 reveal that the aging treatment does not have a significant influence on the grain size and shape, or in the texture, which is relatively weak. Figure 6.5 evidences the similarity between the misorientation distribution histograms (Figure 6.5. (a)), the horizontal line intercept distributions (Figure 6.5. (b)) and the vertical line intercept distributions (Figure 6.5. (c)) corresponding to the as-built and peak-aged FCC lattices.

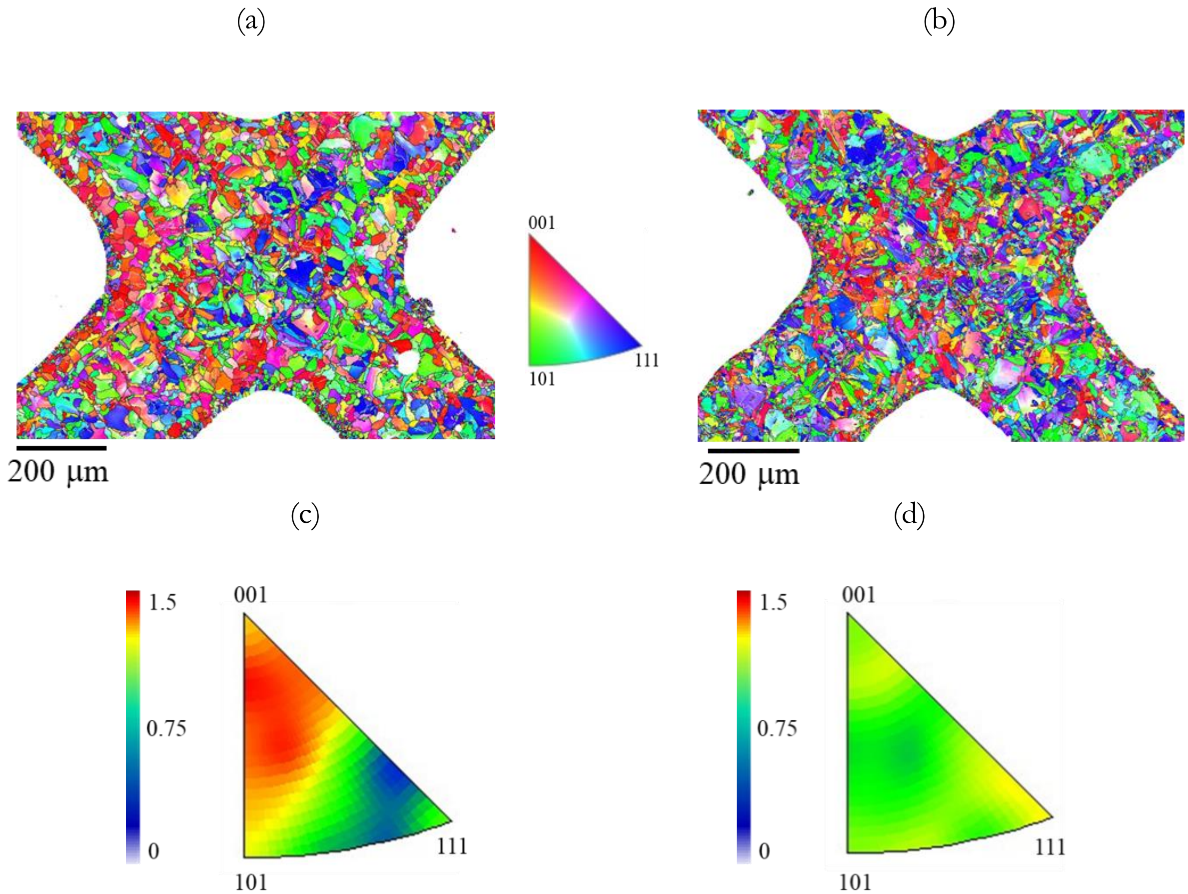

Figure 6.4. EBSD inverse pole figure maps (IPF) in the BD illustrating the microstructure of the FCC lattice in the as-built (a) and peak-aged (b) conditions along a cross-section perpendicular to BD. The colour coding has been added as an inset. The inverse stereographic triangles illustrating the orientation of the BD corresponding to the as-built (c) and peak-aged (d) lattices are also included.

Figure 6.6 consists of two TEM bright field micrographs illustrating the microstructure of the as-built (Figure 6.6 (a)) and heat-treated (Figure 6.6. (b)) Inconel 718 lattices at higher magnification along a $<001>_{\gamma}$ zone axis. The corresponding selected area diffraction (SAD) patterns are included as insets next to each micrograph. It is apparent that, in the as-built condition, only the spots corresponding to the γ phase are present, i.e., the microstructure is a solid solution. However, clear γ″ diffraction spots, highlighted using yellow arrows, are present in the SAD pattern corresponding to the TEM micrograph of the peak-aged condition.

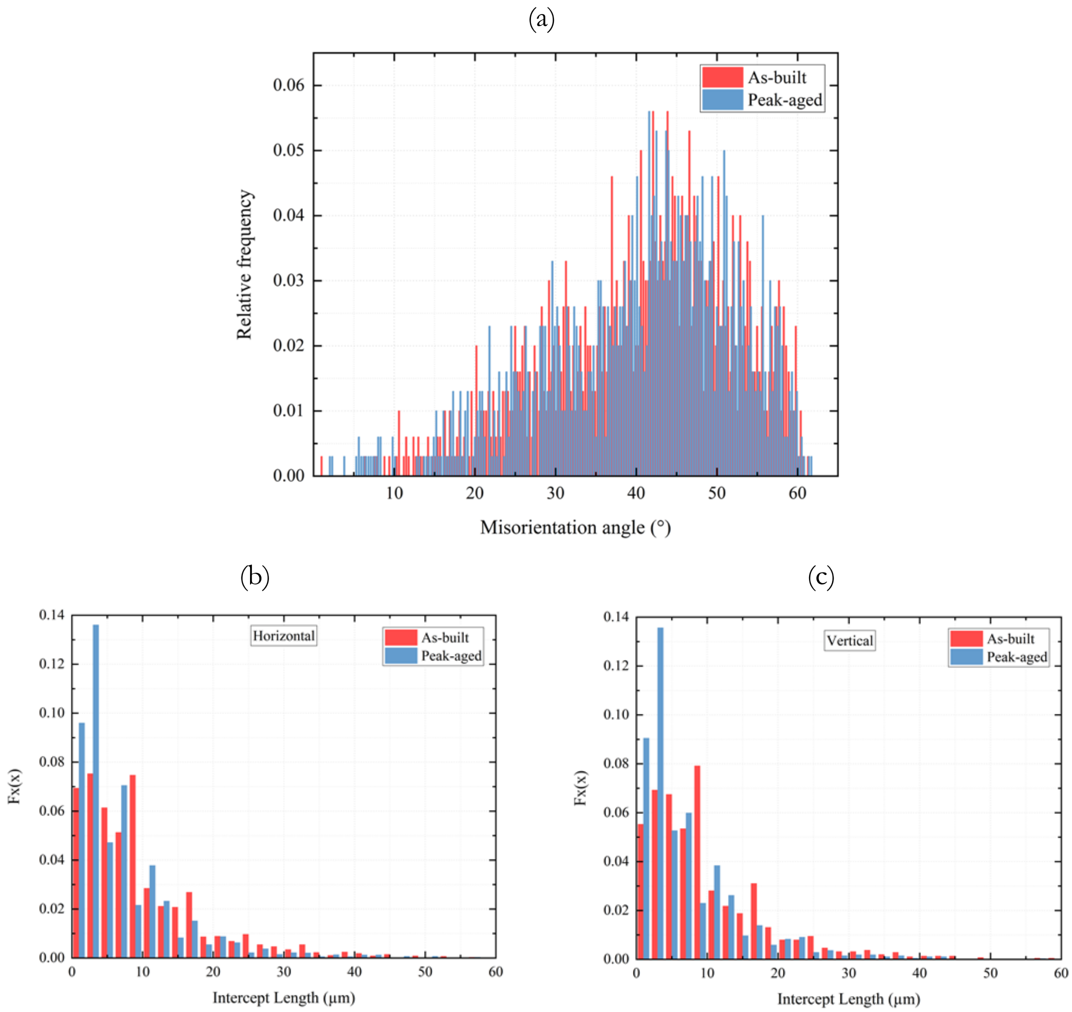

Figure 6.5. Comparison of (a) the misorientation distribution histograms, (b) the horizontal line intercept distributions and (c) the vertical line intercept distributions corresponding to the as-built and peak-aged FCC lattices.

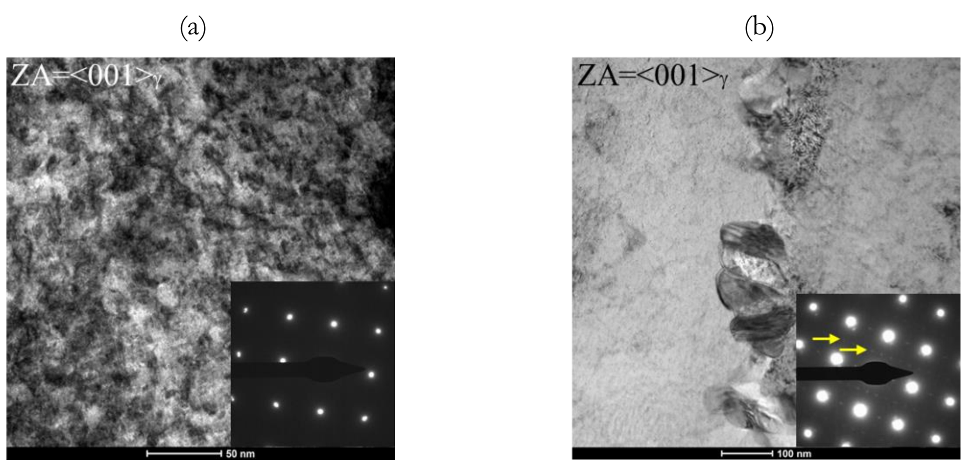

Figure 6.6. TEM bright field micrographs, and the corresponding selected area diffraction patterns, depicting the microstructure of the FCC LPBFed lattice along a <001>γ zone axis. (a) As-built condition; (b) peak-aged condition. The γ″ superlattice diffraction spots have been highlighted using yellow arrows.

6.2.2. Mechanical behaviour and strain localization in as-built Inconel 718 lattice structures

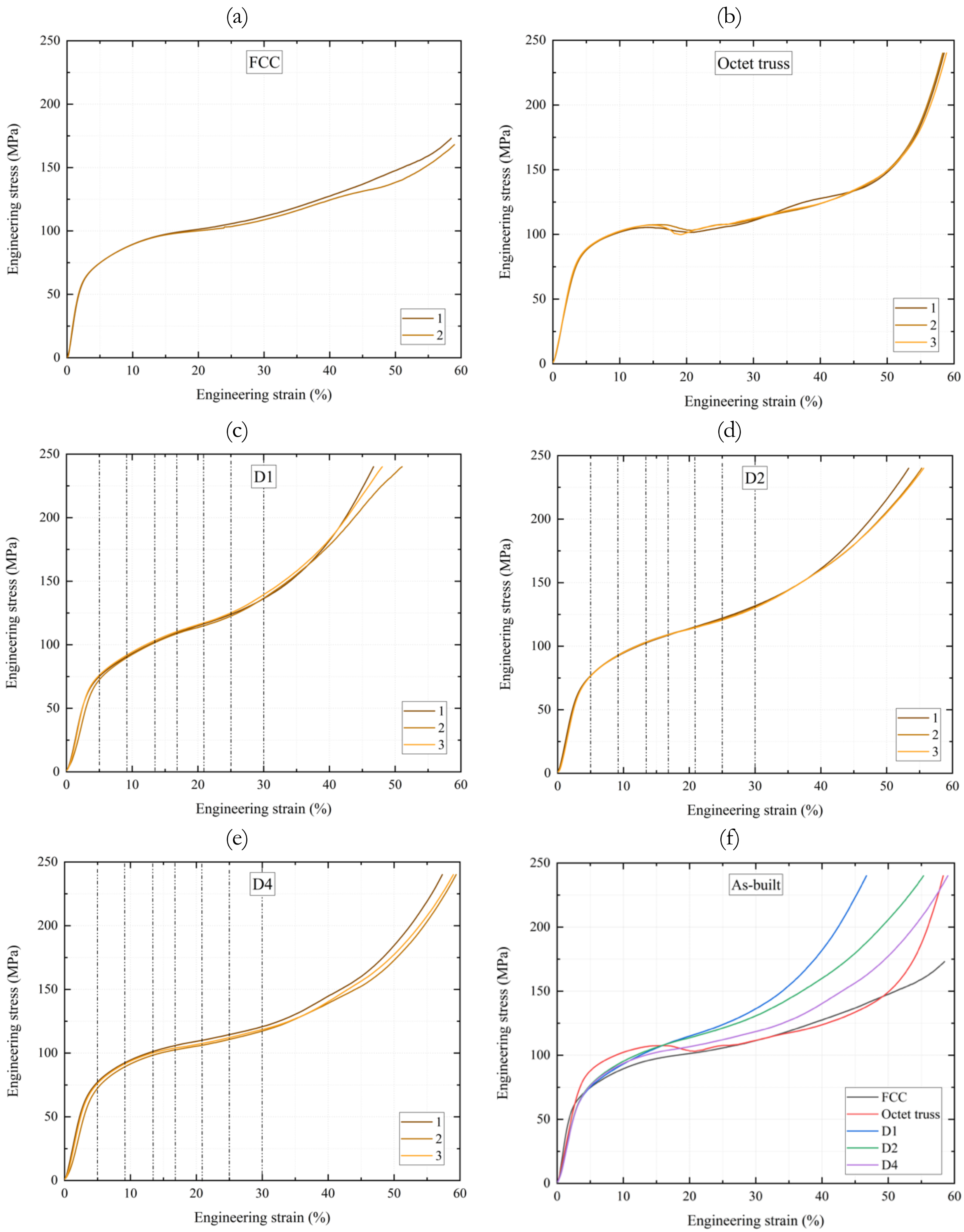

Figure 6.7. Engineering compressive stress-strain response of the Inconel 718 lattice structures in the as-built condition. Tests were performed at room temperature and at a strain rate of 10^{-3} s^{-1}. (a) FCC, (b) OT, (c) D1, (d) D2, and (e) D4. (f) Comparison of all the curves. The vertical black dotted lines indicate the strain levels at which the DIC data shown in Figures 6.8-6.10 was measured.

Table 6.5. Average yield strength values corresponding to the Inconel 718 LPBF manufactured lattice structures in the as-built and peak-aged conditions.

Average yield strength (MPa)	**As-built**	**Peak-aged**
FCC	39 ± 3	132 ± 1
Octet truss	51 ± 1	158 ± 0.3
D1	40 ± 0.5	143 ± 1
D2	39 ± 1	142 ± 1
D4	39 ± 1	136 ± 2

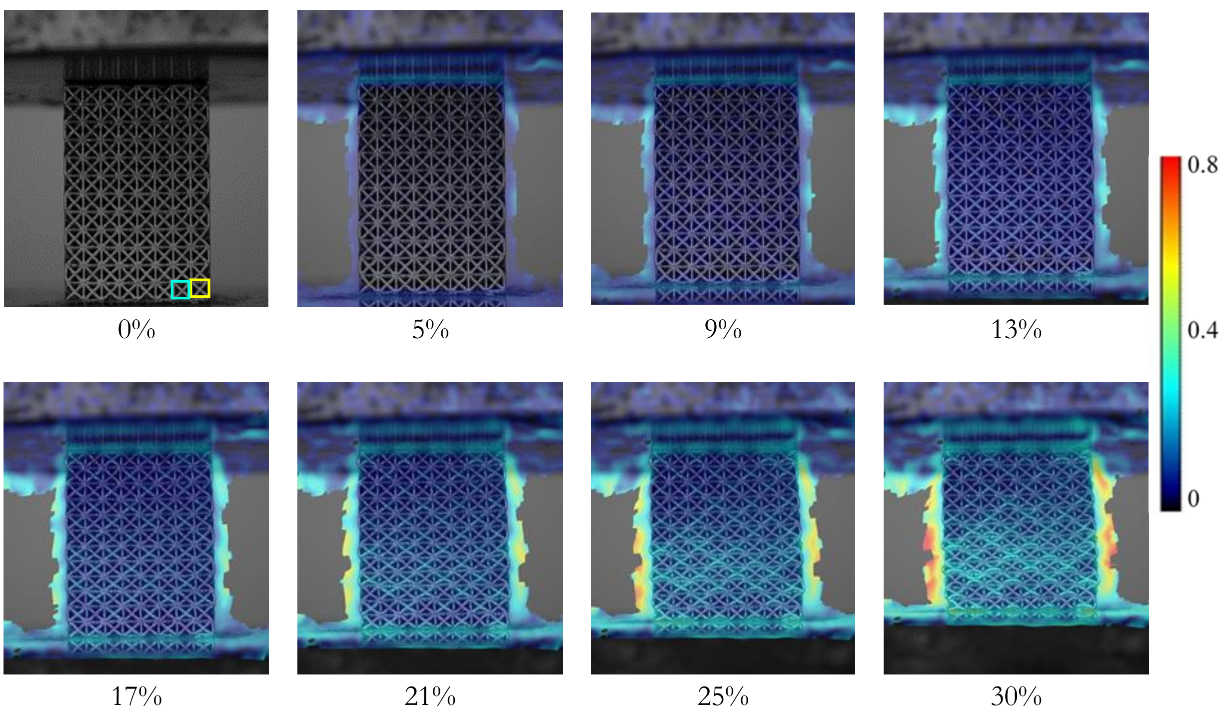

Figure 6.8. Strain localization at different nominal compression strain levels (indicated below each image) in as-built D1 lattices. The scale bar indicates maximum shear strain levels, measured by DIC. The FCC and OT domains are highlighted in yellow and blue, respectively, in the image corresponding to 0% strain.

Figure 6.7 illustrates the room temperature compressive behaviour corresponding to the Inconel 718 LPBF manufactured lattices in the as-built condition. Engineering stress-strain curves corresponding to the FCC (Figure 6.7. (a)) and OT (Figure 6.7. (b)) structures, as well as to the hybrid D1 (Figure 6.7. (c)), D2 (Figure 6.7. (d)), and D4 (Figure 6.7. (e)) lattices are shown.

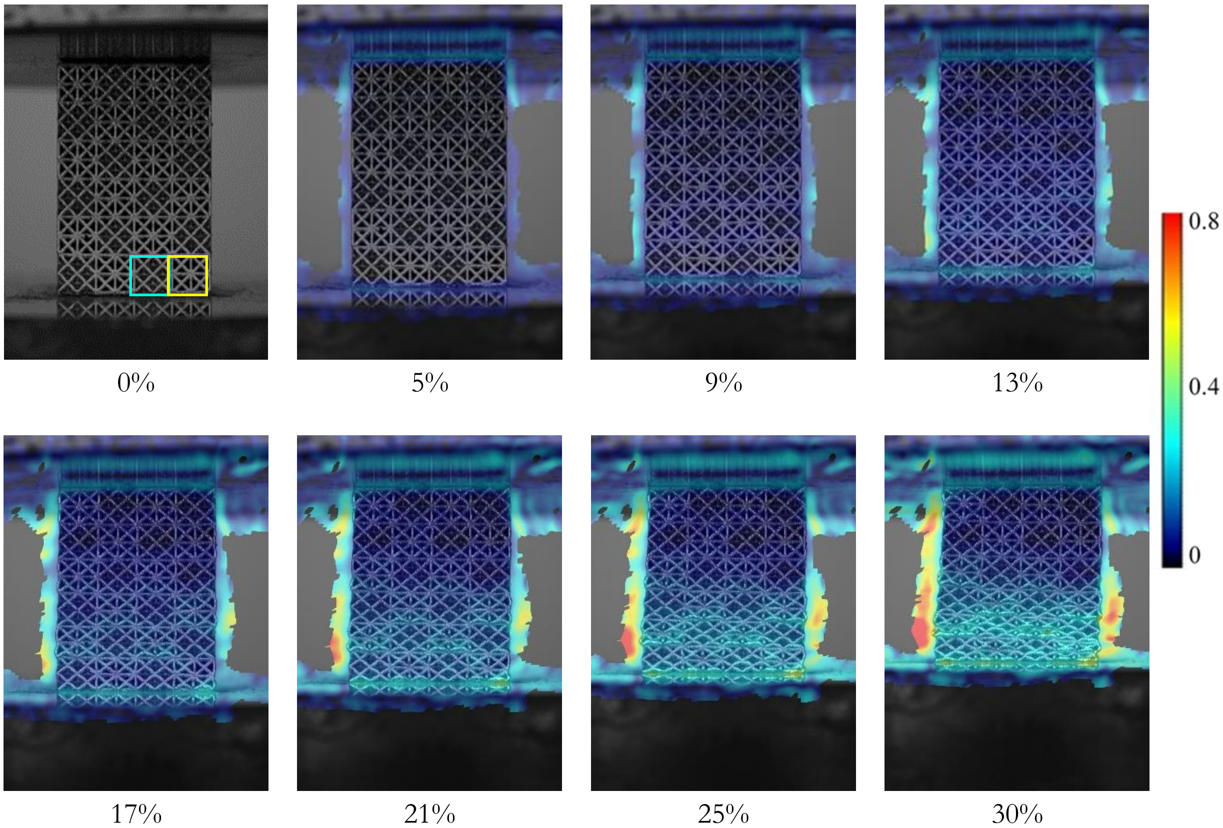

Figure 6.9. Strain localization at different nominal compression strain levels (indicated below each image) in the as-built D2 lattices. The scale bar indicates maximum shear strain levels, measured by DIC. The FCC and OT domains are highlighted in yellow and blue, respectively, in the map corresponding to 0% strain.

It can be seen first that, for a given lattice structure, the reproducibility of the mechanical response is very high, attesting to the robustness of the fabrication process. Second, Figure 6.7 evidences that, irrespective of the lattice topology, all as-built samples exhibit a bending-dominated behaviour, where the elastic regime is followed by a stress plateau that, in turn, precedes lattice densification where the stress increases rapidly due to the significant contacts of collapsed struts.

As shown earlier for Inconel 718 LPBF-manufactured lattices with BCC, FCC, and HCP topologies [33,34], this homogeneous mechanical response is related to the good ductile nature of the solid-solution microstructure in the as-built condition (Figure 6.4. (c) and 6.6. (a)). In Figure 6.7. (f) the curves corresponding to all the as-built lattices are superimposed. The corresponding σ_y values are listed in Table 6.5. It can be seen that σ_y is very similar (~39-40 MPa) in the FCC, D1, D2, and D4 configurations, while it is 25% higher in the OT lattice (~51 MPa).

Figures 6.8-6.10 depict the evolution of the local strain distributions measured by DIC at different nominal engineering compressive strain levels (5,9,13,17,21,25,30 %) in the D1 (Figure 6.8), D2 (Figure 6.9), and D4 (Figure 6.10) as-built lattices.

As expected, compression proceeds homogeneously by strut bending and in the absence of any significant strain localization up to relatively large nominal strain levels. In the D4 lattice the horizontal interphase boundaries (IBs) and the softer FCC domains carry a larger amount of strain than the harder OT domains, particularly at nominal strains higher than approximately 20%. This behaviour resembles that of two-phase alloys, where the softer phase accommodates plastic deformation first.

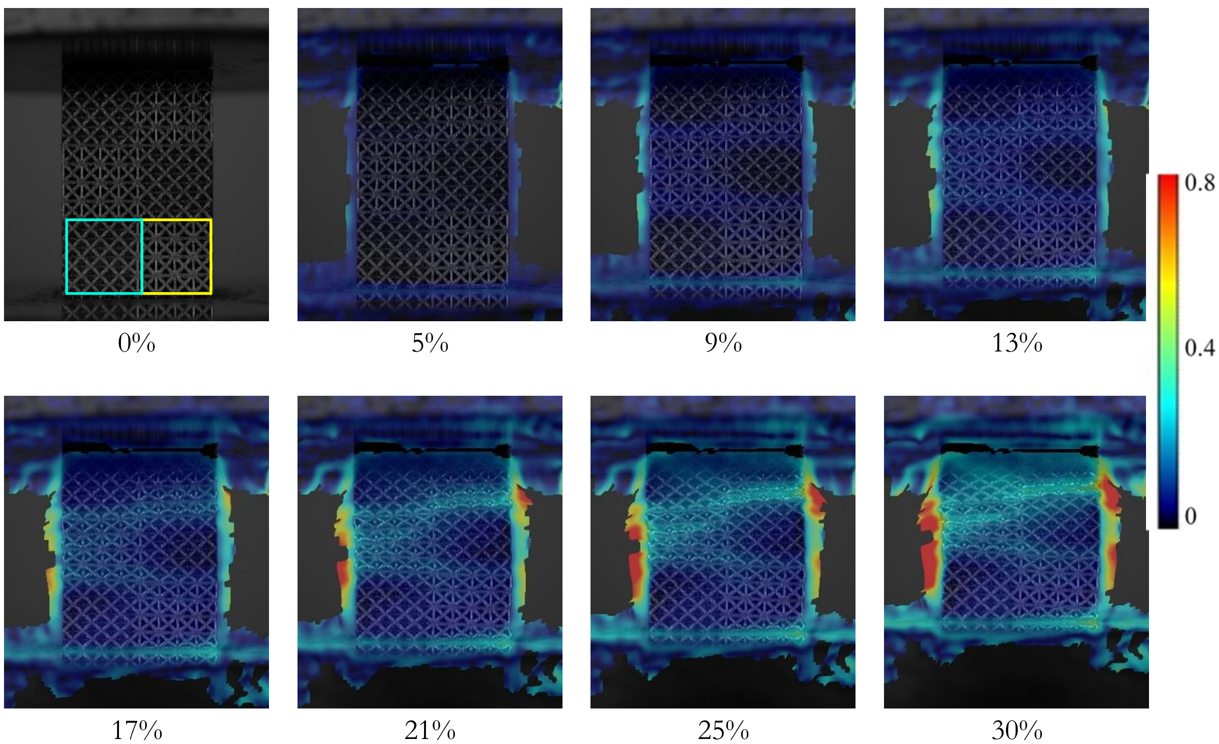

Figure 6.10. Strain localization at different nominal compression strain levels (indicated below each image) in the as-built D4 lattices. The scale bar indicates maximum shear strain levels, measured by DIC. The FCC and OT domains are highlighted in yellow and blue, respectively, in the map corresponding to 0% strain.

6.2.3. Influence of precipitation on the mechanical behaviour of hexagonal lattice structures

Figure 6.11 illustrates the room temperature compressive behaviour corresponding to the Inconel 718 LPBF lattices in the peak-aged condition. Engineering stress-strain curves corresponding to the FCC (Figure 6.11. (a)) and OT (Figure 6.11. (b)) structures, as well as to the hybrid D1 (Figure 6.11. (c)), D2 (Figure 6.11. (d)), and D4 (Figure 6.11. (e)) lattices are shown. Three stress-strain curves are plotted for each architecture. The yield strength is indicated with a red dotted line.

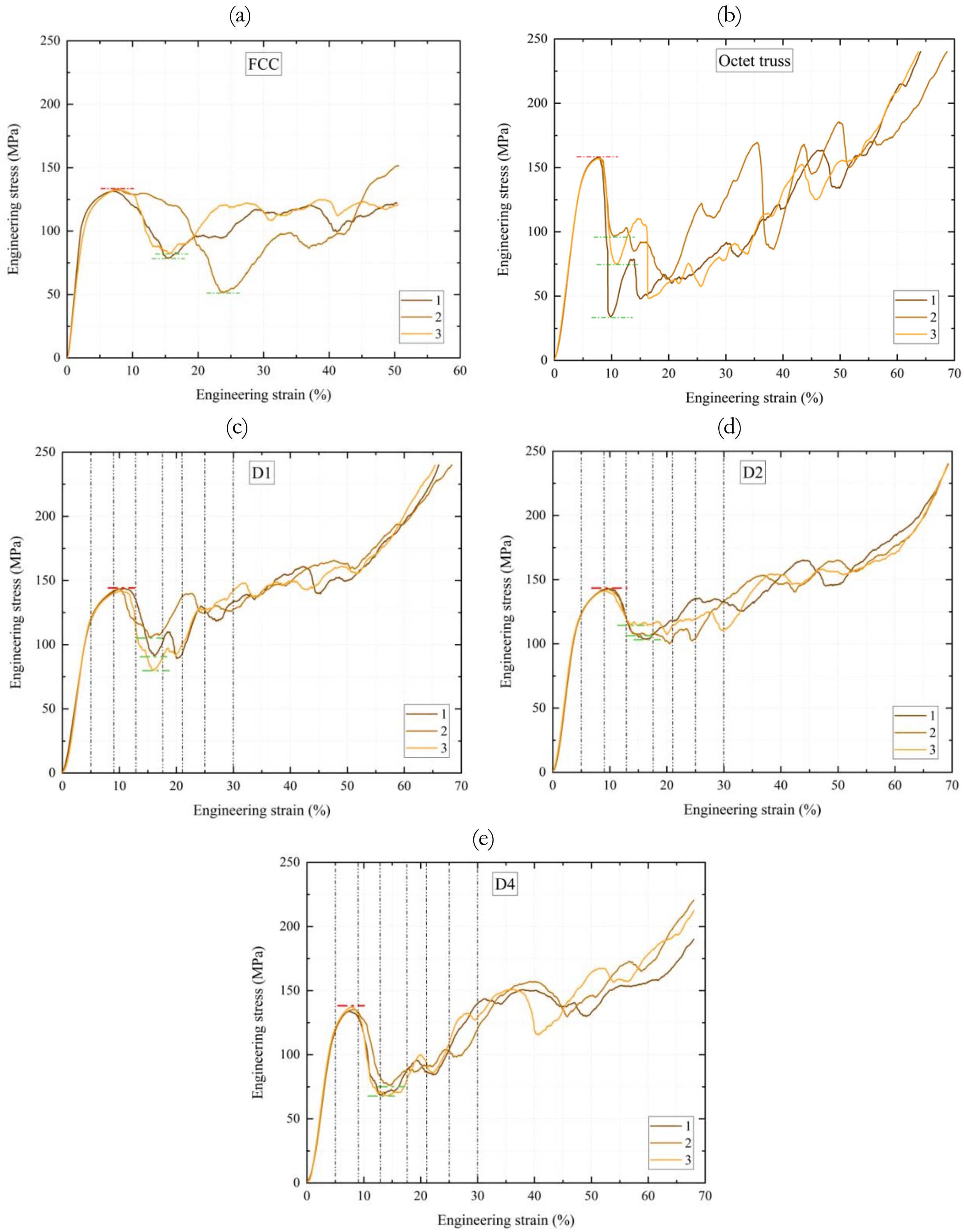

Figure 6.11. Engineering compressive stress-strain response of the Inconel 718 lattice structures in the peak-aged condition. Tests were performed at room temperature and at a strain rate of 10^{-3} s^{-1}. (a) FCC, (b) OT, (c) D1, (d) D2, and (e) D4. The yield strength is indicated with a red dotted line. The minimum stress value following the first stress drop (σ_{min}) has been highlighted in each curve using a green dotted line. The vertical black dotted lines indicate the strain levels at which the DIC shown in Figures 6.12-6.14 was measured.

It is evident that, irrespective of the lattice architecture, γ'' precipitation leads to an increase in σ_y with respect to the as-built condition. Additionally, as shown in Table 6.5, the yield strength values of the D1, D2, and D4 peak aged lattices, which amount to 143±1, 142±1, and 136±2 MPa, respectively, lie in between those of the softer FCC (132±1 MPa) and the harder OT (158±0.3 MPa) lattices.

Furthermore, γ'' precipitation leads to a transition from a bending-dominated to a stretch-dominated mechanical behaviour in all the lattices investigated. A similar precipitation-induced transition was reported earlier for Inconel 718 LPBFed single-oriented lattices with a wide variety of architectures [33,34]. The stretch-dominated behaviour in the latter is characterized by the occurrence of several stress drops due to strain localization induced by catastrophic strut failure along bands traversing the entire lattice width [14-16,28].

In general, the most pronounced stress drop takes place immediately following yielding as a consequence of the formation of the first band. The minimum stress value following the first stress drop (σ_{min}) has been highlighted in each curve using a green dotted line. The magnitude of this first stress drop ($\Delta\sigma=\sigma_{min}-\sigma_y$) is proportional to the length of the corresponding band, or, in other words, to the damage propagation path length.

Table 6.6. Magnitude of the first stress drop in the peak-aged lattices (Figure 6.11).

	Stress drop (MPa)
FCC	61 ± 18
Octet truss	89 ± 32
D1	51 ± 12
D2	37 ± 7
D4	65 ± 5

As shown in Figures 6.11. (a) and 6.11. (b), in the FCC and OT lattices a pronounced stress decrease takes place immediately after yielding. The average $\Delta\sigma$, measured from the three tests carried out for each condition, amounts to -61±18 MPa (FCC) and -89 ± 32 MPa (OT). The large standard deviations of these measurements (29% and 36%, respectively) reflect the low predictability of the mechanical behaviour of the "single crystal" lattices. The σ_{min} is attained at average strains (e_{min}) of 18.3 ± 4.7 % and 10.3 ± 0.5 %, respectively. The average strain softening rate during the first stress drop (θ), defined here as the slope of a line connecting σ_y and σ_{min} ($\theta = \Delta\sigma/(e_{min} - e_{\sigma y})$), amounts to -8.1 GPa and -62.7 GPa in the FCC and OT lattices, respectively, indicating the OT lattice is significantly more unstable than FCC lattice.

As shown in Figure 6.11. (c-e) and in Table 6.6, $\Delta\sigma$ in the D1, D2, and D4 architectures amounts, respectively, to -51±12, -37±7, and -65±5 MPa. It must be noted here that $\Delta\sigma$ in D2 is significantly smaller, in absolute terms, than $\Delta\sigma$ in D1 and D4 and in the FCC and OT lattices, suggesting a shorter damage propagation path length. Additionally, the standard deviations (23, 18 and 8% for D1, D2 and D4, respectively) are smaller than those of the FCC and OT structures, attesting to the higher reproducibility of the mechanical response of the hybrid lattices, at least during the early deformation stages. Finally, while e_{min} is similar in D1, D2, and D4 (e_{min}=15.8 ± 0.5, 14.1 ± 0.4, and 13.9 ± 0.9 %, respectively), the absolute value of θ is significantly smaller in D2 ($\theta = -20.7, -8.2$ and -20.7 GPa in D1, D2, and D4, respectively), suggesting the D2 lattice architecture has better resistance to the shear band propagation and thereby higher stability after yielding.

Figures 6.12-6.14 depict the evolution of the local strain distributions measured by DIC at different nominal engineering compressive strain levels (5, 9, 13, 17, 21, 25, 30 %) in the D1 (Fig. 12), D2 (Figure 6.13), and D4 (Figure 6.14) peak-aged lattices. Unlike the homogeneous deformation and bending of struts seen in the as-built lattices (Figures 6.8-6.10), the deformation of peak-aged lattices was governed by the buckling-induced fracture of struts due to the higher strength and lower ductility of the peak-aged base material, as reported earlier [34].

Figure 6.12 corresponds, in particular, to D1 test number 2 in Figure 6.11. (c). A band of broken struts forms at nominal strains comprised between 13 and 17%, at which the minimum stress following the first stress drop is also reached (Figure 6.11. (c)), and propagates across the entire width of the lattice at 45° with respect to the applied stress. The local strain along the band increases progressively with deformation, as the top part of the lattice slides along the plane of the band as a consequence of the continued applied stress. Shear band propagation at 45□ leading to the observed strut failure has been reported profusely in single-oriented additively manufactured lattices of a wide range of alloys [e.g. 64-67].

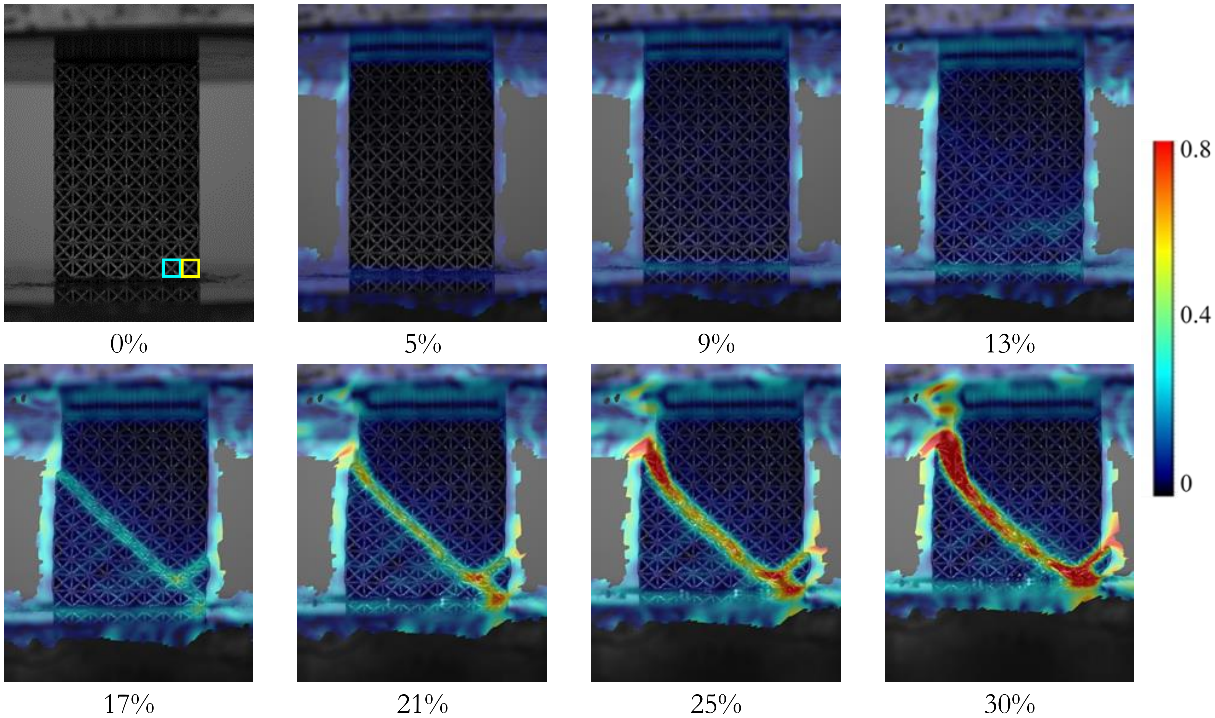

Figure 6.12. Strain localization at different nominal strain levels in peak-aged D1 lattices. Scale bar indicates the maximum shear strain levels, measured by DIC. FCC and OT domains are marked in yellow and blue, respectively.

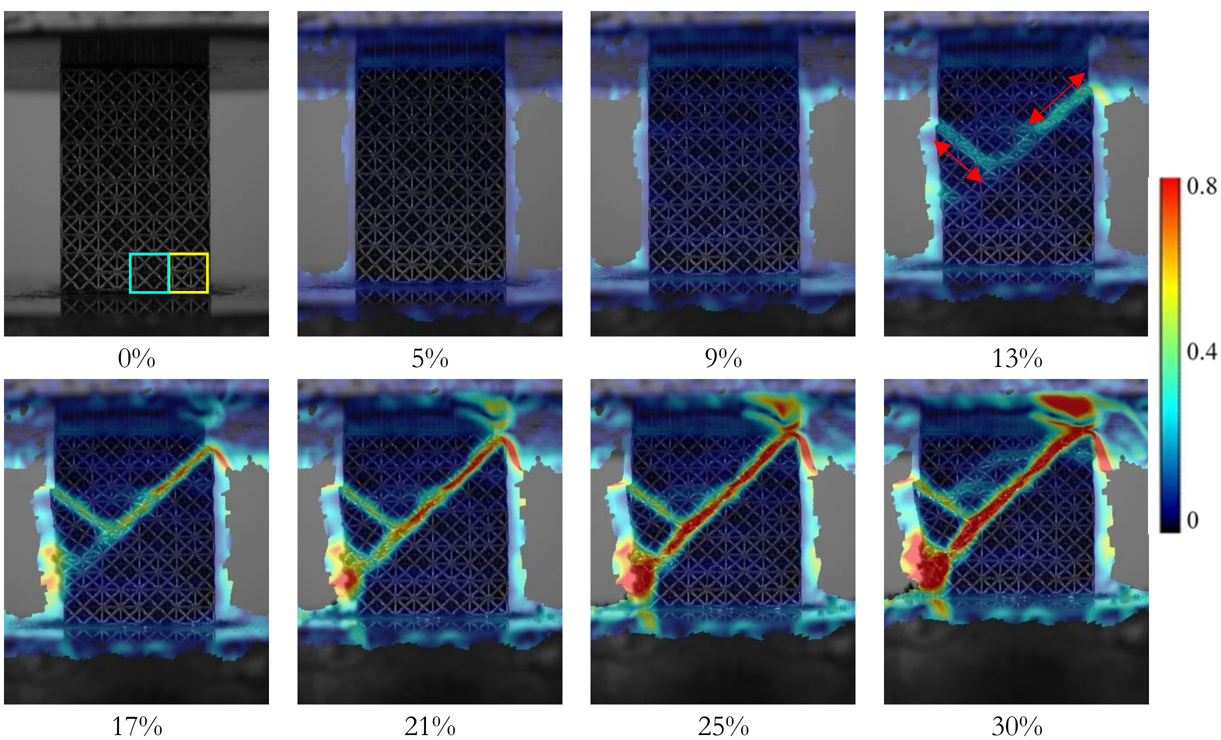

Figure 6.13. Strain localization at different nominal strain levels in peak-aged D1 lattices. Scale bar indicates the maximum shear strain levels, measured by DIC. FCC and OT domains are marked in yellow and blue, respectively. The red arrows inserted corresponding to 13% strain indicate the length of two growing bands.

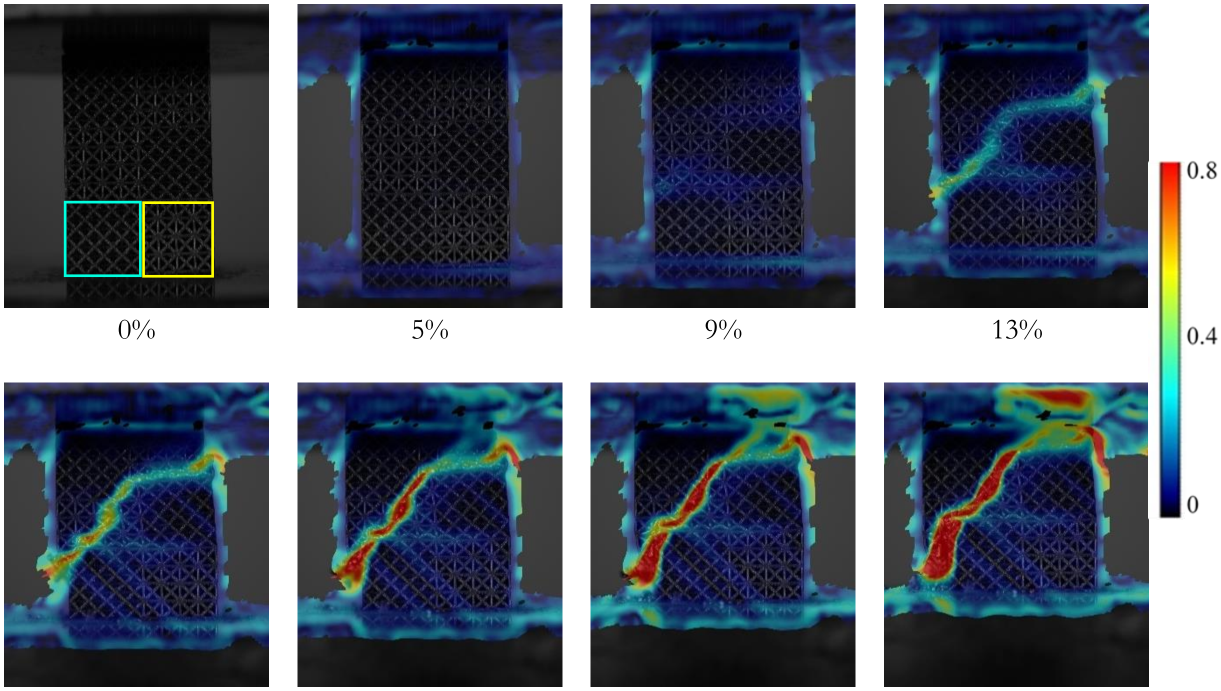

Figure 6.14. Strain localization at different nominal strain levels in peak-aged D1 lattices. Scale bar indicates the maximum shear strain levels, measured by DIC. FCC and OT domains are marked in yellow and blue, respectively.

Figure 6.13 corresponds to D2 test number 3 in Figure 6.11. (d). In this test the first stress drop occurs at a nominal strain interval ranging between 9 and 13%. It can be seen that, within this strain interval, two shear bands initiated from the two opposite lattice surfaces and propagated at 45° with respect to the global applied stress across the softer FCC domains towards the centre of the lattice. The band length at a nominal strain of 13%, at which the minimum stress was reached (Figure 6.11. (d)), is relatively short (see red arrows in Figure 6.13) due to the impediment of vertical IBs. This figure reveals that shear bands initiated and subsequently propagated in FCC domains. Since the size of FCC domains is small compared with that of the global structure ($Width_{FCC}/Width_{global\ lattice} = 0.25$), shear bands interacted with the three vertical IBs upon propagation across the entire width of the global lattice. Such interactions prevented fast propagation of shear bands, resulting in comparatively smaller values of $\Delta\sigma$ and θ (i.e. enhancing the stability) in D2 (Figure 6.11. (d)). At a nominal strain of 17% the two bands intersected and at 21% the largest one eventually grew to propagate through the entire width of the lattice.

Figure 6.14 corresponds to D4 test number two in Figure 6.11. (e). At a nominal strain of 13%, which is close to e_{min} (13.9%), a shear band traversing the entire lattice width is apparent. Shear band propagation occurred preferentially along the horizontal IBs, as well as across FCC domains (at 45° with respect to the applied stress). The larger size of the domains in D4 ($Width_{FCC}/Width_{global\ lattice}$ = 0.5) in comparison with D2 facilitates band propagation through the softer FCC domains, explaining the comparatively larger $\Delta\sigma$ (Figure 6.11. (e)) and θ values. The local strain along the band increases progressively with deformation, as the top part of the lattice slides along the plane of the band as a consequence of the continued applied stress.

6.3. Discussion

6.3.1. FEA simulation of local stress concentrations in as-built and peak-aged lattice structures

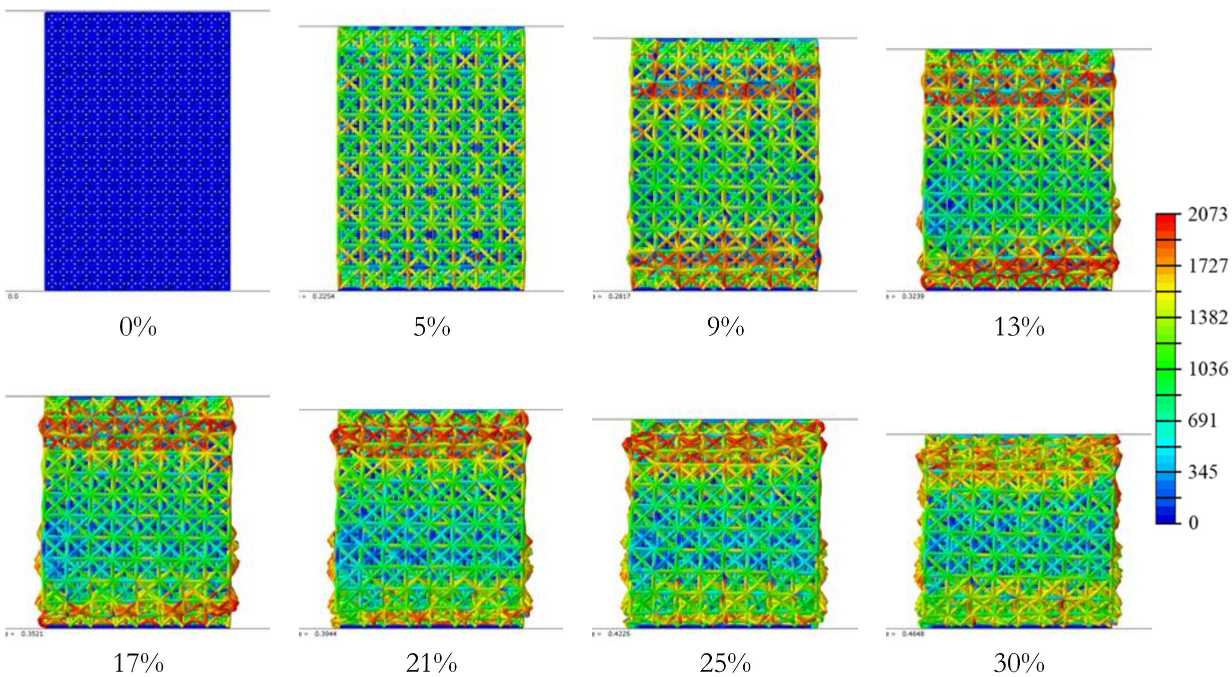

Figure 6.15. Stress distribution at different global compression strain levels (indicated below each image) in the peak-aged D1 lattices. The scale bar indicates Von Mises stress levels in MPa, measured by FEA.

The FEA local stress distribution maps corresponding to global compressive strains of 5, 9, 13, 17, 21, 25, and 30 % in the D1, D2, and D4 as-built lattices are represented in Supplementary Figures S2-S4, (Annex E), respectively. It can be seen that a relatively homogeneous stress distribution occurred throughout the lattice volume in D1 and D2 until relatively high global strain levels and that the D4 lattice showed a tendency for stress to concentrate along horizontal IBs and FCC domains. This is in full agreement with the DIC measurements (Figures 6.8-6.10) and it explains that, irrespective of the OT domain size, the three architectures exhibit a bending-dominated behaviour with almost identical σ_y values.

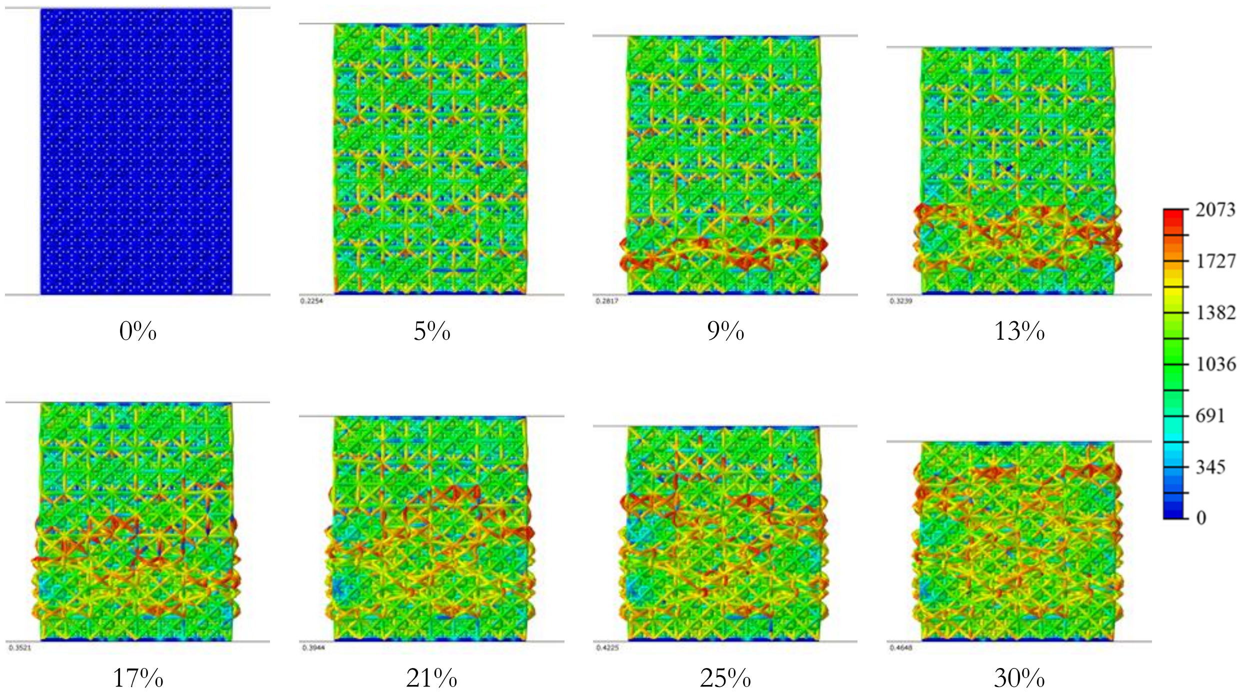

Figure 6.16. Stress distribution at different global compression strain levels (indicated below each image) in the peak-aged D2 lattices. The scale bar indicates Von Mises stress levels in MPa, measured by FEA.

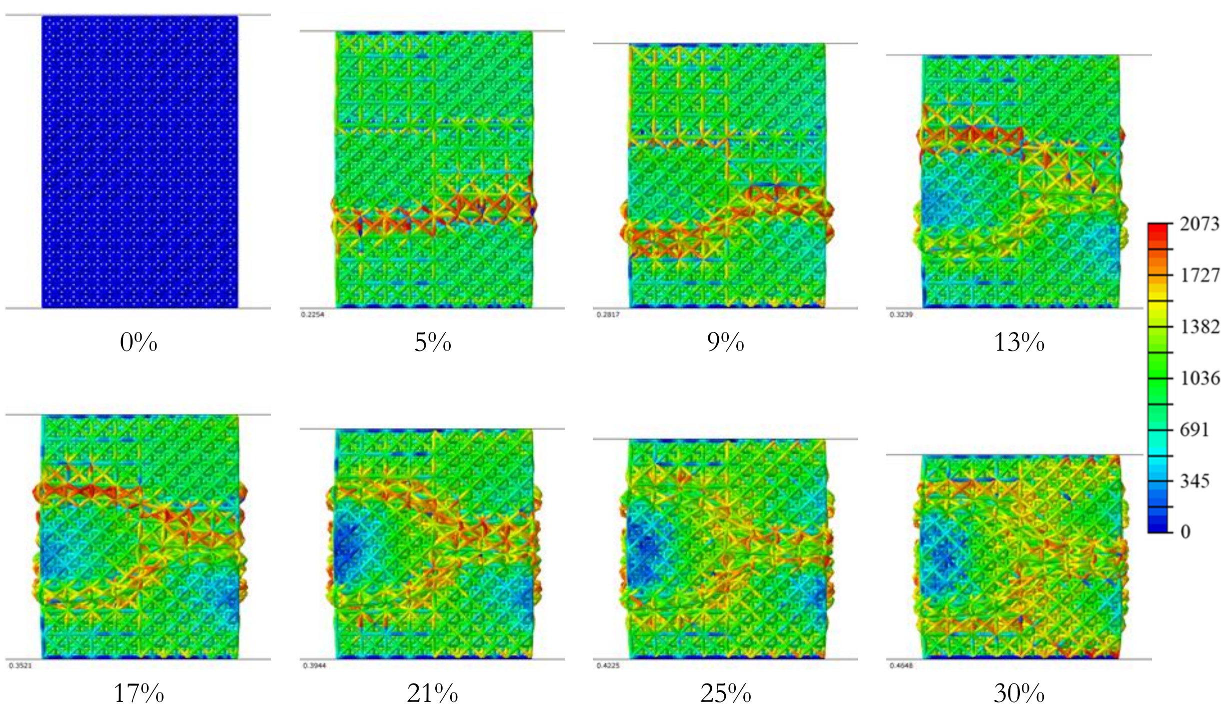

Figure 6.17. Stress distribution at different global compression strain levels (indicated below each image) in the peak-aged D4 lattices. The scale bar indicates Von Mises stress levels in MPa, measured by FEA.

The FEA local stress distribution maps corresponding to global compressive strains of 5, 9, 13, 17, 21, 25, and 30 % in the D1, D2, and D4 peak-aged lattices are represented in Figures 6.15-6.17, respectively. Let us examine each lattice architecture separately.

In the peak aged D1 lattice, high stress concentrations develop first in regions near the top and the bottom of the compressed lattice as well as at some surface sites, which thus constitute preferred sites for shear band nucleation. Since the beam elements were that were used in FEA calculations did not include fracture, the abrupt propagation of the band that is captured by DIC (Figure 6.12) is not visible in the simulations. In the peak-aged D2 architecture, however, Figure 6.16 reveals that stress concentrates both at FCC domains and at horizontal IBs. This is also fully consistent with our DIC measurements (Figure 6.13).

Finally, Figure 6.17 shows that in the D4 architecture stress concentrates mostly at horizontal IBs from the onset of deformation, and that FCC domains become increasingly stressed as compression proceeds. This stress distribution is also in agreement with the preferential damage propagation along horizontal IBs and across FCC domains detected via DIC in this architecture (Figure 6.14). The larger size of the FCC domains, which is associated with larger horizontal IB stretches in between two vertical IBs, is consistent with the easier damage propagation in comparison with D2.

Overall, the high consistency between the experimental results and the FEA simulations reveal that the latter can be utilized to predict the development of local stresses in other lattice architectures, thus reducing the need for time-consuming experimental campaigns.

6.3.2. Influence of hybridization on energy absorption

Table 6.7 summarizes the values of the mean EA during uniaxial compression of the as-built and peak-aged FCC, OT, and hybrid lattices at nominal engineering strains of 10, 30, and 40%. In general, at all strain levels, the EA is higher in the peak-aged lattices that in the as-built lattices for all the investigated architectures, except for the OT structure at strains higher than 10%.

Following the approach used in [52,55], we use the rule of mixtures (RoM) to estimate the σ_y and the EA of the hybrid structures. In the as-built condition, the RoM predicts that, for a 50% volume fraction of OT domains, the yield strength of the hybrid lattices ($\sigma_y = 0.5\ \sigma_{y,FCC} + 0.5\ \sigma_{y,OT}$) should be equal to 45 MPa.

Table 6.7. Mean energy absorbed (EA) during uniaxial compression of the as-built and peak-aged lattices at 10%, 30% and 40% engineering strain.

Mean absorbed energy (J/m³)	**10% strain**		**30% strain**		**40% strain**	
	As-built	**Peak-aged**	**As-built**	**Peak-aged**	**As-built**	**Peak-aged**
FCC	6.7 ± 0.02	10.7 ± 0.1	26.8 ± 0.2	30.6 ± 1.3	38.6 ± 0.4	41.5 ± 2.6
Octet truss	7 ± 0.3	9.9 ± 0.4	28.1 ± 0.3	25.5 ± 3.2	39.9 ± 0.3	36.4 ± 5.2
D1	5.5 ± 0.3	8.6 ± 0.7	28.1 ± 0.5	32.4 ± 1	43.3 ± 0.6	46.5 ± 1
D2	5.6 ± 0.2	8.7 ± 0.5	27.9 ± 0.3	32.6 ± 1	42 ± 0.4	46.4 ± 0.4
D4	5.4 ± 0.2	7.5 ± 0.4	26.5 ± 0.2	26.5 ± 0.5	39.1 ± 0.2	40.7 ± 0.5

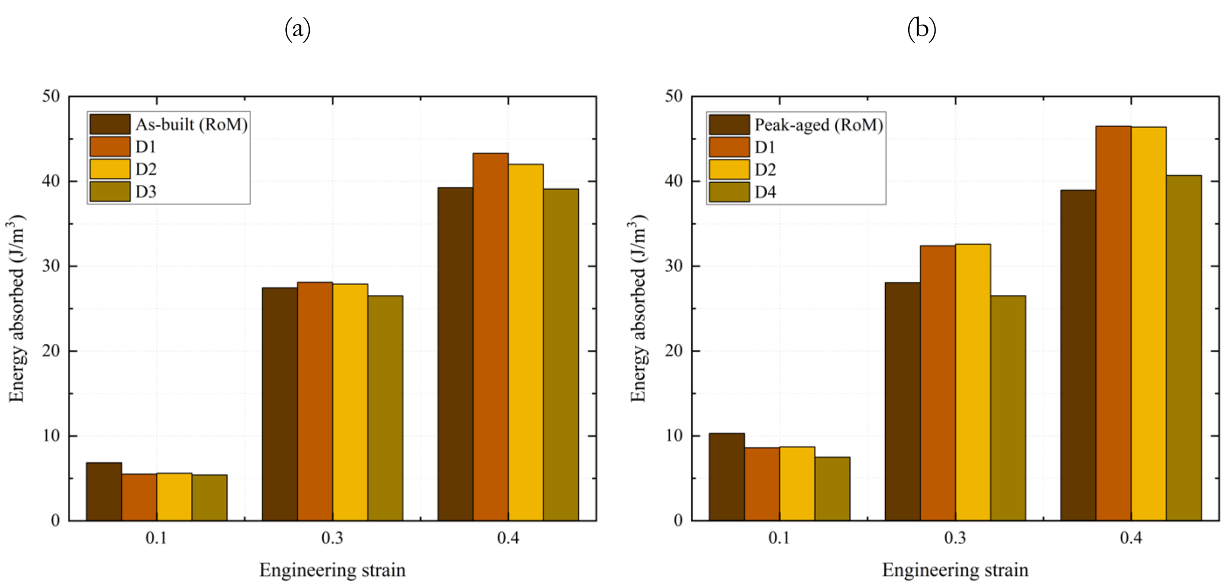

Figure 6.18. Comparison of the absorbed energy of D1, D2 and D4 with respect to that predicted by the rule of mixtures. (a) As-built condition; (b) peak-aged condition.

As can be seen in Table 6.5, σ_y in the D1, D2, and D4 architectures is smaller than the prediction, amounting, instead, to 40, 39, and 39 MPa, respectively. The similarity of these values with the σ_y of the FCC phase (39 MPa) suggests that the deformation of this softer phase is in all cases dominant during yielding. Figure 6.18. (a) compares the EA calculated by RoM ($EA = 0.5\ EA_{FCC} + 0.5\ EA_{OT}$) for nominal engineering strains of 10, 20, and 30%, with the corresponding experimental values measured for the as-built D1, D2, and D4 architectures. The agreement between the experimental and predicted values confirms that the OT phase does contribute to deformation after yielding.

In the peak-aged condition, the RoM predicts that, for a 50% volume fraction of OT domains, σ_y should be equal to 145 MPa. As can be seen in Table 6.5, σ_y in the D1, D2, and D4 architectures amounts to 143, 142, and 136 MPa, respectively. The agreement between the measured and predicted σ_y in D1 and D2 indicates that both phases contribute equally to yielding in these architectures. In D4, however, σ_y is close to the yield strength of the FCC phase (132 MPa) as, at this larger domain size, the deformation of the FCC phase is, instead, dominant during yielding. Figure 6.18. (b) compares the EA calculated by the RoM for nominal engineering strains of 10, 20, and 30% with the corresponding experimental values measured for the peak-aged D1, D2, and D4 lattices. It can be seen, first, that in D4 the experimentally measured EA coincides with the predictions of the RoM. Again, the agreement between the experimental and predicted values confirms that the OT phase does contribute to deformation after yielding in the D4 lattice. However, in D1 and D2 the EA is significantly higher than the prediction of the rule of mixtures at strains larger than 10%.

Some earlier works have also described that the EA of hybrid metallic lattices might exceed the prediction of the rule of mixtures [52,55]. Alberdi et al. [52] made this observation in FCC/BCC multi-morphology 316L steel lattices with FCC fractions ranging from 24 to 75%, and they attributed it to the change in the collapse modes from shear instability in the FCC single-oriented lattice to sequential collapse in the hybrid lattices. Yin et al. [55] reported similarly high EA in stainless steel BCC/FCC mechanical metamaterial composites with different distances between the FCC reinforcements, and they reported that the highest increase in EA was obtained when every truss unit in the (softer) matrix phase was surrounded by reinforcement lattice domains. The current research proves, additionally, that the effectiveness of hybridization, measured as the increase in the EA with respect to the values of single-oriented FCC matrix phase, is highly dependent on the microstructure of the base material.

6.3.3. Influence of interphase boundaries

Liu et al. [50] highlighted the role of IBs on the improvement of damage tolerance of additively manufactured architected materials. In a pioneer effort inspired by physical metallurgy principles, Pham et al. [68] recently demonstrated that meta-polycrystalline lattices, i.e., structures consisting of domains with the same unit cell but different orientations, were observed to have improved damage tolerance because the meta-grain boundaries acted as effective obstacles to shear band and crack propagation [50]. This study suggested, additionally, that the introduction of meta-precipitates (a form of hybridization consisting on embedding domains with a harder lattice structure on a softer matrix structure), could constitute effective avenues for the design of robust architected materials.

Similarly, Guo et al. [57] found that maximizing the IB area was critical to enhance the energy absorption capability of hybrid lattice structures. In agreement with these earlier works, the D2 architecture exhibits a higher EA than the D4 architecture, where the absence of a sufficient number of vertical IBs results in inefficient hindering of shear band propagation.

The current research, however, brings additional evidence regarding the role of IBs in hybrid structures. First, our results show that this role is highly dependent on the microstructure of the base material. In particular, IBs play a critical role in peak-aged lattices, in which the main collapse mode is shear band formation, as they act as obstacles to shear band propagation; however, their role is negligible when the as-built hybrid lattices, which deform homogeneously by strut bending.

Additionally, our work suggests that there is a critical precipitate size below which the role of IBs as enhancers of the damage tolerance changes. In particular, the D1 hybrid structure, despite having the largest fraction of IBs, does not exhibit higher EA or higher σ_y than D2. For such small domain sizes, the lattice behaves as a reinforced "single-phase" structure, such as in metallic solid solutions, and IBs lose their role as shear band stoppers. In such a structure, damage propagates in the form of a single shear band traversing the entire width of the lattice. However, the presence of the reinforcements leads to an increase in the stress required for the nucleation of the shear band in comparison to that required in the single-phase FCC lattice.

6.3.4. Selection of optimal meta-precipitate size

The results described above allow us to select the peak-aged D2 lattice as an optimum microstructure/architecture combination for the investigated LPBFed Inconel 718 strut-based lattices. This choice is justified on the basis that this structure is endowed, simultaneously, with (a) a high yield strength (σ_y= 142±1 MPa), (b) the smallest stress drop ($\Delta\sigma$= -37±7 MPa), (c) a low work softening rate during the first stress peak (θ= 8.2 GPa), (d) the largest absorbed energy (Table 6.7), and (e) a high mechanical stability, reflected in the large reproducibility of the stress-strain curves at strains prior to densification. The high yield strength is known to be a direct consequence of γ'' precipitation in the base material [33,34]. Characteristics (b-e) are consistent with the fact that the D2 structure is, overall, endowed with a higher resistance to damage propagation by the presence of a sufficiently large number of vertical IBs.

6.4. Remarks

The aim of this work is to investigate the coupled effect of microstructure and hybridization on the mechanical behavior of additively manufactured Inconel 718 strut-based lattices. With that purpose, two microstructures, namely the as-built solid solution and a peak aged condition, are coupled with three hybrid architectures formed by alternating FCC (matrix) and OT (reinforcement) domains containing 1, 8, and 64 unit cells, respectively, all with a constant 50% reinforcement volume fraction. The room temperature mechanical behaviours of all six microstructure-architecture combinations are investigated with the aim of deriving guidelines for the design of lattices endowed with high strength and mechanical stability. The main conclusions of this study are the following:

- In the as-built condition, the mechanical behavior of the hybrid lattices was similar to that of the architected single-phase constituents, irrespective of the reinforcement size. The hybrid architectures exhibited a bending dominated response with a similar yield strength value to that of the softer FCC phase and an energy absorption that can be predicted by the rule of mixtures. Deformation under compression proceeds mostly in a homogeneous fashion by strut bending.
- In the peak-aged condition, hybridization led to a significant improvement of the mechanical behavior with respect to that of the individual constituents. Indeed, while in this microstructural condition all lattices (single-phase and hybrid) exhibited stretch-dominated

behaviours, hybridization resulted, simultaneously, in a higher yield strength and higher levels of absorbed energy, which for some architectures exceeded the predictions of the rule of mixtures.

- The mechanism allowing for increased damage tolerance and higher levels of absorbed energy in selected peak-aged hybrid lattices consists on the hindering of shear band propagation by interphase boundaries. In particular, for this study, interphase boundaries parallel to the applied stress proved to be the most effective obstacles to shear band propagation. Thus, the optimum arrangement of reinforcements must be in such a way to maximize interphase boundary – shear band interactions.
- The effect of hybridization is also a function of the size of the reinforcements. In particular, below a critical size, the lattice behaves as a reinforced "single-phase" structure, in which a single shear band traverses the entire lattice width. The presence of the reinforcements leads to an increase in the stress required for the nucleation of the shear band in comparison to that required in the single-phase FCC lattice.
- Our results prove that the efficiency of lattice hybridization is highly dependent on the microstructure of the base material and on the size of the reinforcement lattice domains. It is therefore our contention that other approaches aiming to improve the mechanical behavior of lattices, including functional grading [69], nesting, interpenetration, and multi-material fabrication [70,71], should consider microstructure as a design criterion.

Bibliography

[1] J.U. Surjadi, L. Gao, H. Du, X. Li, X. Xiong, N.X. Fang and Y. Lu, Mechanical metamaterials and their engineering applications, Adv. Eng. Mater. 21 (2019) 1800864.

[2] M. Benedetti, A. du Plessis, R.O. Ritchie, M. Dallago, S.M.J. Razavi, F.Berto, Architected cellular materials: A review on their mechanical properties towards fatigue-tolerant design and fabrication, Mater. Sci. Eng. R 144 (2021) 100606.

[3] X. Zheng, H. Lee, T.H. Weisgraber, M. Shusteff, J. DeOtte, E.B. Duoss, J.D. Kuntz, M.M. Biener, Q. Ge, J. Jackson, N.X. Fang, C.M. Spadaccini, Ultralight, ultrastiff mechanical metamaterials, Science 344 (2014) 1373–1377.

[4] M. Schaeffer, G. Trainiti and M. Ruzzene, Optical measurement of in-plane waves in mechanical metamaterials through digital image correlation, Sci. Rep. 7 (2017) 42437.

[5] Electromagnetic metamaterials: transmission line theory and microwave applications, IEEE eBooks, IEEE Xplore, (n.d.). https://ieeexplore.ieee.org/book/5237794 (accessed June 13, 2021).

[6] C. Wang, Z. Vangelatos, C.P. Grigoropoulos, Z. Ma, Micro-engineered architected metamaterials for cell and tissue engineering, Mater. Today Adv. 13 (2022) 100206.

[7] B. Hanks, J. Berthel, M. Frecker, T. W. Simpson, Mechanical properties of additively manufactured metal lattice structures: Data review and design interface, Addit. Manuf.

35 (2020) 101301.

[8] C. Pan, Y. Jan, J. Lu, Design and optimization of lattice structures: a review, Appl. Sci. 10 (2020) 6374.

[9] V.H. Carneiro, S.D. Rawson, H. Puga, P.J. Withers, Macro-, meso- and microstructural characterization of metallic lattice structures manufactured by additive manufacturing assisted investment casting. Sci. Rep. 11 (2021) 4974.

[10] T. A. Schaedler, A. J. Jacobsen, A. Torrents, A. E. Sorensen, J. Lian, J. R. Greer, L. Valdevit, W. B. Carter, Ultralight metallic microlattices, Science 334 (2011) 962-965.

[11] T. DebRoy, H.L. Wei, J.S. Zuback, T. Mukherjee, J.W. Elmer, J.O. Milewski, A.M. Beese, A. Wilson-Heid, A. De, W. Zhang, Additive manufacturing of metallic components – Process, structure and properties, Prog. Mater. Sci. 92 (2018) 112–224.

[12] D. Herzog, V. Seyda, E. Wycisk, C. Emmelmann, Additive manufacturing of metals, Acta Mater. 117 (2016) 371-392.

[13] A.T. Clare, R.S. Mishra, M. Merklein, H. Tan, I. Todd, L. Chechik, J. Li, M. Bambach, Alloy design and adaptation for additive manufacture, J. Mater. Proc. Tech. 199 (2022) 117358.

[14] Z. Alomar, F. Concli, A review of the selective laser melting lattice structures and their numerical models, Adv. Eng. Mater. (2020) 2000611 (1-17).

[15] T. Maconachie, M. Leary, B. Lozanovski, X. Zhang, M. Qian, O. Faruque, M. Brandt, SLM lattice structures: Properties, performance, applications and challenges, Mater. Des. 183 (2019) 108137.

[16] L.Y. Chen, S.X. Liang, Y. Liu, L.C. Zhang, Additive manufacturing of metallic lattice structures: Unconstrained design, accurate fabrication, fascinated performances, and challenges, Mater. Sci. Eng. R 146 (2021) 100648.

[17] M. Leary, M. Mazur, H. Williams, E. Yang, A. Alghamdi, B. Lozanovski, X. Zhang, D. Shidid, L. Farahbod-Sternahl, G. Witt, I. Kelbassa, P. Choong, M. Qian, M. Brandt, Inconel 625 lattice structures manufactured by selective laser melting (SLM): Mechanical properties, deformation and failure modes, Mater. Des. 157 (2018) 179.

[18] A.A. Zadpoor, Mechanical performance of additively manufactured meta- biomaterials, Acta Biomat. 85 (2019) 41.

[19] L. Bai, J. Zhang, Y. Xiong, X. Chen, Y. Sun, C. Gong, H. Pu, X. Wu, J. Luo, Influence of unit cell pose on the mechanical properties of Ti6Al4V lattice structures manufactured by selective laser melting, Addit. Manuf. 34 (2020) 101222.

[20] A. Takezawa, K. Yonekura, Y. Koizumi, X. Zhang, M. Kitamura, Isotropic Ti–6Al–4V lattice via topology optimization and electron-beam melting, Addit. Manuf. 22 (2018) 634.

[21] A. Moussa, D. Melancon, A. El Elmi, D. Pasini, Topology optimization of imperfect lattice materials built with process-induced defects via Powder Bed Fusion Addit. Manuf. (2020) 101608.

[22] L. Zhang, B. Song, J.J. Fu, S.S. Wei, L. Yang, C.Z. Yan, H. Li, L. Gao, Y.S. Shi, Topology-optimized lattice structures with simultaneously high stiffness and light weight fabricated by selective laser melting: Design, manufacturing and characterization, J. Manuf. Process. 56 (2020) 1166.

[23] Y. Liu, J. Zhang, X. Gu, Y. Zhou, Y. Yin, Q. Tan, M. Li, M.X. Zhang, Mechanical performance of a node reinforced body-centred cubic lattice structure manufactured via selective laser melting, Scr. Mater. 189 (2020) 95.

[24] O. Al-Ketan, R. Rowshan, R.K.A. Al-Rub, Topology-mechanical property relationship of 3d printed strut, skeletal, and sheet based periodic metallic cellular materials, Addit. Manuf. 19 (2018) 167–183.

[25] C. Bonatti, D. Mohr, Large deformation response of additively-manufactured fcc metamaterials: from octet truss lattices towards continuous shell mesostructures, Int. J. Plast. 92 (2017) 122–147.

[26] J. Mueller, K. Shea, Stepwise graded struts for maximizing energy absorption in lattices, Extreme Mechanics Letters 25 (2018) 7–15.

[27] L. Zhang, S. Feih, S. Daynes, S. Chang, M.Y. Wang, J.Wei, W.F. Lu, Energy absorption characteristics of metallic triply periodic minimal surface sheet structures under compressive loading, Additive Manufacturing 23 (2018) 505–515.

[28] V.S. Deshpande, M.F. Ashby, N.A. Fleck, Foam topology: bending versus stretching dominated architectures, Acta Mater. 49 (2001) 1035.

[29] P. Köhnen, C. Haase, J. Bültmanna, S. Ziegler, J. H. Schleifenbaum, W. Bleck, Mechanical properties and deformation behavior of additively manufactured lattice structures of stainless steel, Mater. Des. 145 (2018) 205-217.

[30] I. Maskery, N.T. Aboulkhair, A.O. Aremu, C.J. Tuck, I.A. Ashcroft, Compressive failure modes and energy absorption in additively manufactured double gyroid lattices, Addit. Manuf. 16 (2017) 24-29.

[31] K. Hazeli, B. B. Babamiri, J. Indeck, A. Minor, H. Askari, Microstructure-topology relationship effects on the quasi-static and dynamic behavior of additively manufactured lattice structures, Mater. Des. 176 (2019) 107826.

[32] Z. Zeng, C. Wang, Y. Z. Lek, Y. Tian, S. Y. Kandukuri, P. J. Da Silva Bartolo, K. Zhou, Influence of microstructure on stainless steel 316L lattice structures fabricated by electron beam and laser powder bed fusion, Mater. Sci. Eng. A, 2022, 144225, in press.

[33] S.Banait, X. Jin, M. Campos, M.T. Pérez-Prado, Precipitation-induced transition in the mechanical behavior of 3D printed Inconel718 bcc lattices, Scr. Mater. 203 (2021) 114075.

[34] S.Banait, C. Liu, M. Campos, M.S. Pham, M.T. Pérez-Prado, Coupled effect of microstructure and topology on the mechanical behavior of Inconel718 additively manufactured lattices, Mater. Des. 224 (2022) 111294.

[35] R. Wauthle, B. Vranckenc, B. Beynaerts, K. Jorissen, J. Schrooten, J.-P. Kruth, J. Van Humbeeck, Effects of build orientation and heat treatment on the microstructure and mechanical properties of selective laser melted Ti6Al4V lattice structures, Addit. Manuf. 5 (2015) 77-84.

[36] B.B. Babamiri, B. Barnes, A. Soltani-Tehrani, N.Shamsaei, K. Hazeli, Addit. Manuf. 46 (2021) 102143.

[37] Z.C. Cordero, B.E. Knight, C.E. Schuh, Six Decades of the Hall-Petch Effect – A Survey of Grain-Size Strengthening Studies on Pure Metals, Int. Mater. Rev. 61 (2016) 495-512.

[38] E.O. Hall, The Deformation and Ageing of Mild Steel: III Discussion of Results, Proc. Phys. Soc. London B 64 (1951) 747-752.

[39] N.J. Petch, The Cleavage Strength of Polycrystals, J. Iron Steel Inst, 174 (1953) 25-28.

[40] J.S. Koehler, The Nature of Work-Hardening, Phys. Rev. 86 (1952) 52-58.

[41] J. Gil Sevillano, P. van Houtte, E. Aernoudt, Large strain work hardening and textures, Prog. Mater. Sci. 25 (1980) 69-134.

[42] A. Kelly, R.B. Nicholson, Precipitation hardening, Pergamon Press, Oxford, UK, 1963.

[43] B.B. Babamiri, J.R. Mayeur, K. Hazeli, Synchronous involvement of topology and microstructure to design additively manufactured lattice structures, Addit. Manuf. 52 (2022) 102618.

[44] J. Lertthanasarn, C. Liu, M.S. Pham, Synergistic effects of crystalline microstructure, architected mesostructure, and processing defects on the mechanical behaviour of Ti6Al4V meta-crystals, Mater. Sci. Eng. A, 818 (2021) 141436.

[45] I.E. Ramírez-Chavez, D. Anderson, R. Sharma, C. Lee, D.A. Bhate, Classification of aperiodic architected cellular materials, Designs 6 (2022) 63.

[46] W. Wu, R. Xia, G. Qian, Z. Liu, J. Razavi, F. Berto, H. Gao, Mechanostructures: Rational mechanical design, fabrication, performance evaluation, and industrial application of advanced structures, Prog. Mater. Sci. 131 (2023) 101021.

[47] I. Maskery, A. Aremu, L. Parry, R. Wildman, C. Tuck, I. Ashcroft, Effective design and simulation of surface-based lattice structures featuring volume fraction and cell type grading, Mater. Des. 155 (2018) 220–232.

[48] O. Al-Ketan, D.W. Lee, R. Rowshan, R.K.A. Al-Rub, Functionally graded and multimorphology sheet TPMS lattices: design, manufacturing, and mechanical properties, J. Mech. Behav. Biomed. Mater. 102 (2020) 103520.

[49] D. Kang, S. Park, Y. Son, S. Yeon, S.H. Kim, I. Kim, Multi-lattice inner structures for high-strength and light-weight in metal selective laser melting process, Mater. Des. 175 (2019) 107786.

[50] C. Liu, J. Lertthanasarn, M.S. Pham et al. The origin of the boundary strengthening in polycrystal-inspired architected materials, Nature Comms. 12 (2021) 4600.

[51] J. Lertthanasarn, C. Liu, M.S. Pham, Influence of the base material on the mechanical behaviors of polycrystal-like meta-crystals, (2021) J. Micromec. Molec. Phys. 6 (2) (2021) 2150004.

[52] R. Alberdi, R. Dingreville, J. Robbins, T. Walsh, B. C.White, B. Jared, B. L. Boyce, Multi-morphology lattices lead to improved plastic energy absorption, Mater.Des. 194 (2020) 108883.

[53] L. Xiao, X. Xu, W. Song, M. Hu, A multi-cell hybrid approach to elevate the energy absorption of micro-lattice materials, Materials 13 (2020) 4083.

[54] H. Lei, C. Li, X. Zhang, P. Wang, H. Zhou, Z. Zhao, D. Fang, Deformation behavior of heterogeneous multi-morphology lattice core hybrid structures, Addit. Manuf. 37 (2021) 101674.

[55] S. Yin, W. Guo, H. Wang, Y. Huang, R. Yang, Z. Hu, D. Chen, J. Xu, R. O. Ritchie, Strong and tough bioinspired additive-manufactured dual-phase mechanical metamaterial composites, J. Mech. Phys. Solids 149 (2021) 104341.

[56] N. Novak, O. Al-Ketan, M. Borovnisek, L. Krstulovic-Opara, R. Rowshan, M. Vesenjak, Z. Ren, Development of novel hybrid TPMS cellular lattices and their mechanical characterization, J. Mater. Res. Tech. 15 (2021) 1318-1329.

[57] W. Guo, Y. Huang, R.O. Ritchie, S. Yin, Dissipative dual-phase mechanical metamaterial composites via architectural design, Extreme Mech. Lett. 48 (2021) 101442.

[58] B.C. White, A. Garland, R. Alberdi, B.L. Boyce, Interpenetrating lattices with enhanced mechanical functionality, Addit. Manuf. 38 (2021) 101741.

[59] L. Xiao, X. Xu, G. Feng, S. Li, W. Song, Z. Jiang, Compressive performance and energy absorption of additively manufactured metallic hybrid lattice structures, Int. J. Mech. Sci. 219 (2022) 107093.

[60] L. Li, F. Yang, P. Li, W. Wun, L. Wang, A novel hybrid lattice design of nested cell topology with enhanced energy absorption capability, Aerosp. Sci. Tech. 128 (2022) 107776.

[61] H. A. Alqaydi, K. Drishnan, J. Oyebanji, D.W. Lee, S.A. Alneyadi, N. Ghisi, L. Kindleyside, N.T. Aboulkhair, Hybridisation of AlSi10Mg lattice structures for engineered mechanical performance, Addit. Manuf. 57 (2022) 102935.

[62] C. Bhat, A. Kumar, S.C. Lin, J.Y. Jeng, A novel bioinspired architectured material with interlocking designs based on tessellation, Addit. Manuf. 58 (2022) 103052.

[63] C.Y. Wang, C.M. Cepeda-Jimenez, M.T. Pérez-Prado, Dislocation-particle interactions in magnesium alloys, Acta Mater. 194 (2020) 190-206.

[64] X. Liu, T. Wada, A. Suzuki, N. Takata, M. Kobashi, M. Kato, Understanding and suppressing shear band formation in strut-based lattice structures manufactured by laser powder bed fusion, Mater. Des. 199 (2021) 109416.

[65] Y. Y. Choy, C.N. Sun, K. F. Leong, J. Wei, Compressive properties of Ti-6Al-4V lattice structures fabricated by selective laser melting: Design, orientation and density, Addit. Manuf. 16 (2017) 213-224.

[66] C. Qiu, S. Yue, N. J.E. Adkins, M. Ward, H. Hassanin, P. D. Lee, P. J. Withers, M.M. Attallah, Influence of processing conditions on strut structure and compressive properties of cellular lattice structures fabricated by selective laser melting, Mater. Sci. Eng. A 628 (2015) 188-197.

[67] I. Maskery, N.T. Aboulkhair, A.O. Aremu, C.J. Tuck, I.A. Ashcroft, R.D. Wildman, R.J.M. Hague, A mechanical property evaluation of graded density Al-Si10-Mg lattice structures manufactured by selective laser melting, Mater. Sci. Eng. A 670 (2016) 264-274.

[68] M.S. Pham, C. Liu, I. Todd, J. J. Lertthanasarn, Damage tolerance architected materials inspired by crystal microstructure, Nature 565 (2019) 305-311.

[69] A. Panesar, M. Abdi, D. Hickman, I. Ashcroft, Strategies for functionally graded lattice structures derived using topology optimisation for Additive Manufacturing, Addit. Manuf. 19 (2018) 81-94.

[70] M.J. Mirzaali, A. Caracciolo, H. Pahlavani, S. Janbaz, L. Vergani, A.A. Zadpoor, Multimaterial 3d printed mechanical metamaterials: rational design of elastic properties through spatial distribution of hard and soft phases, Appl. Phys. Lett. 113 (24) (2018) 241903.

[71] M. J. Prajapati, A. Kumar, S.-C. Lin, J.-Y. Jeng, Multi-material additive manufacturing with lightweight closed-cell foam-filled lattice structures for enhanced mechanical and functional properties, Addit. Manuf. 54 (2022) 102766.

CHAPTER 7

Dynamic strain aging in Inconel 718 additively manufactured lattice structures

7.1. Background and design of the study

Strut-based lattice structures are a class of architected metamaterials that find ubiquitous applications in light-weighting of structural components, owing to their outstanding specific mechanical properties [1-3]. They consist of a three-dimensional periodic arrangement of unit cells; whose structure has a critical influence on the properties of the entire part. Lattice fabrication has been greatly facilitated by the availability of additive manufacturing (AM) techniques and, in particular, of laser powder bed fusion (LPBF) [4-6], as it allows to produce components with an unprecedented freedom of design and high dimensional accuracy.

The critical influence of topology on the mechanical behaviour of lattices has now been clearly established [7] and several optimization approaches, including hybridization [8] and functional grading [9-11], have been put in place in order to enhance the strength and energy absorption capacity [12-15]. A few recent studies have also demonstrated that the microstructure of the base material has a significant effect on the mechanical behaviour of lattice metamaterials fabricated by LPBF [16-24]. Wauthle et al. [16] and Lertthanasarn et al. [17] showed that post-processing stress relief heat treatments led to stronger but more brittle Ti6Al4V (wt.%) lattices in comparison with the as-built condition, while hot isostatic pressing reduced the strength but enhanced the ductility. Maskery et al. [18] and Köhnen et al. [19] reported softening of Al-10Mg-Si and 1.4404 steel lattices, respectively, due to post-processing heat treatments which led to microstructural coarsening. Hazeli et al. [20], Banait et al. [21,22], and Babamiri et al. [23] described the coupled effect of microstructure and topology in LPBFed Inconel 718 lattice structures. Further efforts are required in order to investigate the influence of the vast space of micro- and nano-scale microstructural parameters on the mechanical behaviour of architected metamaterials.

Dynamic strain aging (DSA) is an atomic scale phenomenon [24] that takes place during deformation within selected temperature and strain rate intervals in many metals and alloys, including Al, Mg, Cu, Fe, and Ni-base alloys [25-29]. DSA has been commonly attributed to the trapping by solute atmospheres of moving dislocations that are temporarily arrested at obstacles. This phenomenon has well known effects in the mechanical behaviour of bulk metals, including a negative strain rate sensitivity associated to pronounced strain localization, and increased strength levels [30]. Evidence for DSA is found in the macroscopic stress-strain curves, which become populated with different types of serrations, originated by the cyclic stress increase due to dislocation trapping, and the subsequent softening following dislocation release [31]. The occurrence of DSA might be detrimental to the mechanical behaviour, as it reportedly leads to a decrease in ductility and formability, or to a poorer fatigue life, among others. To date, the manifestation of DSA in additively manufactured architected metamaterials has not been studied.

The aim of this work is to investigate the potential manifestations of DSA on the mechanical behavior of Inconel 718 body centered cubic (BCC) and face centered cubic (FCC) strut-based lattices manufactured via LPBF. With that goal, gas atomized powders with spherical morphology and minimal internal porosity were purchased from Oerlikon and were utilized as feedstock for LPBF processing. A detailed description of the powder composition, the particle size distribution, the flowability, and the apparent and tap densities, is provided in Chapter 5, section 5.2. A Renishaw AM 400 LPBF system was used to fabricate BCC (relative density=0.14) and FCC (relative density=0.2) lattice structures with global dimensions of 10x10x15 mm^3, with 2.5x2.5x2.5 mm^3 unit cells, and with strut diameters of 0.4 mm. The process parameters, which were optimized earlier [22] to yield a density of 99.6%, include a laser power (P) of 100 W, a scan speed of 875 mm/s, a hatch distance of 90 □ m, and a layer thickness of 30 μm. The scanning strategy consisted of bidirectional scans with a rotation of 67° between layers. Cylindrical dog-bone tensile specimens with a gauge diameter equivalent to that of the lattice struts (0.4 mm) and a gauge length of 10 mm were also additively manufactured using the same optimized set of LPBF process parameters. The microstructure of the as-built BCC and FCC lattices, as well as that of the gauge length of the tensile specimens consists mainly of a polycrystalline, randomly oriented, supersaturated solid solution with an average grain size of 10 μm. A detailed description of this microstructure, which was thoroughly characterized earlier by electron backscatter diffraction (EBSD) and transmission electron microscopy (TEM), can be found in [21,22].

The single-strut specimens were tested uniaxially in tension at 25, 300, 450 and 600 °C at constant crosshead speed using an initial strain rate of 10^{-3} s^{-1}. Mechanical testing was carried out in an Instron 3384 electromechanical testing machine using a load cell of 500 N. The LPBF manufactured lattices were tested uniaxially in compression at 25, 300, 450 and 600 °C at constant crosshead speed using an initial strain rate of 10^{-3} s^{-1} with the aim of detecting the influence of lattice topology on the potential manifestations of DSA. The strain rate sensitivity ($m=\left(\frac{\partial\sigma}{\partial\dot{\epsilon}}\right)$) of the BCC and FCC lattices at the mentioned testing temperatures was measured from strain rate jump tests performed at strain rates of $1\text{x}10^{-5}$, $5\text{x}10^{-5}$, $1\text{x}10^{-4}$, $5\text{x}10^{-4}$, $1\text{x}10^{-3}$, $5\text{x}10^{-3}$, and $5\text{x}10^{-2}$ s^{-1}. Mechanical testing was carried out in an Instron 3384 electromechanical testing machine furnished with a load cell of 30 kN.

7.2. Results

Figure 7.1 illustrates the tensile engineering stress-strain curves corresponding to the single-strut Inconel 718 specimens deformed using an initial strain rate of 10^{-3} s^{-1} at all the investigated temperatures. The flow stress at that strain remains basically invariant with increasing temperature. In particular, it amounts to 648 MPa at 25°C, to 610 MPa at 300°C, to 590 MPa at 450°C, and to 610 MPa at 600°C.

A magnified view of the curves at a strain of 10%, included as an inset, evidences that serrated plastic flow, a manifestation of DSA, is present at T ≥ 300 °C. In particular, at 300 °C, serrations are mainly of type A or locking serrations [32]. They are periodic oscillations characterized by a steep rise followed by a drop to below the general stress level of the curve. In general, they are indicative of the repeated formation of deformation bands at one extreme of the tensile coupon, which then move towards the opposite side of the gauge length. They are generally observed in the low temperature or high strain rate (or, equivalently, high stress) region of the dynamic strain aging regime. At 450 °C serrated flow is dominated by high frequency oscillations of much smaller amplitude, that are basically symmetric with respect to the general stress level of the curve. Serrations with this morphology are usually classified as type B, and they are usually reported at higher temperatures or lower strain rates (in comparison with type A) within the DSA regime [32]. Finally, at 600 °C, periodic stress drops below the general stress level of the flow curve take place. These oscillations are generally named type C and, as in the present study, are often reported at higher temperatures, or at lower strain rates, (or, equivalently, at lower stress level) than type A and type B [32].

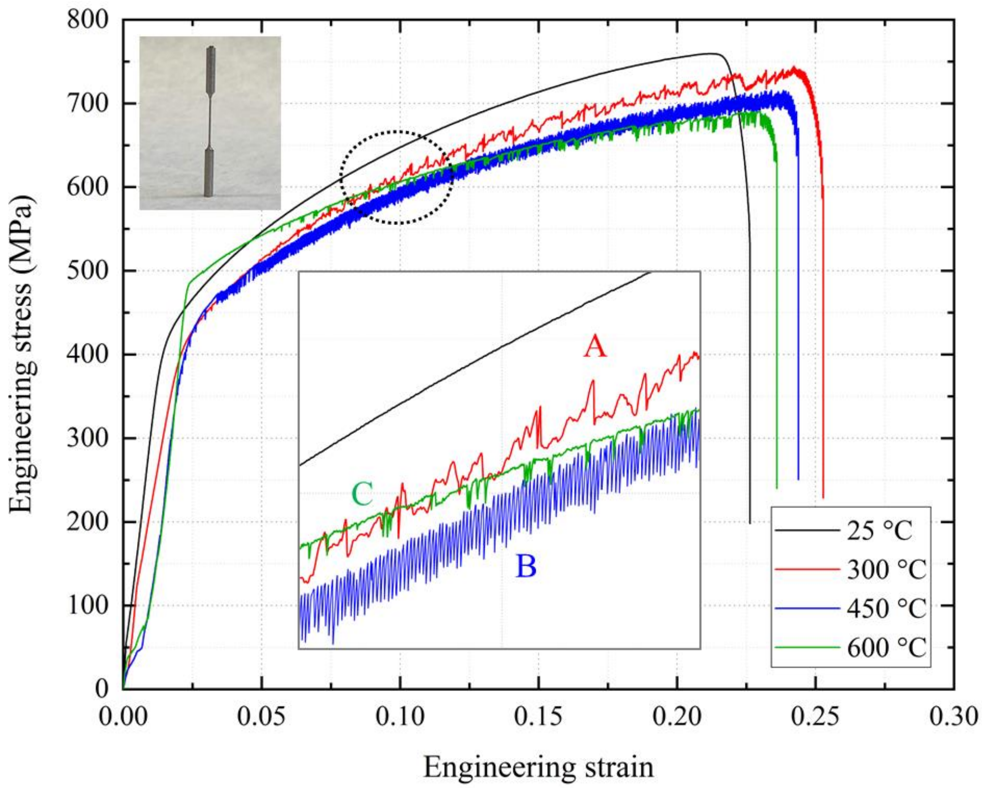

Figure 7.1. Tensile engineering stress-strain curves corresponding to single-strut Inconel 718 specimens deformed using an initial strain rate of 10^{-3} s^{-1} at all the investigated temperatures. The insets show a magnified view of the serrations, indicating the dominant type.

Serrated flow has been observed earlier in Ni-based superalloys [e.g. 33,34], including Inconel 718 [35-42], under similar testing conditions to those of the present study and it has been attributed mostly to the interaction of C atmospheres with dislocations at lower temperatures [37] and to diffusion of substitutional Nb [36,37,42] and Mo [37,38] atoms at higher temperatures. For example, Chen et al. [35] reported the appearance of serrations in a cast and cold rolled Inconel 718 at 300°C and 425°C and at strain rates ranging from 10^{-5} to 10^{-2} s^{-1}. Nalawade et al. [36] observed serrated flow in an Inconel 718 alloy processed by casting and hot rolling, and subsequently solutionized, at temperatures ranging from 300°C to 700°C and at a strain rate of $6.5x10^{-5}$ s^{-1}. The same authors reported that serrations disappeared if an aging treatment was applied to the solutionized superalloy due to the depletion of Nb atoms from the lattice. Max et al. [37] observed serrated flow in an underaged rolled thin Inconel 718 strip at a wide range of testing temperatures (300°C to 650°C) and strain rates ($5x10^{-5}$ to $3.2x10^{-2}$ s^{-1}).

Serrated stress-strain curves have also been reported for additively manufactured Inconel 718 alloys. For example, Yuan et al. [40] observed serrated flow during compression at 630 °C and 10^{-3} s^{-1} of an Inconel 718 superalloy manufactured by laser metal deposition. Vikram et al. [41] reported serrated flow during compression at 550, 600, and 650 °C and 10^{-3} s^{-1} in an as-LPBF Inconel 718. Serrations were, again, observed to disappear following a post-processing aging treatment due to solute depletion. Finally, Galera-Rueda et al. [42] observed serrations during tensile testing at 550°C and 10^{-3} s^{-1} of an Inconel 718 alloy processed by LPBF with and without ZrH_2 microparticle additions, both in the as-built and the underaged condition. In the current study, since the microstructure of the LPBF processed samples is mainly a solid solution [21, 22], the observation of serrations during compression of the as-built single strut specimens at T ≥ 300 °C (Figure 7.1) agrees well with the earlier studies described above.

Figure 7.2 illustrates the engineering stress-strain curves corresponding to the BCC (Figure 7.2. (a)) and FCC (Figure 7.2. (b)) as-built lattices compressed at 25, 300, 450 and 600 °C with an initial strain rate of 10^{-3} s^{-1}. At all temperatures, the BCC lattices exhibit a bending-dominated behavior, in which yielding is followed by a stress plateau that ends once densification starts. This is expected, as the Maxwell factor for this topology is negative (M=-13) *and* the microstructure is mostly a solid solution [21, 22]. The yield strength values corresponding to the different testing temperatures are, respectively, 42.5 MPa at 25°C, 33 MPa at 300°C, 33 MPa at 450°C, and 32.5 MPa at 600°C. Serrated flow in the form of periodic type C serrations (see inset of Figure 7.2. (a)) is observed only at T=450°C. These results confirm the manifestation of an atomic scale phenomenon such as dynamic strain aging, in an additively manufactured metamaterial. The fact that type C serrations become apparent only at 450°C, and that the observed serrations are not type B as in the single-strut specimens, may be attributed to the much lower stress level that is present in the lattice, where the BCC topology favours strut bending. In the stress-strain curves of the FCC lattices (Figure 7.2. (b)), irrespective of the testing temperature, a stress peak is followed by moderate hardening until the onset of densification. This mechanical behavior can be considered a hybrid between bending-dominated and stretch-dominated responses [5,43].

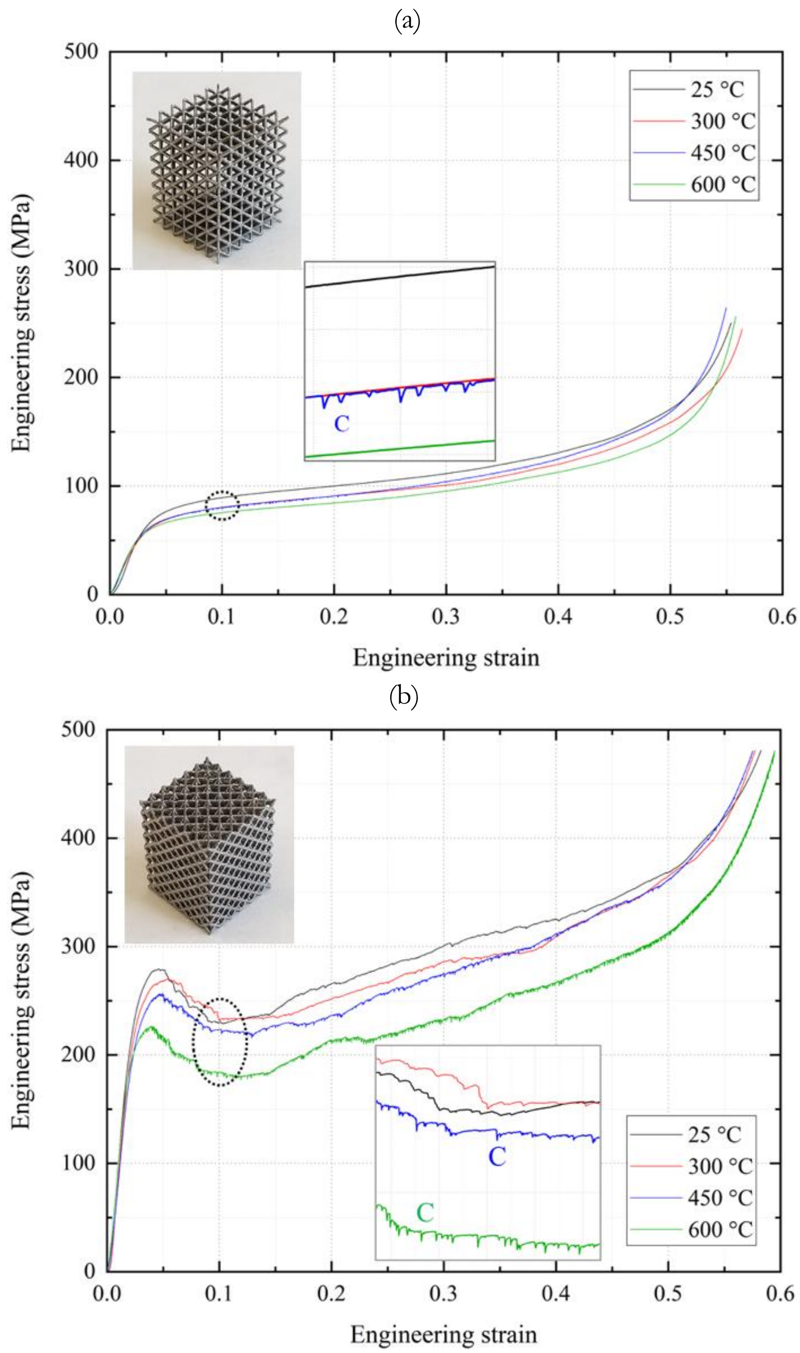

Figure 7.2. Specific engineering stress-strain curves depicting the presence of serrated flow during compression of the (a) BCC and (b) FCC as-built lattice structures at various temperatures and at an initial strain rate of 10^{-3} s^{-1}. The insets show a magnified view of the serrations at a strain of 0.1.

Given that the FCC and the BCC lattices were processed by LPBF using the same optimized parameters, and that therefore both have the same material microstructure, and since the Maxwell factor for the FCC architecture is slightly higher (M=-12), it seems reasonable that the mechanical response of the FCC lattice deviates slightly from a pure bending-dominated response. The yield strength values corresponding to the different testing temperatures are, respectively, 157 MPa at 25°C, 154 MPa at 300°C, 139 MPa at 450°C, and 135 MPa at 600°C. The stress level is, overall, higher in the FCC than in the BCC lattices at all the temperatures investigated. Serrated flow in the form of periodic type C serrations (see inset of Figure 7.2. (b)) is observed at 450°C and 600°C. A close look at the inset of Figure 7.2. (b) reveals that the curves corresponding to testing temperatures of 25°C and 300°C also exhibit some oscillations with relatively irregular shape. In order to rule these oscillations out as manifestations of dynamic strain aging, we have calculated the variation of the work hardening rate with strain for all tests performed in the two investigated architectures.

7.3. Discussion

Figure 7.3 illustrates the work hardening rate versus strain curves corresponding to the BCC (Figure 7.3. (a)) and FCC (Figure 7.3. (b)) lattice structures. In the BCC structure it can be clearly seen that the presence of type C serrations at 450°C gives rise to frequent variations of the work hardening rate above and below the zero level. In the FCC structure, similar oscillations of the work hardening rate can be seen only at 450°C and 600°C. On the contrary, at lower temperatures, the instantaneous work hardening rate oscillates only between the zero level and negative values. Thus, at these temperatures, the observed stress oscillations may be attributed to local softening due to strain localization as the shear band propagates across the lattice [22].

This analysis confirms that type C serrations are observed in the FCC lattice only during compression at 450°C and 600°C. The absence of serrations at 300°C, a temperature at which they were present in the single-strut specimens, is attributed to the comparatively lower stress levels in the FCC lattice.

The above results suggest that the manifestation of DSA in the form of serrated flow is topology-dependent, as serrations are observed at different temperature ranges in BCC and FCC LPBF processed lattices that share the same material microstructure.

(a)

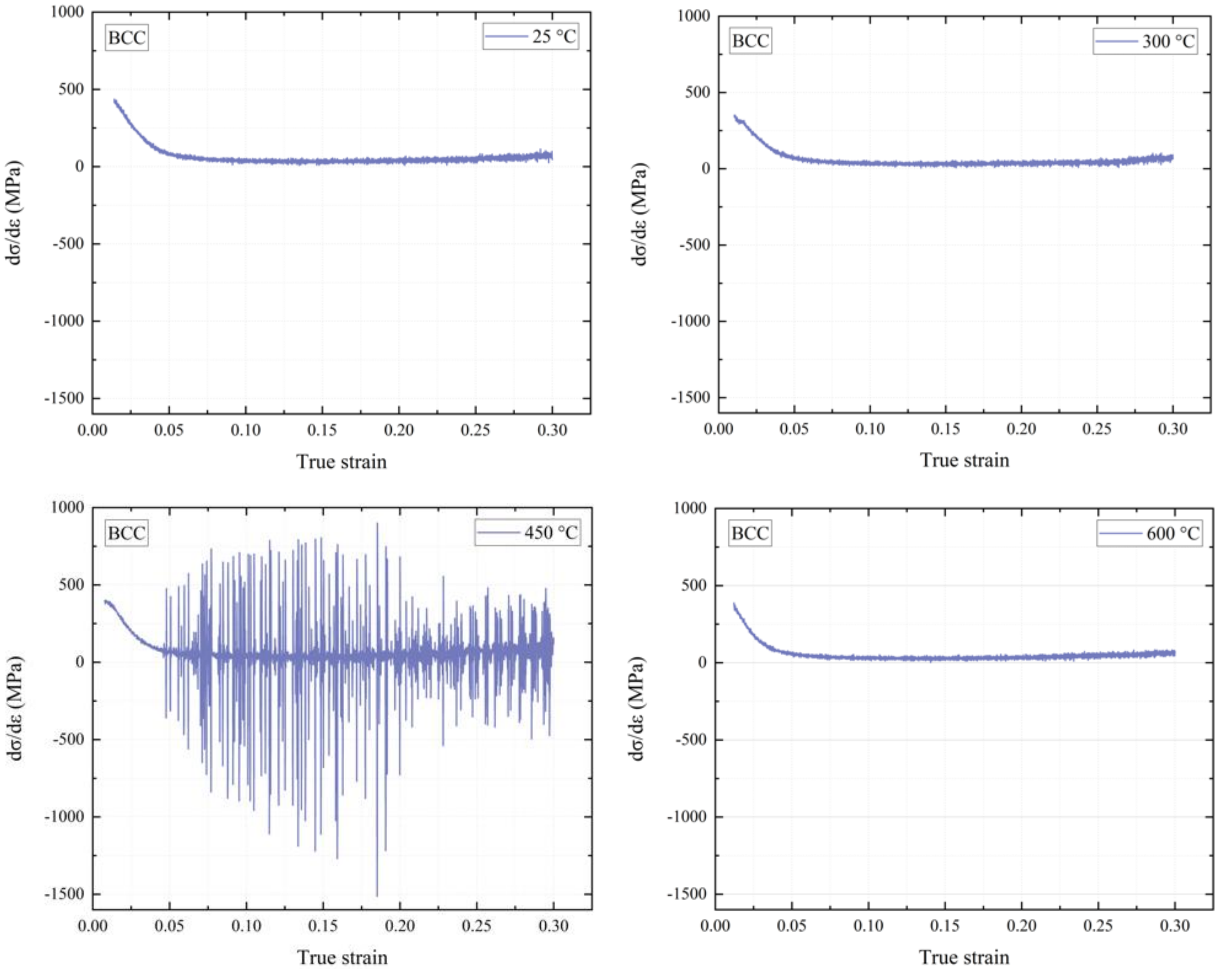
BCC
25 °C
300 °C
450 °C
600 °C
dσ/dε (MPa)
True strain

(b)

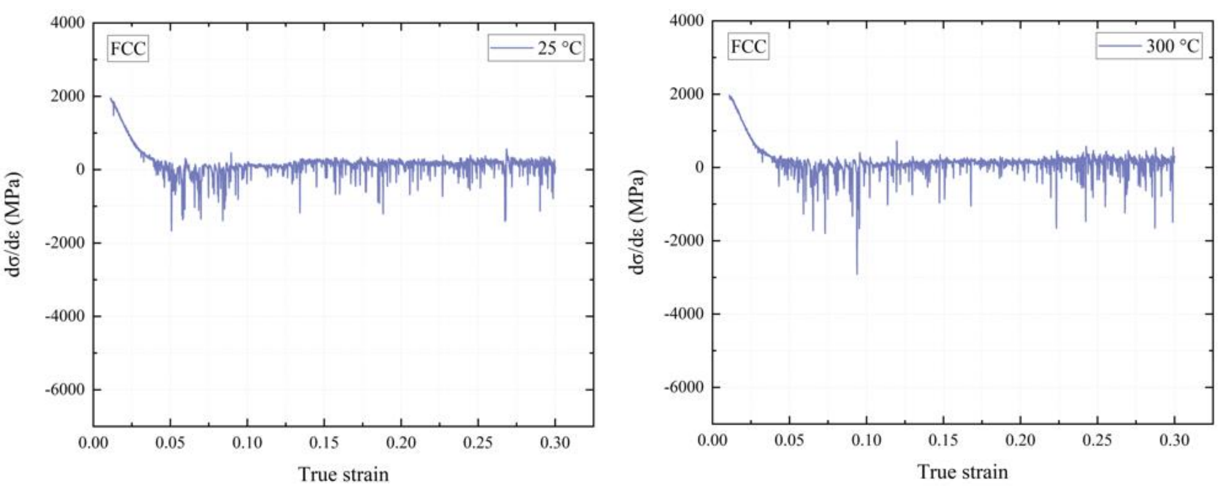
FCC
25 °C
300 °C
dσ/dε (MPa)
True strain

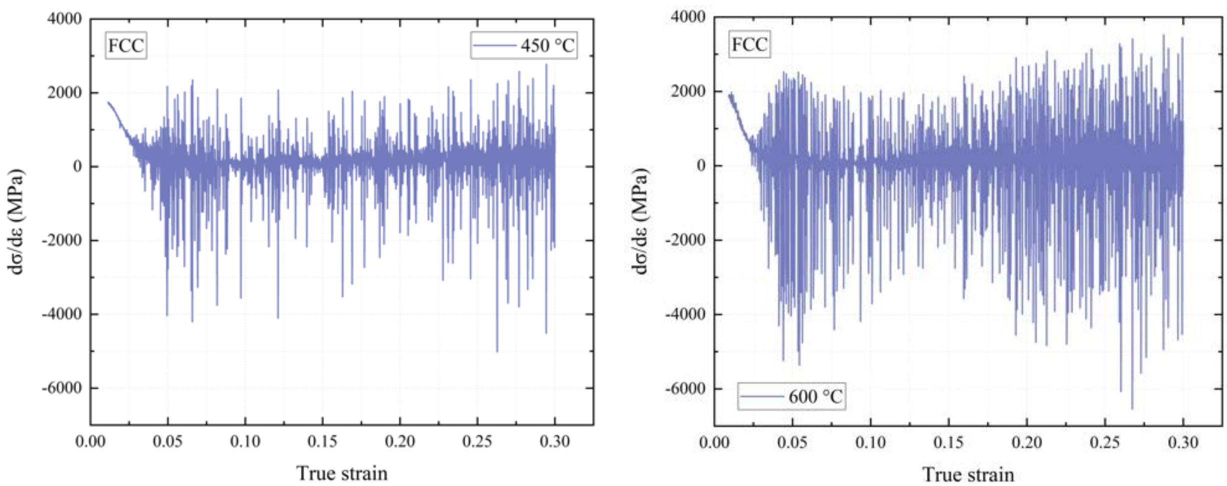

Figure 7.3. Variation of the work hardening rate with respect to strain in the (a) BCC and (b) FCC as-built lattice structures at various temperatures.

In particular, it seems that the higher stress levels that are present during compression of the FCC lattice give rise to serrated flow at a wider range of testing conditions. In order to further confirm this observation, compressive strain rate jump tests were performed at all the temperatures investigated in the two LPBF processed architectures in order to measure the corresponding strain rate sensitivity values. The corresponding stress-strain curves are plotted in Supplementary Figure S1, Annex F, and the values of the sequence of strain rates used are listed in Supplementary Table S1, Annex F. Figure 7.4 illustrates the variation of m with strain rate for BCC (Figure 7.4. (a)) and FCC (Figure 7.4. (c)) lattices. It is well known that DSA leads to negative strain rate sensitivities, and thus analyzing this parameter over a wide range of temperatures and strain rates is deemed suitable to confirm the dependence of topology of DSA.

Several observations can be inferred from Figure 7.4. First, at room temperature m is positive for the two architectures at all the investigated strain rates. This is consistent with the fact that, as also shown in Figure 7.1, the LPBF processed Inconel 718 does not exhibit DSA at this low temperature. Second, at 300°C and 450°C, m is negative in the FCC case for all the strain rates investigated, while in the BCC lattice it becomes positive at $5\text{x}10^{-2}$ s^{-1}. Also, the FCC values are always higher, in absolute value, than the values measured in the BCC architecture. Finally, at 600°C, in the BCC case, m becomes negative only at strain rates higher than 10^{-3} s^{-1}, while in the FCC case it is negative at all strain rates higher than $5\text{x}10^{-5}$ s^{-1}. This analysis, thus, confirms, that the higher stress levels present during compression of the FCC LPBF processed lattice result in a widening of the testing conditions under which DSA takes place.

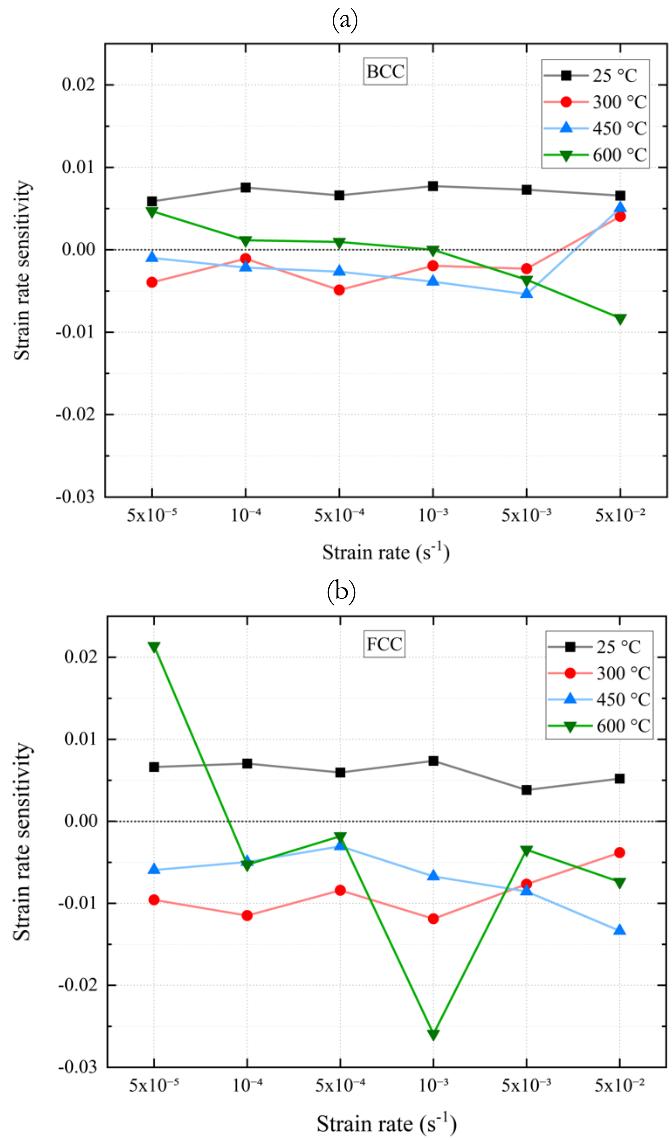

Figure 7.4. Strain rate sensitivity (m) of (a) BCC and (b) FCC as-built lattice structures at various temperatures and strain rates. The values were measured from strain rate jump tests.

7.4. Remarks

In summary, this research demonstrates that atomic scale phenomena such as DSA may manifest at the metamaterial level and that their occurrence is highly dependent on the lattice architecture. Since it is well known that DSA may significantly impact the macroscopic mechanical behaviour, this work highlights the importance of analysing its incidence in additively manufactured lattice structures that are envisioned to have a structural function.

Bibliography

[1] J. U. Surjadi, L. Gao, H. Du, X. Li, X. Xiong, N.X. Fang and Y. Lu, Mechanical metamaterials and their engineering applications, Adv. Eng. Mater. 21 (2019) 1800864.

[2] M. Benedetti, A. du Plessis, R.O. Ritchie, M. Dallago, S.M.J. Razavi, F.Berto, Architected cellular materials: A review on their mechanical properties towards fatigue-tolerant design and fabrication, Mater. Sci. Eng. R 144 (2021) 100606.

[3] X. Zheng, H. Lee, T.H. Weisgraber, M. Shusteff, J. DeOtte, E.B. Duoss, J.D. Kuntz, M.M. Biener, Q. Ge, J. Jackson, N.X. Fang, C.M. Spadaccini, Ultralight, ultrastiff mechanical metamaterials, Science 344 (2014) 1373–1377.

[4] Z. Alomar, F. Concli, A review of the selective laser melting of lattice structures and their numerical models, Adv. Eng. Mater. (2020) 2000611 (1-17).

[5] T. Maconachie, M. Leary, B. Lozanovski, X. Zhang, M. Qian, O. Faruque, M. Brandt, SLM lattice structures: Properties, performance, applications and challenges, Mater. Des. 183 (2019) 108137.

[6] L.Y. Chen, S.X. Liang, Y. Liu, L.C. Zhang, Additive manufacturing of metallic lattice structures: Unconstrained design, accurate fabrication, fascinated performances, and challenges, Mater. Sci. Eng. R 146 (2021) 100648.

[7] O. Al-Ketan, R. Rowshan, R. K. A. Al-Rub, Topology-mechanical property relationship of 3D printed strut, skeletal, and sheet based periodic metallic cellular materials, Addit. Manuf. 19 (2018) 167-183.

[8] W. Wu, R. Xia, G. Qian, Z. Liu, J. Razavi, F. Berto, H. Gao, Mechanostructures: Rational mechanical design, fabrication, performance evaluation, and industrial application of advanced structures, Prog. Mater. Sci. 131 (2023) 101021.

[9] I. Maskery, A.O. Aremu, L. Parry, R.D. Wildman, C.J. Tuck, I.A. Ashcroft, Effective design and simulation of surface-based lattice structures featuring volume fraction and cell type grading, Mater. Des. 155 (2018) 220-232.

[10] O. Al-Ketan, D.W. Lee, R. Rowshan, R.K.A. Al-Rub, Functionally graded and multimorphology sheet TPMS lattices: design, manufacturing, and mechanical properties, J. Mech. Behav. Biomed. Mater. 102 (2020) 103520.

[11] F. Veloso, J. Gomes-Fonseca, P. Morais, J. Correia-Pinto, A. C.M. Pinho, J. L. Vilaça, Overview of methods and software for the design of functionally graded lattice structures, Adv. Eng. Mater. 24(11) (2022) 2200483.

[12] R. Alberdi, R. Dingreville, J. Robbins, T. Walsh, B. C. White, B. Jared, B. L. Boyce, Multi-morphology lattices lead to improved plastic energy absorption, Mater. Des. 194 (2020) 108883.

[13] L. Xiao, X. Xu, G. Feng, S. Li, W. Song, Z. Jiang, Compressive performance and energy absorption of additively manufactured metallic hybrid lattice structures, Int. J. Mech. Sci. 219 (2022) 107093.

[14] L. Li, F. Yang, P. Li, W. Wun, L. Wang, A novel hybrid lattice design of nested cell topology with enhanced energy absorption capability, Aerosp. Sci. Tech. 128 (2022) 107776.

[15] H. A. Alqaydi, K. Drishnan, J. Oyebanji, D.W. Lee, S.A. Alneyadi, N. Ghisi, L. Kindleyside, N.T. Aboulkhair, Hybridisation of AlSi10Mg lattice structures for engineered mechanical performance, Addit. Manuf. 57 (2022) 102935.

[16] R. Wauthle, B. Vranckenc, B. Beynaerts, K. Jorissen, J. Schrooten, J.-P. Kruth, J. Van Humbeeck, Effects of build orientation and heat treatment on the microstructure and mechanical properties of selective laser melted Ti6Al4V lattice structures, Addit. Manuf. 5 (2015) 77-84.

[17] J. Lertthanasarn, C. Liu, M.S. Pham, Synergistic effects of crystalline microstructure, architected mesostructure, and processing defects on the mechanical behaviour of Ti6Al4V meta-crystals, Mater. Sci. Eng. A, 818 (2021) 141436.

[18] I. Maskery, N.T. Aboulkhair, A.O. Aremu, C.J. Tuck, I.A. Ashcroft, Compressive failure modes and energy absorption in additively manufactured double gyroid lattices, Addit. Manuf. 16 (2017) 24-29.

[19] P. Köhnen, C. Haase, J. Bültmanna, S. Ziegler, J. H. Schleifenbaum, W. Bleck, Mechanical properties and deformation behavior of additively manufactured lattice structures of stainless steel, Mater. Des. 145 (2018) 205-217.

[20] K. Hazeli, B. B. Babamiri, J. Indeck, A. Minor, H. Askari, Microstructure-topology relationship effects on the quasi-static and dynamic behavior of additively manufactured lattice structures, Mater. Des. 176 (2019) 107826.

[21] S.Banait, X. Jin, M. Campos, M.T. Pérez-Prado, Precipitation-induced transition in the mechanical behavior of 3D printed Inconel 718 bcc lattices, Scripta Mater. 203 (2021) 114075.

[22] S.Banait, C. Liu, M. Campos, M.S. Pham, M.T. Pérez-Prado, Coupled effect of microstructure and topology on the mechanical behavior of Inconel 718 additively manufactured lattices, Mater. Des. 224 (2022) 111294.

[23] B.B. Babamiri, J.R. Mayeur, K. Hazeli, Synchronous involvement of topology and microstructure to design additively manufactured lattice structures, Addit. Manuf. 52 (2022) 102618.

[24] H. Aboulfadl, J. Deges, P. Choi and D. Raabe, Dynamic strain aging studied at the atomic scale, Acta Mater. 86 (2015) 34-42.

[25] A. van den Beukel, Theory of the effect of dynamic strain aging on mechanical properties, Phys. Stat. Sol. 30 (1975) 197-206.

[26] A.H. Cottrell, B.A. Bilby, Dislocation theory of yielding and strain ageing of iron, Proc. Phys. Soc. A 62 (1945) 49-62.

[27] W.A. Curtin, D.L. Olmsted, L.G. Hector, A predictive mechanism for dynamic strain ageing in aluminium–magnesium alloys, Nature Mater. 5(11) (2006) 875–880.

[28] P. Hidalgo-Manrique, V. Herrera-Solaz, J. Segurado, J. Llorca, F. Gálvez, O.A. Ruano, S.B. Yi, M.T. Pérez-Prado, Origin of the reversed yield asymmetry in Mg-rare earth alloys at high temperature, Acta Mater. 92 (2015) 265-277.

[29] N. Stanford, G. Sha, J.H. Xia, S.P. Ringer, M.R. Barnett, Solute segregation and texture modification in an extruded magnesium alloy containing gadolinium, Scripta Mater. 65 (2011) 919-921.

[30] J. M. Robinson, M. P. Shaw, Microstructural and mechanical influences on dynamic strain aging phenomena, Int. Mater. Rev. 39(3) (1994) 113-122.

[31] Y. Zhao, L. Dezerald, M. Pozuelo, Y. Zhou, J. Marian, Simulating the mechanisms of serrated flow in interstitial alloys with atomic resolution over diffusive timescales, Nat. Commun. 11 (2020) 1227.

[32] P. Rodríguez, Serrated plastic flow, Bull. Mater. Sci. 6 (1984) 653-663.

[33] M. Valsan, D.H. Sastry, K.B. S. Rao, S.L. Mannan, Effect of strain rate on the high-temperature low-cycle fatigue properties of a nimonic PE-16 superalloy, Metall. Mater. Trans. A 25A (1994) 159–171.

[34] C.Y. Cui, C.G. Tian, Y.Z. Zhou, T. Jin, X.F. Sun, Dynamic strain aging in Ni based superalloys with different stacking fault energy, Superalloys 2012: 12th International Symposium on Superalloys, Ed. by E.S. Huron et al., The Minerals, Metals & Materials Society (TMS), 2012.

[35] W. Chen, M. Chaturvedi, On the mechanism of serrated deformation in aged Inconel 718, Mater. Sci. Eng. A 229 (1997) 163-168.

[36] S.A. Nalawade, M. Sundararaman, R. Kishore, J.G. Shah, The influence of aging on the serrated yielding phenomena in a nickel-base superalloy, Scripta Mater. 59 (2008) 991-994.

[37] B. Max, B. Viguier, E. Andrieu, and J.M. Cloue, A Re-examination of the Portevin-Le Chatelier Effect in Alloy 718 in Connection with Oxidation-Assisted Intergranular Cracking, Metall. Mater. Trans. A 45A (2014) 5431–41.

[38] B. Max, J. San Juan, M.L. Nó, J.M. Cloue, B. Viguier, E. Andrieu, Atomic species associated with the Portevin–Le Chatelier effect in superalloy 718 studied by mechanical spectroscopy, Metall. Mater. Trans. 49 (2018) 2057–2068.

[39] M.L. Weaver, C.S. Hale, Effects of precipitation on serrated yielding in Inconel 718, in: E.A. Loria (Ed.), Int. Symp. Superalloys 718, vol. 625, Var. Deriv., Pittsburgh, 2001, pp. 421–432.

[40] K. Yuan, W. Guo, P. Li, J. Wang, Y. Su, X. Lin, Y. Li, Influence of process parameters and heat treatments on the microstructures and dynamic mechanical behaviors of Inconel 718 superalloy manufactured by laser metal deposition, Mater. Sci. Eng. A 721 (2020) 215-225.

[41] R.J. Vikram, A. Singh, S. Suwas, Effect of heat treatment on the modification of microstructure of selective laser melted (SLM) IN718 and its consequences on mechanical behavior, J. Mater. Res. 35 (2020) 1949–1962.

[42] C. Galera-Rueda, E. Nieto-Valeiras, M. Gardon, M.T. Pérez.Prado, J. Llorca, Effect of ZrH_2 particles on the microstructure and mechanical properties of IN718 manufactured by selective laser melting, Mater. Sci. Eng. A, 813 (2021) 141123.

[43] V.S. Deshpande, M.F. Ashby, N.A. Fleck, Foam topology bending versus stretch dominated architectures, Acta Mater. 49 (2001) 1035-1040.

CHAPTER 8

Conclusions

Strut-based lattice structures are truly ubiquitous owing to their properties such as light-weighting, excellent strength to weight ratio, high specific stiffness, auxetic behaviour etc. The innate ability of additive manufacturing to offer form freedom has facilitated the fabrication of such complex and intricate structures. However, some fundamental perspectives still remain unexplored even when cellular materials and in turn, lattice structures have been researched quite widely. One of the unmapped ideas was the effect of microstructure on the mechanical behaviour of the lattice structures. Ample research has been done investigating different topologies of lattice and relating their effect on the mechanical response of the lattice structures. Numerous studies have examined the manufacturability of the lattice structures with a wide variety of base materials via additive manufacturing, especially with laser powder bed fusion, and have attempted to fabricate lattices with the highest achievable density by process parameter optimization.

The dissertation work focuses on investigating the effect of microstructure on basic lattice topologies like BCC, FCC and HCP. The work also explores the route of hybridization to reduce the plastic flow instability in the mechanical response while maintaining a high lattice strength. Lastly, the work investigates the manifestation of dynamic strain aging in lattice structures, reported for the first time in the literature. Major conclusions drawn from the research work are summarized below.

8.1. Precipitation induced transition in the mechanical behaviour of additively manufactured Inconel 718 BCC lattice structures

This research shows that the high cooling rates associated with LPBF manufacturing of BCC Inconel 718 lattice structures with fine struts allow to generate supersaturated solid solutions with high compliance and bending-dominated behaviour that might be converted into stiffer, stronger structures exhibiting a stretch dominated behaviour by precipitation during post-processing solution plus aging treatments. This work proves that careful microstructural design provides a useful tool to tailor the mechanical behaviour of strut-based lattice structures. It is expected that the coupling between microstructure and lattice topology might give rise to unprecedented mechanical behaviour in LPBF fabricated strut-based lattice structures.

8.2. Coupled effect of microstructure and topology on the mechanical behaviour of Inconel 718 additively manufactured lattice structures

The aim of this work is to investigate the coupled effect of microstructure and topology on the mechanical behaviour of Inconel 718 lattices fabricated by LPBF. With that purpose, lattices with FCC, FCCXYZ, HCP0 (c-axis parallel to BD), HCP90 (c-axis at 90° to BD), HCP45 (c-axis at 45° to BD) and HCP45B (c-axis at 90° to BD and with borders) topologies were manufactured by LPBF and their mechanical behaviour in the as-built and peak-aged conditions was tested in compression at room and high temperature. The following conclusions can be drawn from the study:

- The microstructure of as-built lattices is a polycrystal formed by randomly oriented grains, slightly elongated along BD. The average grain length and width were, respectively, 16 ± 28 μm and 10 ± 14 μm. The grain boundary misorientation distribution resembled that of a random distribution of grains (Mackenzie), with an additional strong peak at misorientation angles lower than 5°, that is characteristic of LPBF-processed alloys. Grain interiors are populated by cells, and cell interiors are mostly a solid solution. Nb segregates to cell boundaries. Peak-aging of the lattices following LPBF processing gives rise to a precipitation, while the remaining microstructural features, including grain size, shape, and orientation, and grain boundary network, remained almost unchanged. Segregation of Mo and Ti to cell boundaries is observed following the heat treatment.

- For all the topologies investigated, precipitation leads to significant strengthening of the lattice structures at room and high temperature; in turn, increasing the test temperature resulted in lattice softening in both the as-built and peak-aged conditions. These variations of the lattice strength with precipitation and with the test temperature can be directly correlated to the variation of the strength of the base material in similar microstructure and testing conditions, which is measured using dedicated printed specimens with gauge length with dimensions identical to those of single struts.

- In the peak-aged lattices, which exhibit a stretch-dominated response irrespective of topology, increasing the test temperature results in a reduction in the width of the stress serrations. This can be ascribed to the decrease in strength and ductility of the peak-aged Inconel718 superalloy with increasing temperature.

- In the FCC, FCCXYZ, HCP0, and HCP90 lattices, precipitation induced a transition from bending-dominated to stretch-dominated mechanical response. This may be attributed, in turn, to a transition in the dominant strut deformation mechanism, which is governed by plastic hinges in the as-built condition and by elastic buckling in the peak-aged condition.

- This study proves the influential role of microstructure in the behaviour of additively manufactured metallic lattices and, as such, it highlights an exciting avenue of research focused on combining structure design and microstructure engineering.

8.3. Effect of microstructure on the effectiveness of hybridization in architected metallic materials

The aim of this work is to investigate the coupled effect of microstructure and hybridization on the mechanical behavior of additively manufactured Inconel 718 strut-based lattices. With that purpose, two microstructures, namely the as-built solid solution and a peak aged condition, are coupled with three hybrid architectures formed by alternating FCC (matrix) and OT (reinforcement) domains containing 1, 8, and 64 unit cells, respectively, all with a constant 50% reinforcement volume fraction. The room temperature mechanical behaviours of all six microstructure-architecture combinations are investigated with the aim of deriving guidelines for the design of lattices endowed with high strength and mechanical stability. The main conclusions of this study are the following:

- In the as-built condition, the mechanical behavior of the hybrid lattices was similar to that of the architected single-phase constituents, irrespective of the reinforcement size. The hybrid architectures exhibited a bending dominated response with a similar yield strength value to that of the softer FCC phase and an energy absorption that can be predicted by the rule of mixtures. Deformation under compression proceeds mostly in a homogeneous fashion by strut bending.
- In the peak-aged condition, hybridization led to a significant improvement of the mechanical behavior with respect to that of the individual constituents. Indeed, while in this microstructural condition all lattices (single-phase and hybrid) exhibited stretch-dominated behaviours, hybridization resulted, simultaneously, in a higher yield strength and higher levels of absorbed energy, which for some architectures exceeded the predictions of the rule of mixtures.
- The mechanism allowing for increased damage tolerance and higher levels of absorbed energy in selected peak-aged hybrid lattices consists on the hindering of shear band propagation by interphase boundaries. In particular, for this study, interphase boundaries parallel to the applied stress proved to be the most effective obstacles to shear band propagation. Thus, the optimum arrangement of reinforcements must be in such a way to maximize interphase boundary – shear band interactions.
- The effect of hybridization is also a function of the size of the reinforcements. In particular, below a critical size, the lattice behaves as a reinforced "single-phase" structure, in which a single shear band traverses the entire lattice width. The presence of the reinforcements leads to an increase in the stress required for the nucleation of the shear band in comparison to that required in the single-phase FCC lattice.
- Our results prove that the efficiency of lattice hybridization is highly dependent on the microstructure of the base material and on the size of the reinforcement lattice domains. It is therefore our contention that other approaches aiming to improve the mechanical behavior of lattices, including functional grading [1], nesting, interpenetration, and multi-material fabrication [2,3], should consider microstructure as a design criterion.

8.4. Dynamic strain aging in Inconel 718 additively manufactured lattice structures

In summary, this research demonstrates that atomic scale phenomena such as DSA may manifest at the metamaterial level and that their occurrence is highly dependent on the lattice architecture. Since it is well known that DSA may significantly impact the macroscopic mechanical behaviour, this work highlights the importance of analyzing its incidence in additively manufactured lattice structures that are envisioned to have a structural function.

CHAPTER 9

Future work

Although the research work has presented an entirely novel perspective of effect of microstructure on the mechanical behaviour of additively manufactured lattice structures, it still demands further development. In fact, the research has paved a way for the involvement of microstructure to create efficient, damage-tolerant lattice structures. This chapter highlights the different research lines to further advance this exciting avenue of lattice structure design.

9.1. Expansion of lattice topologies and base materials

Presented work successfully investigated 'single crystal' lattice structures with BCC, FCC and HCP topologies, having Inconel 718 as the base material. The microstructure of lattices was specifically generated to possess peak-aged microstructure with γ'' precipitates and as-built microstructure with a supersaturated solid solution. The study pinpointed the crucial role of microstructure in the transition of the mechanical behaviour.

This novel finding of influence of microstructure on the mechanical behaviour of the lattice structures can be further investigated with various strut-based lattice topologies. There are innumerable strut-based topologies that can be formulated via mathematical equations, and are available in commercial software packages such as *nTopology*®. Chemical structure of organic and inorganic compounds can also be an inspiration for the topological design of innovative lattice structures. Sheet-based lattice structures is another regime that remains hugely unresearched from the viewpoint of microstructure design and its influence on their mechanical behaviour.

Since microstructure is the precursor for the transition in the mode of failure of lattice structures, it becomes only consistent to explore materials that possess the possibility to generate different microstructure states, as the base material for the lattice structures.

Precipitation is one of the metallurgical phenomena employed for strengthening of the material. Precipitation served as an alternative to generate a dissimilar microstructure than the as-built one in the presented work. Strengthening mechanisms such as dispersion strengthening, grain boundary strengthening, twinning can be used to create alternate microstructures depending upon the base material used. This can form a research path to observe the effect of different microstructural states on the mechanical behaviour of the lattice structures.

9.2. Additional means of hybridization

From the viewpoint of real time applications, a controlled mechanical response is absolutely critical in the case of lattice structures. Although the stretch-dominated behaviour signifies an improved strength of the lattice structures, the instabilities transpiring due to strain localization can negatively impact the usage of such lattice structures. Hybridization is one of the many approaches to improve the lattice strength and the damage tolerance.

Further advancement in the regards of hybridization can be explored by combining different topologies with varying strength levels. The sizes and distribution of constituent phases can be altered at will to examine the effectiveness of hybridization. The vast design space of lattice structures can be explored with a myriad of possible combinations of base materials, topologies and hybridization strategies.

9.3. Extension of dynamic strain aging

The study yielded a pioneering discovery of dependence of the material phenomenon of dynamic strain aging on topology of the lattice structures. Dynamic strain aging manifested as serrations in the plastic flow of as-built lattice structures in room temperature deformation. The topology dependent prevalence of dynamic strain aging occurs due to different levels of stress experienced by the lattice structures, in combination with varying strain rates and temperatures.

This study can be extended by achieving varying strength levels in identical lattice structures. The strength variation can be achieved by microstructural strengthening as explained in section 10.1 or hybridization as mentioned in section 10.2. The dependence on topologies can also be further examined by experimenting with different lattice topologies with a number of combinations of temperatures and strain rates.

ANNEX A

OPTIMIZATION OF STRUT DIAMETER

When fabricating a lattice structure, it is important to find the right parameters that are suitable to achieve the lightest structures possible. This section describes the procedure utilized for the fabrication of lattices with the smallest diameter possible but with a robust and reproducible mechanical behaviour.

With that purpose, six BCC lattice structures with strut diameters as 0.3, 0.4 and 0.5 mm were fabricated, two with each strut diameter. The selection of BCC topology and mentioned strut diameters is justified with a reference to an earlier study carried out by Leary et.al. [1], using Inconel 625 as the base material.

The lattice structures were fabricated with the unit cell dimensions of 2.5 x 2.5 x 2.5 mm^3 and the overall dimensions of 10 x 10 x 10 mm^3 via LPBF on Renishaw AM 400 system, described in detail in section 3.2 in Chapter 3. The composition of the base material, that is, Inconel 718 is indicated in table 4.1 from Chapter 4. The process parameters employed for the fabrication are enlisted in table A.1. The specific process parameters were chosen since they are optimized for bulk Inconel 718 from Renishaw. The support structure was detached from the lattices with an abrasive disc cutter (Struers Accutom 5) after the fabrication.

The fabricated lattices were tested in uniaxial compression at room temperature as per the ASTM E9-09 standard, with 0.5 mm/min crosshead speed on an identical universal testing machine described in section 3.4.1 in Chapter 3.

Table A.1. LPBF process parameters

Laser Power	Layer Height	Hatch Distance	Exposure Time	Point Distance	Strategy
200 W	30 µm	90 µm	50 µs	70 µm	Meander

Optimal strut diameter for the lattice structure was selected on the basis of visual inspection and uniaxial compression. Figure A.2 illustrates the fabricated lattice structures with varying strut diameters and the stress-strain curve plotted from the load-displacement of uniaxial compression testing.

In the case of the lattices with 0.5 mm and 0.4 mm strut diameters, the stress increases with strain monotonically, then remains comparatively constant during a plateau stage, before a final increase due to lattice collapse. The final sharp rise in stress, indeed, indicates the interlocking of struts with no further room for compression. The stress-strain curve corresponding to the 0.3 mm strut diameter lattice shows no significant strength due to the breakage of struts immediately upon the application of the compressive stress.

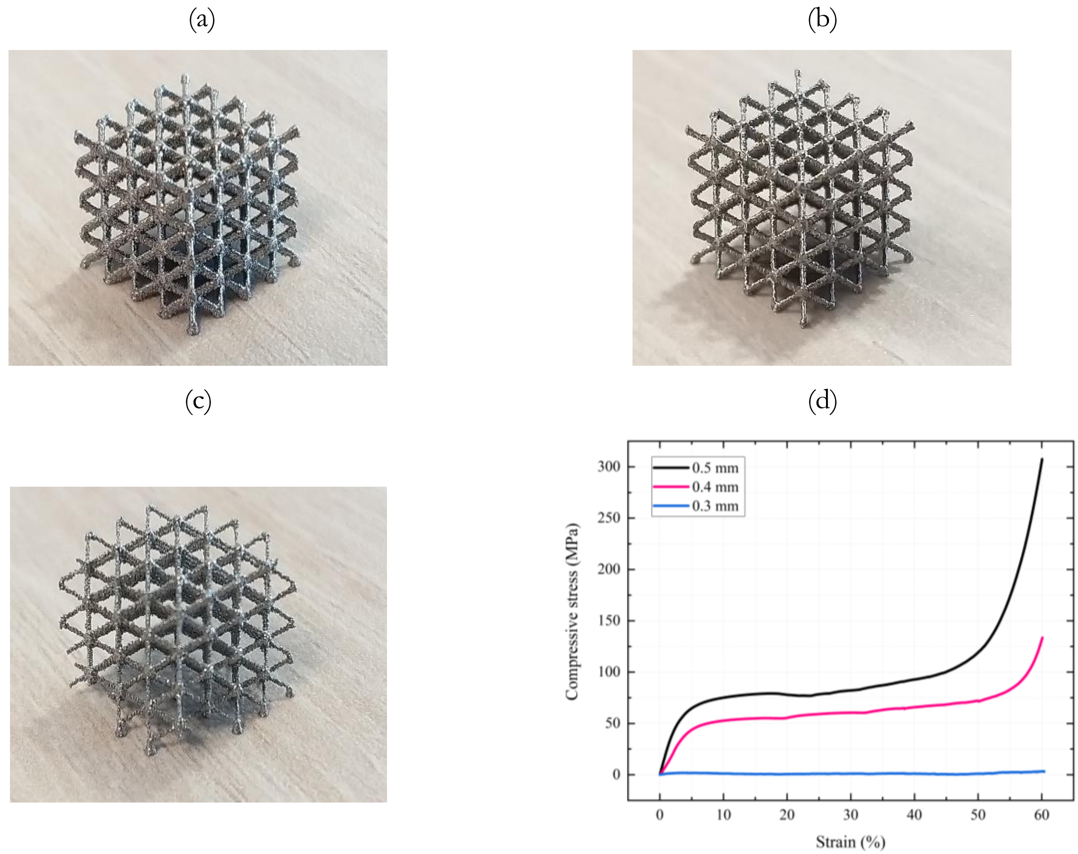

Figure A.1. BCC lattice structures fabricated with process parameters from Table A.1 with strut diameters (a) 0.5 mm, (b) 0.4 mm, (c) 0.3 mm and (d) compressive stress-strain curve for room temperature compression.

Since the strut diameters of 0.4 and 0.5 mm appear to endow the built lattices with a relatively similar mechanical behaviour, the choice between these two diameters was guided by the observations of Leary et. al. [1] who reported an increase of the internal porosity of LPBF printed Ni-superalloy lattices with increasing strut diameter. On the basis of this observation, the 0.4 mm strut diameter was selected as the optimal one. Henceforth, all the results correspond to lattices with strut diameter 0.4 mm.

Bibliography

[1] M. Leary, M. Mazur, H. Williams, E. Yang, A. Alghamdi, B. Lozanovski, X. Zhang, D. Shidid, L. Farahbod-Sternahl, G. Witt, I. Kelbassa, P. Choong, M. Qian, M. Brandt, Inconel 625 lattice structures manufactured by selective laser melting (SLM): Mechanical properties, deformation and failure modes, Mater. Des. 157 (2018) 179.

ANNEX B

OPTIMIZATION OF LPBF PROCESS PARAMETERS

Process parameter optimization is one of the most critical steps in LPBF processing in order to avoid, additionally, the formation of defects during solidification and to achieve the desired microstructures. Moreover, the retention of geometrical features is also imperative in the case of lattice structures.

To achieve maximum density, total 23 lattices were fabricated, with an optimized strut diameter of 0.4 mm and identical unit cell dimensions, as described in Annex A. However, the global dimensions were reduced to 7.5 x 7.5 x 7.5 mm^3 to save building time, with a layer thickness of 30 μm and meander scanning strategy. The fabrication was performed with a Renishaw AM 400 system, described in detail in section 3.2 in Chapter 3. The elemental composition of Inconel 718 is similar as mentioned in table 4.1 from Chapter 4.

The cross section (surface perpendicular to the build direction) of the lattice structures was imaged using an optical microscope (Olympus BX-51) for porosity assessment. The tool of multiple image alignment (MIA) was utilized to create a stitched image. The stitched image is essentially a high-resolution panorama obtained by combining and overlapping multiple optical micrographs. The stitched images were processed to obtain a quantitative fraction of porosity with the help of ImageJ software.

The optimization was carried out in two steps. In the first step, an array of combinations of process parameters was designed, as indicated in table B.1. Eight new combinations were considered, together with the one mentioned in Table A.1 from Annex A for the sole purpose of comparison. These nine combinations were replicated omitting the 'border parameters', therefore making the array consisting 18 combinations altogether.

To investigate the presence of porosity, the lattices fabricated in accordance with the process parameters indicated in table B.1 were examined to calculate the % porosity. Table B.2 shows the respective vales of % porosity for the combinations mentioned in table B.1. All the respective lattice and pore areas are in mm^2. Figure B.1 displays some optical micrographs pertaining to sample number 4 and 7 from tables B.1 and B.2 as examples.

Table B.1. LPBF process parameters employed in step-1

Fill power (W)	Border power (W)	Scan speed fill (mm/s)	Scan speed border (mm/s)	Hatch distance (μm)	Energy density fill (J/mm³)	Energy density border (J/mm³)	Upskin		Downskin	
							Border	Passes	Border	Passes
300	150	875	333	90	126.98	333.67	1	4	5	1
250	150	875	333	90	105.82	333.67	1	4	5	1
150	150	875	333	90	63.49	333.67	1	4	5	1
100	100	875	333	90	42.33	222.44	1	4	5	1
200	150	875	333	50	152.38	333.67	1	4	5	1
200	150	875	333	70	108.84	333.67	1	4	5	1
200	150	875	333	100	76.19	333.67	1	4	5	1
200	150	875	333	90	84.66	333.67	1	4	5	1
200	200	1166.7	333	90	63.49	444.89	1	4	5	1

Table B.2. % Porosity calculated for step – 1

With borders	**1**	**2**	**3**	**4**	**5**	**6**	**7**	**8**	**9**
Pore area (mm^2)	0.52	0.31	0.23	0.09	0.36	0.12	0.33	0.26	0.18
Lattice area (mm^2)	12.52	10.98	9.92	8.76	11.36	6.43	11.22	9.40	11.81
% porosity	4.00	2.72	2.28	1.03	3.05	1.91	2.83	2.74	1.48
Without borders	**10**	**11**	**12**	**13**	**14**	**15**	**16**	**17**	**18**
Pore area (mm^2)	0.23	0.16	0.05	0.02	0.09	0.07	0.08	0.08	0.08
Lattice area (mm^2)	10.37	8.77	7.70	8.45	9.27	7.09	8.78	7.18	7.39
% porosity	2.20	1.80	0.70	0.30	1.00	0.96	0.92	1.13	1.10

It was observed that lattice cross sections with borders exhibit a superior geometrical form as compared to the ones without borders, as evident from Figure B.1. It was also noted that sample number 4 from Table 4.5 exhibits the lowest porosity in the category of lattices with border, seen from figure B.1 (c). However, the downskin was still observed to be irregular. Therefore, another optimization campaign was followed for the purpose of improving the downskin and understand the effect of borders for the process parameters of sample 4.

(a) (b) (c)

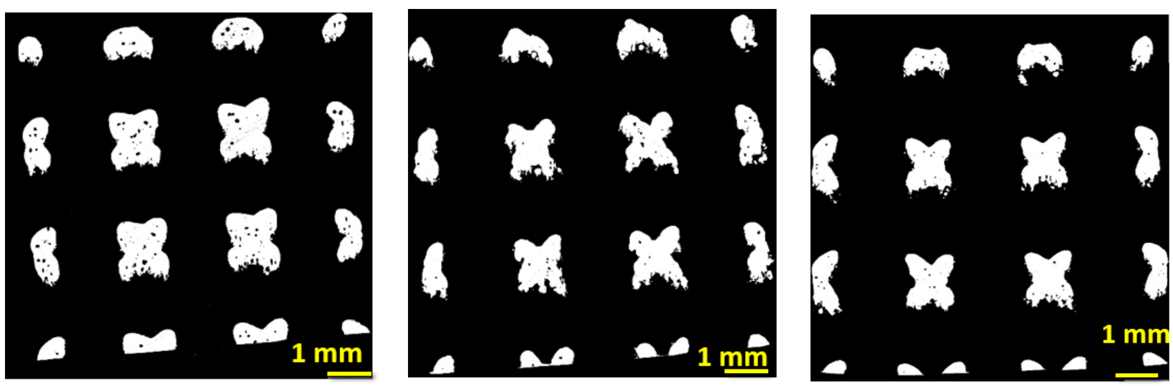

Figure B.1. Optical micrographs of lattices from Table B.1 processed in ImageJ software. (a) Sample 7 with border, (b) sample 7 without border, (c) sample 4 with border

In the second step of optimization, to refine the geometry and the density of the lattices further, this time varying the downskin parameters and number of volume borders, as illustrated in table B.3. The laser power, border power, scan speed fill, scan speed border, hatch distance, energy density fill and energy density border were selected as for combination number 4 from Table B.1.

Table B.3. LPBF process parameters employed in step-2

Upskin		Downskin		Volume border
Border	Passes	Border	Passes	
1	4	4	1	1
1	4	3	1	1
1	4	4	2	1
1	4	3	2	1
1	4	3	1	2

Again to investigate the internal porosity and contour of the lattice, porosity analysis was carried out with the help of ImageJ software. Table B.4 shows the values of % porosity for the levels of parameters indicated in table B.3. All the respective lattice and pore areas are in mm^2.

Table B.4. % Porosity calculated for step – 2

With borders	**1**	**2**	**3**	**4**	**5**
Pore area (mm^2)	0.005	0.008	0.009	0.05	0.035
Lattice area (mm^2)	5.34	5.42	5.94	7.74	7.91
% porosity	0.10	0.15	0.15	0.64	0.44

It was observed that border is indeed important for maintaining the geometry of the lattice, as evident from figure B.2 (a) showing irregular form but low porosity. On the contrary, figure B.2 (b) shows a relatively regular geometric form with a lower porosity value of 0.44% (comparing to sample 4). Thus, process parameters pertaining to sample number 5 from table 4.4 were selected and are used throughout the text as optimized parameters.

(a) (b)

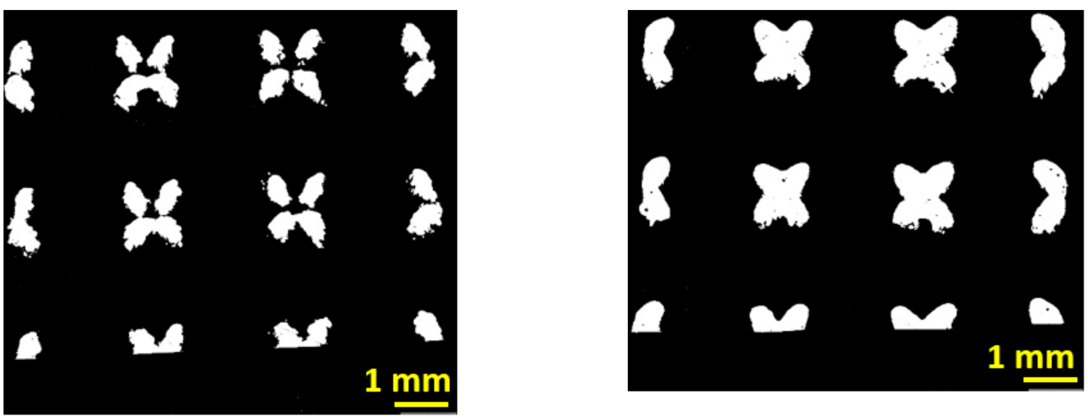

Figure B.2. Optical micrographs of lattices from Table B.4 processed in ImageJ software. (a) Sample 3, (b) sample 5

It was concluded that it is difficult to find a balance between a well-defined contour and a low level of porosity. There is a clear influence of selection of scanning parameters on defining the border, in order to better retain the geometrical shape of the downskin in the lattice and to achieve a significant low level of porosity.

ANNEX C

ASSESSMENT OF OXIDATION IN HEAT-TREATED INCONEL 718 LATTICE STRUCTURE

As seen in full detail in preceding chapters, microstructure design has been carried out by post-processing heat-treatments. The latter may, however, compromise the mechanical performance of the lattice structures by promoting the formation of surface oxides. An assessment of the surface of lattice structures is, thus, essential to examine the degree of oxidation occurred during heat-treatment. This section compares, as well, the oxide layer in as-built and heat-treated LPBF manufactured lattices.

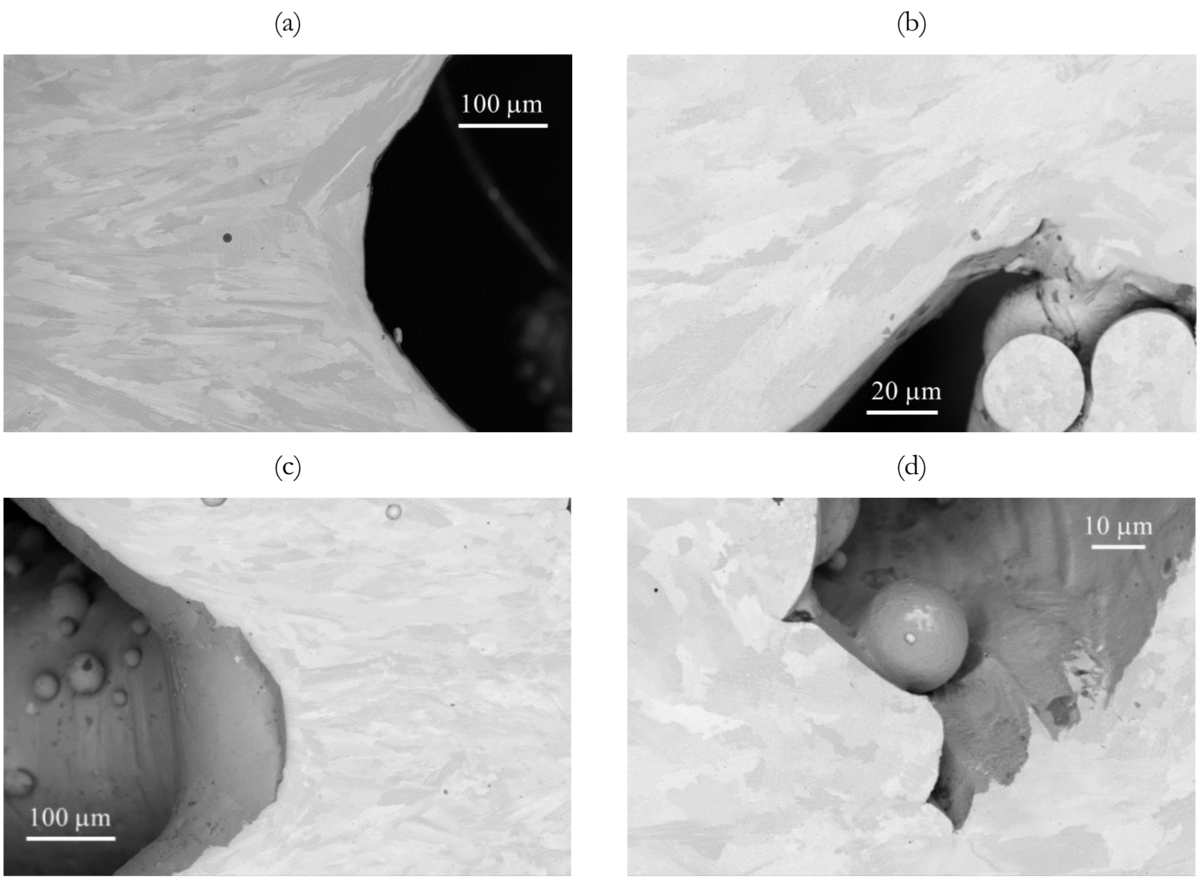

Figure C.1. SEM micrographs illustrating the surface of (a), (b) the as-built lattice, and (c), (d) the heat-treated lattice imaged with backscattered mode. Imaging was performed along a cross-section perpendicular to the building direction.

A lattice structure from parameter optimization campaign was heat-treated with a peak-aging heat treatment as explained in section 5.2 of Chapter 5. For the examination of degree of oxidation, polished surfaces of as-built and muffle furnace treated lattice structures were examined using a scanning electron microscope (SEM) (FEGSEM, FEI Helios Nano-Lab), using the backscattered electron signal. Numerous SEM micrographs at various magnification levels were captured at an operating voltage of 5 kV and 13 nA current.

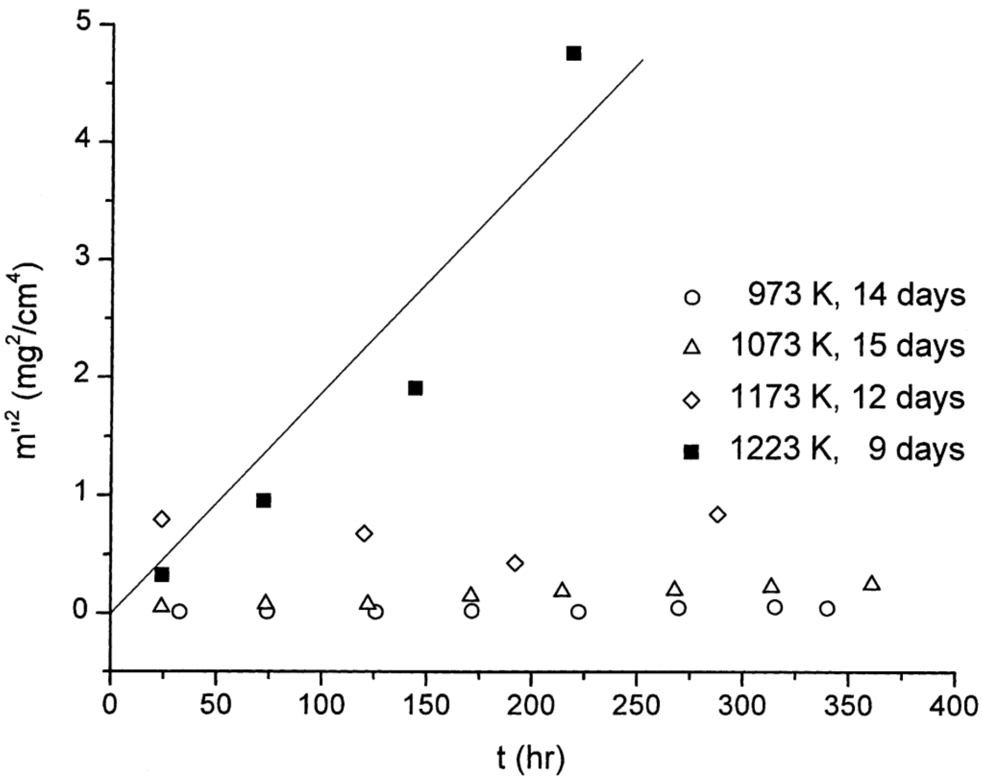

Figure C.2. Square of mass gain per unit area versus oxidation time for Inconel 718, oxidized at atmospheric pressure [5]

Oxidation refers to the chemical reaction in which a constituent metal and oxygen react to form oxides, when exposed to aqueous or gaseous environment. These oxides usually deteriorate the metal and degrade its mechanical performance. Ni-superalloys are distinguished for excellent oxidation resistance at high service temperatures [1]. Specifically for Inconel 718, the high temperature oxidation resistance is imparted by Cr and Al by forming chromia (Cr_2O_3) and alumina (Al_2O_3) scales over the surface [2], depending upon the alloying amount. For the present composition of Inconel 718 (Table 4.1, Chapter 4), the formation of chromia is favoured over alumina [3,4]. The growth of a chromia scale is maintained by a slow diffusion of Cr ions through the chromia scale to reach the oxide-gas interface. The diffusion can also take place inside when the Cr ions react with O ions at the metal-oxide interface [4].

The Cr_2O_3 scale remains stable up to 900-950 °C, beyond which it converts into CrO_3, which is volatile and renders the surface unprotected [3,4,6]. The present work employs an isothermal heat treatment in which Inconel 718 is held at 718 °C for 6 hours. Therefore, the theoretical probability of decomposition of the protective Cr_2O_3 scale in the case of heat-treated Inconel 718 lattice structures is negligible. SEM imaging was nevertheless carried out in order to fully rule out the presence of a deleterious oxide layer in the heat-treated lattices. Figure C.1 displays SEM micrographs imaged using backscattered electrons that illustrate the surface of the as-built and heat-treated lattice structures. It is apparent that no distinguishable oxide film is present.

Oxidation kinetics in Inconel 718 follows a parabolic reaction rate. Greene and Finfrock [5] investigated the low temperature oxidation rate of Inconel 718 and they concluded that this superalloy gets effectively passive at temperatures below 950 °C during the first 24 hrs of heat exposure, as the oxide scale formed efficiently prevents further oxidation at lower temperatures. Mass gain is another indicator of oxidation in metals [7]. Figure C.2 [5] shows that the mass gain due to oxidation was insignificant even after 14 days at 700 °C (973 K). This observation was verified by measuring the mass of the lattice structures before and after the heat treatment, tabulated in table C.1. This attests to the fact that the heat-treatment at 718 °C for 6 hours, used to promote precipitates in Inconel 718 lattice structures, did not form any detrimental oxide scale.

Table C.1. Weight of lattice structures before and after heat treatment

Weight before heat treatment (g)	Weight after heat treatment (g)
34.37	34.32
34.47	34.4
34.59	34.45

Bibliography

[1] A. P. Mouritz, Introduction to aerospace materials, Woodhead Publishing, Cambridge, UK, 2012.

[2] T. M. Pollock, S. Tin, Nickel-Based Superalloys for Advanced Turbine Engines: Chemistry, Microstructure, and Properties, J. Propuls. Power, 22 (2006) 361-374.

[3] M. Kutz, Handbook of Environmental Degradation of Materials, Elsevier, 2018.

[4] T. Sanviemvongsak, D. Monceau, B. Macquaire, High temperature oxidation of IN 718 manufactured by laser beam melting and electron beam melting: Effect of surface topography, Corros. Sci. 141 (2018) 127-145.

[5] G. A. Greene, C. C. Finfrock, Oxidation of Inconel 718 in Air at High Temperatures, Oxid. Met. 55, (2001) 505-521.

[6] S. Kathiravan, G. S. Kaliaraj, A.M. K. Kirubaharan, R. R. Kumar, Study of oxide layer formation on Inconel 718 during isothermal oxidation between 800 ◦C to 1200 ◦C in hot air, Ceram. Int. 48 (2022) 36012–36020

[7] S. J. Park, S. M. Seo, Y. S. Yoo, H. W. Jeong, H. J. Jang, Effects of Cr, W, and Mo on the High Temperature Oxidation of Ni-Based Superalloys, Materials, 12 (2019) 2934-2945.

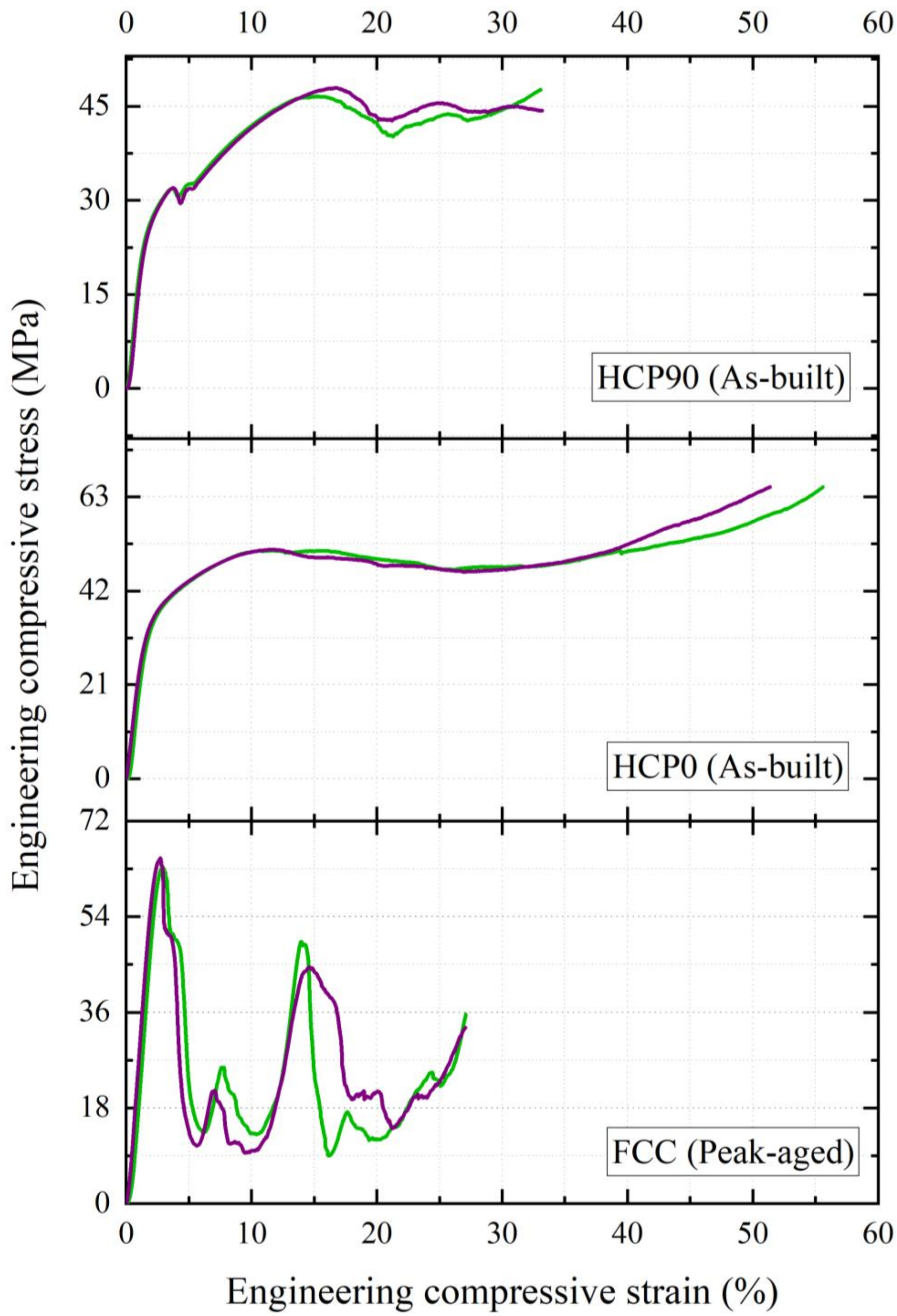

Supplementary Figure S1. Reproducibility of mechanical tests. Engineering compressive stress-strain curves corresponding to room temperature tests of several lattices (2 per condition).

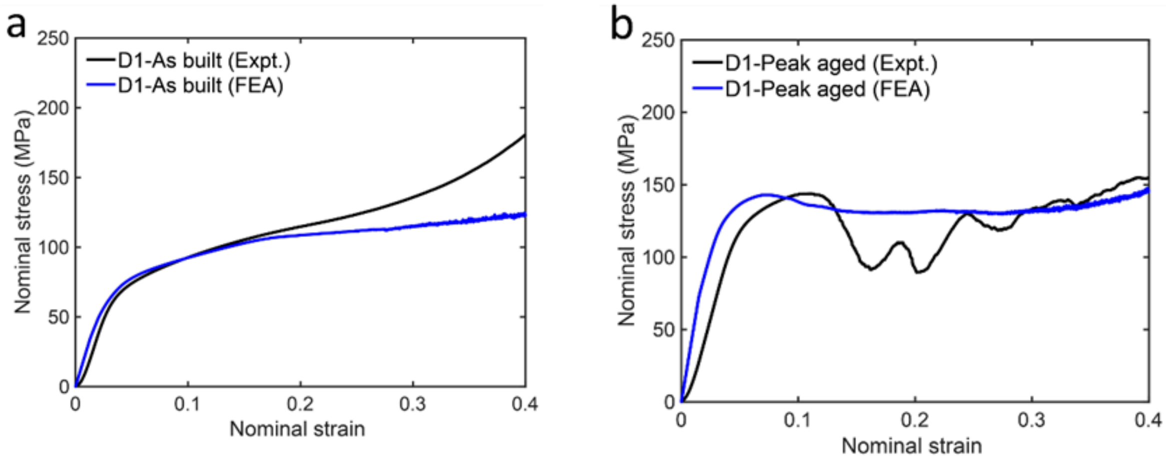

Supplementary Figure S1. Comparison of the room temperature compression stress-strain curves obtained from experiments and from FEA. (a) As-built D1; (b) Peak-aged D1

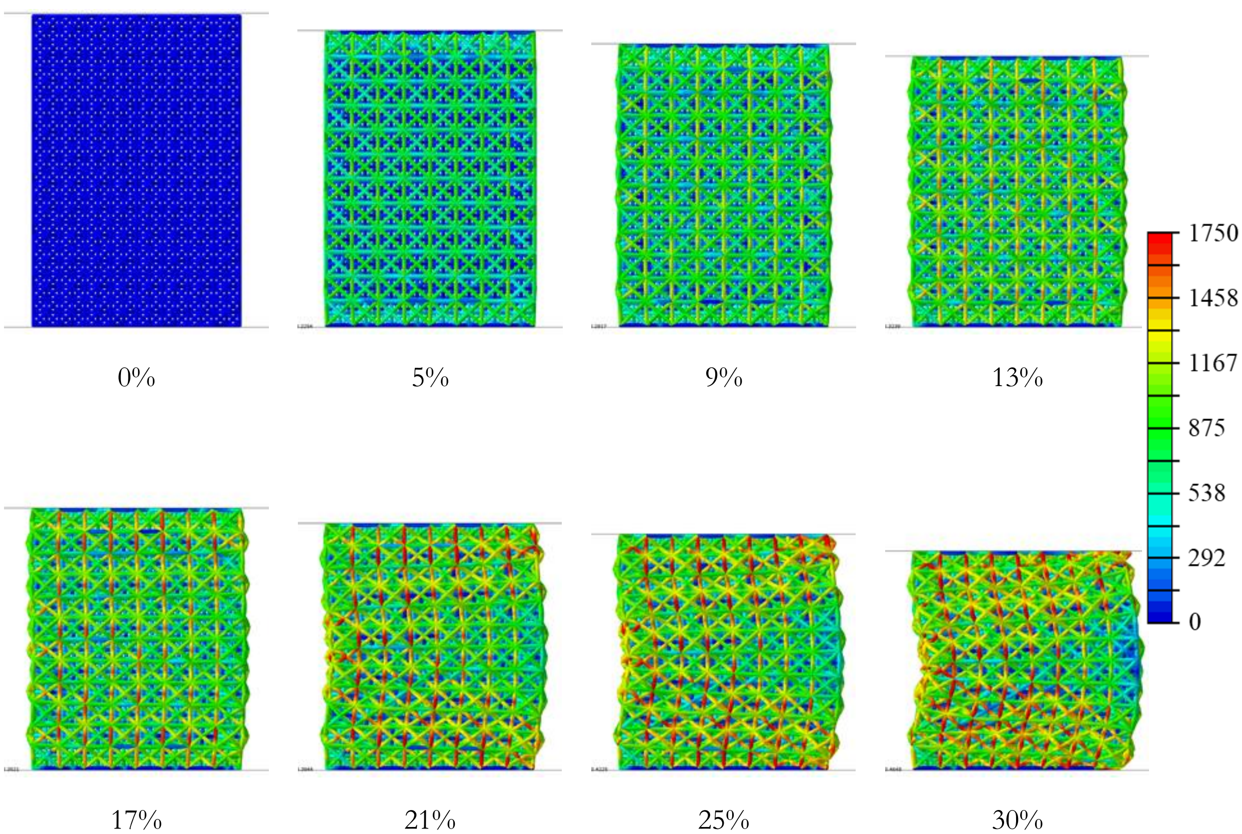

Supplementary Figure S2. Stress distribution at different global compression strain levels (indicated below each image) in the as-built D1 lattices. The scale bar indicates the Von Mises stress levels in MPa, measured by FEA.

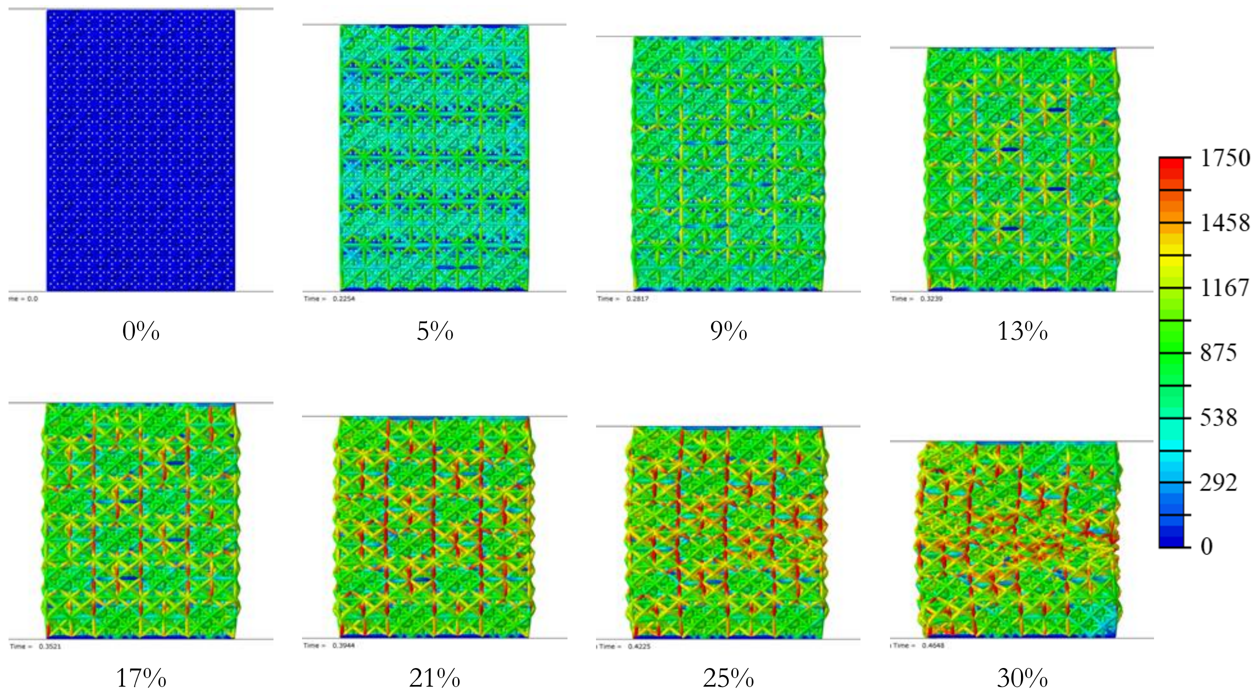

Supplementary Figure S3. Stress distribution at different global compression strain levels (indicated below each image) in the as-built D2 lattices. The scale bar indicates the Von Mises stress levels in MPa, measured by FEA.

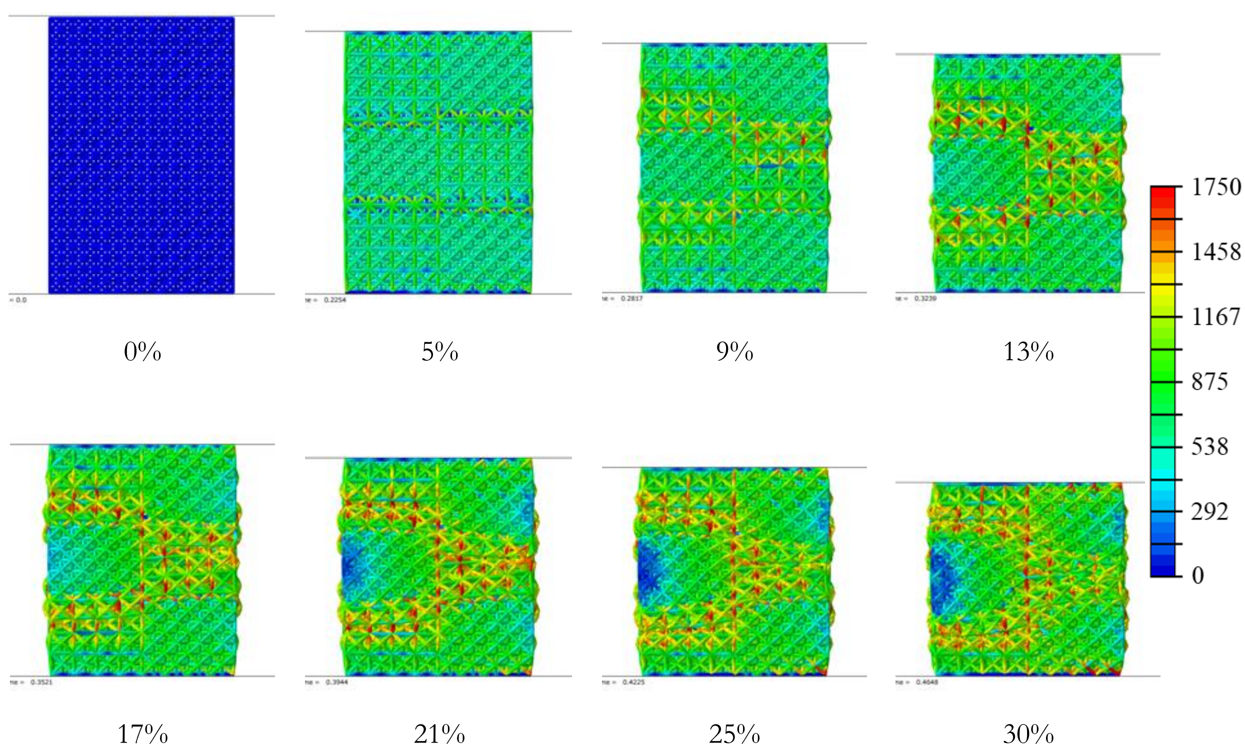

Supplementary Figure S4. Stress distribution at different global compression strain levels (indicated below each image) in the as-built D4 lattices. The scale bar indicates the Von Mises stress levels in MPa, measured by FEA.

(a)

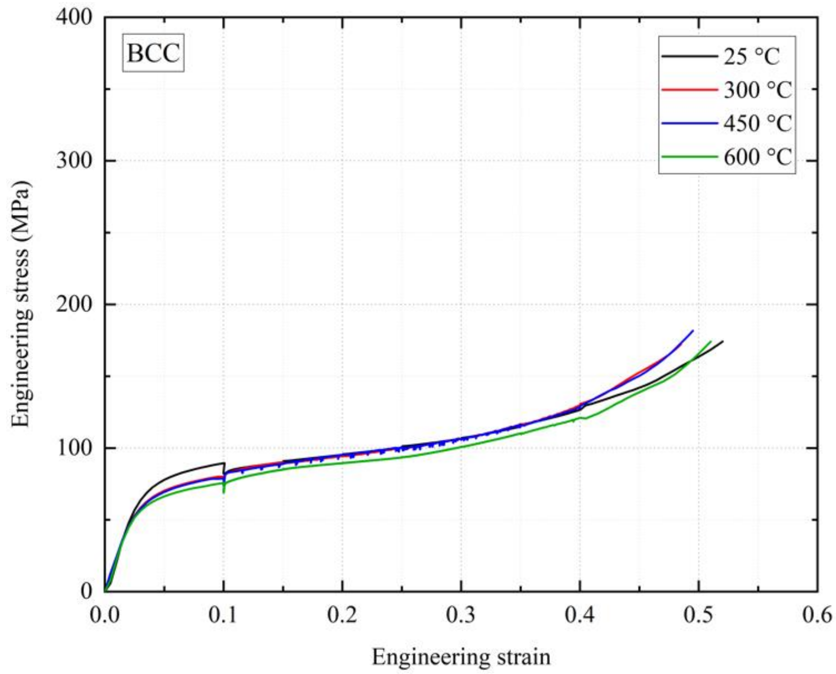

(b)

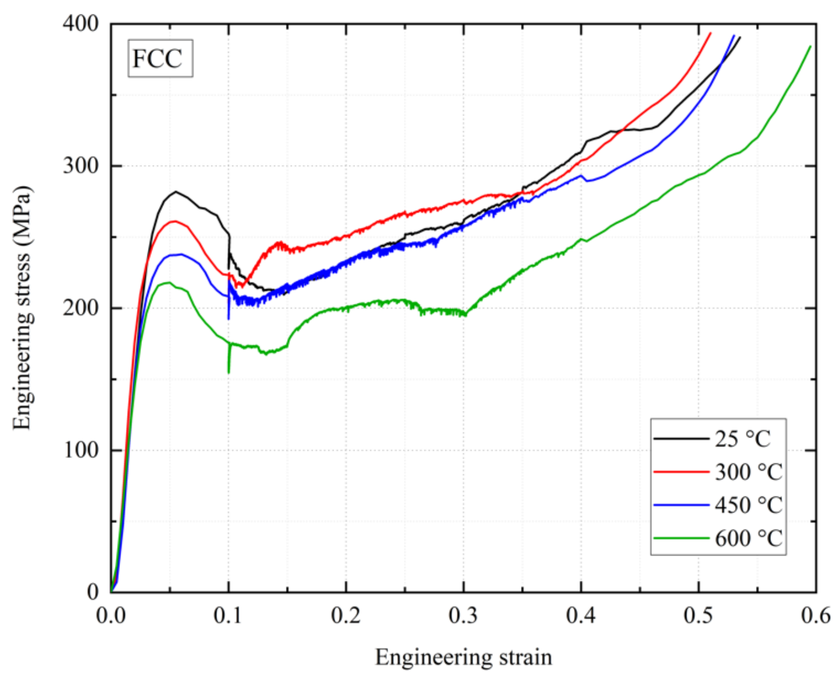

Supplementary Figure S1. Strain rate jump tests carried out in the (a) BCC and (b) FCC lattices at the investigated temperatures. The sequence of strain rates that were selected is listed in supplementary Table S1.

Supplementary Table S1. Sequence of strain rates employed selected for the strain rate jump tests in the BCC and FCC lattice structures.

Strain step	**Strain rate (s^{-1})**
0 – 0.1	$5x10^{-2}$
0.1 – 0.15	$1x10^{-5}$
0.15 – 0.2	$5x10^{-5}$
0.2 – 0.25	$1x10^{-4}$
0.25 – 0.3	$5x10^{-4}$
0.3 – 0.35	$1x10^{-3}$
0.35 – 0.4	$5x10^{-3}$
0.4 ~	$5x10^{-2}$